Spintronics Devices for Advanced Memory and Computing Applications

A DISSERTATION

SUBMITTED TO THE FACULTY OF

THE UNIVERSITY OF MINNESOTA

BY

Zhengyang Zhao

IN PARTIAL FULFILLMENT OF THE REQUIREMENTS

FOR THE DEGREE OF

DOCTOR OF PHILOSOPHY

Advisor: Prof. Jian-Ping Wang

June 2021

© Zhengyang Zhao 2021

Acknowledgments

My dissertation could not have been completed without the incredible support from my mentors, colleagues, family, and friends. It is with their support that this work has been possible.

I would especially like to thank my research advisor, Prof. Jian-Ping Wang, for providing me the opportunity to work here in a collaborative, productive, friendly, and supporting environment in which I conducted my research with talented researchers. I'm grateful for his continuous guidance, support, and encouragement during the past years, without which I wouldn't have gone this far with my PhD study.

I am very honored to have Prof. Sachin Sapatnekar, Prof. Chris Kim and Prof. Xiaojia Wang as my final examination committee members and thankful for their helpful feedback and suggestions. I would also like to thank Prof. Randall Victora, Prof. Beth Stadler, and Prof. Paul Crowell for their support and discussion on my research topics.

The works presented in this thesis are completed through extensive collaborations. I'm truly appreciative of all the collaborations and discussions from all my external collaborators, Prof. Supriyo Bandyopadhyay, Prof. Jayasimha Atulasimha and Dr. Noel D'Souza from Virginia Commonwealth University, and Prof. Christian Binek and his students from University of Nebraska-Lincoln. My sincere gratitude and appreciation for enjoyable and fruitful collaborations also go to all my collaborators within University of Minnesota, especially Prof. Sachin Sapatnekar and his students, Dr. Zhaoxin Liang, Dr. Meghna Mankalale, and Masoud Zabihi, Prof. Chris Kim and his students, Dr. Ibrahim

Ahmed and Dr. Jeehwan Song, Prof. Ulya Karpuzcu and her students, Zamshed Chowdhury and Salonik Resch.

I am also extremely appreciative of all the support I've received from my colleagues within Wang's group. Their engaging discussion and close collaboration provide additional support throughout my research journey. I would especially like to thank Dr. Bin Ma, Dr. Mahdi Jamali, Dr. Delin Zhang, Dr. Junyang Chen, Dr. Peng Sheng, Dr. Angeline Smith, Dr. Yang Lv, Dr. Mahendra DC, Dr. Xuan Li, Dr. Jinming Liu, Dr. Kai Wu, Dr. Diqing Su, Thomas Peterson, Protyush Sahu, Brandon Zink, Deyuan Lyu, Yihong Fan, Hongshi Li, and Onri Jay Benally. It is my great pleasure to work with these talented scholars.

My special thanks go to Dr. Gordon Stecklein, Dr. Timothy Peterson and Zhen Jiang in Prof. Paul Crowell's lab for their support and help on the PPMS system through years, and my undergraduate classmate and good friend Dr. Qingzhong Deng, for his kindly assistance on my COMSOL simulations. Moreover, I would like to thank the staff at Minnesota Nano Center, Characterization Facility, and Institute for Rock Magnetism, for their kind support on the experimental platforms. Also, I'm appreciated for the support from C-SPIN center of Semiconductor Research Corporation (SRC), and the support of the Doctoral Dissertation Fellowship from the University of Minnesota.

Finally, my deepest gratitude goes to my parents, who gave me unconditional love and supports despite decades of ups and downs, and my wonderful friends, Rui Ma, Zengyuan Liu, Yang Zhao, Meng Ma, Bosi Yang, Shirley Zou and Ellen, to name a few, who gave me support and encouragement to go through the tough time during the pandemic, and all the people who have helped, encouraged and guided me become who I am today.

Abstract

Spintronics, as a beyond-CMOS technology, provides many possibilities for the next-generation information storage and processing. This thesis focuses on the development of novel spintronics devices towards low-energy, high-performance memory and computing applications. In this thesis, we present the manipulation of a magnetic storage unit either with a current-induced spin-orbit torque (SOT) or using a voltage via piezoelectric strain. We also propose a novel in-memory computing architecture based on the SOT storage cell.

For the first part, the SOT induced switching is explored for both ferromagnets (FM) and antiferromagnets (AFM) systems. For the study of FM, two fundamental limitations related to the switching of a perpendicular magnetized system are solved. First, this thesis expands the scope of spin torque switchable materials, from interfacial PMA magnets only, to bulk PMA magnets, which have a better thermal stability when scaled down and are regarded as potential candidates in future MRAM. Second, the difficulty of field-free SOT switching is addressed by developing a dipole-coupled composite device. Compared with competitive strategies, the composite device is the most compatible one with existing MRAM technologies and readily applicable for SOT-based memory and logic devices. Beyond the exploration of SOT in FM, this thesis also attempts to tackle the spin torque induced switching in an AFM system, by characterizing the devices with a widely adopted 8-terminal geometry. It is discovered the "saw-tooth" signal, which was previously regarded as the evidence of AFM switching, actually originates from thermal artifacts.

Then, the voltage-controlled device is studied utilizing a piezoelectric / magnetic tunnel junction (MTJ) coupled structure for ultra-low power writing of data. Voltage-

controlled toggling of MTJ is achieved via the piezoelectric strain generated from a pair of local gates. The local gating design allows efficient manipulation of individual cells and opens the door towards realistic strain-based MRAM.

Finally, a new architecture for computational random-access memory (CRAM) is invented based on the 3-terminal SOT-MTJ. Similar to the STT-MTJ based counterpart, the SOT-CRAM allows *true* in-memory computing and thereby meets the energy and throughput requirements of modern data-intensive processing tasks. Moreover, the excellent features of SOT unit cells would provide a large improvement in speed and energy compared with other in-memory computing paradigms.

Table of Contents

Acknowledgments i

Abstract iii

List of Tables viii

List of Figures ix

List of Abbreviations xx

Chapter 1 Introduction 1

1.1 Spintronics basics 1

1.1.1 Magnetic tunnel junctions (MTJ) 1

1.1.2 Perpendicular magnetic anisotropy (PMA) 3

1.2 MRAM writing mechanisms 4

1.2.1 Current-induced switching via spin torques 4

1.2.2 Voltage-induced switching via magnetoelectric effects 12

1.3 Spintronics devices for logic and computing applications 14

1.3.1 Logic-in-memory paradigms with NVMs 14

1.3.2 Spintronics devices for logic operations 16

1.3.3 MTJ based in-memory-computing 20

1.4 Dissertation overview 30

Chapter 2 SOT Switching of a Bulk-PMA Magnet 32

2.1 Motivation and background 32

2.2 Experimental methods 34

2.3 Results and discussions 37

2.3.1 Measurements with an out-of-plane field 37

2.3.2 Measurements with an in-plane field 41

2.3.3 Evaluation of the spin Hall angle 45

2.4 Summary 47

Chapter 3 Robust Field-Free SOT Switching 48

3.1 Motivation and background 48

3.2 Experimental methods 51

3.2.1 Sample preparation and characterization 52
3.2.2 Micromagnetic simulation 55
3.3 Results 56
3.3.1 Measurements with an out-of-plane field 57
3.3.2 Measurements with an in-plane field 61
3.3.3 Robust external-field-free switching 66
3.4 Discussions 67
3.4.1 Comparison of the nanopillars with different aspect ratios 67
3.4.2 Thermal stability of the IPL 70
3.4.3 Analysis on the effect of non-uniform stray field 72
3.4.4 Simulation of field-free switching for 300 × 150 nm^2 nanopillar 74
3.4.5 Simulation of field-free switching for 10 × 10 nm^2 nanopillar 76
3.4.6 Comparison with other types of field-free SH devices 79
3.5 Summary 81
Chapter 4 Voltage Control of MTJ via Piezoelectric Strain 82
4.1 Motivation and background 82
4.2 Experimental methods 85
4.3 Results 88
4.3.1 E-field tuning of the magnetic anisotropy 88
4.3.2 E-field controlled MTJ toggling 94
4.4 Discussions 97
4.4.1 Details on the piezoelectric finite element simulations 97
4.4.2 The variation of the minor loop with different E-fields 101
4.4.3 Result by interchanging the soft layer and the hard layer in MTJ 103
4.4.4 Quantification of the voltage-induced anisotropy 104
4.4.5 Device scalability and energy dissipation 106
4.5 Summary 107
Chapter 5 SOT Switching of Antiferromagnets: Is It Real? 110
5.1 Motivation and background 110
5.2 Experiment with the 8-terminal geometry 114

5.3 Experiment with separated writing and probing paths 119
5.4 Analysis on the quadratic relationship between I_w and ΔR_{xy}........................ 122
5.5 Summary... 125
Chapter 6 SOT-MTJ for Computational Random-Access Memory (CRAM).... 126
6.1 Background of CRAM.. 126
6.2 SOT-CRAM architecture design 129
6.3 SOT-CRAM device feasibility 133
6.4 Summary... 140
Chapter 7 Thesis Conclusion... 141
Bibliography 143
Appendix A. Source Code of SOT Switching Macrospin Model........................... 165
Appendix B. Source Code of SOT Switching Micromagnetic Model 174
Appendix C. Publication List.. 186

List of Tables

Table 1. Sputtering conditions and characteristics of heavy metals Ta and W 35

Table 2. Simulation parameters for SH switching of 10×10 nm^2 nanopillar 78

Table 3. Comparison of three types of external-field-free SH devices 80

Table 4. Strain generated in different gating schemes (with $V_g = +50$ V) 101

Table 5. Status of lines and transistors in SOT-CRAM for different modes 133

Table 6. SOT-MTJ specifications in SOT-CRAM... 134

List of Figures

Figure 1-1. Schematics of in-plane MTJ (i-MTJ) and perpendicular MTJ (p-MTJ). 2

Figure 1-2. Schematics of **(a)** STT-MTJ and **(b)** SOT-MTJ.. 5

Figure 1-3. Magnetization dynamics described by LLG equation.................................. 6

Figure 1-4. STT switching of the MTJ shown in **Figure 1-2 (a)**. **(a)** Directions and relative strengths of the anti-damping torque (denoted by the blue arrows) on the sphere of $\mathbf{m}$, with $\boldsymbol{\sigma}$ pointing to $+z$. **(b)-(c)** STT switching trajectory of $\mathbf{m}$........... 8

Figure 1-5. SOT switching of the MTJ shown in **Figure 1-2 (b)**. **(a)** Directions and relative strengths of the anti-damping torque (denoted by the blue arrows) on the sphere of $\mathbf{m}$, with $\boldsymbol{\sigma}$ pointing to $-x$, and **(d)** directions and relative strengths of the torque of an external field that points to $+y$. **(b)-(c)** Trajectory of $\mathbf{m}$ with SOT exerted. No external magnetic field is applied. **(e)-(f)** Same as **(b)-(c)** except an external field pointing to $+y$ is applied. 11

Figure 1-6. Schematics for three types of magnetoelectric (ME) switching [39]........... 12

Figure 1-7. Possible evolution of the computing architecture [52]. **(a)** A conventional von-Neumann architecture with a separated processor (central processing unit, CPU) and memory; **(b)-(c)** The logic-near-memory (LNM) architecture with plane and 3D implementations by adding a small amount of logic units close to the memory or by adding more memory close to the processor. **(d)** The logic-in-memory (LIM) architecture attempts to embed computation capability into the memory, and to realize the unity of data storage and processing at the smallest grain in the same die. (Reprinted from ref. [52] with the permission from Springer). 15

Figure 1-8. **(a)** All-spin logic device. **(b)** Layout of the ASL-based majority gate [56]. (Reprinted from ref. [56] with the permission from Springer Nature). 17

Figure 1-9. **(a)** Two connected DW-MTJs that can communicate via current induced domain-wall motion [61]. **(b)** Logic unit based on a three terminal DW-MTJ [64,67]. (Reprinted from ref. [61] with the permission from IEEE)..... 18

Figure 1-10. Schematic of the MESO device [37,38]. (Reprinted from ref. [38] with the permission from Springer Nature). 19

Figure 1-11. Hybrid CMOS/MTJ logic network for **(a)** AND gate **(b)** OR gate and **(c)** XOR gate. "LB" and "RB" represent the left and right branches, respectively. The input operand *B* is encoded in the MTJ, while the input operand *A* is represented by the CMOS input voltage. The output signal *Q* can be obtained by a pre-charge sense amplifier (PCSA) [52]. (Reprinted from ref. [52] with the permission from Springer). 22

Figure 1-12. **(a)** Schematic of the CMOS/MTJ LIM architecture. **(b)** Full circuitry of the 1-bit full-adder based on the hybrid CMOS/MTJ LIM architecture. The input operand *B* is encoded in the MTJ, while the input operands *A* and C_i are represented by the CMOS input signals. The output *SUM* and C_o are obtained by PCSA [52,71]. (Reprinted from ref. [52] with the permission from Springer). 23

Figure 1-13. Another circuitry of the 1-bit full-adder based on the hybrid CMOS/MTJ architecture. Different from **Figure 1-12 (b)**, here all the logic inputs are represented by MTJs [63]. (Reprinted from ref. [63] with the permission from IEEE). 24

Figure 1-14. **(a)** Schematic of a STT-MRAM bank with additional peripheral circuitry for logic operations. **(b)** The key concept of using difference reference selections to perform logic operations [81]. (Reprinted from ref. [81] with the permission from IEEE).. 25

Figure 1-15. **(a)** Schematic of a spin-logic device based on a single MTJ element with three independent input lines A, B, and C. **(b)** The switching loops of MTJ operated under the oersted field generated from inputs A and B,

respectively [91]. (Reprinted from ref. [91] with the permission from AIP Publishing). 26

Figure 1-16. Schematic of the 2-input logic gate implemented by connected MTJs. The preset value of the output MTJ and the polarity and magnitude of the bias voltage V_b determine the type of logic gate. 27

Figure 1-17. **(a)** Schematic of the logic gate implemented with 3-input MTJs connected in parallel. **(b)** AP to P switching of the output MTJ for three different resistance states of the inputs [85]. (Reprinted from ref. [85] with the permission from AIP Publishing). 28

Figure 1-18. The STT-CRAM architecture [89]. (Reprinted from ref. [89] with the permission from IEEE). 29

Figure 2-1. Schematic illustration of Hall bar devices and the AHE measurement setup. 34

Figure 2-2. **(a)** The in-plane and out-of-plane hysteresis loops of Ta (5) / TbFeCo (1.8) / MgO (2) multi-layers. **(b)** the out-of-plane hysteresis loops for Ta (5) / TbFeCo (t) / MgO (2) multilayers, where t = 1.8, 2.2, and 2.5 nm, respectively. 36

Figure 2-3. **(a)** R_H-H_z loops measured with I_{ch} = 0.5 mA and 8mA respectively. **(b)** Coercive field H_c as a function of I_{ch}. 39

Figure 2-4. R_H variation upon the injection of a sequence of current pulses. The pulse amplitude is 10 mA and the pulse width is 1 ms. The out-of-plane field is applied with field direction reversed after each current pulse. The amplitude of the field is **(a)** H_z = 50 Oe and **(b)** H_z = 20 Oe. 40

Figure 2-5. Magneto-optical Kerr images of the Hall bar device with the magnetization direction pointing **(a)** upward and **(b)** downward, respectively. 41

Figure 2-6. R_H-I_{ch} loops measured with **(a)** H_y = −390 Oe, and **(b)** H_y = +390 Oe. (c) Critical current I_c as a function of H_y extracted from the R_H-I_{ch} loops. 42

Figure 2-7. R_H as a function of DC current at the presence of the transverse field H_x. (a) H_x = 120 Oe, (b) H_x = 200 Oe and (c) H_x = 500 Oe. 44

Figure 2-8. R_H as a function of **(a)** longitudinal field H_y or **(b)** transverse field H_x, for I_{ch} = ±4 mA respectively. Inset of **(a)**: the difference in the applied field for +2 mA and −2 mA when R_H is the same. 47

Figure 3-1. Previous solutions for the field-free SH switching. **(a)** Introduce an anisotropy gradient in the PMA layer to break the symmetry [139]. **(b)** Use an exchange-bias field to break the symmetry [140]. (Reprinted from ref. [139] and [140] with the permission from Springer Nature). 49

Figure 3-2. The proposed structure of a full SOT p-MTJ stack for external-field-free SH switching utilizing the composite structure. It is composed of a normal p-MTJ stack with an in-plane magnetized biasing layer placed on top, which can provide a stray field and lead to the deterministic SH switching. 51

Figure 3-3. In-plane and out-of-plane *M-H* hysteresis loops of the composite stack. Inset: out-of-plane *M-H* loops of the composite stack and the reference stack, respectively, in a narrow field range. 53

Figure 3-4. **(a)** Schematic of the composite structure Ta(5) / CoFeB(1.2) / MgO(2) / CoFeB(3) / capping, which is patterned into an elliptical nanopillar sitting on top of Ta Hall bar. **(b)** Scanning electron micrograph (SEM) image of the fabricated device and setup of the electrical measurement. The dimension of the elliptical pillar is 285×95 nm^2. 54

Figure 3-5. The R_H-H_z measurement results for the reference sample. **(a)** The schematic of the reference sample showing the magnetization configuration. **(b)** R_H-H_z loops measured with different I_{ch}. **(c)** Coercive field H_c (square symbol) and shift of loop H_{shift} (circular symbol) as a function of I_{ch}. 57

Figure 3-6. The R_H-H_z measurement results for the composite sample, with IPL // $-y$. **(a)** The schematic of the composite sample showing the magnetization configuration and stray field direction. **(b)** R_H-H_z loops measured with different

I_{ch}. **(c)** Coercive field H_c (square symbol) and shift of loop H_{shift} (circular symbol) as a function of I_{ch}. 58

Figure 3-7. The R_H-H_z measurement results for the composite sample, with IPL // $+y$. **(a)** The schematic of the composite sample showing the magnetization configuration and stray field direction. **(b)** R_H-H_z loops measured with different I_{ch}. **(c)** Coercive field H_c (square symbol) and shift of loop H_{shift} (circular symbol) as a function of I_{ch}. 58

Figure 3-8. Coercive field H_c (square symbol) and shift of loop H_{shift} (circular symbol) as a function of I_{ch}, for a composite device with IPL // $+x$. The device is with an elliptical pillar of 95×285 nm^2, where the long axis is along x-direction (the transverse direction) instead of along y-direction, and the channel width is 1 μm. 60

Figure 3-9. R_H-H_y loops measured with **(a)** I_{ch} = +0.55 mA and **(b)** I_{ch} = +0.35 mA for the composite sample. 62

Figure 3-10. R_H-I_{ch} loops under various H_y, which is gradually changed from −270 Oe to +270 Oe. Five points A-E representing five critical states of the device are labelled in the loops, which are corresponding to the A-E labels in **Figure 3-9 (a)**. Right: schematics illustrating the magnetization configurations of the five points A-E, where the lengths of the dash arrows represent the strengths of the fields. 63

Figure 3-11. Critical current I_c as a function of H_y extracted from the R_H-I_{ch} loops, for **(a)** IPL // $-y$ and **(b)** IPL // $+y$, respectively. I_c values obtained from clockwise (CW) and counter-clockwise (CCW) loops are plotted as different symbols. Solid lines are eye-guided fitting to the data. 65

Figure 3-12. R_H-I_{ch}(J_{ch}) loops measured without any external field. The IPL is initialized to IPL // $-y$ in **(a)** and IPL // $+y$ in **(b)**, respectively. 66

Figure 3-13. R_H variation upon application of a sequence of current pulses without external field. The pulse amplitude is 0.6 mA and pulse width is 10 μs. The configurations of IPL // $-y$ and IPL // $+y$ are plotted as different symbols. .. 67

Figure 3-14. Variation of H_c and H_{shift} versus I_{ch} for composite pillars with different aspect ratio. **(a)**, **(d)** SEM images of the device with **(a)** 300 × 120 nm^2 (2.5 : 1) pillar and **(d)** 300 × 150 nm^2 (2 : 1) pillar. **(b)**, **(c)** Coercive field H_c and loop shift H_{shift} as a function of I_{ch} for the 300 × 120 nm^2 composite device, extracted from the R_H-H_z loops, with IPL been initialized to IPL // −y in **(b)** and IPL // +y in **(c)**, respectively. **(e)**, **(f)** H_c and H_{shift} as a function of I_{ch} for the 300 × 150 nm^2 composite device, with IPL being initialized to IPL // −y in **(e)** and IPL // +y in **(f)**, respectively. 68

Figure 3-15. Critical current I_c versus external field H_y for composite pillars with different aspect ratio. **(a)** I_c versus H_y for the 300 × 120 nm^2 (2.5 : 1) composite pillar. **(b)** I_c versus H_y for the 300 × 150 nm^2 (2 : 1) composite pillar. The directions of IPL are all along $-y$. **(c)** The calculated y-component of the stray field, H_{stray}^{y}, generated from the IPL with different aspect ratios. 69

Figure 3-16. Coercive field of IPL versus channel current and the effect of IPL's thermal stability on the switching error. **(a)** The coercive field of IPL H_c^{IPL} as a function of various channel current I_{ch} applied. The three curves are for devices with 285 × 95 nm^2 (3 : 1), 300 × 120 nm^2 (2.5 : 1) and 300 × 150 nm^2 (2 : 1) pillars, respectively. The channel widths of all devices are 500 nm. **(b)**, **(c)** R_H variation upon application of a sequence of current pulses without external field for the composite device with 300 × 150 nm^2 (2 : 1) pillars. In **(b)** the pulse amplitude is 0.45 mA and the pulse width is 500 ms, in **(c)** the pulse amplitude is 0.53 mA and the pulse width is 500 ms. The directions of IPL are all along $+y$... 70

Figure 3-17. **(a)** Schematic showing the non-uniform stray fields from IPL // $-y$, and the resultant non-coherent switching of the magnetization. **(b)** Calculation results showing the stray field profile along the long axis of PL for the 300 × 150 nm^2

pillar. Inset: mapping of the stray field distribution on the PL, where the arrows show the strengths and directions of the in-plane component of the stray field, and color pixels show the strengths and directions of the z-component of the stray field (red = up, blue = down). 73

Figure 3-18. Calculated stray field depending on IPL thickness and PL-to-IPL distance for a 300 × 150 nm^2 elliptical pillar. **(a)-(c)** IPL's stray field profile along the long axis of the PL layer, with the same IPL thickness of 3 nm and different PL-to-IPL distances. (**d)-(f)** IPL's stray field profile along the long axis of the PL layer, with different IPL thickness and the same PL-to-IPL distance. 73

Figure 3-19. Simulated magnetization evolution in the PL of the 300 × 150 nm^2 pillar, under the non-uniform stray field shown in **Figure 3-17 (b)** and a constant channel current along $+y$ (the initial magnetization of PL is pointing down marked as blue color). Although the SHE alone cannot lead to a complete switching, the switching can be completed if involving STT or DMI driven domain wall motion. 75

Figure 3-20. Calculated stray field for a 10 × 10 nm^2 nanopillar. **(a)** Mapping of the stray field distribution across PL for the 10 × 10 nm^2 circular pillar, where the arrows show the strengths and directions of the in-plane component of the stray field, and color pixels show the strengths and directions of the z-component of the stray field (red = up, blue = down). **(b)** Stray field profile along y-axis across PL... 77

Figure 3-21. Micromagnetic simulation showing the switching curves for the 10 × 10 nm^2 nanopillar. The solid line represents SH switching under the stray field of IPL and the dash line represents the switching under a uniform external field of H_y = 550 Oe. Inset: top view of PL magnetization pattern of initial state, intermediate state, and final state. Other parameters of the simulation are shown in **Table 2**. 78

Figure 4-1. **(a)** Schematic showing how the ε-V property of the PMN-PT substrate is characterized. **(b)** In-plane strains ε in the PMN-PT (001) substrate as a function of applied average electric field or voltage. Solid line represents the major loop and dashed line represents the minor loop. The vertical jumps at the maximum E-fields result from the settling of the sample at those E-fields for 10 min. 85

Figure 4-2. **(a)** An optical micrograph image of the actual fabricated device. **(b)** Structure of the strain-MTJ. 86

Figure 4-3. The magnetic hysteresis loop of patterned MTJ films and the MR loop of a MTJ device on PMN-PT (001) without gate voltage application. The magnetic field is along the major axis of the pillars in the y-direction. 87

Figure 4-4. Results for strained-MTJ in Configuration I. **(a)** Schematic of Configuration I, where the gate voltage V_g for generating strain is applied between the MTJ bottom electrode and the back gate. **(b)** Simulation result showing the mapping of the in-plane *anisotropic* strain $\varepsilon_{xx} - \varepsilon_{yy}$ upon application of the gate voltage of $V_g = +50$ V. The solid line ellipse at the origin denotes the MTJ pillar, and the dashed lines denote the positions of electrodes and side gates. **(c)** MR curves characterized under different gate voltages. **(d)** Variation of the hard layer switching field H_c (square-line) and TMR ratio (circle-line) of the MTJ as a function of V_g. 89

Figure 4-5. Results for strained-MTJ in Configuration II. **(a)** Schematic of Configuration II, where V_g is applied between the pair of side gates and the back gate. **(b)** Simulation result showing the mapping of the in-plane *anisotropic* strain $\varepsilon_{xx} - \varepsilon_{yy}$ upon application of the gate voltage of $V_g = +50$ V. The solid line ellipse at the origin denotes the MTJ pillar, and the dashed lines denote the positions of electrodes and side gates. **(c)** MR curves characterized under different gate voltages. **(d)** Variation of the hard layer switching field H_c (square-line) and TMR ratio (circle-line) of the MTJ as a function of V_g. 93

Figure 4-6. Demonstration of voltage manipulation of MTJ toggling between high- and low-resistance states in Configuration II. **(a)** & **(b)** Micromagnetic simulation results demonstrating the magnetization configuration of hard and soft CoFeB layers after application of **(a)** $V_g = -80$ V and **(b)** $V_g = +80$ V. The dimension of the magnet is 3 μm × 6 μm. Black arrows indicate the direction of magnetic moments. **(c)** MR curves for $V_g = -80$ V and $V_g = +80$ V. The blue arrow indicates the switchable high- and low-resistance states. **(d)** Toggling of the MTJ between high- and low-resistance states with application of ±80 V gate voltage pulsing. A small bias magnetic field of 30 Oe is applied along the *y*-axis to overcome the dipole interaction between the two magnetic layers.... 95

Figure 4-7. Finite element simulation demonstrating the out-of-plane E-field strength within the $y = 0$ cross-section, with the application of $V_g = +50$ V. **(a)** Configuration I, **(b)** Configuration II. The thickness of PMN-PT is 0.5 mm.98

Figure 4-8. Finite element simulation showing the mapping of different piezoelectric strain components on the top surface of the substrate, with the application of $V_g =$ +50 V. **(a)** and **(d)**: in-plane strain component ε_{xx}. **(b)** and **(e)**: in-plane strain component ε_{yy}. **(c)** and **(f)**: out-of-plane strain component ε_{zz}. **(a)**-**(c)** are for Configuration I and **(d)**-**(f)** are for Configuration II, respectively................ 99

Figure 4-9. MR major and minor loops (in Configuration II) with **(a)** $V_g = 0$ V, **(b)** $V_g =$ −40 V, and **(c)** $V_g = -80$ V. 102

Figure 4-10. MR loops characterized under different gate voltages (in Configuration I) for the sample: PMN-PT substrate / Ta (8) / CoFeB (4) / MgO (1.8) / CoFeB (10) / Ta (8), where the soft layer is closer to the piezoelectric substrate.......... 104

Figure 4-11. MR curve with the magnetic field swept along the minor axis of the pillars in the *x*-direction (no gate voltage applied). 105

Figure 5-1. Illustration of the concepts for electrical manipulation and detection of AFM order. **(a)** SOT induced switching of AFM order. **(b)** Detection of the AFM

orientation using anisotropic magnetoresistance (AMR), which relies on measuring the R_{xx} signal. **(c)** Detection of the AFM orientation using planar Hall effect (PHE, another phenomenon of AMR), which relies on measuring the R_{xy} signal. 111

Figure 5-2. **(a)** *M-H* loop of MnN(25)/CoFeB(3) bilayers showing the exchange bias with AFM MnN. **(b)** Image of the patterned 8-terminal Hall device. Two writing paths are along the +/− 45° directions (denoted as RH/LH writing path). And the Hall resistance (R_{xy}) can be measured by applying a small probe current I_{probe} along the x direction and detecting the Hall voltage V_{Hall} along the y direction. **(c)** The R_{xy} signal of MnN(5)/Ta(10) sample obtained by conducting the standard electrical SOT switching experiment procedures. A sequence of writing pulses is applied, and the R_{xy} is recorded after each pulse (with I_{probe} = 0.1 mA). The writing pulses are either injected through the LH path (for the regions with red background), or through the RH path (for the regions with green background). The pulse amplitudes and pulse widths are denoted on the figure (pulses are denoted by the blue sticks). The R_{xy} signal (black) shows "saw-tooth" shape. 115

Figure 5-3. The "saw-tooth" shaped R_{xy} signal obtained from **(a)** the Ta sample, and **(b)** the Pt sample without MnN layer. I_{probe} = 0.1 mA. **(c)** Illustration of "localized Joule heating" when the writing current is injected through the LH writing path. **(d)** Normalized resistivity of the Ta sample (blue) and the Pt sample (red) as a function of temperature. **(e)** Illustration of the inhomogeneous distribution of resistivity for the Ta sample after the injection of LH writing pulse. The resistivity gets smaller around the "hot spots". **(f)** Illustration of the inhomogeneous distribution of resistivity for the Pt sample after the injection of LH writing pulse. The resistivity gets larger around the "hot spots". 118

Figure 5-4. **(a)** Image of the second schematic, where the writing (heating) paths are electrically isolated from the Hall measurement cross (HM layer). The HM Hall cross (either Ta or Pt) is first covered by a SiN_x layer. Then the writing

paths (along the +/− 45º directions) composed of Ti (60) / Au (60) are deposited on top of the SiN_x layer. **(b)** and **(c)**: R_{xy} signals of **(b)** the Ta sample and **(c)** the Pt sample with the application of DC heating current on the writing paths. The heating current is either injected through the LH path (for the regions with red background), or through the RH path (for the regions with green background), or turned off (for the regions with yellow background). Heating current of different amplitudes are applied. I_{probe} = 0.1 mA. 120

Figure 5-5. The amplitude of the R_{xy} signal changes as a function of heating current amplitude for **(a)** the Ta sample and **(b)** the Pt sample, extracted from **Figure 5-4** **(b)** and **(c)**, respectively. The blue lines are quadratic fittings. 122

Figure 6-1. A logic operation in the STT-CRAM architecture [89]. 127

Figure 6-2. Schematic of a 2-input logic gate implemented by SOT-MTJs. 130

Figure 6-3. Overall structure of the SOT-CRAM. 131

Figure 6-4. Current flow during: **(a)** memory write operation, **(b)** memory read operation, and **(c)** logic mode. 132

Figure 6-5. **(a)** Schematic of the SOT-MTJ with its dimensions denoted. **(b)** SEM image (taken at 60° from the perpendicular direction) showing a patterned SOT-MTJ (with resist on). 133

Figure 6-6. Demonstration of SOT switching with ultra-low J_{SHE} [35]. The SH layer is composed of $BiSe_x$ (5) /Ta (0.5), and the perpendicular magnetic layer is composed of CoFeB (0.6) /Gd (1.2) /CoFeB (1.1) (all thicknesses in nm). **(a)** Out-of-plane hysteresis loop of the sample and **(b)** SOT switching loop of the device. 136

Figure 6-7. **(a)** Schematic showing a logic operation in a row of SOT-CRAM, and **(b)** the equivalent circuit model. 137

List of Abbreviations

AD: anti-damping

AFM: antiferromagnetic / antiferromagnet

AHE: anomalous Hall effect

aJ: atto-Joules

AMR: anisotropic magnetoresistance

AP state: antiparallel state

CMOS: complementary metal–oxide–semiconductor

CNN: convolutional neural network

CPU: central processing unit

CRAM: Computational random-access memory

CW: clockwise

CVD: chemical vapor deposition

CCW: counter-clockwise

DMI: Dzyaloshinskii–Moriya interaction

DRAM: dynamic random-access memory

DW: domain wall

E-field: electric field

FE: ferroelectric

FFT: Fast Fourier Transform

FL: field-like

FM: ferromagnet / ferromagnet

GMR: giant magnetoresistance

HM: heavy metal

IC: integrated circuit

i-MTJ: in-plane MTJ

IMC: in-memory-computing

IMP: in-memory-processing

IPL: in-plane magnetic layer

LIM: logic-in-memory

LNM: logic-near-memory

LLG: Landau-Lifshitz-Gilbert

ME: magnetoelectric

MOKE: magneto-optical Kerr effect

MR: magnetoresistance

MRAM: magnetic random-access memory

MTJ: magnetic tunnel junctions

NMC: near-memory-computing

NMP: near-memory-processing

NN: neural networks

NVM: Nonvolatile memories

OOMMF: object oriented micromagnetic framework

P state: parallel state

p-MTJ: perpendicular MTJ

PCM: phase change memory

PCSA: pre-charged sense amplifier

PHE: planar Hall effect

PL: perpendicular magnetic layer

ReRAM: resistive random-access memory

RAM: random-access memory

SA: sense amplifier

SEM: scanning electron microscopy

SH: spin Hall

SHA: spin Hall angle

SHE: spin Hall effect

SOC: spin-orbit coupling

SOT: spin-orbit torque

SRAM: static random-access memory

STT: spin-transfer torque

SV: spin valve

TMR: tunneling magnetoresistance

VCMA: voltage-controlled magnetic anisotropy

VSM: vibrating sample magnetometer

Chapter 1 Introduction

Complementary metal oxide semiconductor (CMOS) technology has dominated the development of the integrated circuits (IC) industries for a half century. It defines how information is generated, stored, transmitted, and processed. However, with the technology node currently shrunk down to 5 nm, CMOS has reached its physical limit and encountered fundamental area, power, and performance challenges. On the other hand, in current big data era, the computing workloads are increasing exponentially with the data-intensive tasks such as big data analytics, artificial intelligence, and bioinformatics, which require hardwares to have better performance for data storing and processing. Therefore, beyond-CMOS technologies are highly demanded to make faster and more powerful electronics.

Spintronics technology is a promising candidate to develop beyond-CMOS memory and computing hardwares in this regard, because of its wonderful features including non-volatility, low power operation, high read/write speed and so on. In this chapter, I will briefly introduce the spintronics fundamentals and how it has been used in memory and logic. The rest of this thesis will focus on my efforts on the development of spintronics hardwares towards low-energy, high-performance memory and computing applications.

1.1 Spintronics basics

1.1.1 Magnetic tunnel junctions (MTJ)

Among various spintronics devices that have been developed, magnetic random-access memory (MRAM) is the most mature application so far. In MRAM technology, magnetic tunneling junctions (MTJ) [1–3] comprise the main storage cells. A MTJ consists

of two ferromagnetic (FM) layers separated from each other by an ultra-thin tunnel barrier oxide (e.g. MgO), as illustrated in **Figure 1-1**. Usually one of the FM layers (fixed layer) has a fixed magnetization, while the other layer's (free layer) magnetization can be electrically or magnetically rotated to change the relative orientations of the two layers. Based on the easy axis direction, MTJs can be classified into in-plane MTJ (i-MTJ) and perpendicular MTJ (p-MTJ).

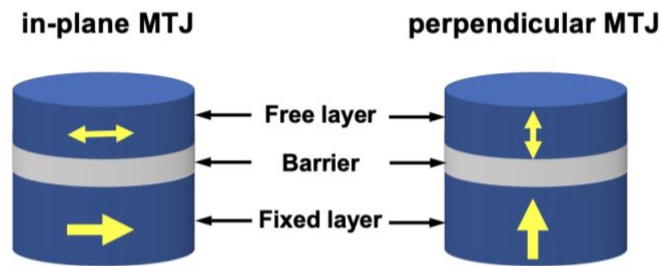

Figure 1-1. Schematics of in-plane MTJ (i-MTJ) and perpendicular MTJ (p-MTJ).

The conductance/resistance of the MTJ is determined by the spin-dependent tunneling process. When electrons are passed through a FM layer, their spins will follow the ratio of available states in the majority-spin band and minority-spin band of the FM. This means the spins of the majority of the electrons will be polarized to be parallel with the magnetization direction of the FM. This is the spin-filter effect of FM. For the case of MTJ, electrons need to tunnel from one FM layer to the other. And the tunnelling through probability of electrons is determined by the available states in both FMs' bands that have the same electron spin orientation. Therefore, when the magnetization of the two FM layers are parallel (P) to each other, electrons have higher probability to tunnel through the barrier and the MTJ has a low resistance (R_P); when the magnetization of the two FM layers are

anti-parallel (AP) to each other, electrons have lower probability to tunnel through the barrier and the MTJ has a high resistance (R_{AP}). The resistance difference is described by the tunneling magnetoresistance (TMR) ratio:

$$TMR = \frac{\Delta R}{R_P} = \frac{R_{AP} - R_P}{R_P} \tag{1-1}$$

In MRAM, the binary data bits are stored in the MTJs represented by their resistance states R_P or R_{AP}. In addition, MTJs can also provide inherent logic operations due to their resistance-based storage mechanisms. The advanced data storing and processing requires high speed and low energy writing mechanisms. These will be introduced in the rest of this chapter.

1.1.2 Perpendicular magnetic anisotropy (PMA)

The magnetic anisotropy of an in-plane MTJ (i-MTJ) and a perpendicular MTJ (p-MTJ) originates from different sources. An i-MTJ is in elliptical shape and its easy axis is along the major axis of the ellipse. Its magnetic anisotropy comes from the shape anisotropy, the value of which is in the order of 10^5 erg/cm^3. A p-MTJ exhibits the perpendicular magnetic anisotropy (PMA), which either originates from the interface of FM and the adjacent layers (e.g. in the Ta/CoFeB/MgO structure), or comes from the crystalline structure of FM itself (e.g. FePd, CoPt, or Heusler alloys). The value of PMA can easily go to the order of 10^7 erg/cm^3.

In modern MRAM, p-MTJs are preferred over i-MTJs for several reasons. First, with the MTJ's lateral dimension shrunk down to sub 50 nm, the shape anisotropy of i-MTJ

could not provide sufficient thermal stability for the nonvolatile requirement. While the p-MTJ with strong PMA makes the sub-50 nm memory cell possible. Besides, p-MTJ is also favored for its lower switching power compared with an i-MTJ with the same thermal stability. Also, the circular shape of p-MTJ can lead to a higher storage density [3–5].

1.2 MRAM writing mechanisms

High performance of spintronics memory and logic applications requires an efficient writing mechanism to store data in the magnetic elements, i.e. using electricity to switch the magnetization orientation. In this section I will introduce two types of writing mechanisms: current-induced switching via spin torques, and voltage-induced switching via magnetoelectric (ME) effects. I will present my works on the spin torques switching in Chapter 2 and Chapter 3 of this thesis, and my work on ME switching in Chapter 4.

1.2.1 Current-induced switching via spin torques

Current-induced MTJ switching via spin torques has led to the success of MRAM in the past decade. It relies on spin-polarized electrons to transfer their spin angular momentum to the magnetization, and thereby reorient the magnetization. Depending on how the spin is generated, spin torques can be classified into two types: spin transfer torque (STT), which happens when a current is passed through the MTJ, and spin-orbit torque (SOT), which originates from a non-magnetic spin Hall (SH) channel. **Figure 1-2 (a)** illustrates the STT switching mechanism for a 2-terminal MTJ, and **Figure 1-2 (b)** illustrates the SOT switching mechanism for a 3-terminal MTJ. The details of these two switching mechanisms are introduced as follows.

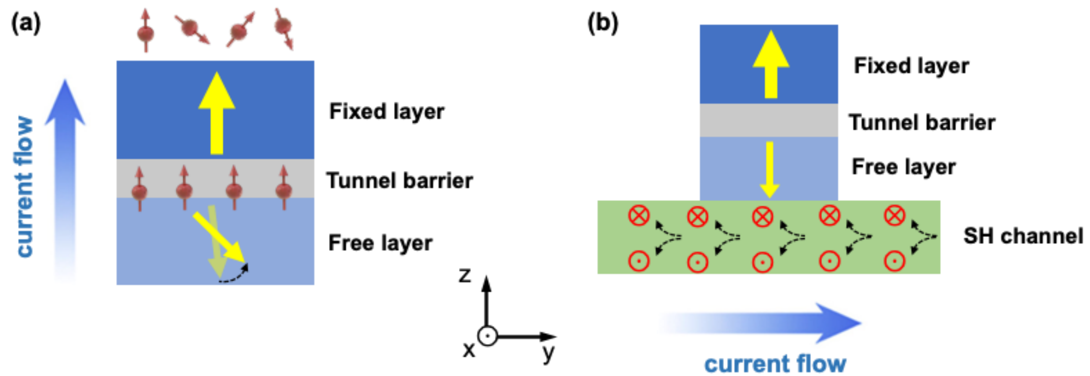

Figure 1-2. Schematics of **(a)** STT-MTJ and **(b)** SOT-MTJ.

Spin transfer torque (STT)

The research on spin transfer torque started from the investigation of current-driven domain wall motion in 1978 pioneered by Berger [6]. In 1996, Slonczewski [7] and Berger [8] independently predicted that STT effect can also happen in magnetic multilayer structures, where the magnetization of the free layer can be switched with the injection of a current through the device. Those theoretical predictions were soon proved by experimental works on spin valves or MTJ [9–11], and triggered the development of STT-MRAM [12–15].

Spin transfer torque happens as a result of the spin-filter effect. As illustrated in **Figure 1-2 (a)**, when electrons pass through a MTJ from the fixed layer to the free layer, they are spin-polarized by the fixed layer so that the majority of their spins are in the same direction as the fixed layer's magnetization. When these electrons reach the free layer, their spin angular momentum would be transferred to the magnetic moment of the free layer, until the free layer's magnetization is parallel with the fixed layer (please note the spin

transfer is a reciprocal effect due to the angular momentum conservation: magnetic moment can reorient the spin of electrons, and the spin-polarized electrons can also reorient the direction of magnetic moment). If the current direction is reversed and electrons are injected from the free layer of MTJ, the magnetization of the free layer is forced to be anti-parallel to the fixed layer. In this way, by injecting a positive or negative current through the MTJ, we can switch it from parallel (P) state to anti-parallel (AP) state, or vice versa.

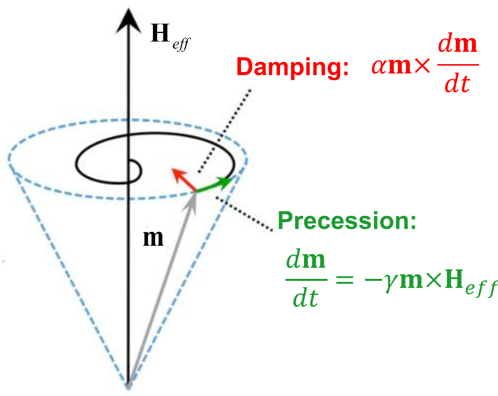

Figure 1-3. Magnetization dynamics described by LLG equation.

To further understand the dynamic of the magnetic moment, we can attribute to the Landau-Lifshitz-Gilbert (LLG) equation:

$$\frac{d\mathbf{m}}{dt} = -\gamma\mathbf{m}\times\mathbf{H}_{eff} + \alpha\mathbf{m}\times\frac{d\mathbf{m}}{dt} \tag{1-2}$$

It describes the magnetization dynamics of any magnet under the influence of an effective field $\mathbf{H}_{eff}$ ($\mathbf{H}_{eff}$ is the combination of the anisotropy field, the demagnetization field, the external field, etc.). $\mathbf{m}$ denotes the magnetization unit vector and $\frac{d\mathbf{m}}{dt}$ represents the

motion of $\mathbf{m}$ versus time. There are two terms on the right side of the equation: the precession term $-\gamma\mathbf{m}\times\mathbf{H}_{eff}$, which keeps the magnetization a precessional motion around the axis of $\mathbf{H}_{eff}$, and the damping term $\alpha\mathbf{m}\times\frac{d\mathbf{m}}{dt}$, which moves the magnetization towards the direction of $\mathbf{H}_{eff}$, as depicted in **Figure 1-3**. Here γ is the gyromagnetic ratio and α is the damping constant. Please note even under equilibrium, $\mathbf{m}$ would hardly be fully aligned with $\mathbf{H}_{eff}$ because of the thermal fluctuation.

With the exertion of spin torques, e.g. STT, two additional terms will be added onto Eq. (1-2):

$$\frac{d\mathbf{m}}{dt}=-\gamma\mathbf{m}\times\mathbf{H}_{eff}+\alpha\mathbf{m}\times\frac{d\mathbf{m}}{dt}-\tau_{ad}{}^{0}\mathbf{m}\times(\mathbf{m}\times\boldsymbol{\sigma})-\tau_{fl}{}^{0}\mathbf{m}\times\boldsymbol{\sigma} \tag{1-3}$$

Where $-\tau_{ad}{}^{0}\mathbf{m}\times(\mathbf{m}\times\boldsymbol{\sigma})$ is called anti-damping torque, and $-\tau_{fl}{}^{0}\mathbf{m}\times\boldsymbol{\sigma}$ is called field-like torque. $\boldsymbol{\sigma}$ denotes the spin polarization unit vector. Usually the anti-damping torque is dominant among the two [16,17], with its amplitude expressed as $\tau_{ad}{}^{0}=\frac{\gamma\hbar}{2eM_S t_{FM}}\left|J_S\right|$, where J_S represents the spin current density, t_{FM} the thickness of the magnetic layer, and M_S the saturation magnetization. The time derivative in the damping term can be removed by multiplying both sides of the equation by $\mathbf{m}\times$ and applying some approximation. Then Eq. (1-3) can be re-written as:

$$\left(1+\alpha^2\right)\frac{d\mathbf{m}}{dt}=-\gamma\mathbf{m}\times\mathbf{H}_{eff}-\gamma\alpha\mathbf{m}\times(\mathbf{m}\times\mathbf{H}_{eff})-\tau_{ad}{}^{0}\mathbf{m}\times(\mathbf{m}\times\boldsymbol{\sigma})-\tau_{fl}{}^{0}\mathbf{m}\times\boldsymbol{\sigma} \tag{1-4}$$

Now, consider a perpendicular MTJ shown as **Figure 1-2 (a)**. At the initial state, the free layer points down ($-z$) and the fixed layer points up ($+z$). So $\mathbf{H}_{eff}$ (mainly the anisotropy field) of the free layer is along the easy axis points down ($-z$), and $\mathbf{m}$ of the free layer precessionally moves around $\mathbf{H}_{eff}$ with a small angle. When a current is injected into the MTJ along $+z$ direction (electrons flow along $-z$ direction from the fixed layer to the free layer), the spin-polarized electrons would exert STT torque on $\mathbf{m}$ of the free layer, with the spin polarization $\boldsymbol{\sigma}$ pointing toward $+z$, i.e. in the opposite direction of $\mathbf{H}_{eff}$. Therefore, the anti-damping torque $-\tau_{ad}{}^{0}\mathbf{m}\times(\mathbf{m}\times\boldsymbol{\sigma})$ cancels out or even overwhelms the damping term $-\gamma\alpha\mathbf{m}\times(\mathbf{m}\times\mathbf{H}_{eff})$, and thus forces $\mathbf{m}$ to rotate toward $+z$ direction. In this way, the current drives the MTJ from AP state to P state. **Figure 1-4** illustrates this switching procedure by simulating the LLG equation, and the source code can be found in Appendix A.

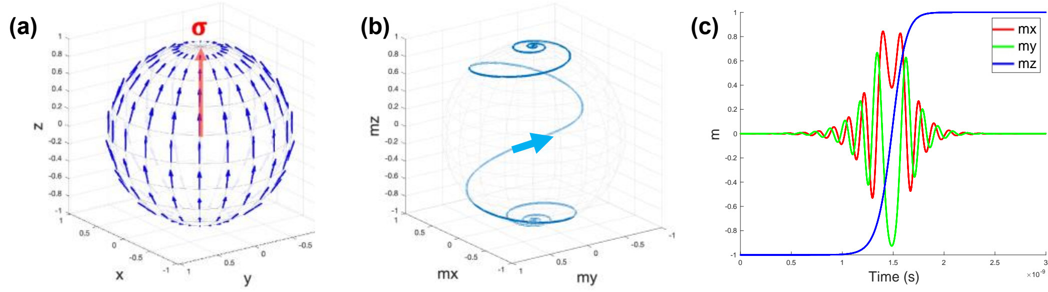

Figure 1-4. STT switching of the MTJ shown in **Figure 1-2 (a)**. **(a)** Directions and relative strengths of the anti-damping torque (denoted by the blue arrows) on the sphere of $\mathbf{m}$, with $\boldsymbol{\sigma}$ pointing to $+z$. **(b)-(c)** STT switching trajectory of $\mathbf{m}$.

Spin-orbit torque (SOT)

Although the STT writing mechanism exhibits many attractive features and has led to the success of STT-MRAM, it still faces some challenging limitations. First, the required high switching current leads to high energy dissipation for writing. Second, the large writing current passing through the tunnel barrier increases the risk of tunnel barrier breakdown and degradates the device endurance. Third, STT needs long incubation delay at the initial switching stage, as shown in **Figure 1-4 (c)**, because of the small deviation angle of $\mathbf{m}$ from the easy axis caused by random thermal fluctuation.

Spin-orbit torque (SOT) as an alternative writing mechanism of STT, has been intensively studied in recent years. A spin-orbit torque is usually generated from a spin Hall (SH) material with large spin-orbit coupling (SOC) [18], e.g. heavy metals such as tantalum or tungsten [19–21], and topological insulators [22,23]. When a current is passed through a SH channel, electrons with opposite spin polarization will be deflected towards opposite directions, resulting in a nonequilibrium spin accumulation at the surfaces/edges of the SH material, as illustrated in **Figure 1-2 (b)**. If the current direction is reversed, the polarization of the accumulated spins will also reverse. This is called spin Hall effect (SHE) [24]. Extrinsic effects such as skew scattering [25] or side-jump scattering [26] are believed to be the sources of SOC in the spin Hall effect. If a magnetic layer is put on top of the SH material, the aforementioned accumulated spins will diffuse into the magnetic layer, exerting a torque on the magnetization. This is the origin of the spin-orbit torque. Same as spin transfer torque, spin-orbit torque also causes the reorientation of the magnetization, the process of which is described by Eq. (1-3) or Eq. (1-4). Apart from the

spin Hall effect, another origin of SOT is Rashba-Edelstein effect arising in structures with inversion asymmetry [27], which is believed to be related with the field-like torque term. The SOT studies in this thesis will mainly focus on the spin Hall effect.

Recently, the SOT/SHE writing mechanism has been applied to implement the SOT-MRAM that uses 3-terminal MTJs as memory cells [19,28–33]. The structure of the 3-terminal SOT-MTJ is illustrated in **Figure 1-2 (b)**, which is composed of a MTJ put on top of the SH channel. To write the MTJ, a current is passed through the SH channel in positive or negative direction, and the free layer of the MTJ on top of the channel will be reoriented by the spin-orbit torque. To read, just pass a small reading current through the MTJ. Therefore, SOT-MRAM has separated write and read paths. This on one hand reduces the possibility of tunnel barrier breakdown during writing and thus increases the endurance of the MTJ, on the other hand reduces the read disturb faults (i.e., accidental writing while reading). Moreover, SOT-MRAM has the potential to get a lower writing power than STT-MRAM, because its write path (SH channel) can be optimized independently, e.g. by using giant spin Hall efficiency materials [22,23,34–36]. Furthermore, SOT switching for a p-MTJ is faster than STT, by eliminating the incubation delay [as shown in **Figure 1-5 (f)**].

SOT can naturally switch the magnetization in an in-plane MTJ, where the easy axis of the magnetization and the spin polarization $\boldsymbol{\sigma}$ are collinear. And the switching dynamics is quite similar to the STT switching case shown in **Figure 1-4**. However, for perpendicular MTJ shown in **Figure 1-2 (b)**, SOT can only pull the perpendicular magnetization toward the in-plane level, but cannot deterministically switch it. This is because the spin-orbit torque is symmetric in respect to the perpendicular magnetization orientation, as depicted

in **Figure 1-5 (a)**, and an additional torque [for example, a torque from an in-plane external magnetic field, shown in **Figure 1-5 (d)**] is required to break this symmetry. Therefore, an external field is needed for the switching to happen, as shown in **Figure 1-5 (b)-(c)** and **(e)-(f)**. The difficulty of external-field-free switching is a key issue of SOT-MRAM. In Chapter 3, I will show how it can be solved using a composite structure.

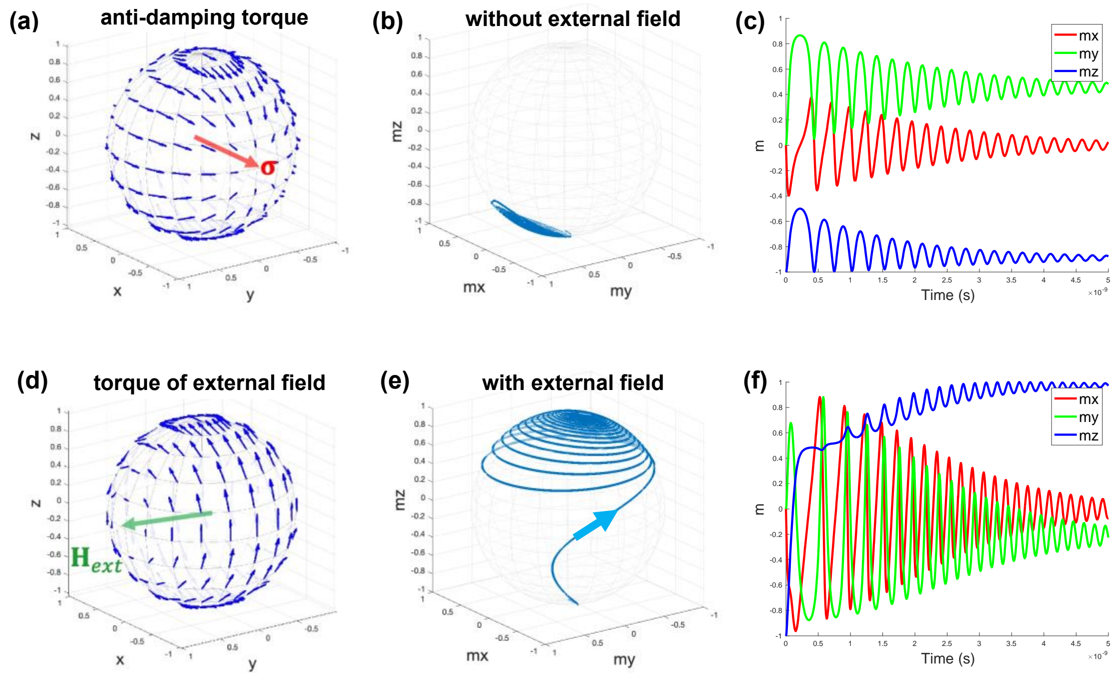

Figure 1-5. SOT switching of the MTJ shown in **Figure 1-2 (b)**. **(a)** Directions and relative strengths of the anti-damping torque (denoted by the blue arrows) on the sphere of $\mathbf{m}$, with $\boldsymbol{\sigma}$ pointing to $-x$, and **(d)** directions and relative strengths of the torque of an external field that points to $+y$. **(b)-(c)** Trajectory of $\mathbf{m}$ with SOT exerted. No external magnetic field is applied. **(e)-(f)** Same as **(b)-(c)** except an external field pointing to $+y$ is applied.

1.2.2 Voltage-induced switching via magnetoelectric effects

Another writing mechanism of spin devices is voltage control of magnesium via the magnetoelectric (ME) effect. ME effect denotes the coupling between the magnetic and the electric properties of a material. Therefore, it allows control of the magnetization of a FM using an electric field. Spintronic devices based on ME effect have the potential to achieve ultra-low energy dissipation (down to attojoule-level) because of the elimination of current injection [37,38].

Within the category of ME materials, artificial ferromagnetic–ferroelectric (FM–FE) multiferroic heterostructures have been intensively studied recently and are believed to be promising candidates for memory and logic applications. So far, voltage control of magnetism has been realized in FM-FE heterostructures via strain coupling, exchange-bias coupling and charge modulation, as illustrated in **Figure 1-6**. In Chapter 4 of this thesis, I will present my work on the strain-mediated voltage control of a MTJ device.

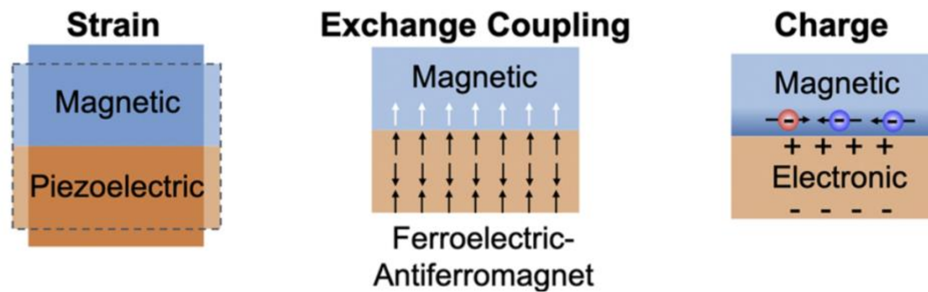

Figure 1-6. Schematics for three types of magnetoelectric (ME) switching [39].

Strain-mediated ME switching

A strain-mediated ME device consists of two layers: a ferromagnetic (FM) thin film and a piezoelectric material. When a voltage (E-filed) is applied across the piezoelectric layer, it results in the change in the shape (expansion or contraction) of the piezoelectric layer. The generated strain will be transferred on to the adjacent FM film. Then due to the magnetostrictive effect of the FM, its magnetic anisotropy would be altered by the strain and magnetization would be reoriented.

Although strain-mediated ME effect is only a simple mechanism that is via mechanical coupling at the interface of two phases, the vast choices of piezoelectric materials and ferromagnetic materials with high-performance at room temperature have made it a major strategy for voltage-controlled spintronics devices [40–46].

Exchange-bias-mediated ME switching

The exchange-bias coupled heterostructure consists of a ferromagnetic (FM) thin film deposited on top of antiferromagnetic (AFM) material with ME property. The AFM layer is a single-phase multiferroic material, within which the ferroelectric (FE) order and antiferromagnetic order are coupled with each other. Therefore, upon the application of an E-field, the AFM domains can be reoriented via the FE–AFM coupling in the multiferroic layer, leading to the change of the exchange-bias field and the switching of the FM.

Due to the scarcity of single-phase multiferroic materials and strict interface requirements, the qualified materials for ME the exchange-bias systems are quite limited, e.g. FM/$BiFeO_3$ [47] and FM/Cr_2O_3 [48].

Charge-mediated ME switching

For this type of ME devices, an ultrathin FM layer is deposited on a dielectric layer (e.g. GdO_x [49]). The application of the E-field would result in the accumulation or dissipation of spin-polarized charges at the interface and produce a change in the orientation or amplitude of the interfacial magnetization [50].

1.3 Spintronics devices for logic and computing applications

1.3.1 Logic-in-memory paradigms with NVMs

Today's computing systems heavily rely on the von-Neumann architecture, as shown in **Figure 1-7 (a)**. In this architecture, the compute and the memory units are physically separated. Therefore, data needs to be fetched from memory, transferred through the interconnects, processed in the compute unit, then sent back to memory. This procedure leads to the bottleneck of the von-Neumann architecture called "memory wall": the limited bandwidth for data transfer between the physically decoupled compute and memory units results in long transfer delay and high transfer power. Besides, since the memories (e.g., SRAM) are volatile, they always need power to maintain the data in stand-by state.

Moreover, in current big data era, the computing workloads are increasing exponentially with the data-intensive tasks such as big data analytics, artificial intelligence, and bioinformatics. This renders the conventional von-Neumann machines inefficient due to the large energy overhead and delay from data transfer. For this reason, new computing paradigms that have high energy efficiency and higher throughput are urgently demanded.

To address the limitations of von-Neumann architecture, novel computing paradigms based on logic-near-memory (LNM) and logic-in-memory (LIM) [51] have attracted a lot of attention. These computing paradigms are illustrated in **Figure 1-7 (b)-(d)**. In LNM architecture, the memory units are placed close to the logic to reduce the data transfer distance. But it wouldn't decrease the memory access. In LIM architecture, the computation capability is embedded into the memory to realize the unity of data. Therefore it meets the energy and throughput requirements demanded by the emerging data intensive applications quite well.

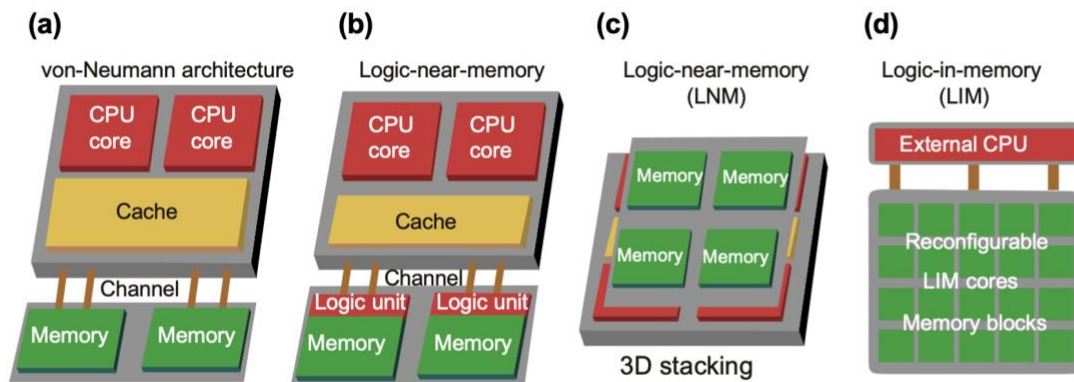

Figure 1-7. Possible evolution of the computing architecture [52]. **(a)** A conventional von-Neumann architecture with a separated processor (central processing unit, CPU) and memory; **(b)**-**(c)** The logic-near-memory (LNM) architecture with plane and 3D implementations by adding a small amount of logic units close to the memory or by adding more memory close to the processor. **(d)** The logic-in-memory (LIM) architecture attempts to embed computation capability into the memory, and to realize the unity of data storage and processing at the smallest grain in the same die. (Reprinted from ref. [52] with the permission from Springer).

Compared with traditional silicon-based volatile memories (e.g., SRAM and DRAM), non-volatile memories (NVMs) are more suitable for implementing LIM hardwares, because they (1) save stand-by power due to the non-volatility, and (2) provide inherent logic functions due to their resistance-based storage mechanisms [52]. Furthermore, among other NVMs such as ReRAM and PCM, spintronics based memory devices such as MTJ are ideal candidates for in-memory computing applications, thanks to their wonderful properties like high read/write speed, unlimited endurance, and CMOS compatibility [53–55]. In the rest of this chapter, I will focus on the research on spintronic LIM. In particular, Section 1.3.3 will introduce the major in-memory computing paradigms based on MTJs.

1.3.2 Spintronics devices for logic operations

There are several promising types of spintronics devices that can be used for logic, including all-spin logic (ASL) devices, domain-wall (DW) devices, magnetoelectric (ME) devices and MTJs. The concept of each of them will be briefly described here.

All-spin logic (ASL)

All-spin logic was proposed in 2010 [56]. It relies on nanomagnets to store information and spin currents to communicate, and eliminates the need for spin-to-charge conversion. This is why it is named "all-spin". An ASL device is shown in **Figure 1-8**. When a voltage is applied to the left node (input) in **Figure 1-8 (a)**, a spin current will be generated and diffuses to the right node (output) through a nonmagnetic channel, with the spin polarization determined by the magnetization direction of the input node. Then the magnetization of the output node will be reoriented by the torque of the spin current. In

this way, different logic functions can be implemented, for example, a 3-input majority gate shown in **Figure 1-8 (b)**. ASL has the potential to be operated with low-power since no charge current is needed in the information communication. However, the communication based on spin diffusions also imposes technical issues for this device because of the limited spin diffusion length. For this reason, proposals of ASL are largely based on modeling.

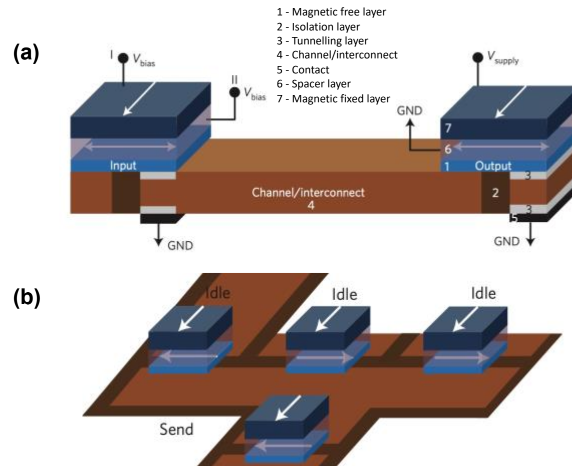

Figure 1-8. **(a)** All-spin logic device. **(b)** Layout of the ASL-based majority gate [56]. (Reprinted from ref. [56] with the permission from Springer Nature).

Domain-wall based logic

domain-wall (DW) style devices rely on the motion of a magnetic DW to move data. The utilization of DW devices for logic operation was first proposed in 2005 [57], which is based on the DW motion driven by external magnetic fields. Since 2008, current-induced DW motion due to spin transfer torque (STT) has attracted extensive attention [58–60] and various logic devices based on this mechanism have been proposed and developed [61–

65]. For example, a multi-bit full-adder has been proposed with a hybrid racetrack memory and CMOS circuit [63], where multiple racetrack MTJs storing the input data configure logic functions and a pre-charged sense amplifier (PCSA) is used to read the resistances of MTJ logic trees. Apart from such hybrid spin/CMOS designs, more proposals implement logic functionality within the magnetic device itself. For instance, in 2010 Lyle, et al. proposed a structure using a DW-MTJ as the output node, the state of which is determined by the position of DW driven by a current [as shown in **Figure 1-9 (a)**] [61]. A three terminal device based on a similar idea was proposed in 2012 [as shown in **Figure 1-9 (b)**] [64] and was experimentally demonstrated in 2016 [65]. Most recently, DW motion driven by spin-orbit torque (SOT) has also been applied to implement logic functions [66]. For real applications, DW devices still face fabrication challenges, e.g. etching stop and pinning defects.

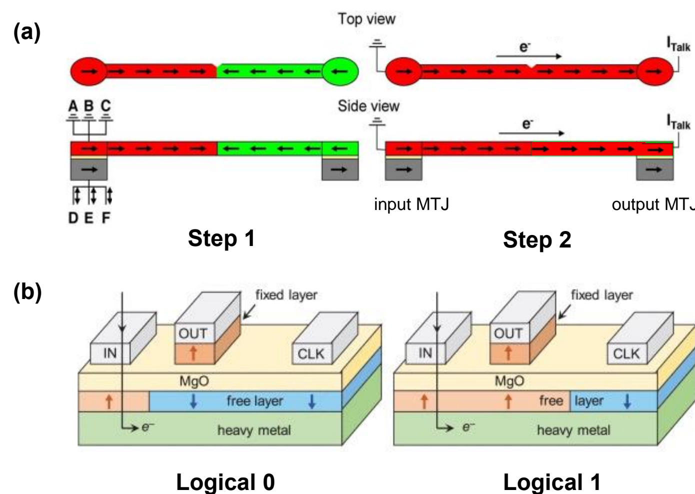

Figure 1-9. **(a)** Two connected DW-MTJs that can communicate via current induced domain-wall motion [61]. **(b)** Logic unit based on a three terminal DW-MTJ [64,67]. (Reprinted from ref. [61] with the permission from IEEE).

ME device based logic

The ME devices introduced in Section 1.2.2 can also be used to implement logic applications with high energy efficiency. One example is the well-known magnetoelectric spin-orbit (MESO) logic proposed by Manipatruni, et al. [37,38], as illustrated in **Figure 1-10**. The MESO device consists of a ME structure as an input unit, which provides the charge-to-spin conversion, and a spin-orbit coupling (SOC) structure as an output unit, which provides the spin-to-charge conversion via the inverse spin-orbit coupling (ISOC) effect. The ME unit and the SOC unit share a same FM layer as the communication route. And the communication between two neighboring MESO devices is via charge current, this is different from the use of spin current in ASL devices. Recently, Mankalale et al. proposed another ME logic called CoMET [68], where the ME structure is applied in both the input and the output units, and domain wall motion is used for the communication between them.

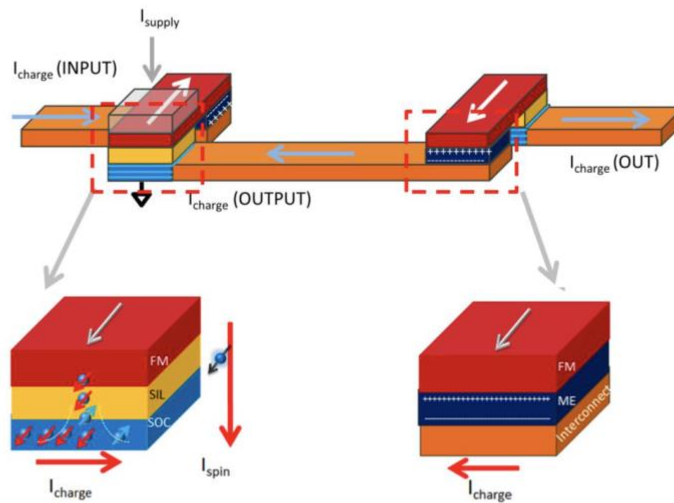

Figure 1-10. Schematic of the MESO device [37,38]. (Reprinted from ref. [38] with the permission from Springer Nature).

Since the energy dissipation of a ME structue is CV^2 (C is the capacitance of the dielectric capacitor), the ME logic has a theoretical operation energy down to attojoule-level [37,38]. However, current ME devices still face several critical issues that need to be addressed, including the realization of 180° magnetization switching, scaling-down, CMOS compatibility, device reliability, etc.

MTJ based logic

Compared with the above listed innovative concepts, MTJ would be the most promising candidate not only for MRAM, but also for logic and computing applications. Because the MTJ technology, after decades of development, is the most mature one among various spintronic tech tracks, due to its good compatibility with CMOS circuit, high read/write speed, infinite endurance, high reliability and small size [69,70]. Both STT-MTJ and recent SOT-MTJ can fit in various LIM paradigms. This will be introduced in detail in the section below.

1.3.3 MTJ based in-memory-computing

There are three major paradigms to implement MTJ-based in-memory processing so far:

- **Hybrid CMOS/MTJ-based LIM**. This paradigm heavily relies on the CMOS devices to implement the logic operation. MTJs, which are embedded into the CMOS logic trees, are only responsible for a small portion of the functionality.
- **MRAM block with peripheral circuitry**. The basic idea behind this paradigm is to activate multiple MTJ cells in a MRAM array as logic input and read-out a

voltage which is proportional to the desired logic computations. Therefore it relies on the peripheral read circuits (i.e. sense amplifiers) to implement the actual computations.

- **Computational random-access memory (CRAM)**. Different from the previous two paradigms where the output of the logic function is determined peripheral circuits, in CRAM the logic operations are performed *in situ* with MTJ cells, and the output is directly encoded in MTJ as well. Therefore, CRAM is a *true* in-memory computing paradigm and the logic computation is fully non-volatile.

I will briefly introduce each paradigm as follows.

Hybrid CMOS/MTJ-based LIM

The the hybrid CMOS/MTJ-based LIM architecture is usually composed of three main parts [52,71], as shown in **Figure 1-12 (a)**:

(1) A sense amplifier to obtain the logic output signal.

(2) A write circuit to program the data stored in MTJs, using STT writing mechanism.

(3) A logic block composed of CMOS transistors and MTJs to perform logic computing with (partial) nonvolatility.

In the logic block, the logic data '0's or '1's is either encoded in the nonvolatile MTJs by programming the MTJ to have high resistance (R_{AP}) or low resistance (R_{P}), or represented by the volatile input voltage of the CMOS transistors. **Figure 1-11** shows the combined CMOS+MTJ logic configurations for different logic gates [72]. With such architecture, various logic circuits have been proposed [73] including look-up-table [74],

flip-flop [75,76], and full-adder [71,77,78]. The first test chip of magnetic full-adder was fabricated by Matsunaga et al. in 2008, using 0.18 μm CMOS technology and 100 × 200 nm^2 in-plane STT-MTJs [79,80]. **Figure 1-12 (b)** shows the full circuitry of a 1-bit magnetic full-adder [71,77] that implements the logic described in Eq. (1-5) and (1-6).

$$SUM = A \oplus B \oplus C_i = ABC_i + A\overline{B}\overline{C_i} + \overline{A}B\overline{C_i} + \overline{A}\overline{B}C_i \quad (1\text{-}5)$$

$$C_o = AB + AC_i + BC_i \quad (1\text{-}6)$$

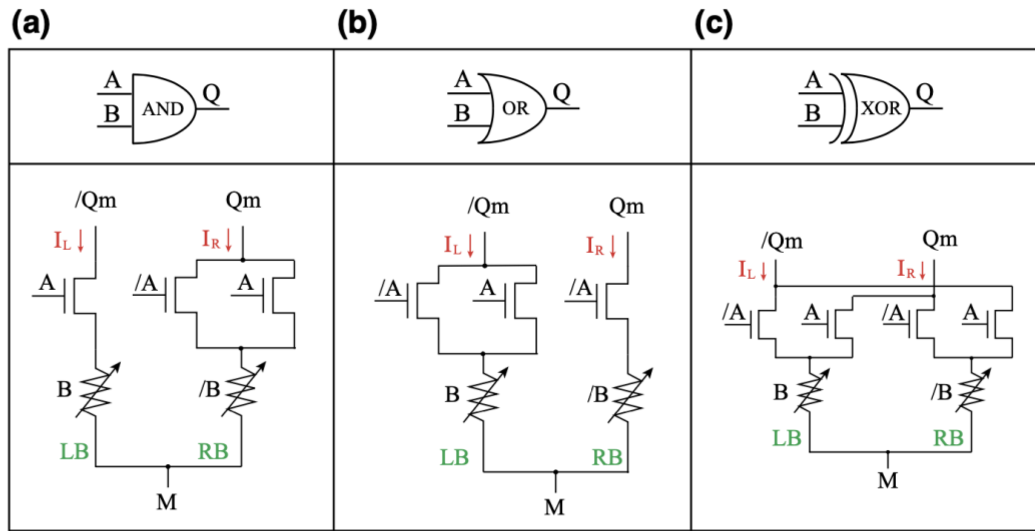

Figure 1-11. Hybrid CMOS/MTJ logic network for **(a)** AND gate **(b)** OR gate and **(c)** XOR gate. "LB" and "RB" represent the left and right branches, respectively. The input operand *B* is encoded in the MTJ, while the input operand *A* is represented by the CMOS input voltage. The output signal *Q* can be obtained by a pre-charge sense amplifier (PCSA) [52]. (Reprinted from ref. [52] with the permission from Springer).

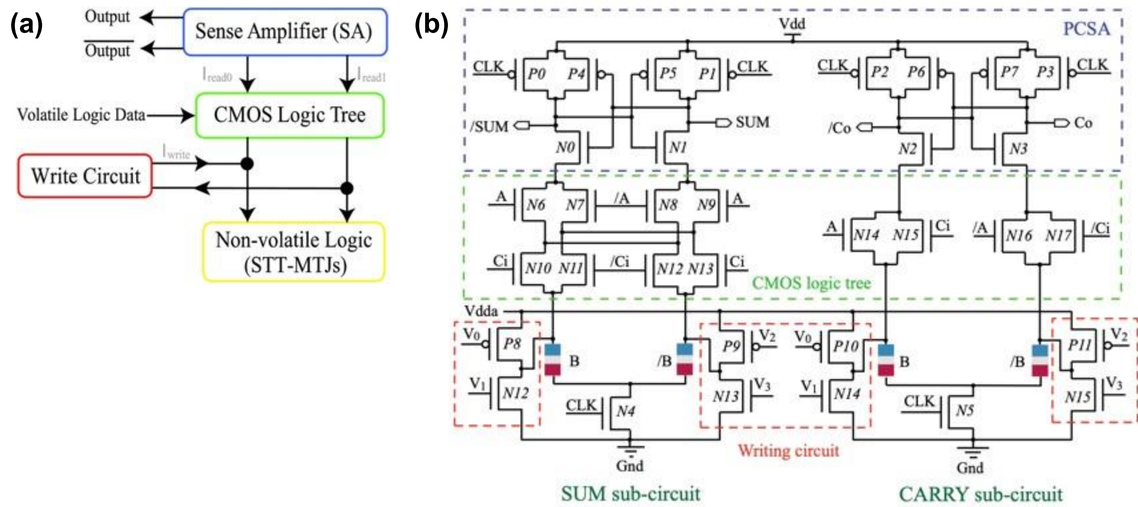

Figure 1-12. **(a)** Schematic of the CMOS/MTJ LIM architecture. **(b)** Full circuitry of the 1-bit full-adder based on the hybrid CMOS/MTJ LIM architecture. The input operand *B* is encoded in the MTJ, while the input operands *A* and C_i are represented by the CMOS input signals. The output *SUM* and C_o are obtained by PCSA [52,71]. (Reprinted from ref. [52] with the permission from Springer).

As can be seen from **Figure 1-11** and **Figure 1-12 (b)**, the logic configurations heavily rely on the CMOS devices, and MTJs are only responsible for a small portion of the functionality. Only one of the logic input operands is provided by MTJ, while all other inputs and outputs are still electrical quantities, i.e. voltages or currents that drive or are generated from the CMOS circuit. Therefore, it would lead to degraded benefits in throughput and energy of using NVM. In another approach (as shown in **Figure 1-13**), all the input states are obtained from MTJs, though the output is still relied on the SA.

However, in this approach each input operand has to be stored in multiple MTJs, which requires extra overhead for MTJ synchronization.

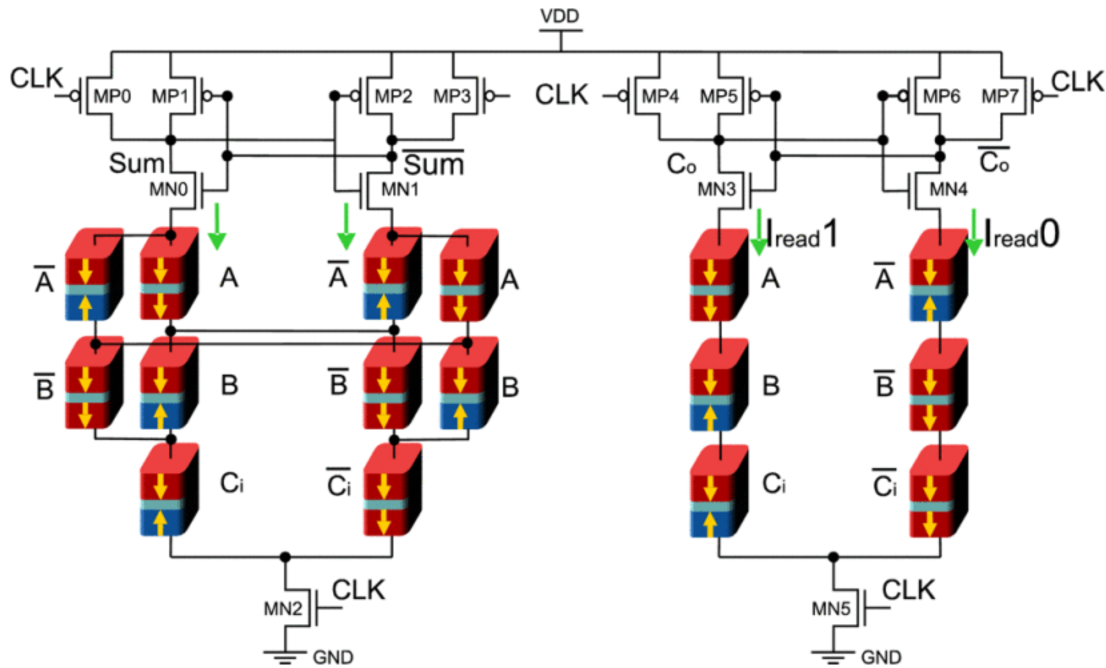

Figure 1-13. Another circuitry of the 1-bit full-adder based on the hybrid CMOS/MTJ architecture. Different from **Figure 1-12 (b)**, here all the logic inputs are represented by MTJs [63]. (Reprinted from ref. [63] with the permission from IEEE).

MRAM block with peripheral circuitry

The in-memory processing can also be configured by leveraging STT-MRAM peripheral circuits [81,82], as shown in **Figure 1-14**. The basic idea for this paradigm is to activate multiple MTJ cells in the MRAM array as input and read-out a voltage which is proportional to the desired logic computations. For example, **Figure 1-14 (b)** depicts the sensing-based logic operations where two memory cells are addressed simultaneously. There would be three possible sense voltages, corresponding to the three resistance

combinations of the two MTJs: (R_{AP}, R_{AP}), (R_P, R_{AP}), (R_P, R_P). Then by setting proper reference (denoted by the red dash lines), the SA can perform an AND or OR logic operation by outputting binary ‘0’ or ‘1’. Therefore, this architecture relies on the peripheral read circuits to implement the actual computations. Recently, this concept has been extended to SOT-MTJ [83,84].

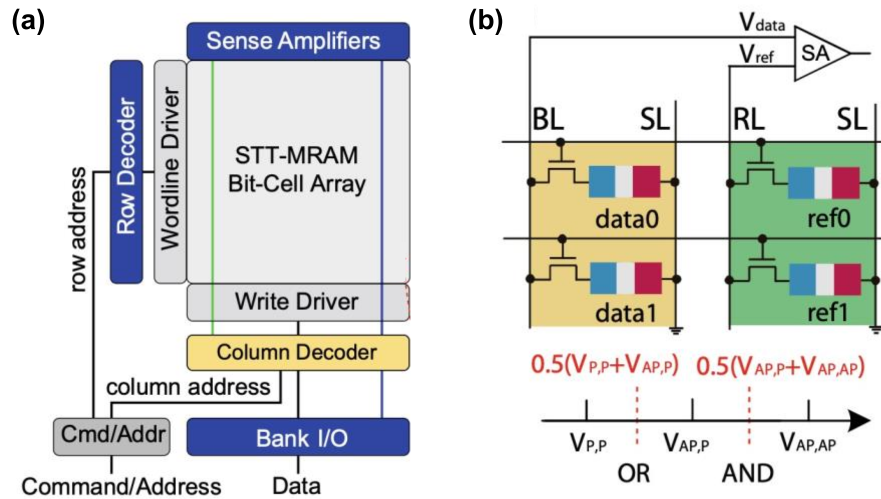

Figure 1-14. **(a)** Schematic of a STT-MRAM bank with additional peripheral circuitry for logic operations. **(b)** The key concept of using difference reference selections to perform logic operations [81]. (Reprinted from ref. [81] with the permission from IEEE).

Computational random-access memory (CRAM)

In order to fully take advantage of the non-volatile of MRAM, in-memory compute designs that do computations ‘*in situ*’ using ‘stateful’ devices are preferred. ‘*In situ*’ computation requires the memory cells to act as compute units as well, instead of relying on heavy extra CMOS logic or peripheral read circuitry. On this technical track, many exciting works have been reported, from device level demonstrations [85,86] to recent

proposals of full computation architectures called computational random-access memory (CRAM) [87–89].

The early version of computing within stateful MTJs was based on the utilization of current-induced oersted field [90]. In such devices, each logic input is represented by a current that passes through one of the current wires placed above the MTJ element, and the output is represented and recorded by the MTJ resistance. With certain combinations of input current, the overall oersted field would be sufficient or not for reversing the free layer of the MTJ. Therefore, different logic gates can be implemented, as depicted in **Figure 1-15 (a)**. The experimental demonstration of logic gates based on this idea was reported by Wang et al. [as shown in **Figure 1-15 (b)**] [91], and the implementation of a full-adder was reported by Meng et al. [92] in 2005. Later in 2012, Yao et al. proposed the logic design that uses STT, instead of the oersted field, for MTJ switching [93].

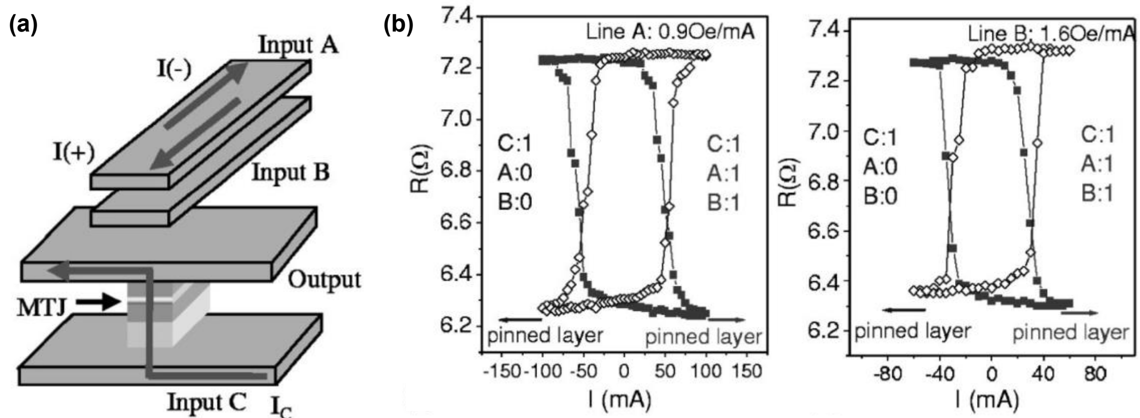

Figure 1-15. **(a)** Schematic of a spin-logic device based on a single MTJ element with three independent input lines A, B, and C. **(b)** The switching loops of MTJ operated under the oersted field generated from inputs A and B, respectively [91]. (Reprinted from ref. [91] with the permission from AIP Publishing).

In these early works, although the outputs of the logic gates can be directly recorded in a memory cell, the inputs are represented by currents. Therefore, extra reading operations are required. To address these drawbacks, designs that connect MTJs together to form the logic circuits have been proposed. In this approach, all the input and output operands are represented by the resistances of MTJs and each MTJ is switchable by STT, as shown in **Figure 1-16**. Antiparallel (AP) and parallel (P) of MTJ define logic '1' and '0', respectively. For a two-input gate shown in **Figure 1-16**, the two MTJs in parallel are the inputs to the logic gate, and the MTJ in series with them is the output. Logic state 00 corresponds to both input MTJs being P; 01 or 10, to one of the MTJs being AP; and 11, to both being AP. The final state of the output MTJ is determined by the amplitude of $I_1 + I_2$ which is the quotient of the bias voltage V_b and the overall resistance of the circuit. Therefore, the output MTJ should be preset to a known value before the logic operation, and type of logic gate is determined by the output preset value and the polarity and magnitude of V_b.

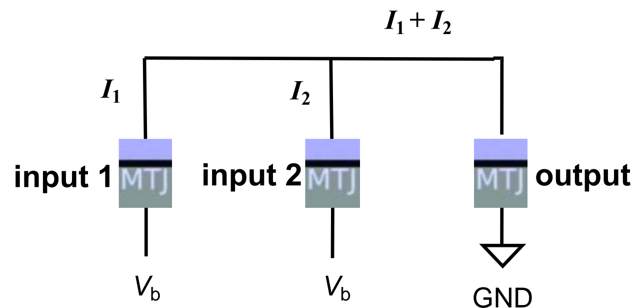

Figure 1-16. Schematic of the 2-input logic gate implemented by connected MTJs. The preset value of the output MTJ and the polarity and magnitude of the bias voltage V_b determine the type of logic gate.

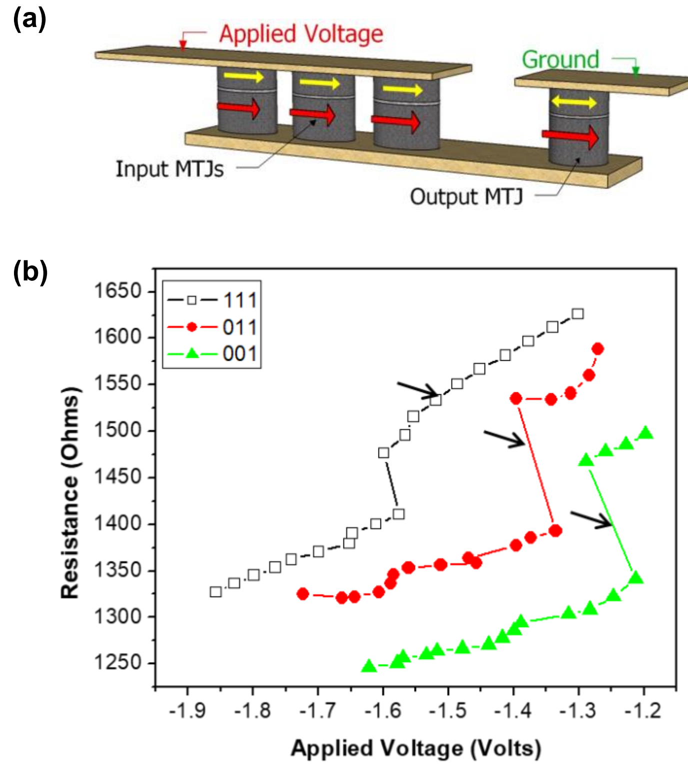

Figure 1-17. **(a)** Schematic of the logic gate implemented with 3-input MTJs connected in parallel. **(b)** AP to P switching of the output MTJ for three different resistance states of the inputs [85]. (Reprinted from ref. [85] with the permission from AIP Publishing).

The experimental demonstration of such a logic circuit composed of multiple connected STT-MTJs was reported by Lyle et al. in 2010 [85,86], as shown in **Figure 1-17**. The three input MTJs are connected in parallel, and the state of each can be set independently using an external magnetic field since they have different switching fields. **Figure 1-17 (b)** shows the AP to P STT switching of the output MTJ for three different input states. Changing the input state causes a shift in the voltage required to switch the

output. A 150–200 mV separation in the switching voltages occurs for progressive input states, which provides a sufficient window to set V_b. For example, if $V_b = -1.5$ V, only the '111' input combination would lead to '1' (AP) of the output and all other input cases would give '0' output. So the circuit would work as an AND gate.

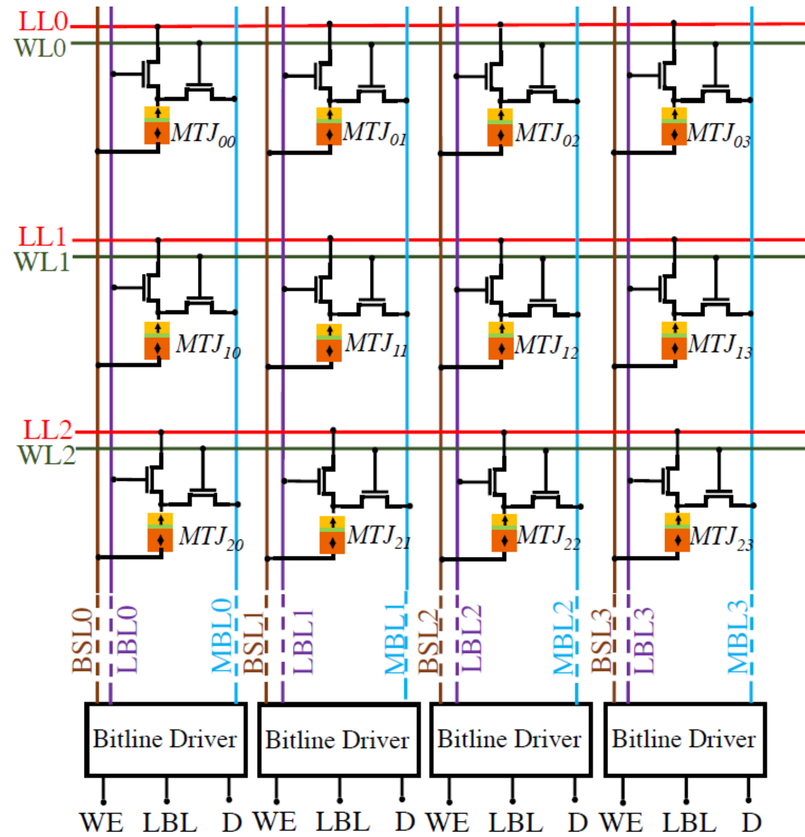

Figure 1-18. The STT-CRAM architecture [89]. (Reprinted from ref. [89] with the permission from IEEE).

This all-MTJ-based computing operation can be performed within a memory array, as shown in **Figure 1-18**. We call it computational random-access memory, or CRAM [87–89]. This architecture fits the description of *true* in-memory computing, where

computations are performed natively within the memory array and massive parallelism is possible. Therefore, it could provide a way to realize high-performance and ultra-low power computation for the next generation processor. Most recently, the concept of STT-MTJ based CRAM has been extended to SOT-CRAM [94,95], which uses the 3-terminal SOT(or SHE)-MTJs as the elementary computing units. The details of STT-CRAM and SOT-CRAM will be introduced in Chapter 6. Till now, studies have applied this in-memory computing paradigm to multiple data-intensive applications, such as machine learning and deep learning accelerators [89,96,97], FFT accelerator [98], and sequence matching [99,100].

1.4 Dissertation overview

In this dissertation, my research efforts on the development of spintronics devices for advanced memory and computing applications will be presented. In Chapter 2 through Chapter 4, I focus on my experimental works on better writing of ferromagnets / ferromagnets (FM), either using current-induced SOT, or using voltage-generated piezoelectric strain. In Chapter 5, I extend the SOT study to antiferromagnet (AFM). And in Chapter 6, I explore the potential application of SOT devices for computing, and invent a new in-memory computing architecture. The details of each chapter are shown as follows:

- Chapter 2 expands the scope of SOT switchable materials, from interfacial PMA magnets only, to bulk PMA magnets, which have a better thermal stability when scaled down and are regarded as potential candidates in future MRAM.
- Chapter 3 presents how the “SOT switching requires a magnetic field” issue is addressed with a dipole-coupled composite device. The idea is to use the stray field

projected by an in-plane magnetized layer placed on top of the conventional spin Hall structure, to substitute the external magnetic field. Compared with the other solutions for field-free switching, our composite device is the most compatible one with existing MRAM technologies and readily applicable for SOT-based memory and logic applications.

- Chapter 4 presents the voltage-controlled device utilizing a piezoelectric / MTJ coupled structure for ultra-low power writing of data. Highly effective voltage manipulation of MTJ was demonstrated via the generation of localized strain from the local gating configurations. This prototype has the potential to be scaled down to a sub 100-nm memory cell with write energy of a few tens of aJ/bit.
- Chapter 5 attempts to tackle the spin torque induced switching in an antiferromagnetic (AFM) system, by characterizing the devices with a widely adopted 8-terminal geometry. Surprisingly, it's found the "saw-tooth" signal, which was previously regarded as the evidence of AFM switching, actually originates from thermal artifacts related to the inhomogeneous Joule heating.
- Chapter 6 presents a new architecture for computational random-access memory (CRAM) based on the 3-terminal SOT-MTJ. The SOT-CRAM allows *true* in-memory computing and thereby meets the energy and throughput requirements of modern data-intensive processing tasks. Moreover, the excellent features of SOT unit cells would provide a large improvement in speed and energy compared with other in-memory computing paradigms.
- Chapter 7 concludes the thesis.

Chapter 2 SOT Switching of a Bulk-PMA Magnet

2.1 Motivation and background

Current-induced spin-orbit torques (SOT) have been intensively studied in recent years, due to its potential impact on next-generation memory and logic devices [19,30,101]. As introduced in Chapter 1, the SOT refers to the torques generated by a nonequilibrium spin accumulation at the interface of heavy-metal (HM) / ferromagnet (FM), due to either the bulk spin Hall effect (SHE) in the HM [19,20] or the Rashba-Edelstein effect at the HM/FM interface [27]. As the nonequilibrium spin accumulation diffuses into FM, the magnetization of FM can be reversed via the spin-transfer torque mechanism [7,8].

Prior to this work [21], most of the studies of SOT focused on the switching of FM with an interfacial perpendicular magnetic anisotropy (interfacial-PMA), by using the structures like Pt/Co/Oxide [20,27,102–104], Pt/Co/Pt [105,106], Ta/CoFeB/MgO [107–111], and Ta/CoFe/MgO [112]. Here, the PMA originates from the interface of FM and the adjacent layers. For instance, the PMA in the Ta/CoFe(B)/MgO systems originates from the hybridization effects at the FM/oxide interface, and the PMA in the Co/Pt systems originates from the Co/Pt interface. Due to the inherent interfacial nature of this PMA, the FM films must be grown very thin (usually between 0.8 nm and 1.4 nm). This imposes a fundamental bottleneck on the scaling of the SOT devices, since the interfacial anisotropy energy density is insufficient to maintain the thermal stability for bits scaled below ~20

nm [113], despite the enhancement of the interfacial-PMA with various engineering approaches [114,115].

One way to overcome this problem is to use magnetic materials with bulk-PMA, where the perpendicular anisotropy is an intrinsic property of the material and is less relied on the interfaces, thus the magnetic layer can be grown thicker. Therefore, the effect of scaling down the footprint area can be compensated by increasing the thickness of the magnet. Bulk-PMA materials such as $L1_0$-ordered alloys (FePt, FePd, CoPt, etc.) [116,117], Heusler alloys [118,119], and transition metal-rare earth alloys [5,120], are potential candidates for devices since they exhibit considerably larger volume anisotropy energy barriers. Furthermore, since the bulk-PMA is less sensitive to the nature of the interfaces, the adjacent HM layer can be optimized to maximize the spin Hall efficiency without affecting the PMA property. However, prior to this work, there have been only a few studies on the SOT with bulk-PMA system [121], focusing mainly on current-induced domain wall motion [122–124]. The following questions were yet to be answered:

- Whether the bulk-PMA materials can be switched by SOT/SHE as well.
- Is the SHE torque able to switch a perpendicular magnetic layer thicker than ~1nm.

In this chapter, I will demonstrate the spin Hall effect induced switching of perpendicular magnetization with a bulk-PMA. The switching is investigated using the ferrimagnetic TbFeCo layer of 1.8 nm in thickness, which has a strong intrinsic perpendicular anisotropy, with a Ta underlayer as the SHE metal. The current-induced magnetization switching is thoroughly investigated in the presence of a perpendicular field,

a longitudinal field, or a transverse field. I will show the SHE induced switching in the Ta/TbFeCo system which is similar to the previous works on the interfacial-PMA systems.

The rest of this chapter is organized as follows. Section 2.2 introduces the structure of the device, the fabrication process, and the measurement setups. Section 2.3 presents the measurement results and analysis. Section 2.4 concludes the chapter. The content of this chapter has been published as a research article in Applied Physics Letters [21].

2.2 Experimental methods

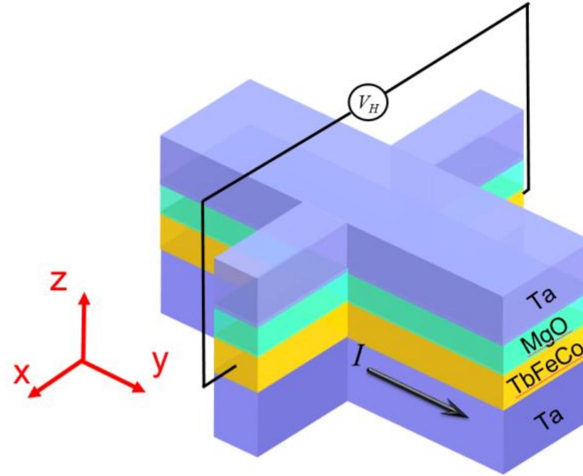

Figure 2-1. Schematic illustration of Hall bar devices and the AHE measurement setup.

The film stack for the study of SOT switching consists of, from the substrate, Ta (5) / TbFeCo (1.8) / MgO (2) / Ta (4) (thickness in nm), as illustrated in **Figure 2-1**. The films are deposited by DC and RF sputtering in our Shamrock sputter tool, on thermally oxidized silicon wafers at room temperature. For the efficient generation of spin current from spin Hall effect, the β-phase (the distorted tetragonal phase) of heavy metals like Ta and W is

required [125]. The α-phase films typically have lower resistivity than β-phase films. For example, resistivity for the stable α-W phase is typically below 40 μΩ•cm, and for the metastable β-W phase is typically above 150 μΩ•cm [126]. We have investigated various sputtering conditions to develop the heavy metals Ta and W, as listed in **Table 1**. For this work, I used the β-Ta film with resistivity of 288 μΩ•cm (5 nm-thick) as the heavy metal layer.

Table 1. Sputtering conditions and characteristics of heavy metals Ta and W

Heavy Metal	Sputtering Power (W)	Sputtering Pressure (mTorr)	Film Resistivity (μΩ.cm)	Phase
Ta (used in this work)	150	3	288	β
Ta	100	3	320	β
W	150	10	67	α
W	75	10	347	β

For the deposition of the TbFeCo layer, A ternary alloy target is used. Since TbFeCo is a ferrimagnetic material, where Tb atoms and Co/Fe atoms are antiferromagnetic coupled, the concentration of Tb directly affects the magnetic properties including the coercivity field H_c and the saturated magnetization M_s [127,128]. The composition is determined to be $Tb_{20}Fe_{64}Co_{16}$ by Rutherford backscattering spectrometry (RBS) and X-ray photoelectron spectroscopy (XPS) measurements. For this composition, the magnetization is dominated by the Fe/Co moments. The resistivity of the 1.8 nm-thick TbFeCo layer is determined to be about 200 μΩ•cm.

The as-deposited films demonstrate a strong intrinsic perpendicular anisotropy [129–131] as shown in **Figure 2-2 (a)**. The 1.8 nm-thick TbFeCo film shows PMA with a perfect

square hysteresis loop in the out-of-plane direction with H_c = 70 Oe. The in-plane hysteresis loop is saturated at about 10 kOe indicating a strong perpendicular anisotropy field of 1.5 T. Upon increasing the thickness of TbFeCo layer from 1.8 nm to 2.5 nm, the PMA and H_c increases with the thickness of TbFeCo, as can be seen in **Figure 2-2 (b)**. For the sample with TbFeCo thickness increased to 5nm (not shown here), H_c reaches up to 2000 Oe. This indicates the PMA of TbFeCo originates from the bulk rather than induced by the interface. And the increasing of H_c upon increasing the TbFeCo thickness is a feature of the transition metal-rare earth alloys with bulk-PMA property [131]. We also compared the hysteresis loops of TbFeCo deposited on different spin Hall metals (Ta, W and TaW alloy), and all systems exhibit similar perpendicular properties, which implies the robust behavior of the bulk-PMA in TbFeCo films.

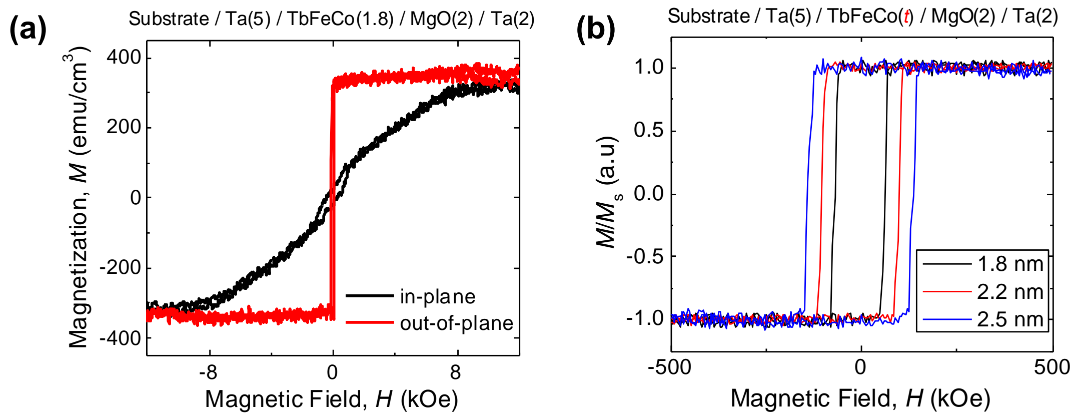

Figure 2-2. **(a)** The in-plane and out-of-plane hysteresis loops of Ta (5) / TbFeCo (1.8) / MgO (2) multi-layers. **(b)** the out-of-plane hysteresis loops for Ta (5) / TbFeCo (*t*) / MgO (2) multilayers, where t = 1.8, 2.2, and 2.5 nm, respectively.

Then, the film stack is patterned into Hall bars with a width ranging from 5 μm to 30 μm, and length of 65 μm, using optical lithography and Ar-ion etching. To characterize the magnetization direction of the TbFeCo layer, the Hall resistance R_H due to the anomalous Hall effect (AHE) is measured at a given channel current I_{ch}. The current is injected into the cross bar along the longitudinal direction (y-direction), and the voltage is detected by a nano-voltmeter in the transverse direction (x-direction), as shown in **Figure 2-1**. A Keithley 6221 current source and a Keithley 2182A nanovolt meter were used in the Hall measurement. The external in-plane and out-of-plane magnetic fields were generated by coils driven by a Kepco power supply. The Keithley 6221 was also used to generate current pulses in the pulse switching measurement.

2.3 Results and discussions

In this section, I will present the results of electrical measurements for the Ta/TbFeCo Hall bar devices and demonstrate the spin Hall (SH) induced switching of TbFeCo.

2.3.1 Measurements with an out-of-plane field

First, the hysteresis loop of the Hall resistance R_H, is measured as a function of an out-of-plane magnetic field H_z, as shown in **Figure 2-3**. Due to the anomalous Hall effect (AHE), the value of R_H is proportional to the out-of-plane component of the magnetization, M_z [132]. Therefore, by measuring R_H, the magnetization state of TbFeCo can be detected. In this experiment, positive R_H represents TbFeCo magnetization pointing up ($+z$), and negative R_H represents TbFeCo magnetization pointing down ($-z$).

The R_H-H_z hysteresis loop is measured with different channel current I_{ch}, as shown in **Figure 2-3 (a)**. When I_{ch} is very small (0.5 mA), the coercive field H_c of the loop is 240 Oe, and the amplitude of the loop is 4.0 Ω. H_c is much larger than that of un-patterned thin film in **Figure 2-2**, because the incoherent switching in the un-patterned film will reduce the coercivity [133]. Once I_{ch} is increased from 0.5 mA to 8 mA, H_c reduces dramatically to 50 Oe, and the amplitude of the loop also drops to 3.65 Ω. The reductions of H_c and loop amplitude result from two reasons. One is Joule heating generated by I_{ch}, which results in the thermal fluctuation of the magnetization and makes it easier to be switched by the out-of-plane field. The other is the spin-orbit torque (SOT) induced by the spin Hall effect. As introduced in Chapter 1, the anti-damping spin-orbit torque is expressed as:

$$\boldsymbol{\tau}_{ST} = -\tau_{ST}{}^{0}\mathbf{m}\times(\mathbf{m}\times\boldsymbol{\sigma}) \tag{2-1}$$

Where $\boldsymbol{\sigma}$ denotes the spin polarization unit vector, $\mathbf{m}$ denotes the magnetization unit vector, and the magnitude of the torque is $\tau_{ST}{}^{0} = \frac{\gamma\hbar}{2eM_S t_{FM}}|J_S|$, where J_S represents the spin current density, and t_{FM} is the thickness of the magnet. For a charge current I_{ch} flowing along the $+y$ direction, electrons with spin polarization $\boldsymbol{\sigma}$ pointing to the $-x$ direction are accumulated on the top surface of the Ta layer and injected into the TbFeCo layer. Since the magnetization vector $\mathbf{m}$ is along $+z$ or $-z$, according to Eq. (2-1), $\boldsymbol{\tau}_{ST}$ would be pointing to the $-x$ direction, as shown in **Figure 1-5 (a)** in Chapter 1. The equilibrium orientation of $\mathbf{m}$ requires the spin torque to be balanced with other torques, for example, the torque of the anisotropy field $\boldsymbol{\tau}_{an}$. Therefore, $\boldsymbol{\tau}_{ST}$ tilts the magnetization

away from the z-axis, until the equilibrium is achieved. The equilibrium orientation of $\mathbf{m}$ would in the y-z plane, where all the torques are collinear (along the x-axis). Since the magnitude of the torque $\tau_{ST}{}^{0}$ is proportional to I_{ch}, larger I_{ch} will tilt $\mathbf{m}$ more. Then the coercive field H_c and the loop amplitude would decrease with I_{ch}. As seen in the phase diagram of **Figure 2-3 (b)**, H_c can be modulated from 240 Oe to 10 Oe by varying the current from 0.5 mA (corresponding to a current density of 0.4×10^6 A/cm^2 in the bottom Ta layer) to 12 mA (9.6×10^6 A/cm^2 in the bottom Ta layer).

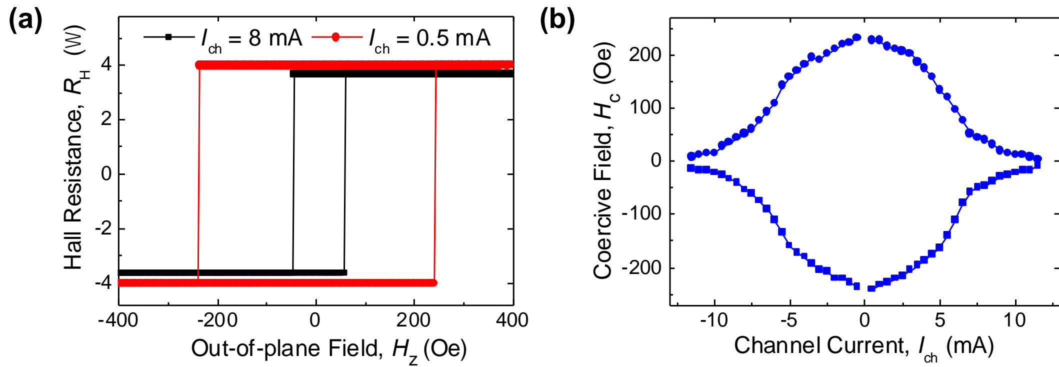

Figure 2-3. **(a)** R_H-H_z loops measured with I_{ch} = 0.5 mA and 8mA respectively. **(b)** Coercive field H_c as a function of I_{ch}.

Next, we perform the experiment with applying a sequence of current pulses and varying the out-of-plane magnetic field H_z, as exhibited in **Figure 2-4**. Each current pulse is injected along the $+y$ direction with an amplitude of 10 mA and duration of 1 ms. The Hall resistance is measured 20 μs after the rise of each current pulse. H_z is applied with its direction reversed back and forth after each current pulse. When the strength of H_z is 50 Oe, R_H changes back and forth synchronously with H_z, varying between +3.6 Ω and −3.6

Ω [**Figure 2-4 (a)**]. It indicates that the complete magnetization reversals between up state and down state. When the strength of H_z decreases to 20 Oe for the same current pulses, R_H can only vary between +3.6 Ω and +2.5 Ω [**Figure 2-4 (b)**]. Such small variation in R_H indicates the magnetization can't be completely switched with the 20 Oe out-of-plane field, and only small reversed domains can be nucleated at the edge of the Hall bar. The results in **Figure 2-4 (a)** and **(b)** are consistent with the switching phase diagram in **Figure 2-3 (b)**: for the current of 10 mA, H_z of 20 Oe is located near the boundary of the phase diagram and thereby barely enough for domain nucleation, while H_z of 50 Oe is located in the reversal region in the diagram and thereby forming a completed switching of magnetizations.

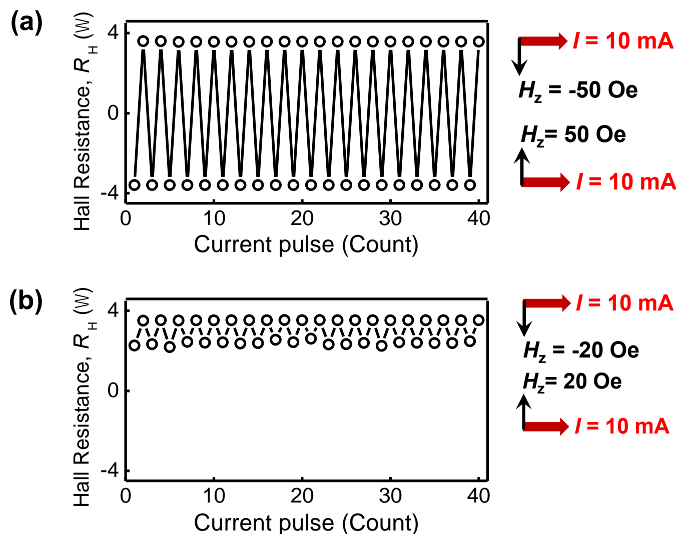

Figure 2-4. R_H variation upon the injection of a sequence of current pulses. The pulse amplitude is 10 mA and the pulse width is 1 ms. The out-of-plane field is applied with field direction reversed after each current pulse. The amplitude of the field is **(a)** $H_z = 50$ Oe and **(b)** $H_z = 20$ Oe.

The magnetization states are also captured by the magneto-optical Kerr effect (MOKE) images, as given in **Figure 2-5**, where the two MOKE images of the Hall bar with different brightness correspond to down state ($M_z < 0$) and up state ($M_z > 0$) of the magnetization, respectively.

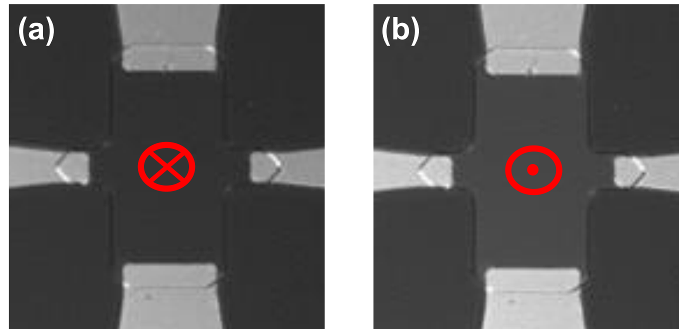

Figure 2-5. Magneto-optical Kerr images of the Hall bar device with the magnetization direction pointing **(a)** upward and **(b)** downward, respectively.

2.3.2 Measurements with an in-plane field

Next, the reversal of the magnetization is studied by sweeping the current in the presence of an in-plane field along the *y* direction, as shown in **Figure 2-6**. As can be seen from **Figure 2-6 (a)** and **(b)**, sweeping a quasistatic in-plane current then generates hysteretic magnetic switching between up ($M_z > 0$) and down ($M_z < 0$) states, with the presence of an unchanged in-plane field H_y. With H_y pointing to $-y$ ($H_y < 0$), a positive I_{ch} favors the switching from up state to down state, and a negative I_{ch} favors the switching from down state to up state [resulting in a clockwise (CW) R_H-I_{ch} loop]. On the contrary, with H_y pointing to $+y$ ($H_y > 0$), a positive I_{ch} favors the switching from down state to up

state, and a negative I_{ch} favors the switching from up state to down state [resulting in a counter-clockwise (CCW) R_H-I_{ch} loop].

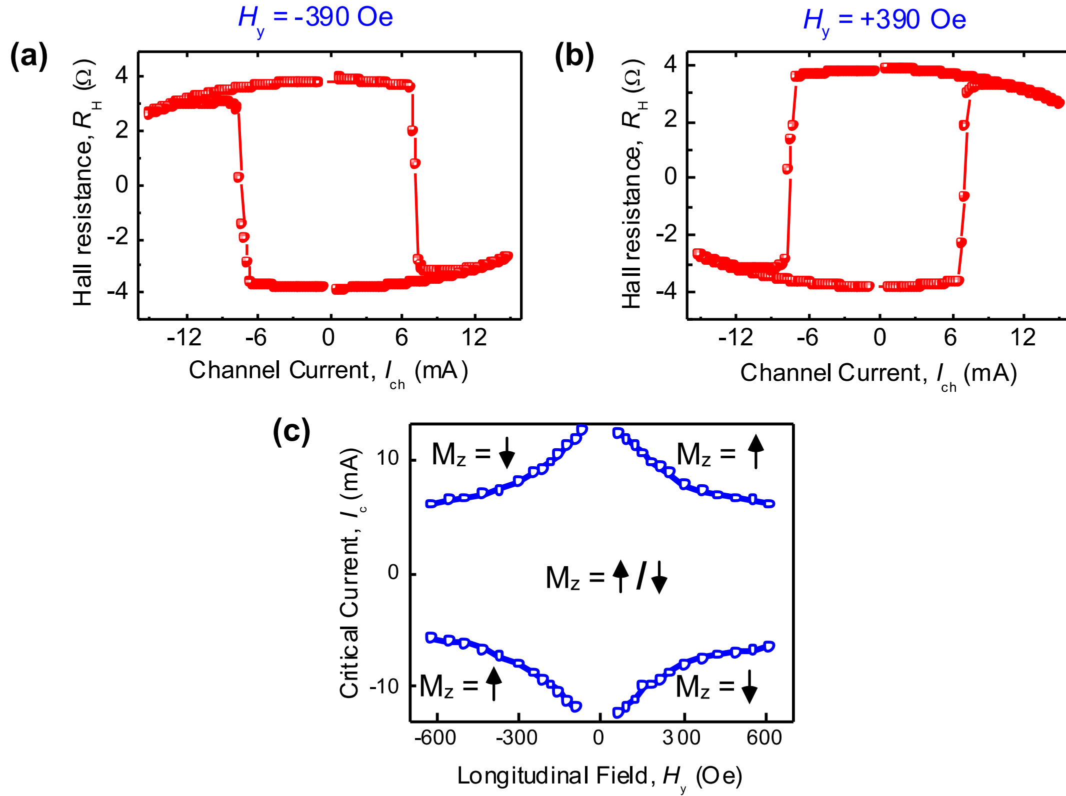

Figure 2-6. R_H-I_{ch} loops measured with **(a)** H_y = −390 Oe, and **(b)** H_y = +390 Oe. (c) Critical current I_c as a function of H_y extracted from the R_H-I_{ch} loops.

The reason for this switching pattern is, although the external in-plane field H_y wouldn't favor either magnetic orientation by itself, H_y breaks the symmetry in the response to the SHE torque. This symmetry breaking mechanism has been briefly introduced in Section 1.2.1 and illustrated in **Figure 1-5**. For H_y pointing to $-y$, according to the expression of the torque of the external field:

$$\boldsymbol{\tau}_{ext} = -\mathbf{m} \times \mathbf{H}_{ext} \tag{2-2}$$

$\boldsymbol{\tau}_{ext}$ would be pointing to $-x$ for up magnetization and pointing to $+x$ for down magnetization. Then for a positive I_{ch}, the direction of the spin torque $\boldsymbol{\tau}_{ST}$ (which points to $-x$ for both up and down magnetization) is the same as $\boldsymbol{\tau}_{ext}$ for the up state, and opposite to $\boldsymbol{\tau}_{ext}$ for the down state. As a result, with $H_y < 0$ and $I_{ch} > 0$, $\boldsymbol{\tau}_{ST}$ and $\boldsymbol{\tau}_{ext}$ together favors the rotation of $\mathbf{m}$ from $\mathbf{m}_z > 0$ to $\mathbf{m}_z < 0$. Similar analysis based on the torques can also be done for the other scenarios (i.e. $H_y < 0$ and $I_{ch} < 0$, $H_y < 0$ and $I_{ch} > 0$, $H_y < 0$ and $I_{ch} < 0$). From the other point, we can alternatively use the effective field to represent each torque. For example, the anti-damping torque $\boldsymbol{\tau}_{ST}$ expressed in Eq. (2-1) can be understand as the torque of an effective field:

$$\mathbf{H}_{ST} = \tau_{ST}{}^{0}(\mathbf{m} \times \boldsymbol{\sigma}) \tag{2-3}$$

Then, with $\mathbf{H}_{ST}$ parallel with the external field $\mathbf{H}_{ext}$, $\mathbf{m}$ will switch to the opposite direction; with $\mathbf{H}_{ST}$ anti-parallel with the external field $\mathbf{H}_{ext}$, $\mathbf{m}$ won't switch.

By measuring the switching loops with different H_y, the relationship between the critical current I_c and H_y can be plotted, as shown in **Figure 2-6 (c)**. The value of the switching current I_c decreases from 12 mA to 5 mA as the in-plane field increases from 50 Oe to 600 Oe, in agreement with SHE switching in the Pt/Co system [20].

More interesting results can be obtained by sweeping the current in the presence of a transverse in-plane field, H_x, instead of the longitudinal field, H_y, as shown in **Figure 2-7**.

When H_x is around 120 Oe or less [**Figure 2-7 (a)**], the contour of R_H in the shape of an arch is obtained with the current varying from -20 mA to +20 mA or vice versa. The gradual drop of R_H from about 4 Ω at I = 0 mA to less than 2 Ω at I = 20 mA reflects the tilt of magnetization due to the SOT. No switching is obtained here, because the torque of the transverse field H_x is vertical to $\boldsymbol{\tau}_{ST}$ and can't break the symmetry.

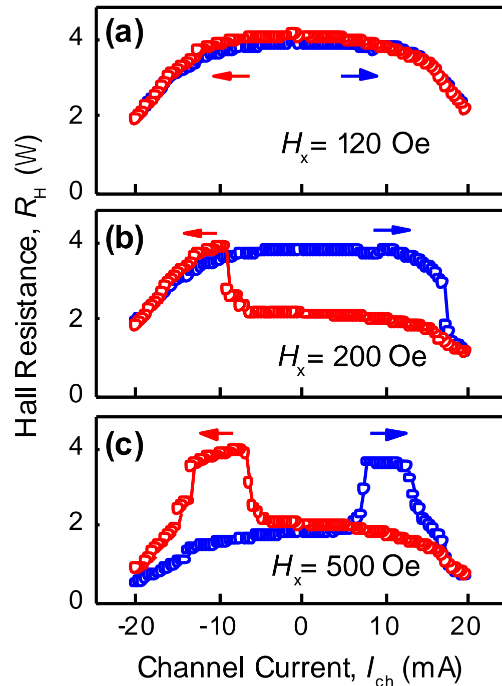

Figure 2-7. R_H as a function of DC current at the presence of the transverse field H_x. (a) H_x = 120 Oe, (b) H_x = 200 Oe and (c) H_x = 500 Oe.

However, when H_x gets larger [**Figure 2-7 (b)** and **(c)**], the contour of R_H changes noncontinuously with two bumps appearing. For example, with the presence of H_x = 500 Oe, as the current increases from zero to positive values, R_H jumps up abruptly from nearly

2Ω to 4Ω (at I = 7 mA) and then jumps back (at I = 13 mA). I call this unexpected phenomenon partial-switching, since the magnetization just switches partially, from the up state (R_H = 4Ω) to an intermediate state (R_H = 2Ω). Intuitively, this phenomenon might be related with the multi-domain states in the Hall bar device. The external field H_x itself wouldn't lead to these abrupt changes of magnetization. Instead, DMI could be a reason for such an intermediate state by generating stable helical magnetization patterns [134]. And the bumps could be due to the competition of DMI and SHE. The partial-switching phenomenon was not reported before. Whether it is a unique feature of TbFeCo still requires further study.

2.3.3 Evaluation of the spin Hall angle

Finally, the strength of SHE torque is quantitatively evaluated. According to the LLG equation, the dynamics of the magnetization is influenced by three torques: the spin torque $\boldsymbol{\tau}_{ST}$ induced by SHE [Eq. (2-1)], the torque of the external field $\boldsymbol{\tau}_{ext}$ [Eq. (2-2)], and the torque of the anisotropy field:

$$\boldsymbol{\tau}_{an} = -\mathbf{m} \times \mathbf{H}_{an} \tag{2-4}$$

As mentioned in the previous section, the equilibrium orientation of $\mathbf{m}$ would be in the y-z plane, where all three torques are collinear (along the x-axis). Then we have the torque balance equation [20]:

$$\begin{aligned} \tau_{tot} &= \hat{\mathbf{x}} \cdot (\boldsymbol{\tau}_{ST} + \boldsymbol{\tau}_{ext} + \boldsymbol{\tau}_{an}) \\ &= \tau_{ST}{}^{0} + H_y \sin\theta - H_{an}^{0} \sin\theta \cos\theta = 0 \end{aligned} \tag{2-5}$$

Where θ is the angle between $\mathbf{m}$ and the x-y plane.

To calibrate the strength of the SHE torque $\tau_{ST}{}^{0}$, we apply an in-plane field H_y and compare field sweeps for the same magnitude of current, positive and negative [for example, I_{ch} = ±4 mA as shown in **Figure 2-8 (a)**]. In this case, the gap between the curve with positive I_{ch} and negative I_{ch} is attributed to the anti-damping torque $\boldsymbol{\tau}_{ST}$. With a positive current, Eq. (2-5) becomes [20]:

$$\tau_{ST}{}^{0} + H_y^{+} \sin\theta - H_{an}^{0} \sin\theta \cos\theta = 0 \tag{2-6}$$

And with a negative current, Eq. (2-5) becomes:

$$-\tau_{ST}{}^{0} + H_y^{-} \sin\theta - H_{an}^{0} \sin\theta \cos\theta = 0 \tag{2-7}$$

Then, the strength of the anti-damping torque can be calculated as:

$$\tau_{ST}{}^{0} = (H_y^{-} - H_y^{+}) \sin\theta / 2 \tag{2-8}$$

We calculate $\tau_{ST}{}^{0} / I_{\text{ch}} = 1.5\text{mT/mA}$ and spin Hall angle is estimated to be about $J_S / J_C = 0.12$. This value is similar to that previously reported in Ta/CoFeB/MgO system [19]. Then we repeat this measurement with the field applied along the transverse direction x, as presented in **Figure 2-8 (b)**. In this case, there's no discernible difference between two R_H-H_x curves, indicating the field-like torque related with the Rashba effect is negligible in the Ta/TbFeCo system. This is predictable because the Rashba effect is an interfacial effect originating from the ultrathin asymmetric sandwiched structure, which is not the case for our bulk-PMA system.

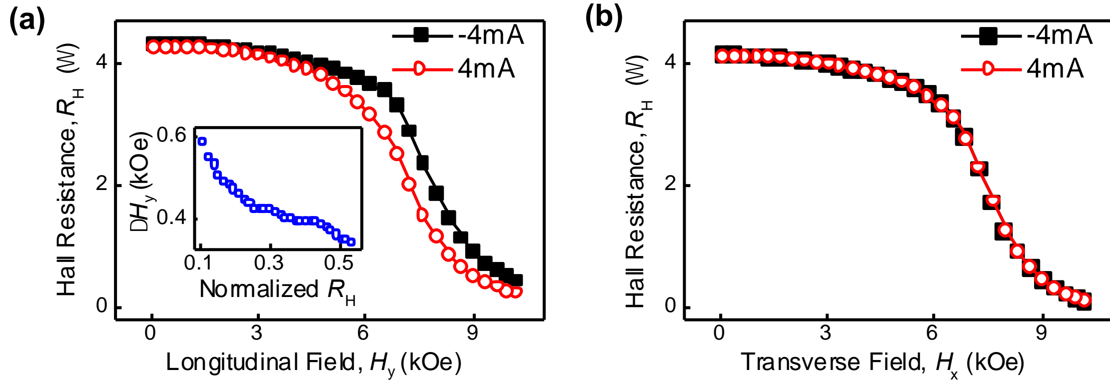

Figure 2-8. R_H as a function of **(a)** longitudinal field H_y or **(b)** transverse field H_x, for I_{ch} = ±4 mA respectively. Inset of (**a**): the difference in the applied field for +2 mA and −2 mA when R_H is the same.

2.4 Summary

In this chapter, I answered the question: whether the SHE/SOT induced magnetization switching can happen in bulk-PMA magnet. I studied the spin Hall effect in Ta/TbFeCo structures with bulk-PMA. The current-induced magnetization switching is achieved in the presence of a longitudinal field while the partial-switching phenomenon is obtained in the presence of a transverse field. The strength of anti-damping torque (or spin Hall efficiency) is in accordance with that in Ta/CoFeB/MgO systems reported previously, and the field-like torque (Rashba torque) is negligible in Ta/TbFeCo system. This work has inspired many following studies. For example, it has been reported SOT can successfully switch an ultra-thick bulk-PMA ferrimagnet (30 nm in thickness) [135].

Chapter 3 Robust Field-Free SOT Switching

3.1 Motivation and background

This chapter introduces my work on achieving the external-field-free SOT switching of perpendicular nanomagnets [136,137]. As discussed in previous chapters, SOT arising from spin Hall effect (SHE) promises the next generation of spintronics based memory and computing applications [55]. Compared with conventional STT [4,138] generated by a current passing across an ultrathin tunnel barrier in a MTJ, SHE-induced writing mechanism allows the implementation of a 3-terminal memory cell [19,28–31] where the writing current is injected in the spin Hall (SH) channel instead of the tunnel barrier thus it increases the reliability and endurance of the memory cell. Moreover, utilizing giant spin Hall efficiency materials [22,23,34–36] promises a path for drastic reduction of the writing current.

However, the early version of SOT devices has a key issue, which is that the switching of the perpendicular magnetization requires the assistance of an external magnetic field [19–21,27,34,104,109,110]. This is because the SHE-induced SOT is symmetric in respect to the perpendicular magnetization orientation, and an additional torque (for example, a torque from an external magnetic field) is required to break this symmetry. Without the external magnetic field, the perpendicular SOT devices would just fail to switch (for the switching of an in-plane magnetization, the external magnetic field is not necessary). This limitation of SOT has been discussed in Section 1.2.1 and illustrated in **Figure 1-5**. Since perpendicular MTJ (p-MTJ) is preferred over the in-plane MTJ (i-MTJ)

in MRAM cells (for the reasons discussed in Section 1.1.2), the difficulty of external-field-free switching of perpendicularly magnetized SOT devices imposes a big challenge for its applications.

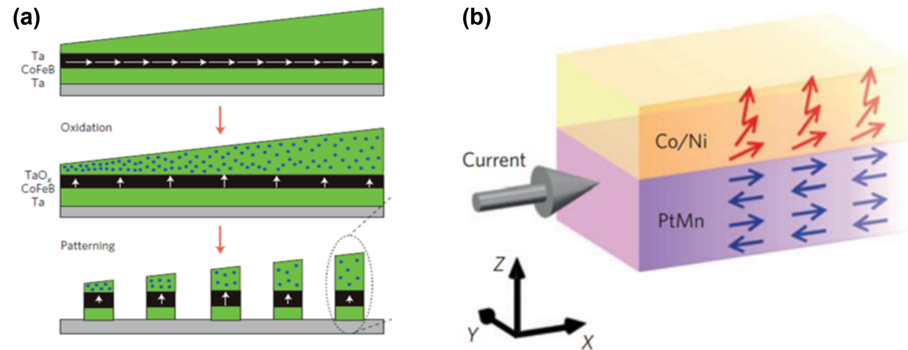

Figure 3-1. Previous solutions for the field-free SH switching. **(a)** Introduce an anisotropy gradient in the PMA layer to break the symmetry [139]. **(b)** Use an exchange-bias field to break the symmetry [140]. (Reprinted from ref. [139] and [140] with the permission from Springer Nature).

Recently, attempts have been made to achieve field-free SH switching by substituting the applied magnetic field with an effective field embedded into a device. The first approach is to introduce lateral symmetry breaking in the magnetic structure [139,141–145], as illustrated in **Figure 3-1 (a)**. The idea is by developing a film stack with thickness gradients, to introduce an anisotropy gradient in the PMA layer. With the anisotropy gradient, an effective out-of-plane field-like torque is induced, which can lead to field-free switching. However, this approach would be difficult to manufacture for high areal density memory arrays.

The second approach is based on having an anti-ferromagnetic (AFM) layer to provide an in-plane exchange field H_{ex} that breaks the symmetry [140,146–152], as shown in **Figure 3-1 (b)**. If the AFM layer also serves as the spin Hall channel [140,148,149,151], then the structure can be integrated into a 3-terminal MTJ. However, the challenges of obtaining sufficient H_{ex} [140,147–151], the existence of multi-domain states in the AFM layer [140,147,150,151], as well as the low blocking temperature in the AFM-SH systems [150] make its implementation for memories not so straightforward. Other field-free switching approaches include generating an out-of-plane spin polarization [153,154] or an electric field [155] from the bottom layer that assists the deterministic switching to happen. But all these strategies require structures with specific bottom layer(s), which eliminate the possibility of the usage of a wide range of more efficient SH materials such as tungsten and topological insulators [22,23,34–36]. Finally yet importantly, most of the above works were based on micro-scale Hall bar devices (see **Table 3**). Robust field-free switching of a nano-scaled magnetic pillar is yet to be demonstrated.

In this chapter, I will propose and demonstrate a more straightforward strategy to realize external-field-free SH switching. The idea is to use the stray field projected by an in-plane magnetized layer placed on top of the conventional PMA spin Hall structure, to substitute the external magnetic field. We call this structure a dipole-coupled composite structure. I will show the robust external-field-free SH switching of the composite nanopillar and analyze the switching process by performing the micromagnetic simulations. I will also compare our solution for field-free switching with previous works.

The rest of this chapter is organized as follows. Section 3.2 introduces experimental methods, including the fabrication of the composite devices, the measurement setup, and the parameters of micromagnetic simulations. The measurement results including the field-free switching demonstration are presented in Section 3.3, followed by more detailed discussions on switching process, device scalability, and comparison with other strategies in Section 3.4. Finally, Section 3.5 concludes the chapter. The content of this chapter has been published as a research article in Advanced Electronic Materials [137].

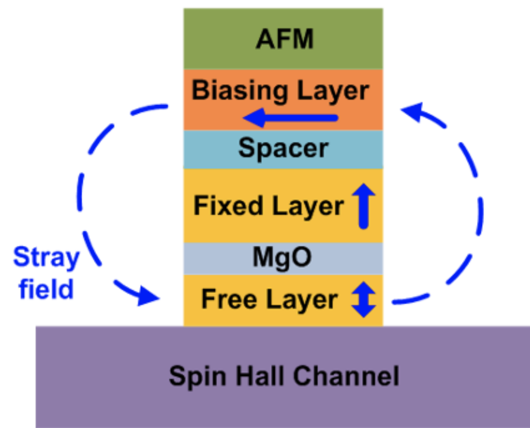

Figure 3-2. The proposed structure of a full SOT p-MTJ stack for external-field-free SH switching utilizing the composite structure. It is composed of a normal p-MTJ stack with an in-plane magnetized biasing layer placed on top, which can provide a stray field and lead to the deterministic SH switching.

3.2 Experimental methods

Conventional PMA spin Hall device consists of a perpendicular magnetic layer (PL) developed on a spin Hall channel layer. In our proposed composite structure for field-free

switching, an additional in-plane magnetic layer (IPL) is incorporated on top of the PMA structure which may be separated from the PL by a nonmagnetic metal/oxide layer [as illustrated in **Figure 3-4 (a)**]. With the film stack patterned into a nanopillar, the IPL generates a magnetic dipolar field (stray field) projected on the position of the PL. The stray field can be parallel or anti-parallel with the direction of the channel current, thus it can replace the role of the external field, leading to a deterministic switching of the PL. Therefore, with the composite structure, we don't need to exert any external magnetic field for the switching to happen. This composite structure could be incorporated into the SOT p-MTJ stack with a minimal modification on the p-MTJ structure, as illustrated in **Figure 3-2**.

3.2.1 Sample preparation and characterization

In this work, two film stacks were developed: the reference stack (same as conventional PMA spin Hall stack), and the composite stack (the reference stack with an in-plane biasing layer PL added on top). All the film stacks were deposited on thermally oxidized silicon substrates using DC and RF sputtering in our Shamrock sputter tool. The reference stack consists of Ta (5) / CoFeB (1.2) / MgO (2) / Ta (5) (from bottom to top, with thicknesses in nanometers). And the composite stack consists of Ta (5) / CoFeB (1.2) / MgO (2) / CoFeB (3) / MgO (2) / Ta (5), where the 1.2 nm-thick CoFeB layer is the PL, and the 3 nm-thick CoFeB layer is the IPL. The composition of CoFeB is $Co_{20}Fe_{60}B_{20}$, and layer thicknesses were chosen after careful optimization.

After film deposition, the magnetic property of the two film stacks were measured using VSM. The hysteresis (*M*-*H*) loops are shown in **Figure 3-3**. The perpendicular

anisotropy of the PL in both stacks is verified by the out-of-plane loops presented in the inset of **Figure 3-3**. And the effective perpendicular anisotropy field is determined to be $H_k \approx 0.35$ T for both stacks, from the saturation point of the in-plane loops. This indicates the PMA of the PL in the composite stack is barely affected by the IPL layer on top.

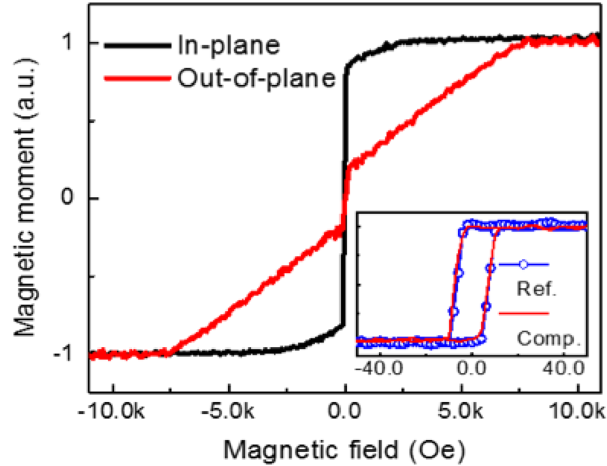

Figure 3-3. In-plane and out-of-plane *M-H* hysteresis loops of the composite stack. Inset: out-of-plane *M-H* loops of the composite stack and the reference stack, respectively, in a narrow field range.

Then, both the composite stack and the reference stack were patterned into nano devices using electron-beam (e-beam) lithography and ion milling procedures. Each device is composed of an elliptical nanopillar on top of the Ta Hall bars, as illustrated in **Figure 3-4 (a)**. **Figure 3-4 (b)** shows the SEM image of a patterned device. The nanopillar is in elliptical shape with its long axis being parallel with the SH channel in the *y*-direction. In this way, the magnetization direction of IPL would be along the *y*-axis, determined by the

shape anisotropy. And the stray field generated from IPL would be along the *y*-axis as well, parallel or anti-parallel with the direction of the channel current. This can satisfy the condition of the SH switching of the PL. Note the nanopillar could also be in circular shape, as long as the orientation of the IPL magnet is fixed along the *y*-axis (for example, pinned by an AFM layer on top). The elliptical pillars were patterned into three sizes (in order to study the effect of different pillar aspect ratios): 285 × 95 nm^2 (3:1), 300 × 120 nm^2 (2.5:1), and 300 × 150 nm^2 (2:1). For the rest of this chapter, we mainly focus on the result of the 285 × 95 nm^2 (3:1) device except where specified in the text. For the dimensions of the Hall bar, the width of the current channel is 500 nm, and the width of the voltage branch is 200 nm for all devices. The etching time of the pillar was carefully optimized to ensure that the PL CoFeB layer was fully etched. The sheet resistance of the remaining Ta layer after etching is around 640 Ω for both the composite and the reference samples, indicating the post-etching thicknesses of the Ta channel in both stacks are quite close.

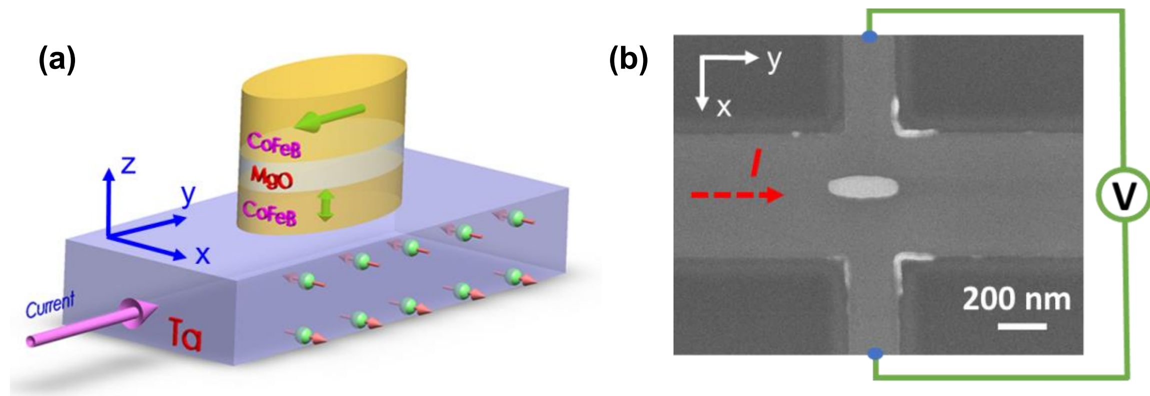

Figure 3-4. **(a)** Schematic of the composite structure Ta(5) / CoFeB(1.2) / MgO(2) / CoFeB(3) / capping, which is patterned into an elliptical nanopillar sitting on top of Ta

Hall bar. **(b)** Scanning electron micrograph (SEM) image of the fabricated device and setup of the electrical measurement. The dimension of the elliptical pillar is 285×95 nm^2.

It's worth mentioning that at the early stage of this work, we have tried to use photolithography to pattern the device, and the pillar size was in several microns. However, it turned out the results of the micron-sized devices were fuzzy, and the switching result is not clear. This is due to the multiple domains and domain walls in the micron-sized pillar, which make the stray field messed up. After the initial trial, we turned to e-beam lithography and patterned nano-scaled devices, for which we got robust switching results.

To characterize the magnetization direction of the CoFeB PL layer, the Hall resistance R_H due to the anomalous Hall effect (AHE) is measured at a given channel current I_{ch}. The current is injected into the cross bar along the longitudinal direction (y-direction), and the voltage is detected by a nano-voltmeter in the transverse direction (x-direction), as shown in **Figure 3-4**. A Keithley 6221 current source and a Keithley 2182A nanovolt meter were used in the Hall measurement. The external in-plane and out-of-plane magnetic fields were generated by coils driven by a Kepco power supply. The Keithley 6221 was also used to generate current pulses in the pulse switching measurement.

3.2.2 Micromagnetic simulation

Besides the measurement of patterned devices, I have also performed micromagnetic simulations to further demonstrate the switching process in this work. The micromagnetic simulations were performed utilizing the Object Oriented Micro Magnetic Framework

(OOMMF) [156,157]. The *Oxs_SpinXferEvolve* evolver can be directly used to model the spin Hall effect induced SOT. However, *Oxs_SpinXferEvolve* won't work if I also want to consider the STT induced from the channel current, which would play a role in the domain walls motion in PL. My final solution is to combine the xf_stt extension with the *Anv_SpinTEvolve* evolver to simulate this. SOT is described by the *xf_stt* extension, and STT driven domain wall motion is described using the *Anv_SpinTEvolve* evolver [157]. In addition, the Dzyaloshinskii–Moriya interaction (DMI) is also considered in my simulation, which is described by the *DMExchange6Ngbr* extension. The parameters used in the simulations are: saturation magnetization M_s = 1200 emu/cm^3, exchange constant A = 20 × 10^{-12} J/m^1, uniaxial anisotropy field of PL H_k = 1.8 T, Gilbert damping α = 0.02, spin polarization P = 0.5, non-adiabatic parameter β = 0.04, spin Hall angle θ_{SH} = 0.15, Dzyaloshinskii–Moriya constant |D| = 0.5 mJ/m^2, and current density J = 30 × 10^{11} J/m^2. The device geometry in the simulation is the close to what was patterned in the experiment, i.e. 300 × 150 nm^2 ellipses with the thickness of 1 nm for PL and 3 nm for IPL. All the micromagnetic simulations were performed without the consideration of thermal effects. The script of the micromagnetic simulations can be found in Appendix B.

3.3 Results

In this section, I will present the results of electrical measurements for the composite sample and demonstrate the external-field-free SH switching. The magnetization direction of PL can be identified by measuring the Hall resistance R_H, which has been stated in Chapter 2. In my experiment setup, positive R_H represents PL's magnetization pointing up (+z), and negative R_H represents PL's magnetization pointing down (−z). Since the

magnetization direction of PL and IPL can be affected either by an out-of-plane external field H_z, or by an in-plane external field H_y, or by the channel current I_{ch}, we performed the following measurements using various configurations to investigate how the preferred magnetization is tuned in a composite device.

3.3.1 Measurements with an out-of-plane field

First, R_H is examined by scanning the out-of-plane field H_z, at different channel currents I_{ch}. **Figure 3-5 (b)** shows the R_H-H_z loops for the reference sample. **Figure 3-6 (b)** and **Figure 3-7 (b)** shows the R_H-H_z loops for the composite sample. The phase diagrams are plotted in **Figure 3-5 (c)**, **Figure 3-6 (c)** and **Figure 3-7 (c)**, which shows how the coercive field H_c and loop center H_{shift} are changed as a function of I_{ch}.

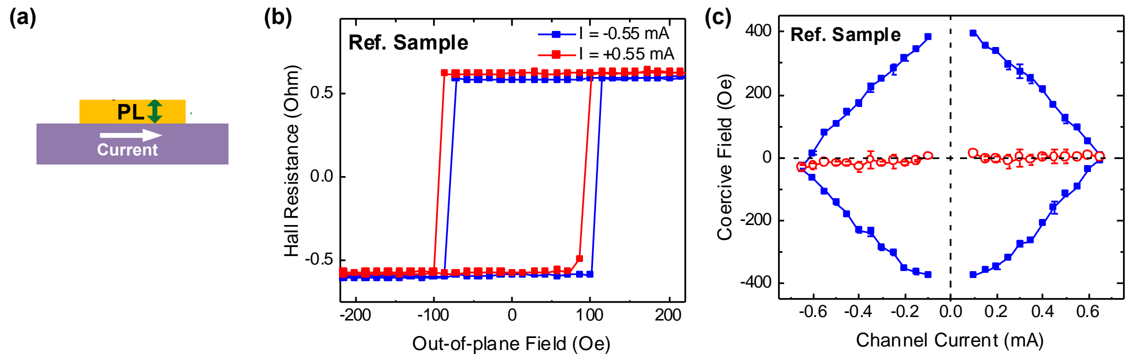

Figure 3-5. The R_H-H_z measurement results for the reference sample. **(a)** The schematic of the reference sample showing the magnetization configuration. **(b)** R_H-H_z loops measured with different I_{ch}. **(c)** Coercive field H_c (square symbol) and shift of loop H_{shift} (circular symbol) as a function of I_{ch}.

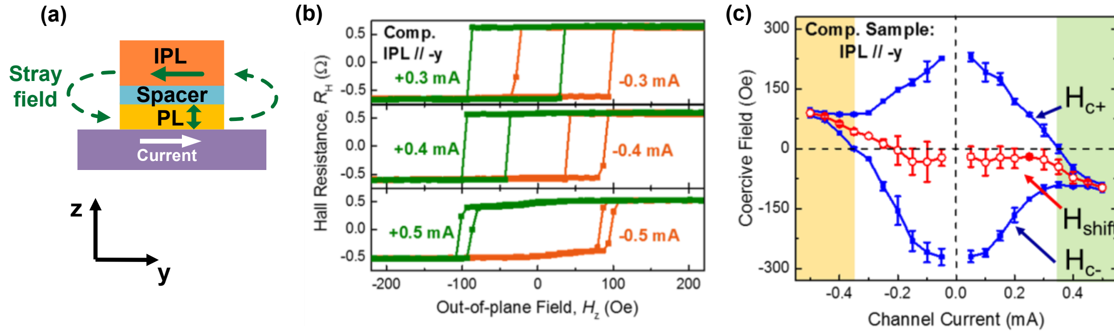

Figure 3-6. The R_H-H_z measurement results for the composite sample, with IPL // −*y*. **(a)** The schematic of the composite sample showing the magnetization configuration and stray field direction. **(b)** R_H-H_z loops measured with different I_{ch}. **(c)** Coercive field H_c (square symbol) and shift of loop H_{shift} (circular symbol) as a function of I_{ch}.

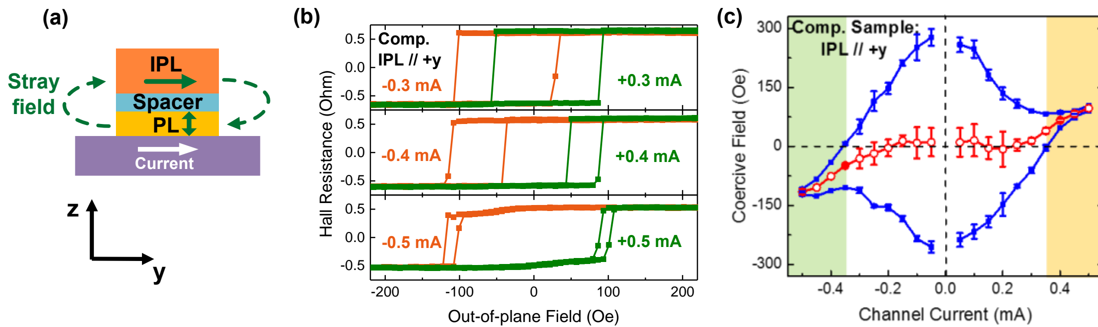

Figure 3-7. The R_H-H_z measurement results for the composite sample, with IPL // +*y*. **(a)** The schematic of the composite sample showing the magnetization configuration and stray field direction. **(b)** R_H-H_z loops measured with different I_{ch}. **(c)** Coercive field H_c (square symbol) and shift of loop H_{shift} (circular symbol) as a function of I_{ch}.

For the result of the reference sample shown in **Figure 3-5**, it is similar to the result of Ta/TbFeCo sample shown as **Figure 2-3** in Chapter 2: the R_H-H_z loops gets narrower as the I_{ch} is increased due to the increase of SOT as well as Joule heating, but all the R_H-H_z loops are symmetric about zero-field point without any shift. This indicates without an in-plane field, I_{ch} alone won't result in a preferrable magnetization direction of PL.

In contrast, the results of the composite sample shown in **Figure 3-6** and **Figure 3-7** are quite different. In **Figure 3-6 (b)** and **Figure 3-7 (b)**, the R_H-H_z loops were obtained at I_{ch} = ±0.3 mA, ±0.4 mA, and ±0.5 mA (corresponding to J_{ch} = $\pm 1.2\times 10^7$ A/cm^2, $\pm 1.6\times 10^7$ A/cm^2, and $\pm 2.0\times 10^7$ A/cm^2) respectively. Note positive I_{ch} corresponds current along +y direction, and negative I_{ch} corresponds current along −y direction. The IPL's magnetization is set to –y direction for **Figure 3-6**, and +y direction for **Figure 3-7**. With $|I_{ch}|$ increased, the coercive field of the loop (H_c) gradually decreases, similar to the reference sample. Remarkably, the center of the loop is shifted toward left or right at large $|I_{ch}|$. At I_{ch} = ±0.5 mA, the separation between the two loops is H_{shift} (–0.5 mA) – H_{shift} (+0.5 mA) ≈ 187 Oe. This indicates I_{ch} with opposite signs favors opposite orientations of PL in the composite structure. In addition, with IPL pointing to opposite directions (–y or +y), the R_H-H_z loop is shifted oppositely, by comparing **Figure 3-6 (b)** and **Figure 3-7 (b)**. The full dependence of H_c and H_{shift} on channel current I_{ch} is presented in **Figure 3-6 (c)** and **Figure 3-7 (c)**.

Similar symmetry breaking behavior has also been observed in some of the recent field-free SH switching devices, induced either by an PMA gradient [139,141,142,145], or by an in-plane exchange bias field [140,146,151]. Here in the dipole-coupled composited structure, the breaking of symmetry is induced by the stray field from the IPL. When IPL

is set to $-y$ direction (**Figure 3-6**), the direction of its stray field experienced by the PL is mainly along $+y$. As a result, up magnetization of PL is preferable at $I_{ch} > 0$ and down magnetization of PL is preferable at $I_{ch} < 0$. When IPL is set to $+y$ direction (**Figure 3-7**), the preferred state becomes opposite. The value of $|H_{shift} / J_{ch}|$ [139,145] may partially reflect the strength of the inversion asymmetry. For our devices, $|H_{shift} / J_{ch}|$ is determined to be around 45 Oe / 10^7 A cm^{-2} [from **Figure 3-6 (c)**, **Figure 3-7 (c)**, and **Figure 3-14** in the next section]. $|H_{shift} / J_{ch}|$ value of previous works can be found in **Table 3**. Besides, the diagrams in **Figure 3-6 (c)** and **Figure 3-7 (c)** give a hint about when the field-free switching can happen. We notice for the regions of $|I_{ch}| < 0.35$ mA in **Figure 3-6 (c)** and **Figure 3-7 (c)**, H_c^+ and H_c^- are of opposite sign. Whereas for the regions of $|I_{ch}| > 0.35$ mA (marked with green/yellow background), H_c^+ and H_c^- are of the same sign, reflecting the R_H-H_z loop is completely shifted beyond the zero-field point, and only one orientation of PL, either up or down, is stable at $H = 0$. This implies that the external-field-free switching could be obtained within these regions.

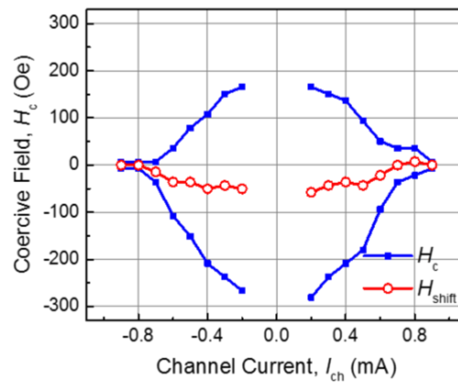

Figure 3-8. Coercive field H_c (square symbol) and shift of loop H_{shift} (circular symbol) as a function of I_{ch}, for a composite device with IPL // $+x$. The device is with an elliptical

pillar of 95 × 285 nm^2, where the long axis is along *x*-direction (the transverse direction) instead of along *y*-direction, and the channel width is 1 μm.

Then in **Figure 3-8**, the result of another device is shown for comparison, which was patterned from the same composite stack but with nanopillar's long axis along *x*-axis (in the transverse direction). Then the IPL magnetization would point to +*x* or –*x* direction due to the shape anisotropy. **Figure 3-8** shows the result for this device by performing the same measurement as in **Figure 3-6 (c)** and **Figure 3-7 (c)**. As can be seen, the curves under positive I_{ch} and negative I_{ch} are symmetric and H_{shift} is zero at a large current, unlike the symmetry-breaking behavior appeared in **Figure 3-6 (c)** and **Figure 3-7 (c)**. The non-zero shift under a small current in **Figure 3-8**, as also appeared in **Figure 3-6 (c)** and **Figure 3-7 (c)**, is probably due to the existence of a perpendicular component in the magnetization of IPL. The zero-H_{shift} at a large current in **Figure 3-8** indicates that if the magnetization of the IPL is oriented in the *x* direction, it wouldn't assist the switching of PL to happen. This is in consistence with the fact that an applied field H_x along the transverse direction would not result in the SH switching of a PMA layer.

3.3.2 Measurements with an in-plane field

The influence of the IPL biasing layer in the composite nanopillar is then studied by sweeping the external field H_y in the presence of various channel currents, as shown in **Figure 3-9**. First, let's look at the case with a positive current I_{ch} = +0.35 mA [**Figure 3-9 (b)**]. In this case, PL has a up magnetization when $H_y > 0$ (as suggested by the positive R_H

values), and a down magnetization when $H_y < 0$ (as suggested by the negative R_H values). This can be explained by the symmetry breaking due to the application of the external field H_y [20]. However, the switching of PL occurs before H_y is swept across the zero point, which is different from conventional unbiased SH devices [110]. Then, if the channel current I_{ch} is increased to +0.55 mA, the result is shown in **Figure 3-9 (a)**. It's interesting to note that multiple switching events occur within the external field range of –150 Oe ~ +150 Oe, which hasn't been observed in previous perpendicular SH devices.

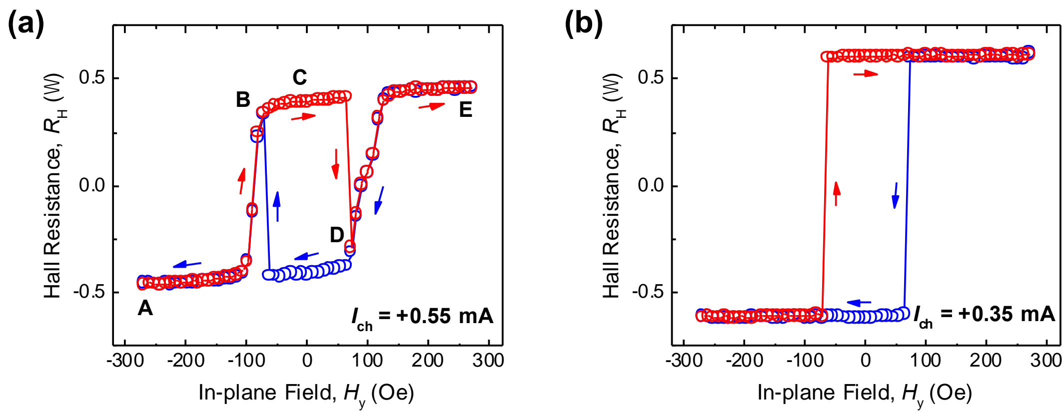

Figure 3-9. R_H-H_y loops measured with **(a)** I_{ch} = +0.55 mA and **(b)** I_{ch} = +0.35 mA for the composite sample.

Such unique behaviors of the composite nanopillar can be well explained by the competition between the stray field H_{stray} of IPL and the external field H_y. For better understanding of the switching behaviors, the current switching loops (R_H-I_{ch}) are measured under various H_y, gradually changing from −270 Oe to +270 Oe, as presented in **Figure 3-10**. Five critical points A-E labelled in **Figure 3-9 (a)** are also pointed out in

Figure 3-10, with the magnetization configuration of each state plotted on the right side of the R_H-I_{ch} loops. For the sack of simplicity, it is assumed the stray field of IPL is a uniform field along +*y*/−*y* direction. In real case, H_{stray} is not uniform accompanying with an out-of-plane component as well that is further discussed in next section.

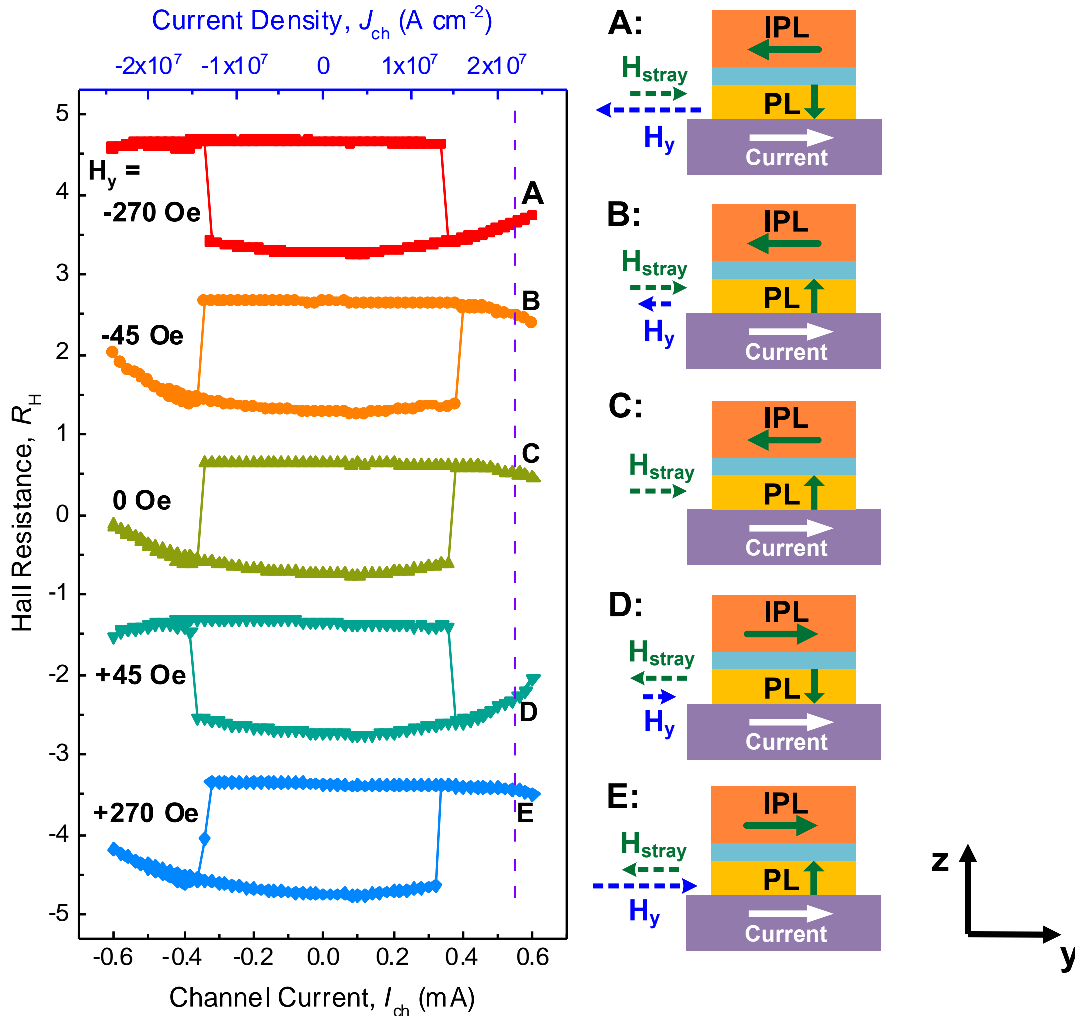

Figure 3-10. R_H-I_{ch} loops under various H_y, which is gradually changed from −270 Oe to +270 Oe. Five points A-E representing five critical states of the device are labelled in the loops, which are corresponding to the A-E labels in **Figure 3-9 (a)**. Right: schematics

illustrating the magnetization configurations of the five points A-E, where the lengths of the dash arrows represent the strengths of the fields.

Initially upon the application of $H_y = -270$ Oe, the IPL is aligned along H_y pointing to $-y$ direction (point A). As a result, the stray field projected on PL is along $+y$ thus opposing the external field. The total field experienced by PL is $H_{tot} = H_y + H_{stray}$. Considering $|H_y| > |H_{stray}|$, H_{tot} is dominated by H_y pointing to $-y$ direction. Therefore, the R_H-I_{ch} loop is clockwise (CW). Upon decreasing H_y down to -45 Oe (point B), the R_H-I_{ch} loop becomes counter-clockwise (CCW), suggesting H_{stray} is dominant over H_y thus H_{tot} is along $+y$ direction. This CW to CCW transition corresponds to the switching between point A and point B in **Figure 3-9 (a)**. With further reduction of H_y to 0 (point C), $H_{tot} = H_{stray}$ still points to $+y$, and the CCW loop remains unchanged. When H_y becomes $+45$ Oe, the polarity of R_H-I_{ch} loop changes back to CW, corresponding to the sudden jump between point C and point D in **Figure 3-9 (a)**. This is due to the reversal of IPL and H_{stray}, since $H_y = +45$ Oe is larger than IPL's coercive field H_c^{IPL} [note H_c^{IPL} depends on the Joule heating induced by the channel current, as described in the next section; and this is why the valley at point D in **Figure 3-9 (a)** doesn't appear in **Figure 3-9 (b)**]. Finally, by increasing H_y above $|H_{stray}|$, the R_H-I_{ch} loop in **Figure 3-10** transits again from CW to CCW, corresponding to the jumping up from point D to point E in **Figure 3-9 (a)**. This is because H_y again becomes the dominant field in the switching process. In summary, the multiple jumps in **Figure 3-9 (a)** and the multiple changes of the loop polarity in **Figure 3-10** are due to the competition between H_{stray} and H_y: under a large $|H_y|$ the favored orientation of PL is

determined by the direction of H_y, similar to the case of conventional unbiased SH devices; under a small $|H_y|$ or without any external field, PL also has a preferred orientation which is determined by the direction of H_{stray} instead of H_y.

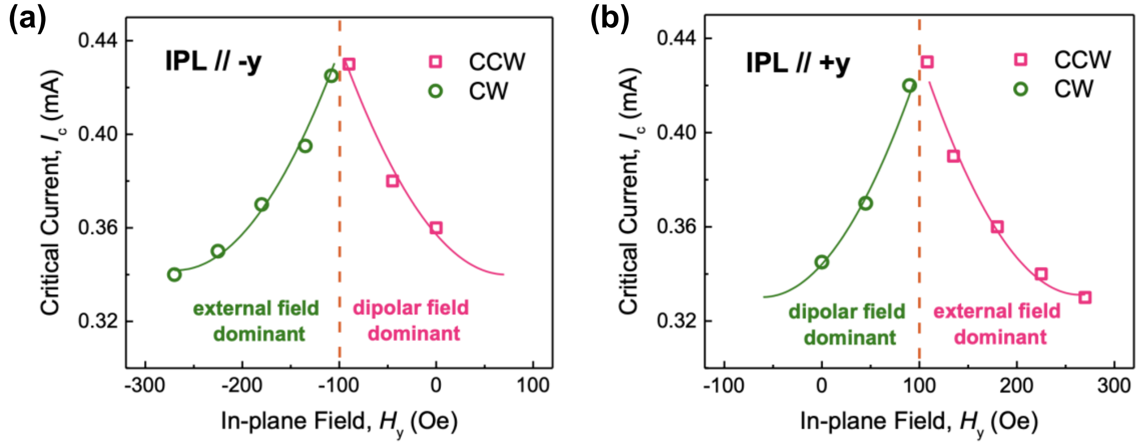

Figure 3-11. Critical current I_c as a function of H_y extracted from the R_H-I_{ch} loops, for **(a)** IPL // $-y$ and **(b)** IPL // $+y$, respectively. I_c values obtained from clockwise (CW) and counter-clockwise (CCW) loops are plotted as different symbols. Solid lines are eye-guided fitting to the data.

The variation of the critical current I_c (the switching point of R_H-I_{ch} loop) as a function of H_y is then plotted in **Figure 3-11**. Especially, the 3 points at $H_y = -270$ Oe, -45 Oe and 0 Oe in **Figure 3-11 (a)** correspond to the top 3 switching loops in **Figure 3-10**, and the 2 points at $H_y = +45$ Oe and $+270$ Oe in **Figure 3-11 (b)** correspond to the bottom 2 switching loops in **Figure 3-10**, respectively. The polarity of the switching (CW or CCW) is specified in **Figure 3-11** as well. Compared the result of the unbiased SH devices shown in **Figure 2-6 (c)** in Chapter 2, the boundary between the CW and CCW loops for the composite

device [denoted by the vertical dash lines in **Figure 3-11 (a)** and **(b)**] locates at ±100 Oe as opposed to 0. I define the compensation point H_{comp} to represent the boundary field. So H_{comp} is 100 Oe for the 285 × 95 nm^2 nanopillars, 108 Oe for the 300 × 120 nm^2 nanopillars, and 135 Oe for the 300 × 150 nm^2 nanopillars (from **Figure 3-15** in the next section). H_{comp} directly reflects the strength of H_{stray} and the strength of symmetry breaking. The value of H_{comp} for our composite device is larger than most of the previous works (as shown in **Table 3**).

3.3.3 Robust external-field-free switching

From **Figure 3-10** we have already observed the switching of PL nanomagnet in the absence of any external field. **Figure 3-12** presents the external-field-free switching loops with IPL // −y and IPL // +y, respectively. Consistent with previous analysis, I_{ch} parallel with IPL (i.e. anti-parallel with H_{stray}) favors down magnetization of PL, while I_{ch} anti-parallel with IPL (i.e. parallel with H_{stray}) favors up magnetization of PL.

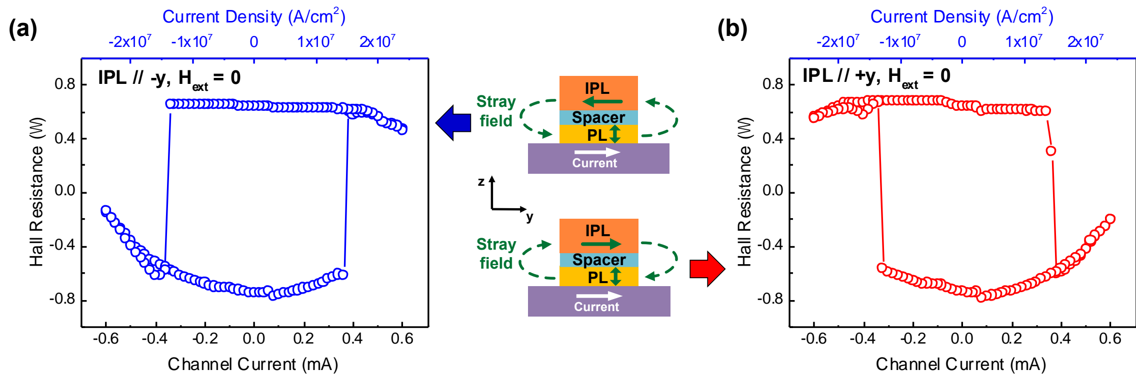

Figure 3-12. R_H-I_{ch}(J_{ch}) loops measured without any external field. The IPL is initialized to IPL // −y in **(a)** and IPL // +y in **(b)**, respectively.

Till now, all the measurements were performed with DC current. Next, we use current pulses to demonstrate the robust field-free toggling of the nanopillar, as presented in **Figure 3-13**. The pulse amplitude is 0.6 mA and pulse width is 10 μs. Unlike the partial switching obtained in the exchange-coupled devices [140,147,148,150–152] which is attributed to the multi-domain state in the anti-ferromagnetic layer, the switching in our device is abrupt and completed, suggesting the dipole-coupled devices would be more desirable for memory applications.

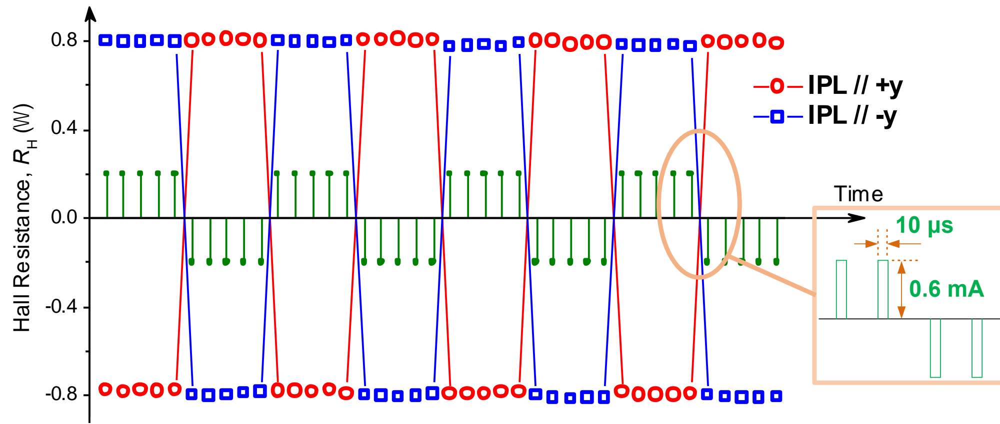

Figure 3-13. R_H variation upon application of a sequence of current pulses without external field. The pulse amplitude is 0.6 mA and pulse width is 10 μs. The configurations of IPL // −*y* and IPL // +*y* are plotted as different symbols.

3.4 Discussions

3.4.1 Comparison of the nanopillars with different aspect ratios

In the previous section, I present the results obtained from the composite nanopillar with the dimension of 285 × 95 nm^2 (3 : 1). Now I will show the results of devices with

other aspect ratios, i.e. 300 × 120 nm^2 (2.5 : 1) pillar and 300 × 150 nm^2 (2 : 1) pillar, in **Figure 3-14** and **Figure 3-15**. In **Figure 3-14**, the curve shows H_c and H_{shift} versus I_{ch} for 300 × 120 nm^2 and 300 × 150 nm^2 composite pillars. The two-fold symmetry behavior of the curves are similar to that shown in **Figure 3-6 (c)** and **Figure 3-7 (c)** for the 285 × 95 nm^2 composite pillar, and the amplitude of H_{shift} is also close to that of the 285 × 95 nm^2 composite pillar (shift around 100 Oe at I_{ch} = 0.5 mA). This indicates the pillar is not necessarily to have a large aspect ratio in order to be switchable without an external field. With the IPL being pinned, the aspect ratio of the pillar could be decreased to 1. The reason for making elliptical pillars with large aspect ratios in this work is to guarantee the magnetization of IPL is thermally stable, since we don't get the IPL pinned. As will be seen in the next section, the thermal stability of IPL decreases dramatically with the aspect ratio decreasing.

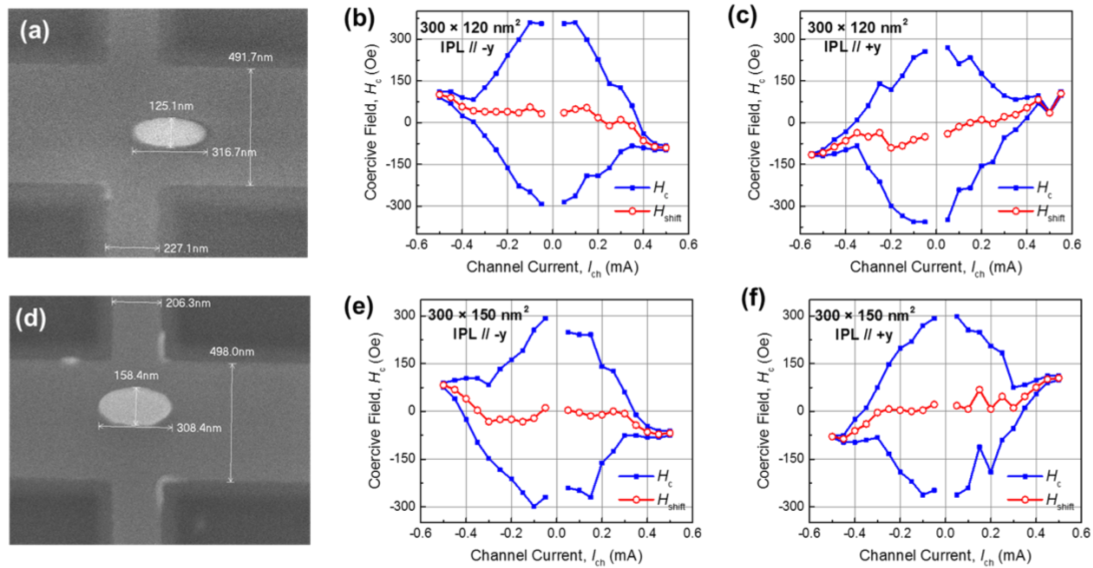

Figure 3-14. Variation of H_c and H_{shift} versus I_{ch} for composite pillars with different aspect ratio. **(a)**, **(d)** SEM images of the device with **(a)** 300 × 120 nm^2 (2.5 : 1) pillar and **(d)** 300

× 150 nm^2 (2 : 1) pillar. **(b)**, **(c)** Coercive field H_c and loop shift H_{shift} as a function of I_{ch} for the 300 × 120 nm^2 composite device, extracted from the R_H-H_z loops, with IPL been initialized to IPL // −y in **(b)** and IPL // +y in **(c)**, respectively. **(e)**, **(f)** H_c and H_{shift} as a function of I_{ch} for the 300 × 150 nm^2 composite device, with IPL being initialized to IPL // −y in **(e)** and IPL // +y in **(f)**, respectively.

Figure 3-15 plots the critical current I_c as a function of H_y for the 300 × 120 nm^2 and the 300 × 150 nm^2 composite pillars, by performing the same measurement as in **Figure 3-11**.The boundary between CCW and CW switching loops is denoted by the vertical dash lines in **Figure 3-15 (a)** and **(b)**. As can be seen, with the aspect ratio approaching 1, the compensation field H_{comp} increases from 100 Oe (3 : 1 pillar) to 108 Oe (2.5 : 1 pillar) to 135 Oe (2 : 1 pillar). This is due to the increasing of the stray field in the *y*-direction, as can be seen from the calculated result in **Figure 3-15 (c)**.

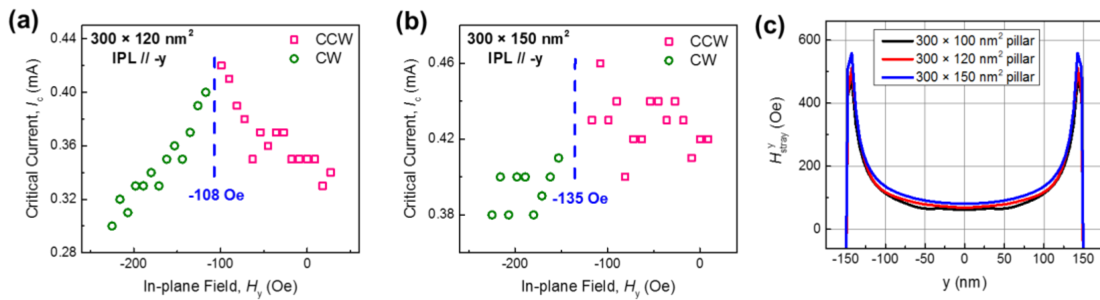

Figure 3-15. Critical current I_c versus external field H_y for composite pillars with different aspect ratio. **(a)** I_c versus H_y for the 300 × 120 nm^2 (2.5 : 1) composite pillar. **(b)** I_c versus H_y for the 300 × 150 nm^2 (2 : 1) composite pillar. The directions of IPL are all along $-y$.

(c) The calculated *y*-component of the stray field, H_{stray}^{y}, generated from the IPL with different aspect ratios.

3.4.2 Thermal stability of the IPL

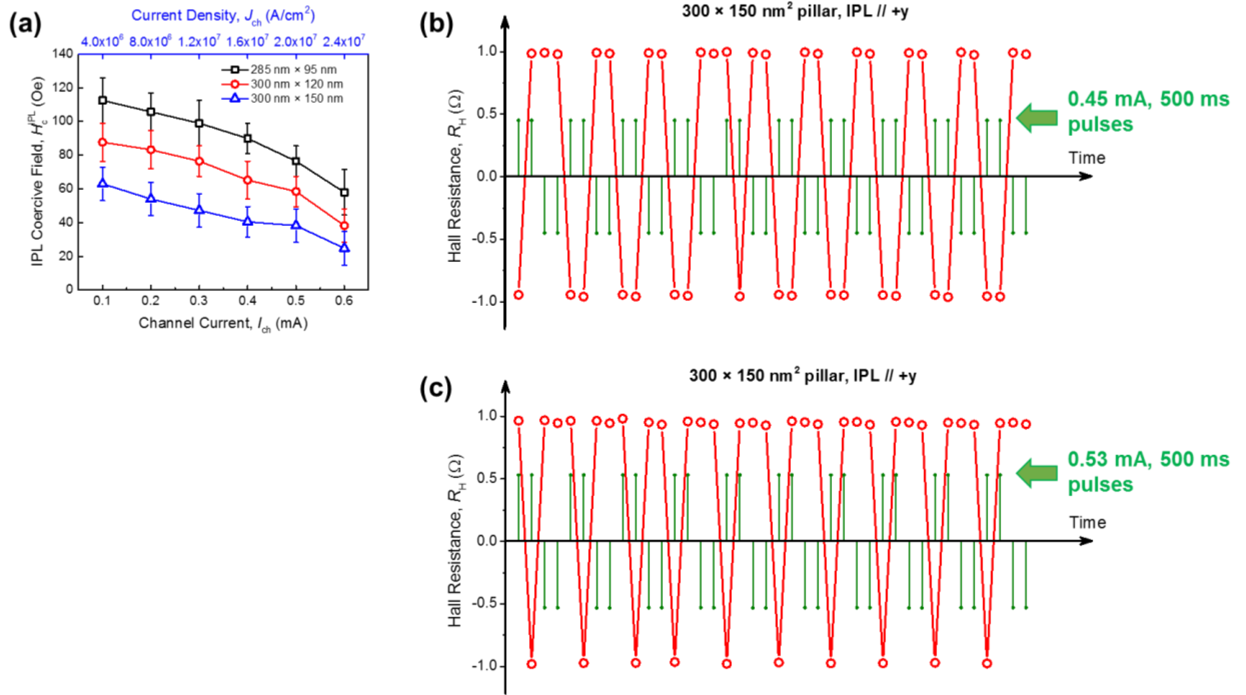

Figure 3-16. Coercive field of IPL versus channel current and the effect of IPL's thermal stability on the switching error. **(a)** The coercive field of IPL H_c^{IPL} as a function of various channel current I_{ch} applied. The three curves are for devices with 285 × 95 nm^2 (3 : 1), 300 × 120 nm^2 (2.5 : 1) and 300 × 150 nm^2 (2 : 1) pillars, respectively. The channel widths of all devices are 500 nm. **(b)**, **(c)** R_H variation upon application of a sequence of current pulses without external field for the composite device with 300 × 150 nm^2 (2 : 1) pillars.

In **(b)** the pulse amplitude is 0.45 mA and the pulse width is 500 ms, in **(c)** the pulse amplitude is 0.53 mA and the pulse width is 500 ms. The directions of IPL are all along $+y$.

In the previous section, I mention the switching of PL between C and D in **Figure 3-9 (a)** is because IPL is reversed by the external field H_y. Apparently, the coercive field of IPL H_c^{IPL} relies on the thermal stability of IPL. Therefore, H_c^{IPL} is a function of both the channel current (which induces Joule heating) and the aspect ratio of the elliptical pillar (larger aspect ratio corresponds to larger shape anisotropy and thermal stability), as shown in **Figure 3-16 (a)**. H_c^{IPL} was determined by consecutively detecting the magnetization direction of IPL after applying H_y with a series of different strengths; and the direction of IPL was determined from the polarity of the switching loop of PL.

The thermal stability of IPL is essential for a successful field-free switching. As shown in **Figure 3-16 (b)** and **(c)**, with the pulse current increasing from 0.45 mA to 0.53 mA, the error rate for the switching of a 300×150 nm^2 nanopillar increases significantly. This is because the stray field generated from IPL becomes weaker under a large channel current, due to the thermal fluctuation of the IPL's magnetization. Additionally, with the same current pulse, the error rate for the 285×95 nm^2 nanopillar is much lower (see **Figure 3-13** in the previous section), because of its stronger shape anisotropy induced from larger aspect ratio of IPL. For practical memory applications, the thermal stability of IPL can be enhanced with a pinning layer instead of the geometry with large aspect ratios.

3.4.3 Analysis on the effect of non-uniform stray field

In the previous section, the experimental results are qualitatively explained by assuming H_{stray} as a uniform field projected on PL nanomagnet along the *y*-axis. In reality, however, the stray field has a non-uniform profile, as shown in **Figure 3-17**. **Figure 3-17 (a)** illustrates *y*- and *z*-components of the stray field (H^{y}_{stray} and H^{z}_{stray}) at different locations of PL (with IPL pointing to −*y*), and **Figure 3-17 (b)** plots the profile of H^{y}_{stray} and H^{z}_{stray} based on micromagnetic calculations. It can be seen both H^{y}_{stray} and H^{z}_{stray} are weaker at the center and stronger at the edge of the pillar along the long axis, and the direction of H^{z}_{stray} reverses at the center. The stray field relies on multiple factors, including the saturation magnetization of IPL, the thickness of IPL, the distance from PL to IPL, and the dimension of the nanopillar. **Figure 3-18** shows the stray field profiles with different IPL thicknesses and different PL-to-IPL distances for the 300 × 150 nm^2 elliptical pillar. Therefore, the stray field can be tuned by engineering aforementioned factors, to make it suitable for various applications.

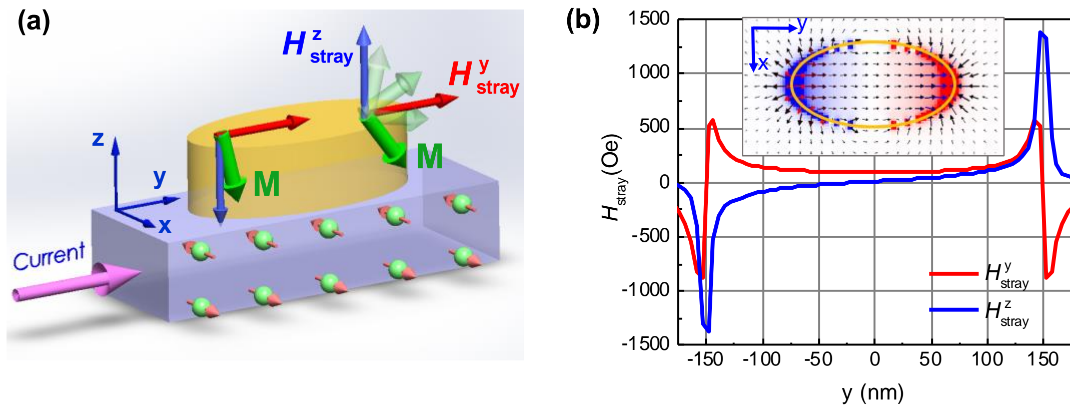

Figure 3-17. **(a)** Schematic showing the non-uniform stray fields from IPL // −*y*, and the resultant non-coherent switching of the magnetization. **(b)** Calculation results showing the stray field profile along the long axis of PL for the 300 × 150 nm^2 pillar. Inset: mapping of the stray field distribution on the PL, where the arrows show the strengths and directions of the in-plane component of the stray field, and color pixels show the strengths and directions of the *z*-component of the stray field (red = up, blue = down).

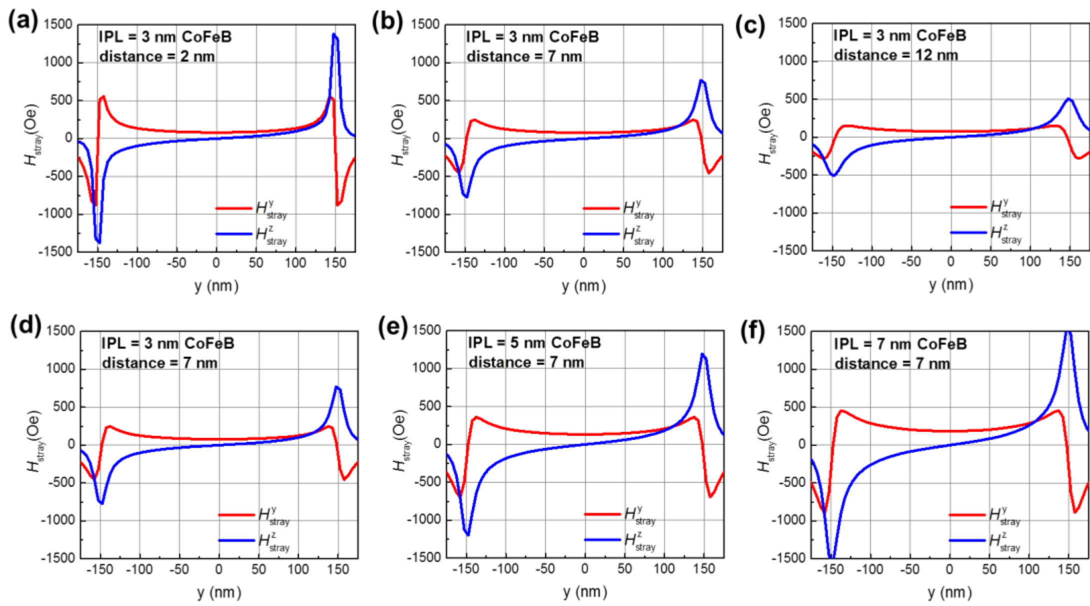

Figure 3-18. Calculated stray field depending on IPL thickness and PL-to-IPL distance for a 300 × 150 nm^2 elliptical pillar. **(a)-(c)** IPL's stray field profile along the long axis of the PL layer, with the same IPL thickness of 3 nm and different PL-to-IPL distances. (**d)-(f)** IPL's stray field profile along the long axis of the PL layer, with different IPL thickness and the same PL-to-IPL distance.

In order to study the effect of the non-uniform stray field on the switching process, I performed the micromagnetic simulations [156,157]. It has been reported for nanomagnets with the dimension of a few hundred nanometers, both the SH switching process [158–161] and field induced switching process [162] contain two steps: domain nucleation and domain wall propagation. With the non-uniform stray field, the reversal of the perpendicular magnetization would start from one side of the pillar, where both $H_{\mathrm{stray}}^{\mathrm{y}}$ and $H_{\mathrm{stray}}^{\mathrm{z}}$ favors the reversal (this would be where the domain nucleation happens). On the other side of the the pillar, where $H_{\mathrm{stray}}^{\mathrm{y}}$ favors the reversal whereas $H_{\mathrm{stray}}^{\mathrm{z}}$ opposes the reversal, the switching might be slower [as shown in **Figure 3-17** (**a**)]. For a thorough understanding of our SH switching process, the micromagnetic simulation results are shown below.

3.4.4 Simulation of field-free switching for 300 × 150 nm^2 nanopillar

Figure 3-19 shows the results of micromagnetic simulations, trying to reproduce the field-free switching behavior observed from experiments. The simulation parameters and details are described in 3.2.2, and the simulation code is attached in Appendix B. Let's first look at the first column in **Figure 3-19**. It shows the simulated evolution of PL magnetization under the non-uniform stray field (no external field is applied). Initially the PL magnet is pointing down, represented by all-blue pixels. Upon the application of the channel current, a reversed domain is first nucleated near the +*y* end of the pillar followed by the expansion of the domain. This is because both $H_{\mathrm{stray}}^{\mathrm{y}}$ pointing to +*y* and $H_{\mathrm{stray}}^{\mathrm{z}}$ pointing to +*z* favors the reversal. However, if only considering the SOT induced from

SHE, the reversed domain can hardly expand to the whole pillar, because H_{stray}^{z} pointing to $-z$ at the other end of the pillar favors down magnetization. This does not agree with the experiments where complete switching has been obtained.

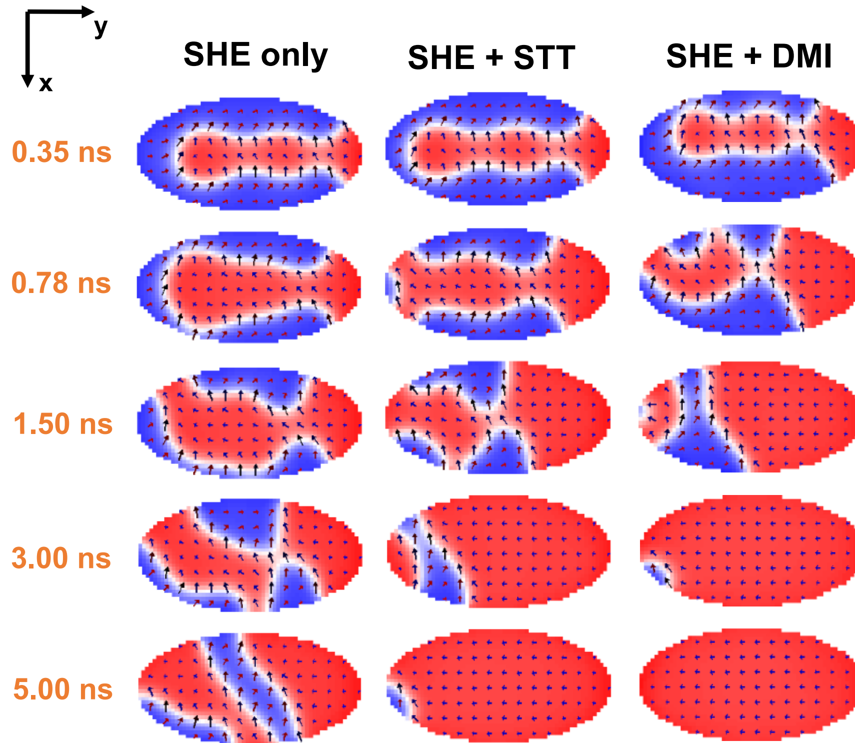

Figure 3-19. Simulated magnetization evolution in the PL of the 300 × 150 nm^2 pillar, under the non-uniform stray field shown in **Figure 3-17 (b)** and a constant channel current along $+y$ (the initial magnetization of PL is pointing down marked as blue color). Although the SHE alone cannot lead to a complete switching, the switching can be completed if involving STT or DMI driven domain wall motion.

To solve this discrepancy, I also considered two additional mechanisms that may assist the expansion of the reversed domain: (a) domain wall propagation driven by spin-

transfer torque (STT) in the PL layer (as shown in the second column of **Figure 3-19**); and (b) domain wall propagation controlled by SHE in the presence of Dzyaloshinskii-Moriya interaction (DMI) [110,112,163,164] (as shown in the third column of **Figure 3-19**). Simulations show both mechanisms can drive the expansion of the reversed domain to the entire pillar. For our case, the full switching of the nanomagnet is more likely via the simultaneous action of spin orbit torque and DMI, since STT-driven domain wall motion tends to take place in structures with thinner underlayer [144]. Note DMI has been recently investigated in exchange coupled systems (FM/Ru/FM) [165,166]. Such an effect is not relevant with my device, because in our device the 2 nm MgO layer between PL and IPL would not allow any exchange coupling to happen.

3.4.5 Simulation of field-free switching for 10 × 10 nm^2 nanopillar

If the nanopillar is shrunk down to below 40 nm, the magnetization switching mode would change from nucleation type to single domain type [159]. Then the switching process would be different from the case of a 300 × 150 nm^2 pillar. The micromagnetic simulation of the field-free switching for a 10 × 10 nm^2 circular pillar is presented in **Figure 3-20** and **Figure 3-21**. **Figure 3-20** shows the profile of the stray field across PL in a 10 × 10 nm^2 composite nanopillar, where the distance between IPL and PL is set to 7 nm to mimic the distance in a full MTJ stack. Large IPL saturation magnetization of 1700 emu/cm^3 and IPL thickness of 7 nm are used to enhance the stray field. The magnetization direction of IPL is set to –*y* direction assuming it has been pinned by a top anti-ferromagnetic layer. Other simulation parameters are shown in **Table 2**. It can be seen that

H^{y}_{stray} gets its maximum at the center of the pillar, different from the case of the 300 × 150 nm² pillar where H^{y}_{stray} gets its maximum at the edges of the pillar.

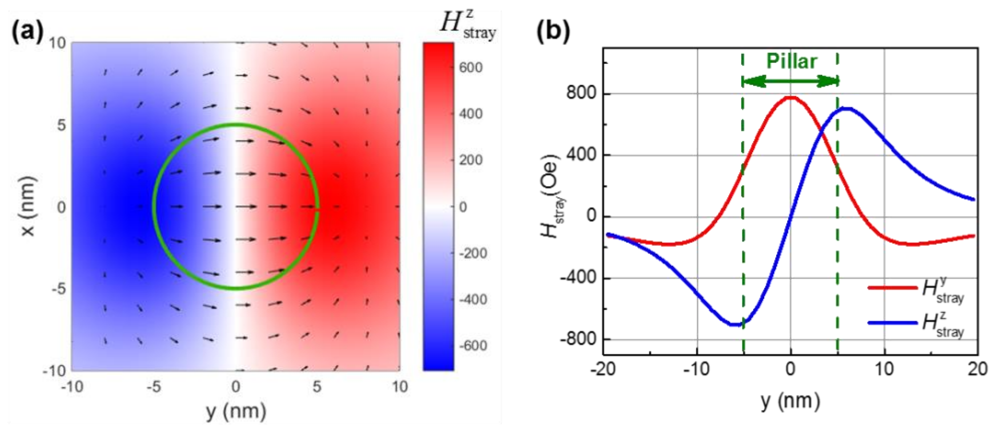

Figure 3-20. Calculated stray field for a 10 × 10 nm² nanopillar. **(a)** Mapping of the stray field distribution across PL for the 10 × 10 nm² circular pillar, where the arrows show the strengths and directions of the in-plane component of the stray field, and color pixels show the strengths and directions of the *z*-component of the stray field (red = up, blue = down). **(b)** Stray field profile along *y*-axis across PL.

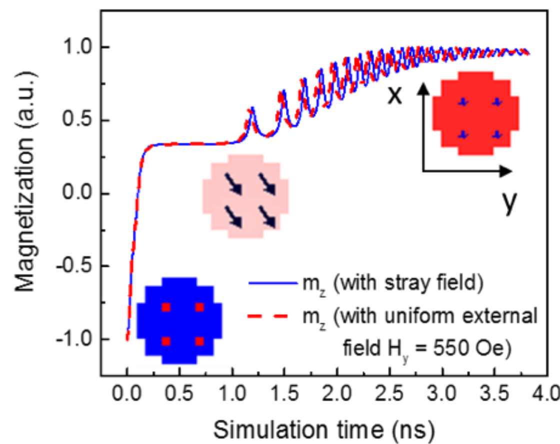

Figure 3-21. Micromagnetic simulation showing the switching curves for the 10×10 nm^2 nanopillar. The solid line represents SH switching under the stray field of IPL and the dash line represents the switching under a uniform external field of $H_y = 550$ Oe. Inset: top view of PL magnetization pattern of initial state, intermediate state, and final state. Other parameters of the simulation are shown in **Table 2**.

Table 2. Simulation parameters for SH switching of 10×10 nm^2 nanopillar

IPL dimensions	10 nm × 10 nm × 7 nm
PL dimensions	10 nm × 10 nm × 1 nm
Cell size	1 nm × 1 nm × 0.5 nm
PL-to-IPL distance	7 nm
IPL saturation magnetization	1700 emu/cm^3
PL saturation magnetization	1200 emu/cm^3
Exchange constant	20×10^{-12} J/m^1
Gilbert damping	0.02
PL perpendicular anisotropy	1.5 T
Spin Hall angle	0.15
Current density	20×10^{11} A/m^2

For nanopillars of sub-40 nm, the magnetization switching mode would be single domain type rather than nucleation type. Therefore, the non-uniform profile of the stray field would no longer be an issue for the 10×10 nm^2 pillar as it is for the 300×150 nm^2 pillar. In **Figure 3-21**, the solid curve shows the successful SH switching of the 10×10 nm^2 nanomagnet only with the assistance of the stray field. For comparison, the dash curve shows the SH switching of the same nanomagnet but only with a uniform external field of

H_y = 550 Oe. The two trajectories are quite close to each other, indicating the effect of the stray field is similar to the effect of a uniform external field on the PL nanomagnet. Since the nanomagnet switches as a single domain, only the average value of the dipolar field across the pillar matters for SH switching. According to **Figure 3-20 (b)**, the average value of H_{stray}^{y} across the pillar is around 500 Oe, in agreement with **Figure 3-21**. These results prove the scalability of the composite structure and promise its applications in high areal density memory arrays.

3.4.6 Comparison with other types of field-free SH devices

As has been mentioned in the first section of this chapter, previous field-free SH switching of PMA materials mainly follows two paths: introducing a lateral structural asymmetry [139,141–145] or using a symmetry-breaking exchange field [140,146–152]. **Table 3** compares our dipole-coupled composite device with those approaches. Among all the characteristics, the in-plane compensation field H_{comp}, which has been discussed in **Figure 3-11**, reflects the strength of symmetry-breaking, for which our device has significantly greater values than most of the other two types of devices. This is reasonable because the local dipolar field is more likely to be stronger than either the PMA gradient induced effective field or the in-plane exchange bias field in a PMA system. In addition, the strength of the dipolar field is tunable via engineering the distance between PL and IPL, the saturation magnetization of IPL, or the shape of the IPL layer. This makes the dipole-coupled devices more practical than exchange-coupled devices, which requires high field post-annealing, suffers from the trade-off between PMA and H_{ex}, and is sensitive to Joule heating [150].

In terms of memory integration, although the utilization of AFM as spin Hall material [140,148,149,151] also enables the exchange-coupled SH devices to be integrated with p-MTJ, this strategy exclude the possibility of using various SH materials that are not AFM but have a larger spin Hall efficiency such as tungsten and topological insulators [22,23,34–36]. In contrast, the dipole-coupled devices, being compatible with a wide range of giant spin Hall materials and readily integrated with p-MTJ, would be more desirable for SOT based memory applications. Most recently, the field-free switching has been demonstrated in a full MTJ using the dipole-coupled composite structure [33].

Table 3. Comparison of three types of external-field-free SH devices

Concept	**Ref.**	**Structure**	**Device Type**	H_k	H_{comp}	H_{shift} **/ J**	J_c
Anisotropy gradient	[139]	//Ta(5) / CoFeB(1) / TaO	Hall bar	0.04 T ~0.12 T	n/a	0~56 Oe / 10^7 A cm^{-2}	0.25 ×10^7 A cm^{-2}
	[143]	//Ta (10) / CoFeB (1) / MgO (1)	Nano-pillar	0.5 T	n/a	n/a	2.5 ×10^7 A cm^{-2}
Exchange coupling	[146]	//Ta(1) / Pt(5) / CoFe(0.8) / Ru(2) / CoFe(1.5) / IrMn(10) / Pt(2)	Hall bar	n/a	400 Oe (0.8T annealing)	22 Oe / 10^7 A cm^{-2}	3×10^7 A cm^{-2}
	[147]	//Ta(1) / Pt (3) / Co (0.7) / Pt (0.3) / IrMn (6) / TaOx (1.5)	Hall bar	1T	50 Oe (2T annealing)	n/a	8×10^7 A cm^{-2}
	[148]	//Ta(5) / CoFeB(3) / IrMn(3) / CoFeB(1) / MgO(1.6) / Ta(2)	Hall bar	0.5 T	50 Oe (0.8T annealing)	n/a	4.2×10^7 A cm^{-2}
	[140]	//PtMn(8) / [Co(0.3) / Ni(0.6)]$_2$ / MgO	Hall bar	0.15 T	83 Oe (1.2T annealing)	28 Oe / 10^7 A cm^{-2}	0.6×10^7 A cm^{-2}
	[150]	//Ta(2) / Pt(3) / CoFe(1.1) / IrMn (3) / Pt(1)	Hall bar	1 T	95 ~ 215 Oe (1.5T annealing)	n/a	3.1×10^7 A cm^{-2}
	[151]	//Ta(5) / PtMn(10) / CoFeB / Gd / CoFeB / MgO	Hall bar	0.3 T	22 Oe (0.5T annealing)	10 Oe / 10^7 A cm^{-2}	0.96×10^7 A cm^{-2}
Dipole coupling	**This work**	//Ta(5) / CoFeB(1.2) / MgO(2) / CoFeB (3) / MgO(2) / Ta	Nano-pillar	0.35 T	100 ~ 135 Oe	45 Oe / 10^7 A cm^{-2}	1.5×10^7 A cm^{-2}

3.5 Summary

For the early version of SOT devices, the switching of the perpendicular magnetization requires the assistance of an external magnetic field. This imposes a huge limitation for the applications of SOT devices in real world scenarios. In this chapter, I have demonstrated an external-field-free SOT induced perpendicular magnetization switching by using a dipole-coupled composite structure, where an in-plane magnet can provide a sufficiently large biasing field to break the lateral symmetry. Robust switching of nano-scale Ta/CoFeB/MgO pillars in a composite stack has been experimentally demonstrated with both DC and pulse currents in the absence of the external field, with the critical current density of about 1.5×10^{7} A cm^{-2}. A large in-plane compensation field of 135 Oe and an out-of-plane loop shift of 45 Oe / 10^{7} A cm^{-2} have been obtained. Moreover, the switching process under a non-uniform stray field profile has been analyzed with the help of micromagnetic simulations. The scalability of the composite structure has been verified by performing the simulation with a 10×10 nm^{2} pillar. Furthermore, I compared the performance of our device with previously proposed devices, showing our approach can effectively eliminate the tradeoff between PMA and exchange bias, and is well compatible with various giant spin Hall angle materials. All these advantages make our composite structure readily applicable for SOT-based memory and logic devices. In fact, the same field-free switching mechanism has been successfully applied to SOT-MRAM recently [33].

Chapter 4 Voltage Control of MTJ via Piezoelectric Strain

4.1 Motivation and background

In Chapter 2 and Chapter 3, I have presented my works using current-induced spin-orbit torques (SOT) to obtain magnetization switching. This chapter introduces another magnetization control strategy which is also applicable to advanced memories with low energy dissipation – manipulating the magnetization direction using voltage-induced piezoelectric strain.

In MRAM technology, magnetic tunneling junctions (MTJ) comprise the main storage cells. Low-energy writing of bits requires an electrically tunable mechanism to reorient the magnetization of the MTJ, as has been introduced in Chapter 1. The traditional switching mechanism is using spin-transfer-torque (STT) [14,15] generated by a spin polarized current passing through the MTJ. A more recent switching mechanism is based on SOT produced by the giant spin Hall effect (SHE) in heavy metals [19,21] or topological insulators [22,23], which has been investigated in Chapter 2 and Chapter 3. However, for both methods the writing current density required for the magnetization switching is relatively high [30,167,168]. Writing mechanisms that have a lower energy dissipation are demanded. In recent years, several mechanisms based on using voltage (instead of current) to control the magnetization of the free layer have emerged as promising routes for ultra-low power writing of data [48,169–173], which have been introduced in Section 1.2.2. Among these approaches, the strain-induced control of the magnetic anisotropy in (two-phase) multiferroic heterostructures (a magnetostrictive layer elastically coupled with an

underlying piezoelectric layer) stands out as a remarkably energy-efficient switching mechanism [40–46]. It has been widely investigated in different piezoelectric/magnetostrictive bilayer thin films [174–178] or nano-structures [179–182]. There are also several theoretical predictions [183–185] that such a method will dissipate only a few atto-Joules (aJ) of energy to write data. This establishes the promise of using strain to control MTJ's for ultra-energy-efficient memory applications.

The key for strain control of the in-plane magnetization in a magnetostrictive/piezoelectric system is that the in-plane strain should be *anisotropic*. In most of previous reports [176–179,186], single crystalline piezoelectric substrates $Pb(Mg_{1/3}Nb_{2/3})O_3$-$PbTiO_3$ (PMN-PT) with (011) orientation were utilized to generate an intrinsic *anisotropic* strain. However, for realistic strain-mediated MRAM, MTJ's would be grown on top of a layer of polycrystalline piezoelectric thin film deposited on a traditional Si substrate for compatibility with silicon technology [43,184,187,188]. In that case, one can no longer rely on the intrinsic anisotropy of the piezoelectric material to generate the required strain. Moreover, the integration of piezoelectric layer with MTJ stack requires a practical gating scheme to achieve high scalability, low energy dissipation and individual control. Thus, local gating of individual MTJ cells using a practical substrate is urgently needed to incept a viable strain-mediated ultralow-energy MRAM technology.

In this chapter, I will demonstrate the giant voltage manipulation of an MgO MTJ on PMN-PT substrate with (001) orientation. Two local gating configurations are applied to produce strong *anisotropic* strain from the *isotropic* piezoelectric layer for MTJ control. It will be presented that the magnetic easy axis, as well as the switching field (H_c) and the

tunnel magnetoresistance (TMR) ratio of the MTJ, can be efficiently controlled by strain from the underlying PMN-PT substrate generated by a gate voltage. And the voltage controlled MTJ toggling between the high- and low-resistance states will be demonstrated. Our work is fundamentally different from the previous one by Li et al [186]. Instead of relying on the intrinsic anisotropy of the piezoelectric substrate (which is not practical), our device utilizes the *anisotropic* strain generated via the local gating schemes and is more amenable to practical memory applications [187,188]. Moreover, the localized strain allows the control of an individual MTJ with a relatively small voltage, thus enabling scalability and overcoming the substrate clamping issue [188]. The adoption of crystalline MgO as the tunnel barrier results in high-TMR strained-MTJ devices. Most importantly, the side-gated MTJ prototype paves the way to realizing complete magnetization "reversal", i.e. 180° rotation of the magnetization with a voltage [43], which is the ultimate goal of strain-based magnetization manipulation [186,189].

The rest of this chapter is organized as follows. Section 4.2 introduces experimental methods, including the characterization of the piezoelectric substrate and the MTJ stack, and the design of the gated MTJ. The MTJ measurement results along with the piezoelectric finite element simulation results are presented in Section 4.3, followed by more supplemental results and discussions in Section 4.4. Finally, Section 4.5 concludes the chapter. The content of this chapter has been published as a research article in Applied Physics Letters [190].

4.2 Experimental methods

The MTJ stack, with the structure (from bottom to top, thicknesses in nm) Ta (8) / CoFeB (10) / MgO (1.8) / CoFeB (4) / Ta (8), were directly deposited on the PMN-PT(001) substrate by ultra-high vacuum DC and RF magnetron sputtering in our Shamrock sputter tool. Before the film deposition, the PMN-PT substrate was electrically polarized along the out-of-plane direction with an electric field of 8 kV/cm. The in-plane strain of the PMN-PT substrate, as a function of the out-of-plane electric field, is characterized with a general purpose 120 Ω Constantan linear foil strain gauge (EA-06-062ED-120, Vishay Precision Group, Micro-Measurements), and the result is shown in **Figure 4-1**. The ε-V loop was measured on a bare PMN-PT substrate without any device delineated on the surface. The strain curve under bipolar electric field poling from -8 kV/cm to +8 kV/cm (solid line) exhibits typical butterfly-like behavior, and the curve under electric field with a smaller range (dashed line) exhibits almost linear strain vs. electric field behavior with a very small hysteresis [191].

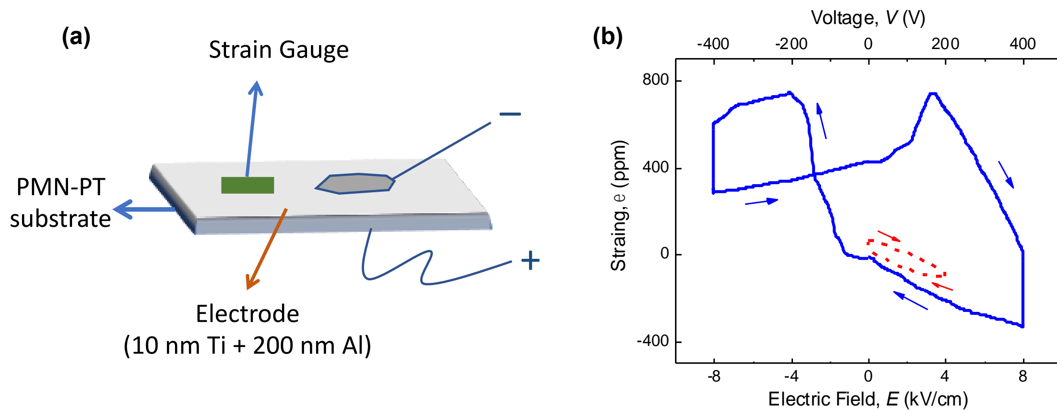

Figure 4-1. **(a)** Schematic showing how the ε-V property of the PMN-PT substrate is characterized. **(b)** In-plane strains ε in the PMN-PT (001) substrate as a function of applied

average electric field or voltage. Solid line represents the major loop and dashed line represents the minor loop. The vertical jumps at the maximum E-fields result from the settling of the sample at those E-fields for 10 min.

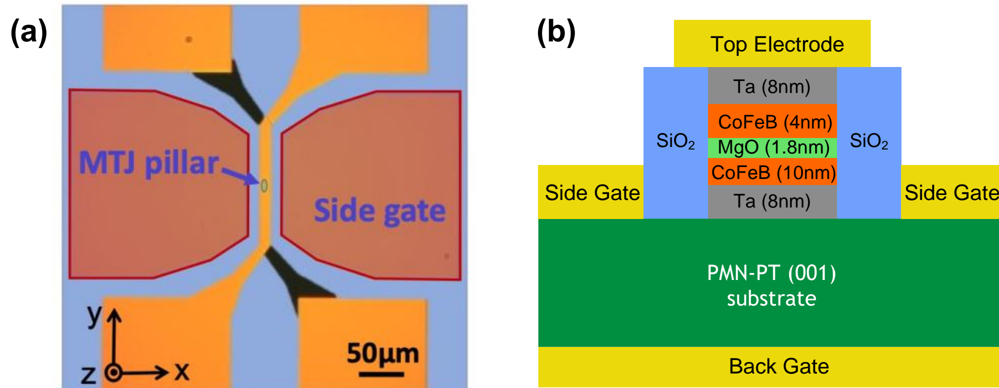

Figure 4-2. **(a)** An optical micrograph image of the actual fabricated device. **(b)** Structure of the strain-MTJ.

Then, the MTJ devices on the PMN-PT substrate were fabricated using photolithography and Ar ion milling. Two side gates (metallic contacts) were patterned next to the MTJ on the top surface of the substrate, and a common back gate (a continuous metallic contact) is deposited on the bottom surface of the substrate, as shown in **Figure 4-2**. Both the sides gates and the back gate are electrically isolated from the MTJ. Using the side and back gates, one can apply an electric field (E-field) across the PMN-PT substrate to generate localized strains around the MTJ. The MTJ pillar is elliptical in shape with its easy axis (major axis) along the *y*-direction and is located between a pair of side

gates on [as shown in the optical image in **Figure 4-2 (a)**]. The dimension of the pillar is 8 μm × 3 μm. The separation between the two side gates is 40 μm to ensure their electrical isolation from the MTJ. A post-annealing process was performed in vacuum under a magnetic field of about 0.4 T at 250 °C for 1 hour, to improve the crystallization of the MgO tunnel barrier.

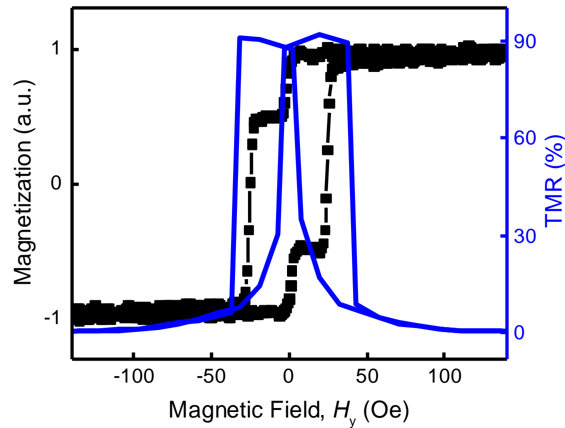

Figure 4-3. The magnetic hysteresis loop of patterned MTJ films and the MR loop of a MTJ device on PMN-PT (001) without gate voltage application. The magnetic field is along the major axis of the pillars in the *y*-direction.

The magnetic hysteresis (*M-H*) loop of patterned MTJ films is obtained using vibrating sample magnetometry (VSM), as shown in **Figure 4-3**, indicating that the thicker CoFeB layer is magnetically hard (with a larger coercivity), while the thinner layer is soft (with a smaller coercivity). The magnetoresistance (MR) loop of the MTJ device is also shown in **Figure 4-3** with a TMR ratio of about 90%. The resistance of MTJ was measured at room temperature using the four-probe technique under a bias current of 5 μA. A

Keithley 6221 current source generated the DC current, and the output voltage was characterized using a Keithley 2182A nanovolt meter. The gate voltage was applied with a Keithley 2400 source meter. The MR loops were obtained by sweeping the magnetic field along the y-direction (long-axis of the MTJ).

4.3 Results

In this work, I characterized the MTJ with two different gating scenarios: a gate voltage V_g is applied either between the back gate and the bottom electrode of the MTJ [Configuration I, as shown in **Figure 4-4 (a)**], or between the back gate and a pair of side gates [Configuration II, as shown in **Figure 4-5 (a)**]. In both cases, an *anisotropic* strain is produced, which is highly localized in the MTJ region and would control the anisotropy of the MTJ. Please note the positive V_g is defined as the electric field in the PMN-PT substrate being parallel to the piezoelectric polarization (poling) direction along the z-axis, and negative V_g corresponds to the electric field being anti-parallel to the polarization direction.

4.3.1 E-field tuning of the magnetic anisotropy

Figure 4-4 (c) shows the MR loop of the MTJ measured by sweeping the magnetic field H_y (along the long-axis of MTJ pillar), under three different gate voltages $V_g = -150$ V, 0 and +150 V. At $V_g = 0$, a normal MR loop which is similar to that shown in **Figure 4-3** is obtained, with sharp transitions between high- and low-resistance states. However, when a negative gate voltage $V_g = -150$ V is applied, the sharp transitions in the MR loop change to gradual slopes, indicating that the easy axes of both free (soft) and fixed (hard) layers have rotated towards the transverse direction (x-direction). On the other hand, when

V_g is positive, the switching field of the hard layer, H_c, increases significantly upon increasing the gate voltage, suggesting enhancement of the magnetic anisotropy along the major axis (*y*-axis). H_c as a function of V_g is extracted from the MR loops and plotted in **Figure 4-4 (d)**. It can be seen H_c increases almost linearly and becomes more than 4-fold larger when V_g is increased from 0 to +150V.

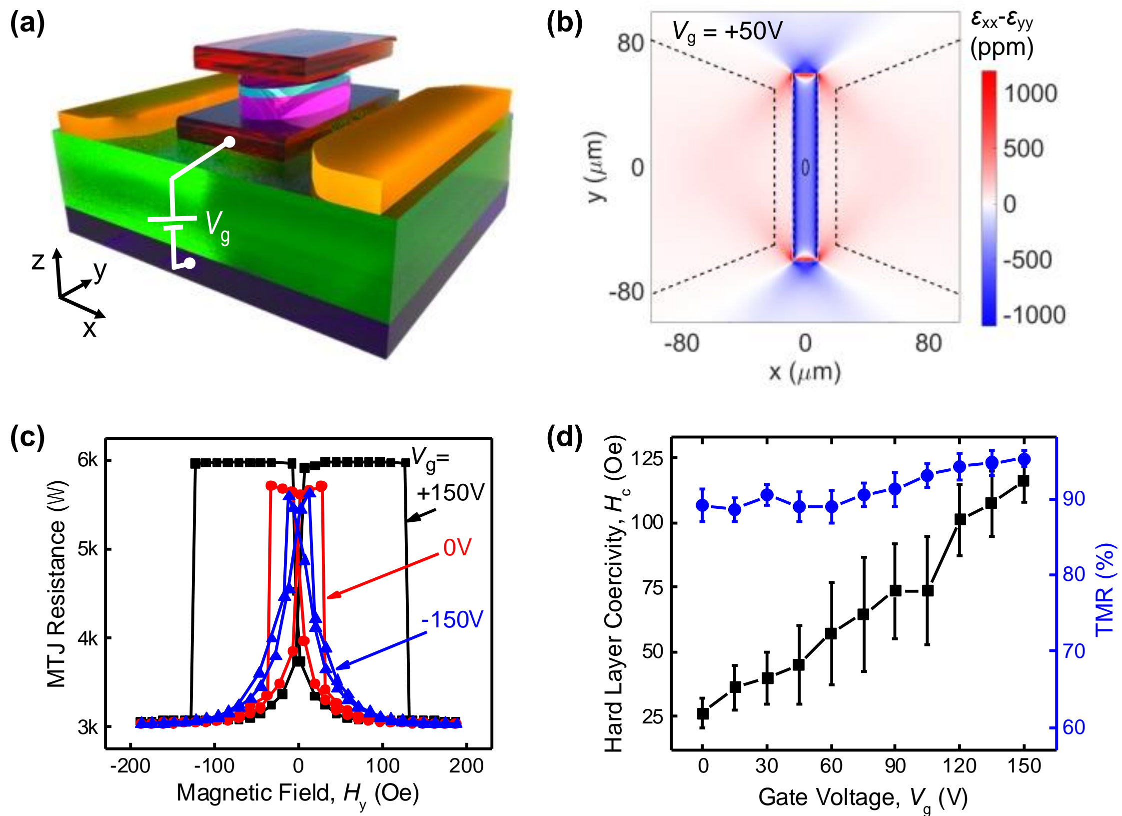

Figure 4-4. Results for strained-MTJ in Configuration I. **(a)** Schematic of Configuration I, where the gate voltage V_g for generating strain is applied between the MTJ bottom electrode and the back gate. **(b)** Simulation result showing the mapping of the in-plane *anisotropic* strain $\varepsilon_{xx} - \varepsilon_{yy}$ upon application of the gate voltage of $V_g = +\ 50$ V. The solid line ellipse at the origin denotes the MTJ pillar, and the dashed lines denote the positions

of electrodes and side gates. **(c)** MR curves characterized under different gate voltages. **(d)** Variation of the hard layer switching field H_c (square-line) and TMR ratio (circle-line) of the MTJ as a function of V_g.

To have a better understanding of how the magnetization of the ferromagnetic layers are affected by the gate voltage in our devices, 3D piezoelectric finite element simulations were performed using the COMSOL Multiphysics package. The piezoelectric strain mapping on the top surface of the substrate is presented in **Figure 4-4 (b)**, at V_g = +50 V. A positive E-field applied in the out-of-plane direction (z-direction) produces an out-of-plane expansion (d_{33}) and in-plane contraction (d_{31}) in the substrate. Therefore, upon application of a positive V_g [see **Figure 4-4 (a)**], an in-plane bi-axial strain is generated in the region beneath the stripe-shaped electrode where the voltage is applied, and the strain is compressive in both x- and y-directions. Since the electrode is long in the y-direction and narrow in the x-direction, the strain component ε_{xx} along the x-direction is dominant (the mapping of each strain component is presented in **Figure 4-8** in the next section), resulting in an *anisotropic* strain on the MTJ. We define the in-plane *anisotropic* strain as $\varepsilon_{xx} - \varepsilon_{yy}$. From the simulation results of **Figure 4-4 (b)**, it is found that a strain of $\varepsilon_{xx} - \varepsilon_{yy} = -274$ ppm is produced on the MTJ at V_g = +50 V. Such an *anisotropic* strain compresses the MTJ along the x-direction. Since the magnetostriction coefficient of CoFeB is positive [192], this compression increases the magnetic anisotropy along the y-direction. As a result, the MR loops in **Figure 4-4 (c)** are significantly broadened with a positive V_g

since it will now take a larger magnetic field to dislodge the magnetization from the *y*-axis. On the other hand, with negative V_g, the ε_{xx} component is dominant over ε_{yy} with a positive value (tensile). Hence, the *anisotropic* strain $\varepsilon_{xx} - \varepsilon_{yy}$ is positive. When this tensile stress is applied to the MTJ along the *x*-direction, the easy axis of the MTJ rotates from the *y*-axis towards the *x*-axis owing to the positive magnetostriction coefficient of CoFeB. This change of the magnetic anisotropy direction from *y*-axis to *x*-axis can be seen in our experimental results in **Figure 4-4 (c)** for $V_g = -150$ V. It is noted that only the modification in coercivity of the hard CoFeB layer is observed in **Figure 4-4 (c)**. If the minor MR loop is measured, the modification in the anisotropy of the soft layer can also be observed, which is presented in **Figure 4-9** in the next section.

In addition to tuning the switching field H_c, V_g also changes the TMR ratio, as shown in **Figure 4-4 (c)** and **(d)**. The TMR ratio increases slightly from 90% at $V_g = 0$ to 95% at $V_g = +150$ V. Though the change is small, the TMR enhancement is verified by repeated experiments on different devices. We believe there are two main factors that contribute to it. One is that the strain makes the magnetizations in the soft layer and hard layer align better along the easy axis (*y*-axis) due to the enhancement of the magnetic anisotropy when the gate voltage is positive. The other is the modification of the MgO tunnel barrier height by the strain which can affect band alignments between MgO and CoFeB. The height changes because strain alters the bandgap of MgO. This influences the spin-dependent tunneling through the MgO spacer and hence the TMR ratio. The quantum transport properties of the MTJ could be significantly changed by even a small stretching/squeezing of the crystalline lattice of MgO [193].

Next, the strained-MTJ is investigated in Configuration II, where the gate voltage is applied between side gates of the MTJ and the back gate [as shown in **Figure 4-5 (a)**] [188]. In this scenario, the E-field is generated directly underneath the two side gates. The simulation result of strain mapping for this configuration is presented in **Figure 4-5 (b)**. As we can see, when a positive $V_g = +50$ V is applied, the strain fields are formed due to the out-of-plane expansion and in-plane contraction of the region underneath the side gates. In the central gap between the pair of side gates, a strong *anisotropic* strain ($\varepsilon_{xx} - \varepsilon_{yy} > 0$) is produced with a tensile component ε_{xx} and a compressive component ε_{yy}, resulting from the interaction of the strain fields under the side gates [188]. For this case, the sign of $\varepsilon_{xx} - \varepsilon_{yy}$ exerted on the MTJ pillar is opposite to that of Configuration I [**Figure 4-4 (b)**]. Hence, the modification of the MR loop by the gate voltage [shown in **Figure 4-5 (c)** and **(d)**] is opposite to that of Configuration I [shown in **Figure 4-4 (c)** and **(d)**] as expected. A negative gate voltage of $V_g < 0$ results in $\varepsilon_{xx} - \varepsilon_{yy} < 0$; therefore, the magnetic anisotropy of CoFeB layers is enhanced along the *y*-axis and the switching field is increased by 4-fold from 25 Oe ($V_g = 0$) to 95 Oe ($V_g = -150$ V). Similarly, a positive gate voltage of $V_g > 0$ leads to $\varepsilon_{xx} - \varepsilon_{yy} > 0$ and consequently the magnetic anisotropy is induced along the *x*-direction and the MR loop becomes slanted. Moreover, the TMR ratio slightly increases upon the application of a negative gate voltage as shown in **Figure 4-5 (d)**. Clearly, the variations of the MR loop as a function of gate voltage in Configuration II are opposite to that of Configuration I due to the opposite sign of the *anisotropic* strain produced in these two scenarios.

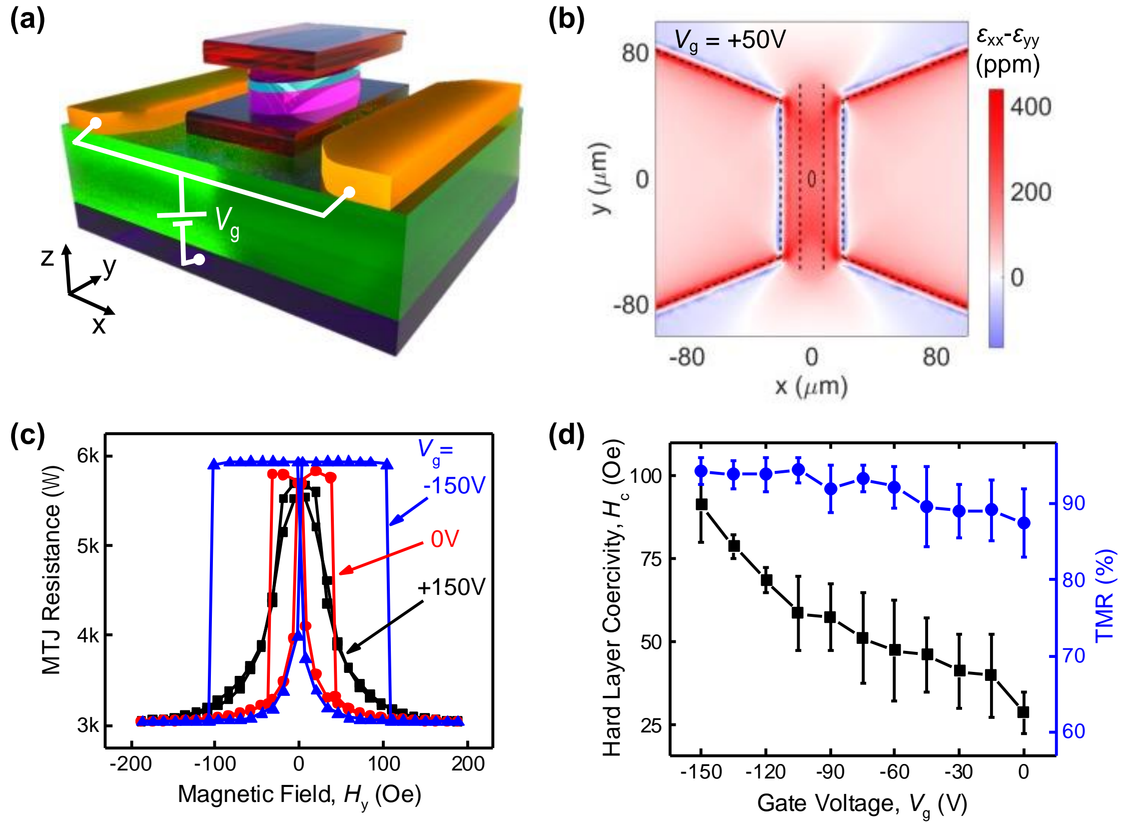

Figure 4-5. Results for strained-MTJ in Configuration II. **(a)** Schematic of Configuration II, where V_g is applied between the pair of side gates and the back gate. **(b)** Simulation result showing the mapping of the in-plane *anisotropic* strain $\varepsilon_{xx} - \varepsilon_{yy}$ upon application of the gate voltage of $V_g = +50$ V. The solid line ellipse at the origin denotes the MTJ pillar, and the dashed lines denote the positions of electrodes and side gates. **(c)** MR curves characterized under different gate voltages. **(d)** Variation of the hard layer switching field H_c (square-line) and TMR ratio (circle-line) of the MTJ as a function of V_g.

4.3.2 E-field controlled MTJ toggling

Next, we have also successfully demonstrated strain induced MTJ resistance toggling by utilizing gate voltage pulsing. By applying gate voltage pulses of ±80 V in Configuration II, the MTJ is toggled between high- and low-resistance states as seen in **Figure 4-6 (d)**. Similar to the results of **Figure 4-5**, when a negative gate voltage of V_g = −80 V is applied, the MR loop of the MTJ shown in **Figure 4-6 (c)** becomes rather square with an enhanced coercivity. On the other hand, with a positive gate voltage V_g = +80 V, the MR loop becomes slanted owing to the rotation of the magnetization of both CoFeB layers away from the major (easy) axis toward the minor (hard) axis of the ellipse.

A micromagnetic simulation has been performed utilizing the Object Oriented Micro Magnetic Framework (OOMMF) [156] to better understand the details of the switching mechanism under the positive and negative gate voltages. At a gate voltage V_g = −80 V, once a small bias magnetic field (H = 30 Oe) is applied along the +y-direction, the magnetizations of both hard and soft CoFeB layers in the MTJ become parallel along the +y-axis [as shown in **Figure 4-6 (a)**], leading to the low-resistance state denoted by the arrow in **Figure 4-6 (c)**. The bias magnetic field of 30 Oe is enough to overcome any dipole interaction between the two layers and make both of their magnetizations mutually parallel and point in the direction of the bias field. Once V_g changes to +80 V, magnetizations of the soft layer and the hard layer rotate towards the ± x-directions (i.e. opposite directions) because of the generated strain (which overcomes both shape anisotropy and the bias magnetic field). They rotate in opposite directions because of the magnetostatic dipole coupling between the layers, which favors their anti-parallel alignment [as shown in **Figure**

4-6 (b)]. This increase in the angular separation between the magnetizations of the two layers results in a high-resistance state for the MTJ. When the voltage is switched back to −80 V, the magnetizations of the two layers again become parallel along the +y-direction because of the bias magnetic field, and the MTJ resistance drops. Therefore, by alternative application of the gate voltages of +80 V and −80 V (and a small magnetic field of H = 30 Oe in the +y-direction), the MTJ cell can be toggled between high (anti-parallel) and low (parallel) resistance states [**Figure 4-6 (d)**].

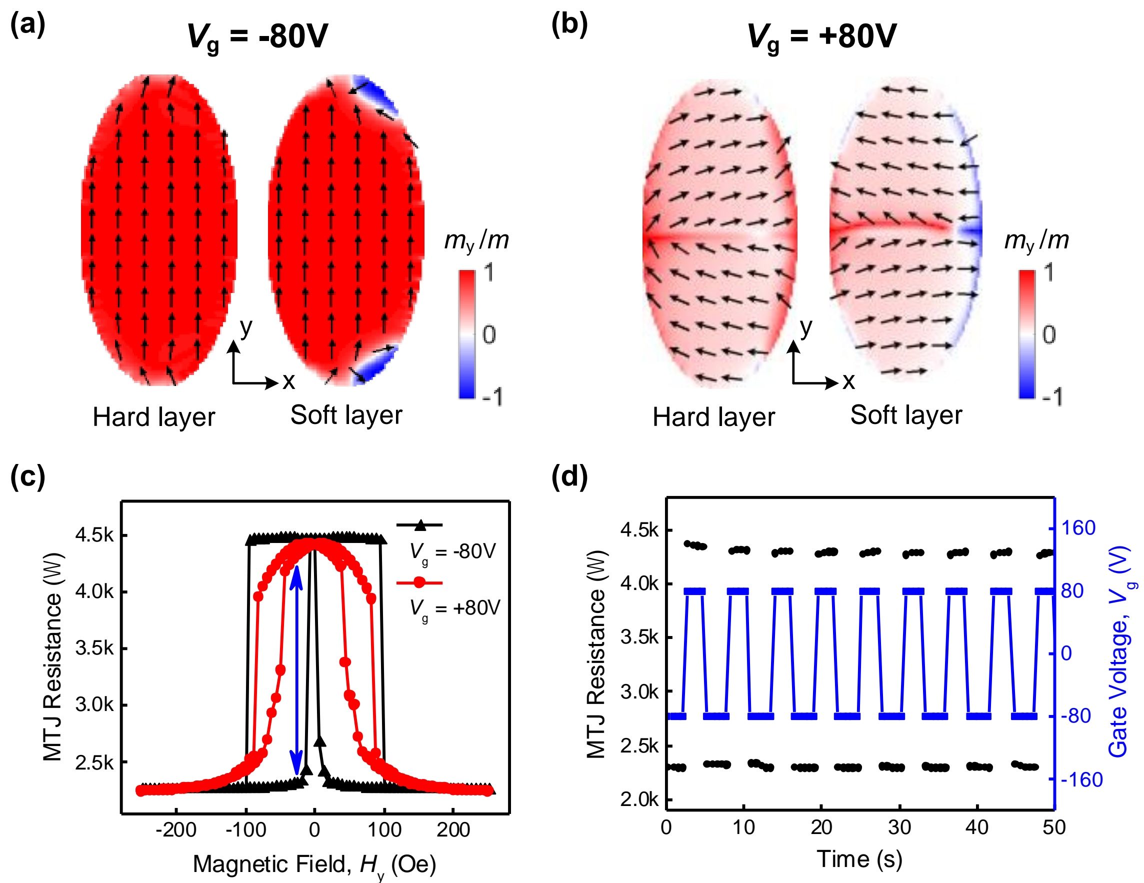

Figure 4-6. Demonstration of voltage manipulation of MTJ toggling between high- and low-resistance states in Configuration II. **(a)** & **(b)** Micromagnetic simulation results demonstrating the magnetization configuration of hard and soft CoFeB layers after

application of **(a)** $V_g = -80$ V and **(b)** $V_g = +80$ V. The dimension of the magnet is 3 μm × 6 μm. Black arrows indicate the direction of magnetic moments. **(c)** MR curves for $V_g = -80$ V and $V_g = +80$ V. The blue arrow indicates the switchable high- and low-resistance states. **(d)** Toggling of the MTJ between high- and low-resistance states with application of ±80 V gate voltage pulsing. A small bias magnetic field of 30 Oe is applied along the *y*-axis to overcome the dipole interaction between the two magnetic layers.

There are several advantages of using our local gating schemes compared to previous voltage control approaches [186,194]. The simulations of the strain distribution in **Figure 4-4 (b)** and **Figure 4-5 (b)** vindicate the generation of an *anisotropic* strain from the *isotropic* piezoelectric substrate with our gating scheme. Hence, having a piezoelectric single crystalline substrate with a specific orientation [like PMN-PT (011)] is no longer a necessity to provide an *anisotropic* strain profile. Moreover, since the generated strain field is highly localized and confined around the MTJ, it allows manipulating individual MTJ cells and overcoming the substrate clamping issue when utilizing a thin piezoelectric film grown on a traditional Si substrate [187,188]. Additionally, the strength of the strain generated in such local gating schemes is much larger than the strain produced in the uniform gating scheme. If the dimensions of the MTJ and the gates are further optimized, the device might be scaled down to nanoscale, and the efficiency of strain generation would be further improved. These will be further discussed in the next section. Furthermore, it has been predicted that with one more pair of side gates, a deterministic 180° reversal of

the magnetization can be achieved [43,184]. Therefore, our work paves the way toward this fully strain-induced MTJ switching.

4.4 Discussions

4.4.1 Details on the piezoelectric finite element simulations

In the previous section I present the strain mapping for two gating setups: Configuration I in **Figure 4-4 (b)** and Configuration II in **Figure 4-5 (b)**, obtained via the piezoelectric finite element simulations. In this section, more details of the simulations are presented, including the electric field distribution in the piezoelectric layer, and the mapping of the three strain components ε_{xx}, ε_{yy} and ε_{zz}, respectively. Based on the simulation results, it will be shown that local gating schemes can be scaled down to nanoscale.

The finite elements model was developed using COMSOL Multiphysics to approximate the E-fields and strains observed around the MTJ device. The PMN-30PT was modeled as a 1.5 mm × 1.5 mm × 0.5 mm element using the piezoelectric module. To decrease the complexity of the simulation, all the deposited thin films, including the MTJ stack and the electrode layer, were not considered in the simulation (this will not change the simulation results too much because the thicknesses of the MTJ films are negligible compared with the thickness of the PMN-PT substrate). The PMN-30PT material properties are [195]: $d_{33} = 1981\times 10^{-12}$ C/N, $d_{31} = -921\times 10^{-12}$ C/N, and density $\rho = 8.043\times 10^{3}$ kg/m^3. All the boundaries of the PMN-PT element are mechanically free except the bottom surface of the element which is restricted in the $z = 0$ plane. A voltage of $V_g = +50$

V is applied to the top contacts with the bottom surface grounded (according to gating scenarios in Configuration I/II); that is, the electric field is applied through the thickness of the PMN-PT.

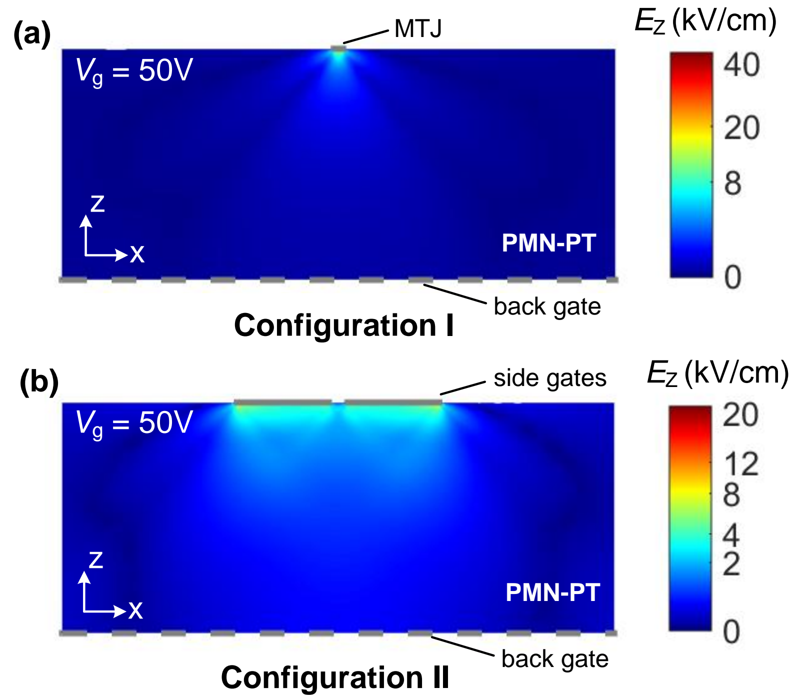

Figure 4-7. Finite element simulation demonstrating the out-of-plane E-field strength within the $y = 0$ cross-section, with the application of $V_g = +50$ V. **(a)** Configuration I, **(b)** Configuration II. The thickness of PMN-PT is 0.5 mm.

The distribution of the electric field when applying the gate voltage in Configuration I/ II is simulated and presented in **Figure 4-7**. Due to the small dimensions of the electrodes and side gates compared with the large common back gate, the E-field is highly concentrated. In Configuration I, the E-field is concentrated under the MTJ bottom

electrode; in Configuration II, the E-field is concentrated just beneath the side gates. The highly concentrated E-field is the reason for the highly localized strain profile generated in the substrate. The concentration of the E-field also allows us to use a relatively small voltage to generate a large strain for MTJ controlling (see **Table 4**).

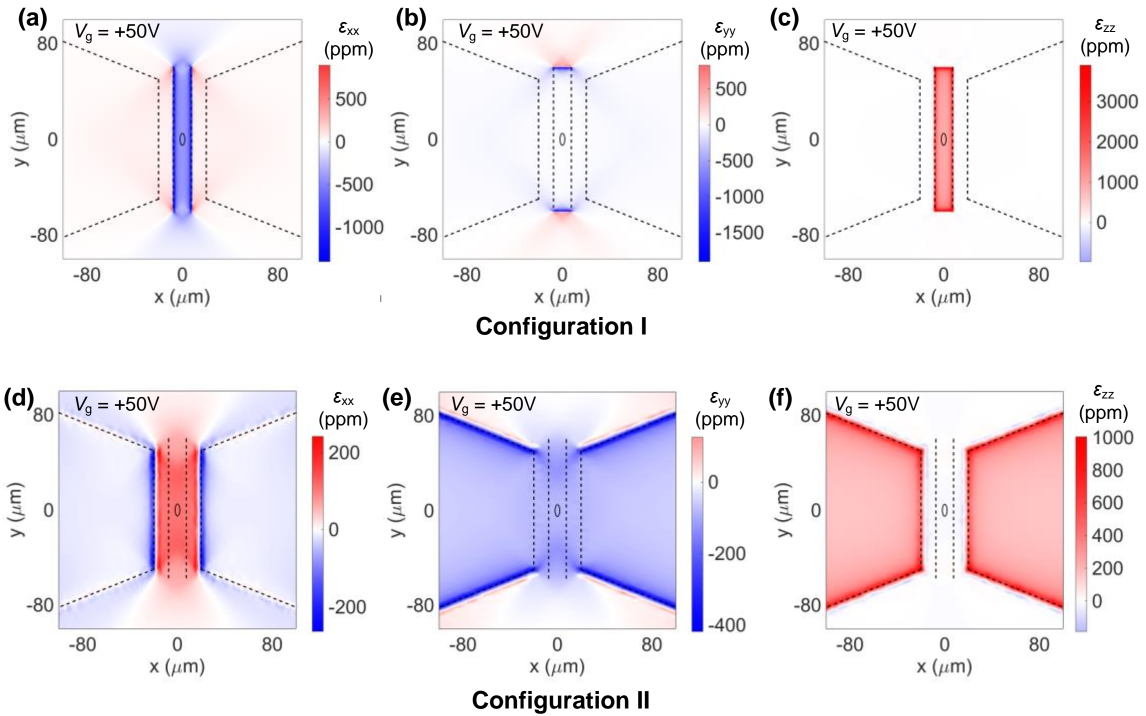

Figure 4-8. Finite element simulation showing the mapping of different piezoelectric strain components on the top surface of the substrate, with the application of $V_g = +50$ V. **(a)** and **(d)**: in-plane strain component ε_{xx}. **(b)** and **(e)**: in-plane strain component ε_{yy}. **(c)** and **(f)**: out-of-plane strain component ε_{zz}. **(a)-(c)** are for Configuration I and **(d)-(f)** are for Configuration II, respectively.

In **Figure 4-4 (b)** and **Figure 4-5 (b)**, I present the mapping of the *anisotropic* strain, i.e. $\varepsilon_{xx} - \varepsilon_{yy}$, on the top surface of the sample. Now I will show the distribution of each individual strain component. **Figure 4-8** gives the simulation results showing the mapping of the strains along *x*, *y* and *z* directions, with the same gate voltage V_g = +50 V. For Configuration I [**Figure 4-8 (a)-(c)**], the component ε_{xx} is dominant over ε_{yy} in the MTJ region, since the electrode is a narrow stripe along the *y*-direction. Therefore, the strain exerted on the MTJ is *anisotropic*. By subtracting the value of ε_{yy} at each spatial point from ε_{xx} at the corresponding point, I get the distribution of $\varepsilon_{xx} - \varepsilon_{yy}$ shown in **Figure 4-4 (b)**. For Configuration II [**Figure 4-8 (d)-(f)**], the interaction of the strains underneath the pair of side gates induces an *anisotropic* strain field in the central gap [188], where the strain along *x*-axis is tensile ($\varepsilon_{xx} > 0$) and strain along *y*-axis is compressive ($\varepsilon_{yy} < 0$) for a positive gate voltage. The distribution of $\varepsilon_{xx} - \varepsilon_{yy}$ has been given in **Figure 4-5 (b)**.

Table 4 summarizes the strains produced in the MTJ region using different gating schemes. The values of strains are obtained from the finite element simulation results. Clearly, in our local gating schemes (Configurations I and II), the strain generation is much more efficient than in the uniform gating scheme (applying voltage on uniform contacts) [186]. The localized strain $\varepsilon_{xx} - \varepsilon_{yy}$ exerted on the MTJ is 3.0 times (Configuration I) or 1.4 times (Configuration II) larger than the in-plane strain that can be produced by uniform gating. Therefore, by using the local gating design, not only can we get the required *anisotropic* strain from *isotropic* piezoelectric materials, but the strain generation efficiency also improves significantly.

The high efficiency of strain generation in the local gating schemes can be attributed to two factors. First, for uniform gating, the E-field is uniformly distributed everywhere within the substrate. Whereas by using the local gating schemes, the E-field is highly concentrated in the regions of interest and thus the E-field around the MTJ is much stronger (see **Figure 4-7**). Second, in Configuration II, the in-plane strains along the *x*-direction and along the *y*-direction have opposite signs and can compensate each other, making the *anisotropic* strain $\varepsilon_{xx} - \varepsilon_{yy}$ larger. Obviously, by further optimizing the dimensions of the contacts in the local gating schemes (for example, the width of the gap between two side gates) the strain generation efficiency can be further improved.

Table 4. Strain generated in different gating schemes (with V_g = +50 V)

Gating schemes	In-plane Strain in MTJ region	Out-of-plane Strain in MTJ region
Configuration I	-274 ppm *(anisotropic)*	618 ppm
Configuration II	123 ppm *(anisotropic)*	n/a
Uniform Gating	-92 ppm *(isotropic)*	196 ppm

4.4.2 The variation of the minor loop with different E-fields

In **Figure 4-4 (c)** and **Figure 4-5 (c)**, the voltage-controlled variation in H_c of the hard CoFeB layer of MTJ was observed. But the modification in the soft CoFeB layer of MTJ is not observable from the MR major loops. It is because the dipolar field from the hard layer plays a dominant role in the switching of the soft layer. In order to illustrate that both CoFeB layers of the MTJ can be controlled by voltage, I measured the MR minor loop with different V_g applied, as shown in **Figure 4-9**. The MR minor loops were obtained by performing a sweep of the magnetic field H_y in a small range (from −100 Oe to 15 Oe),

within which only the soft CoFeB layer is flipped by the magnetic field, and the hard CoFeB layer stays unchanged. As can be seen, as V_g is changed from 0 to −80V, not only does the switching field of the hard CoFeB layer increase (in the major loops), but the coercivity of the soft layer also increases from 7 Oe to 18 Oe (in the minor loops). Therefore, we can conclude that the magnetic anisotropy of both CoFeB layers in the MTJ can be effectively controlled by the gate voltage.

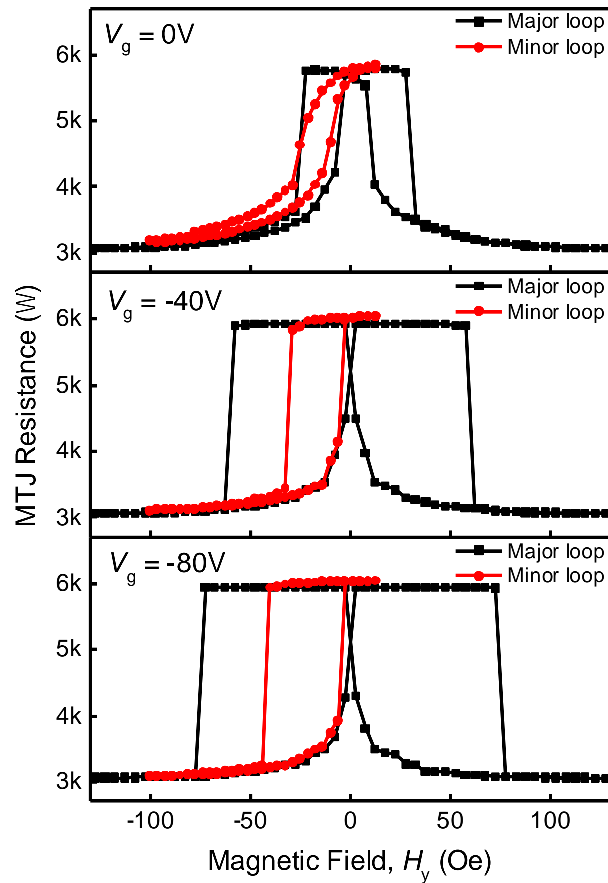

Figure 4-9. MR major and minor loops (in Configuration II) with **(a)** V_g = 0 V, **(b)** V_g = −40 V, and **(c)** V_g = −80 V.

4.4.3 Result by interchanging the soft layer and the hard layer in MTJ

The MTJ structure described in Section 4.3 is: PMN-PT substrate / Ta (8) / CoFeB (10) / MgO (1.8) / CoFeB (4) / Ta (8). This arrangement places the hard layer (thicker CoFeB) close to the piezoelectric substrate in the bottom, and the soft layer (thinner CoFeB) farther away from the substrate. We have seen the magnetic anisotropy of both CoFeB layers can be affected by the strain, because neither of them is pinned by an anti-ferromagnetic layer. And we argue that the strain exerted on the soft layer and that exerted on the hard layer is very close to each other, although the hard layer is closer to the piezoelectric substrate. This is because the strain relaxation through the MTJ stack is negligible, considering the thickness of the MTJ stack is much smaller than its lateral dimensions. To confirm this, we have made a second sample with the position of the hard and soft CoFeB layers interchanged: PMN-PT substrate / Ta (8) / CoFeB (4) / MgO (1.8) / CoFeB (10) / Ta (8). Now with the hard layer (CoFeB 10 nm) placed farther from the substrate, we would like to find out whether the voltage still has the same influence on the switching field of it, as has been shown in **Figure 4-4 (c)** and **(d)**. The result of this sample is presented in **Figure 4-10**. It can be seen the variations of the MR loop are quite similar to the results for the previous sample, where a positive gate voltage enhances the switching field of the hard layer, and a negative gate voltage squeezes and slants the loop. Therefore, for our devices, interchanging the positions of the soft layer and hard layer doesn't make observable difference.

However, it should be noted that for a further scaled devices (where the MTJ lateral dimensions is down to sub-100 nm, and the thickness of the piezoelectric layer also in x100

nm range), the strain relaxation needs to be considered, and the soft (free) layer should be deposited closer to the piezoelectric layer in order to experience maximal strain.

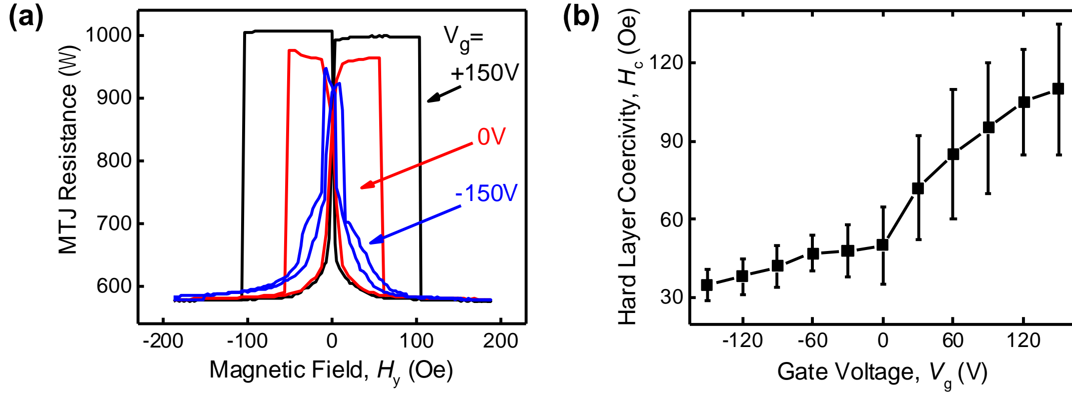

Figure 4-10. MR loops characterized under different gate voltages (in Configuration I) for the sample: PMN-PT substrate / Ta (8) / CoFeB (4) / MgO (1.8) / CoFeB (10) / Ta (8), where the soft layer is closer to the piezoelectric substrate.

4.4.4 Quantification of the voltage-induced anisotropy

From the variation of the MR loops in **Figure 4-4 (c)** and **Figure 4-5 (c)**, the magnetic anisotropy induced by strain can be evaluated. Consider Configuration II in **Figure 4-5 (c)**, for example. When zero gate voltage is applied, the anisotropy of the CoFeB layers comes from the shape anisotropy, and the anisotropy field can be determined by the saturation field of the MR loop with magnetic field swept along the short axis of the pillar (**Figure 4-11**), which is $H_K^{shape} = 120\ \text{Oe}$. With a positive or negative gate voltage applied, the strain will induce an additional anisotropy field. Then, the total anisotropy field would be:

$$H_K = H_K^{shape} + H_K^{strain} \tag{4-1}$$

Assuming the switching field is proportional to the anisotropy field: $H_c \propto H_K$, then with the value of H_c increases 3.5 times from V_g = 0 V to V_g = + 150 V according to **Figure 4-5 (c)** and **(d)**, the strain-induced anisotropy field at V_g = + 150 V would be:

$$H_K^{strain} \approx 2.5 \times H_K^{shape} \approx 300\,\text{Oe} \tag{4-2}$$

And the strain-induced anisotropy energy at V_g = + 150 V would be:

$$K_{me} = \frac{1}{2} H_K^{strain} M_s = 150 \times 10^3\ \text{erg/cm}^3 \tag{4-3}$$

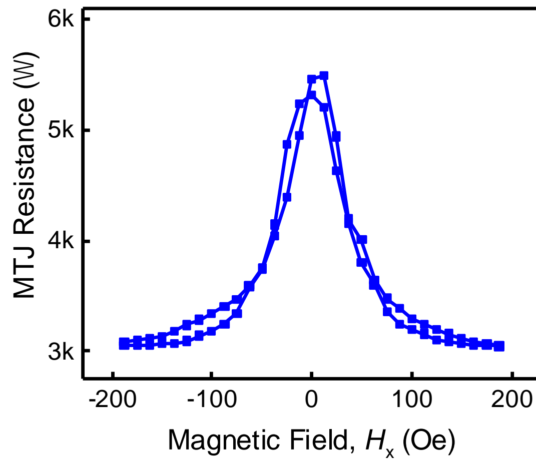

Figure 4-11. MR curve with the magnetic field swept along the minor axis of the pillars in the *x*-direction (no gate voltage applied).

Note above is just a rough quantification, because $H_K^{shape} = 120\,\text{Oe}$ estimated from **Figure 4-11** may not be quite accurate considering the interaction of the two CoFeB layers,

and the assumption of $H_c \propto H_K$ is debatable for magnets containing multi-domain. But the order of magnitude of K_{me} estimated above should be reliable. It's also worth noting that, though the strain-induced anisotropy is sufficient to rotate an in-plane magnetized layer, it's not strong enough to switch a perpendicular magnet. Because the typical value of the perpendicular anisotropy (PMA) is at least one order larger than that can be induced by strain (see Section 1.1.2). This is a challenge that needs to be solved in the future.

Using the value of K_{me} obtained above, we can further estimate the strength of the *anisotropic* strain that is produced on the MTJ. Considering:

$$K_{me} = \frac{3}{2}\lambda\sigma = \frac{3}{2}\lambda Y(\varepsilon_{xx} - \varepsilon_{yy}) \tag{4-4}$$

and $Y = 160\text{GPa}$, $\lambda = 3\times10^{-5}$ for CoFeB thin film [192,196], the *anisotropic* strain is determined to be $\varepsilon_{xx} - \varepsilon_{yy} = 1950$ ppm at V_g = + 150 V in Configuration II. This value is in the same order as that estimated using the piezoelectric finite element simulation (in **Table 4**).

4.4.5 Device scalability and energy dissipation

For realistic applications, the strain-mediated MTJ requires using a piezoelectric thin film deposited on a Si substrate [43,187,188], as opposed to a 0.5 mm thick piezoelectric substrate used here. And the device should be scaled down to sub-100 nm [197]. Therefore, we need to examine the scaling potential of our side-gated MTJ device. If the 0.5 mm thick piezoelectric substrate is scaled down to a thin film of 100 nm in thickness (reduced by a factor of 5000), the lateral dimensions of the side gates should be correspondingly scaled

from ~200 μm to 50 nm (now the lateral dimensions of the side gates are in the same order as the dimension of the MTJ pillar, and the strain generation would still be efficient [187]). And the gate voltages V_g would have been reduced by a factor of roughly 5000, from 100 V in our experiment down to about 20 mV. Although there are no reports of switching the magnetization of nanomagnets on a 100 nm piezoelectric film, there is a recent report of switching the magnetization of nanomagnets on a 1000 nm thick piezoelectric film deposited on a Si substrate [182]. In such a clamped thin film, the piezoelectric coefficient dropped by 40%. If we assume an 80% drop in the piezoelectric coefficient in a 100 nm piezoelectric thin film, then the gate voltage will increase five-fold to 100 mV.

For such a scaled device, we can calculate its energy dissipation. The gate capacitance C has been estimated in previous works to be about 2 fF depending on the dimensions of the electrodes [43,184]. Hence the energy dissipated to toggle the MTJ resistance would have been $CV_g^2 = 20$ aJ, which would make our proposal the lowest energy writing scheme extant.

4.5 Summary

Strain-mediated voltage control of magnetization in piezoelectric/ferromagnetic systems is a promising mechanism to implement energy-efficient spintronic memory devices. In this chapter, I have demonstrated a giant voltage manipulation of CoFeB / MgO / CoFeB MTJ deposited on PMN-PT (001) substrate. By designing a local gating scheme, I have realized efficient voltage-control of the magnetic easy axis, switching field, and the tunnel magnetoresistance (TMR) ratio of the MTJ. The magnetic anisotropy of the CoFeB

layers can be either strongly enhanced, resulting in an increase of the switching magnetic field of the MTJ by more than 4 times, or reduced, leading to a 90° rotation of the magnetization and hence a switching of the MTJ resistance. Which occurrence takes place depends on the sign of the strain in the free layer – tensile or compressive. Our work displays significant improvements over the previous work on strain-mediated MTJ device [186]:

- The voltage-controlled rotation of the magnetization requires the generation of *anisotropic* strain. In the previous work, the required strain relied on the intrinsic anisotropy of the piezoelectric substrate of certain special cuts [186]. For our device, we designed the local gating schemes, which would generate the required *anisotropic* strain from an ordinary *isotropic* piezoelectric layer, to realize the control of each individual MTJ. This design makes our devices scalable and amenable to practical memory applications.
- The local gating schemes also allow the control of MTJ with a relatively small voltage, thus enabling scalability and overcoming the substrate clamping issue [188]. The operating voltage V_g required for 90° rotation of magnetization is 4× smaller in our devices (~100 V) compared with previously reported devices (~8 kV/cm or 400 V) [175,177,178,186].
- We for the first time realized the strain-mediated voltage control of MgO-based MTJ with high TMR ratio, as opposed to the adoption of MTJ with an amorphous Al_2O_3 tunnel barrier in the other work [186]. The success of our devices proves the piezoelectric material is compatible with the modern MRAM fabrication

technology (especially the post-annealing treatment, though the annealing temperature is above the Curie temperature of PMN-PT: ~140 °C).

- The side-gated MTJ prototype paves the way to realizing complete magnetization "reversal", i.e. 180° rotation of the magnetization with a voltage [43], which is the ultimate goal of strain-based magnetization manipulation [186,189].

Therefore, the demonstration of highly effective voltage manipulation of MTJ via localized strain represents a key step towards realizing realistic strain-based MRAM with write energy of a few tens of aJ/bit in appropriately scaled structures.

Chapter 5 SOT Switching of Antiferromagnets: Is It Real?

5.1 Motivation and background

The previous chapters are all about controlling the magnetization in ferromagnets/ferrimagnets (FM). Especially, in Chapter 2 and Chapter 3, I have investigated spin-orbit torques (SOT) induced magnetization switching. In this chapter, I will expand the study of SOT switching to antiferromagnets (AFM), by examining the widely adopted 8-terminal geometry for switching and detecting the AFM state.

Antiferromagnets are magnetically ordered materials without net magnetization, which feature negligible magnetic stray fields, insensitivity against external magnetic field perturbations, and ultrafast spin dynamics [198–204], in contrast to ferromagnets. Thus, the prospects of developing reliable, high-speed, and high-density nonvolatile memory devices through antiferromagnetic materials are now recognized [55,205]. However, due to the absence of a net magnetic moment, both the manipulation and detection of the antiferromagnetic states (Néel vector) are significantly challenging.

Various approaches have been explored to control the magnetic states in AFMs before, which usually rely on external magnetic fields [206–209], ferromagnets [210–213], optical excitation [214–219], terahertz pump pulse [220–225], strain and electric field [48,207,226–231] and so on [232]. Nevertheless, within the context of controllability and practical use, direct all-electrical switching and detection of the AFM states are particularly desired and have attracted intensive interest in the antiferromagnetic spintronics study. Recently, breakthrough progresses have been made in metallic AFMs,

such as CuMnAs and Mn_2Au [233–236]. Their special crystal symmetries enable the generation of staggered Néel spin-orbit torques (NSOT) through applying electrical current, which efficiently switches the antiferromagnetic order on each opposite spin-sublattices. While the special requirement of broken inversion in crystallographic symmetries restricts the choice of potential antiferromagnetic materials. Most recently, SOT switching of an AFM has been reported by using bilayers of AFM and heavy metal (HM), for example, NiO/Pt [237–240], α-Fe_2O_3/Pt and metallic MnN/Pt [241–243]. The concept is similar to the SOT switching of a FM as presented in in Chapter 2 and Chapter 3: a charge current in the HM Pt layer generates a spin current that can transport into the AFM layer and switch its Néel orders, without relying on the special crystal symmetries of AFMs and an external field. It could provide a more feasible route towards all-electrical manipulation in AFMs. This switching concept is illustrated in **Figure 5-1 (a)**.

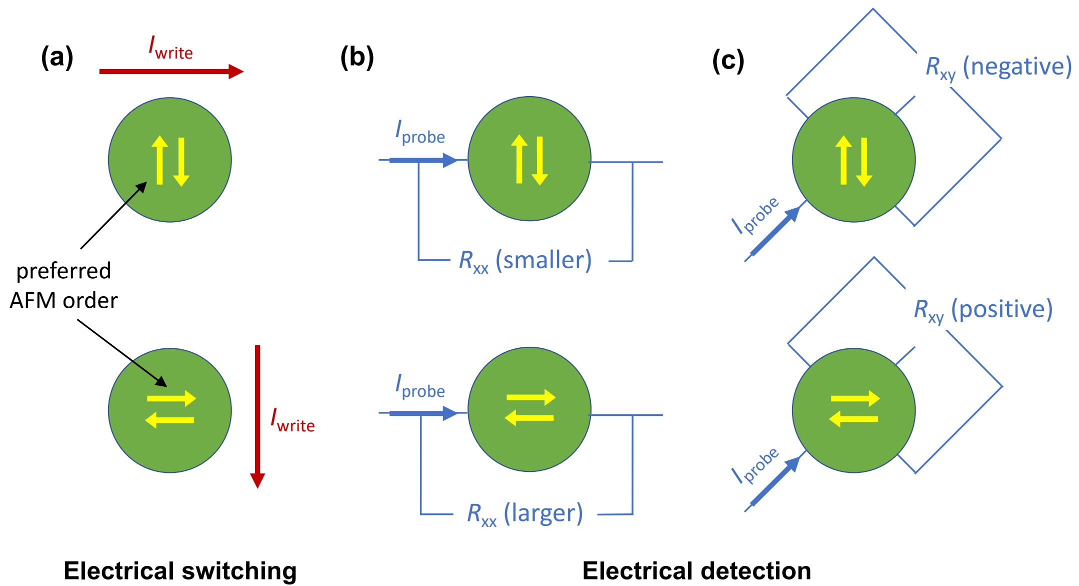

Figure 5-1. Illustration of the concepts for electrical manipulation and detection of AFM order. **(a)** SOT induced switching of AFM order. **(b)** Detection of the AFM orientation

using anisotropic magnetoresistance (AMR), which relies on measuring the R_{xx} signal. **(c)** Detection of the AFM orientation using planar Hall effect (PHE, another phenomenon of AMR), which relies on measuring the R_{xy} signal.

On the other hand, the detection of AFM state is quite tricky because of the absence of net magnetic moment. One way to detect the AFM orientation is by measuring the anisotropic magnetoresistance (AMR), as illustrated in **Figure 5-1 (b)**, or performing the PHE measurement (which essentially originates from AMR), as illustrated in **Figure 5-1 (c)**. If we want to perform the electrical switching [**Figure 5-1 (a)**] and electrical detecting [**Figure 5-1 (c)**] on the same device, an 8-terminal geometry is needed, as shown in **Figure 5-2 (b)**. Recently, the 8-terminal geometry has been widely used for AFM manipulation/detection. And the “read out” signal R_{xy} with the “saw-tooth” shape [233–237,243] or “steplike” shape [239,241,242] is identified as the signature of antiferromagnetic order switching. However, other studies found that the qualitatively same R_{xy} signals also appeared in non-magnetic films, such as Pt and Nb in the absence of AFM layer, which suggested the crucial role of non-magnetic contribution in the electrical antiferromagnetic switching experiments with SOT [242,244–246]. The localized Joule heating and electromigration are considered as the origin of the probed R_{xy} with “saw-tooth” and “steplike” shape respectively, since the high-density writing currents (I_w) is utilized [244–246]. As all the works mentioned above are mainly limited to samples consisting of antiferromagnetic insulators (AFI) and heavy metal Pt, it is essential to expand the study to other materials in order to examine the origin of the R_{xy} signals.

In this chapter, utilizing the 8-terminal geometry, I examine the origin of the "saw-tooth" shaped R_{xy} signals observed in the electrical AFM "switching" experiments with the MnN/Ta bilayers. MnN is a metallic AFM material with high Néel temperature [247]. Ta is a commonly used HM with *opposite* sign of spin Hall angle (SHA) as Pt [19,112]. The same measurement is then repeated with two control samples without the MnN layer: Ta sample and Pt sample. The "saw-tooth" shaped R_{xy} signals, which are similar to those observed in previous reports [233–237,241–245], is obtained in all three samples (MnN/Ta sample, Ta sample and Pt sample), indicating the non-magnetic (thermal) origin for such signals. In addition, the Ta sample and the Pt sample show *opposite* read out R_{xy} signal, which is determined by the *opposite* temperature coefficient of resistivity (TCR) of the two HM. Moreover, by utilizing a geometry with separated writing and reading paths, the quadratic relationship between the "read out" signal ΔR_{xy} and the "writing" current is observed. This quadratic relationship can be explained through semi-quantitative analysis, which further manifests the decisive role of "localized Joule heating" in such AFM "switching" experiments. Owing to the thermal influence, the electrical detection method for AFM switching through Hall crosses geometry has to be re-examined and the thermal artifacts have to be carefully evaluated.

The rest of this chapter is organized as follows. Section 5.2 presents the result with the 8-terminal devices. Section 5.3 presents the second device geometry, where the writing and reading paths are isolated, to further confirm the thermal origin of the detected R_{xy} signal. Section 5.4 analyzes the quadratic relationship between I_w and ΔR_x. Finally, Section 5.5 concludes the chapter.

5.2 Experiment with the 8-terminal geometry

As stated above, I studied three film stacks: the MnN/Ta sample [substrate / MnN (5) / Ta (10)], the Ta sample [substrate / Ta (7) / MgO (4)], and the Pt sample [substrate / Cr (2) / Pt (7)] (all thicknesses are in nm, and substrate here is thermally oxidized silicon substrate). The Ta sample and Pt sample only contain a heavy metal layer without the AFM layer. They are used as the control samples.

All the films were grown using DC sputtering in a Shamrock sputter tool at room temperature (RT), except for the antiferromagnetic MnN thin films which is deposited in the same way as described in our previous work [248]. To confirm the antiferromagnetism of the MnN film, the magnetic hysteresis (*M*-*H*) loop of bilayers with MnN (25) / CoFeB (3) is measured. A distinct shift of 480 Oe in the hysteresis loop is observed compared to its coercivity of 250 Oe, as seen in **Figure 5-2 (a)**, which manifests a strong exchange bias and verifies the antiferromagnetism of the MnN thin film.

The films were then patterned into devices with the 8-terminal Hall crosses geometry using photolithography and Ar ion milling procedures, as shown in **Figure 5-2 (b)**. The width of the vertical and horizontal Hall terminals is 6 μm and the other four terminals (45° apart from the vertical and horizontal bars) are 10 μm wide. Then the metallic Hall crosses were covered by a 50 nm-thick SiN_x film to avoid oxidation. For the measurement, a Keithley 6221 current source and a Keithley 2182A nanovolt meter were used to conduct the Hall measurement, and the other Keithley 6221 current source was used to generate the writing current (I_w). As depicted in **Figure 5-2 (b)**, I_w is injected through the writing paths along the +/− 45° directions (which are called the LH writing path and the RH writing path).

The Hall measurement is performed in the x and y direction, with a small probe current I_{probe} injected along the x direction, and the Hall voltage V_{Hall} measured along the y direction. The Hall resistance signal R_{xy} can be calculated as: $R_{\text{xy}} = V_{\text{Hall}} / I_{\text{probe}}$.

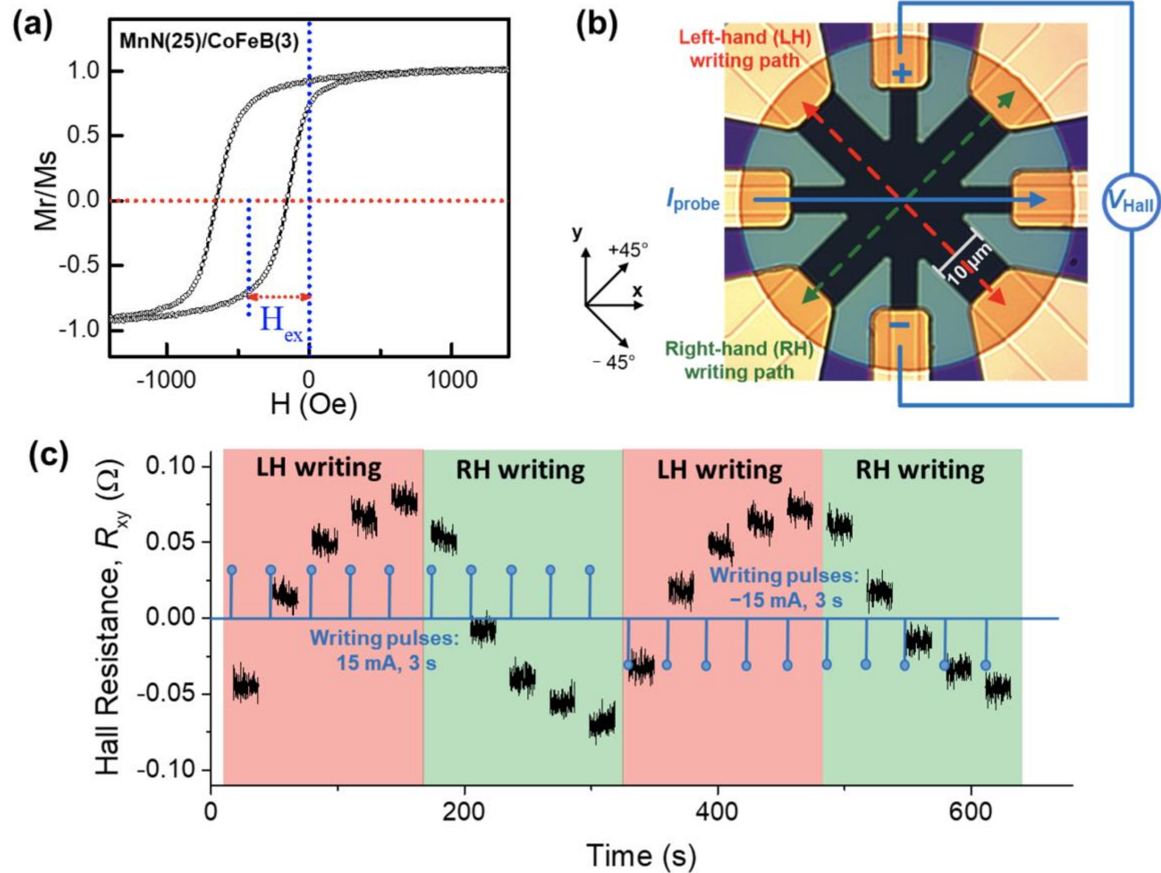

Figure 5-2. **(a)** *M-H* loop of MnN(25)/CoFeB(3) bilayers showing the exchange bias with AFM MnN. **(b)** Image of the patterned 8-terminal Hall device. Two writing paths are along the +/− 45º directions (denoted as RH/LH writing path). And the Hall resistance (R_{xy}) can be measured by applying a small probe current I_{probe} along the x direction and detecting the Hall voltage V_{Hall} along the y direction. **(c)** The R_{xy} signal of MnN(5)/Ta(10) sample obtained by conducting the standard electrical SOT switching experiment procedures. A sequence of writing pulses is applied, and the R_{xy} is recorded after each pulse (with I_{probe} =

0.1 mA). The writing pulses are either injected through the LH path (for the regions with red background), or through the RH path (for the regions with green background). The pulse amplitudes and pulse widths are denoted on the figure (pulses are denoted by the blue sticks). The R_{xy} signal (black) shows "saw-tooth" shape.

In the experiment of the 8-terminal geometry, first a writing pulse I_w would be applied either along the LH path or the RH path. Then R_{xy} as a read-out signal would be tracked by performing the Hall measurement. If the magnetic state of the AFM is rotated by the SOT generated by the I_w, it would be reflected on R_{xy} according to the planar Hall effect as depicted in **Figure 5-1 (c)**.

We first conducted the standard electrical SOT switching experiment procedures on the MnN(5)/Ta(10) sample: apply a sequence of writing current pulses and measure the Hall signal after each pulse. The pulse amplitude and pulse width are denoted in **Figure 5-2 (c)**. Firstly, five current pulses are applied along the −45º axis [left-hand (LH) writing path] and R_{xy} after each pulse is gradually increased (from negative to positive value). Then, five pulses with the same amplitude and width are applied along the +45º axis [right-hand (RH) writing path], and R_{xy} decreases accordingly (from positive to negative value). Reversing the direction of the pulse by 180º won't affect such trend on R_{xy}. We repeated this experimental procedure for several cycles, and **Figure 5-2 (c)** shows the change of R_{xy} within one cycle. Such "saw-tooth" shaped signal is consistent with the AFM/Pt system as reported before [237,241–245].

To clarify the mechanism of the probed "saw-tooth" shaped R_{xy} signal in MnN/Ta sample, we performed the same experiment on the two control samples: the Ta sample and the Pt sample without the MnN layer. Both of the control samples are patterned in the same way as shown in **Figure 5-2 (b)**. The same "switching" experiment procedures were carried out on them: 10 LH writing pulses followed by 10 RH writing pulses, with R_{xy} measured after each pulse. The recorded R_{xy} signals of the Ta and Pt samples are plotted in **Figure 5-3 (a)** and **(b)**, respectively. Surprisingly, both figures show the "saw-tooth" shaped R_{xy} signals even though there is no antiferromagnetic MnN layer existent. These results of the control samples reflect the non-magnetic origin of the "saw-tooth" shaped R_{xy} signals. In addition, it is interesting to find R_{xy} for the Pt sample changes in the *opposite* direction to that of the Ta and MnN/Ta samples [by comparing **Figure 5-3 (b)** with **Figure 5-3 (a)** and **Figure 5-2 (c)**]. This phenomenon is very easily associated with the *opposite* sign of SHA in Ta and Pt [19,112]. However, this possibility can be excluded because: (a) the change of R_{xy} is obtained even without any FM or AFM layer, indicating the non-magnetic origin of the R_{xy} signal, and (b) even if for AFM/HM bilayers, and assuming the change of R_{xy} is mainly determined by the Néel vector of AFM which is controllable by SOT, the polarity of R_{xy} still wouldn't be affected by the sign of SHA, because R_{xy} will have 2-fold symmetry as the the Néel vector rotates from 0º to 360º.

Now we infer that the thermal artifact could be the origin of the "saw-tooth" shaped R_{xy} signal, which is also pointed out in Refs. [245,246]. Upon the application of a writing current (along the +/− 45º path), the whole writing path is heated up by the electrical current. Especially, within the Hall cross area at the center of the device, the heating is non-uniform

due to the inhomogeneous distribution of writing current density. Higher temperature appears around the two constricting corners ("hot spots"), as illustrated in **Figure 5-3 (c)**. The resistivity of the film will be changed with the temperature. Then, during the Hall measurement stages, the path of I_{probe} is deviated due to the inhomogeneous resistivity. The deviation of I_{probe} then leads to the variation of the R_{xy} signal. When the writing path is changed from LH to RH, the deviation of I_{probe} is also changed, and the trend of R_{xy} signal reverses accordingly. In short, it is the inhomogeneous heating of I_w in the Hall cross area that generates the "saw-tooth" shaped R_{xy} signal.

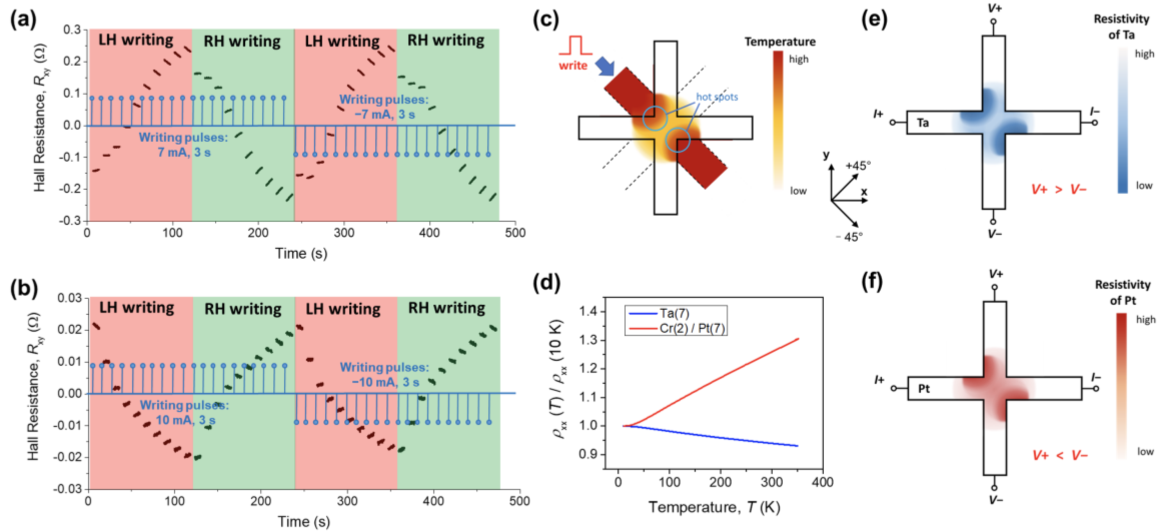

Figure 5-3. The "saw-tooth" shaped R_{xy} signal obtained from **(a)** the Ta sample, and **(b)** the Pt sample without MnN layer. $I_{\text{probe}} = 0.1$ mA. **(c)** Illustration of "localized Joule heating" when the writing current is injected through the LH writing path. **(d)** Normalized resistivity of the Ta sample (blue) and the Pt sample (red) as a function of temperature. **(e)** Illustration of the inhomogeneous distribution of resistivity for the Ta sample after the injection of LH writing pulse. The resistivity gets smaller around the "hot spots". **(f)** Illustration of the

inhomogeneous distribution of resistivity for the Pt sample after the injection of LH writing pulse. The resistivity gets larger around the "hot spots".

In addition, we still need to figure out in detail how the resistivity changes with temperature, and why the R_{xy} signal of the Ta sample and the Pt sample is *opposite*. Therefore, we measured the resistivity of both Ta and Pt films as a function of temperature, which is plotted in **Figure 5-3 (d)**. We found that the resistivity of Ta film decreases, whereas the resistivity of Pt film increases as the temperature, revealing the *opposite* signs of TCR for Ta and Pt. It should be noted that the negative sign of TCR for Ta reflects the formation of tetragonal β phase [249]. Now, the *opposite* trends of R_{xy} for Ta and Pt can be well explained. When applying I_w, the thermal effect and the *opposite* signs of TCR induced *opposite* changes in the resistivity of Ta and Pt. Then the path of I_{probe} is deviated in *opposite* ways within the Ta film and the Pt film, resulting in the *opposite* R_{xy} responses, as illustrated in **Figure 5-3 (e)** and **(f)**. From the analysis above, it can thus be concluded that all of the experimental results are in accordance with the "localized Joule heating" mechanism [245,246].

5.3 Experiment with separated writing and probing paths

To get a better understanding of thermal influence on the detected R_{xy} signals, we designed a second schematic, where the "writing" or "heating" paths are electrically isolated from the Hall measurement cross, as illustrated in **Figure 5-4 (a)**. First, the HM film (either Ta or Pt) is patterned into a 4-terminal cross bar along the x and y direction (for

the Hall measurement). Then, a 50-nm thick SiN_x film is deposited on the HM cross bar for electrical isolation. Finally, another cross along the +/− 45º directions is deposited, which consists of Ti (60)/Au (60) films. The top cross bar is used as the heating source. In this way, we can simultaneously apply the heating/writing current on the top paths and track the R_{xy} signals on the bottom HM layer. Consequently, the detected R_{xy} signal directly reflects the influence of Joule heating. Both the Ta and the Pt films were patterned into this schematic, and the measurement results are shown in **Figure 5-4 (b)** and **(c)**, respectively.

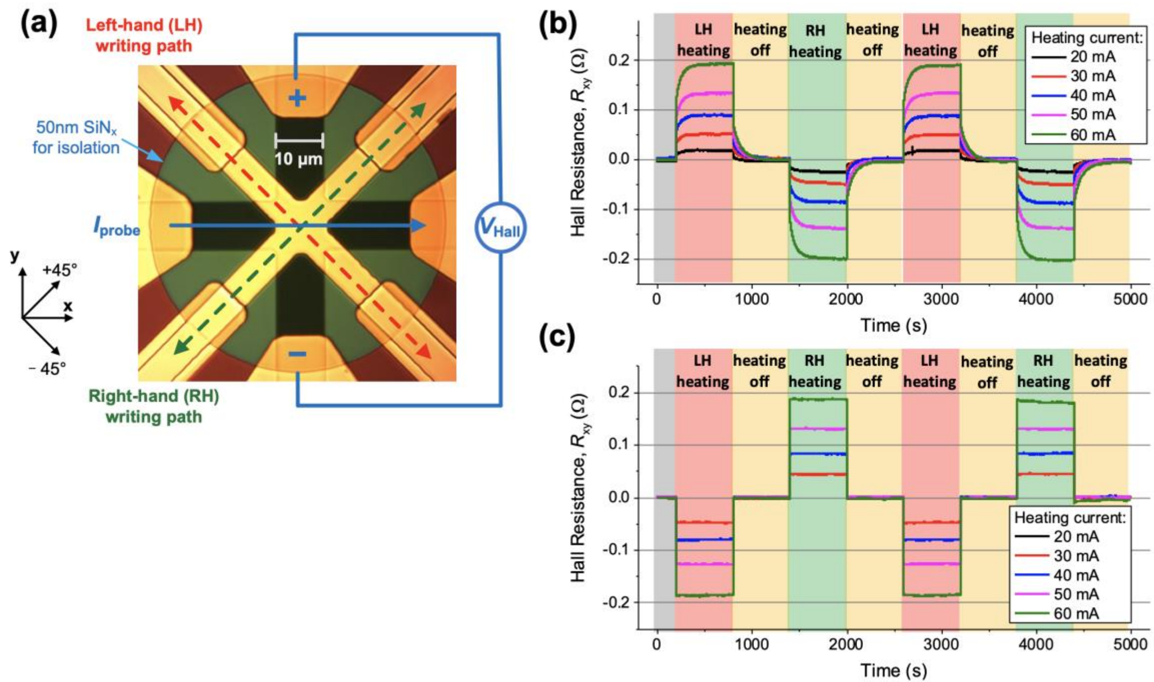

Figure 5-4. **(a)** Image of the second schematic, where the writing (heating) paths are electrically isolated from the Hall measurement cross (HM layer). The HM Hall cross (either Ta or Pt) is first covered by a SiN_x layer. Then the writing paths (along the +/− 45º directions) composed of Ti (60) / Au (60) are deposited on top of the SiN_x layer. **(b)** and **(c)**: R_{xy} signals of **(b)** the Ta sample and **(c)** the Pt sample with the application of DC

heating current on the writing paths. The heating current is either injected through the LH path (for the regions with red background), or through the RH path (for the regions with green background), or turned off (for the regions with yellow background). Heating current of different amplitudes are applied. $I_{probe} = 0.1$ mA.

The experiment procedure is described as follows: initially, a DC current I with a fixed amplitude is applied along −45° axis (LH path) for 600 s. Then I is off for 600 s to cool the device down to room temperature. After that, I is applied along +45° axis (RH path) for 600 s, and then turned off for cooling down. Such an experiment procedure is repeated for several cycles. The R_{xy} signal is simultaneously recorded throughout this procedure. As depicted in **Figure 5-4 (b)** and **(c)**, the R_{xy} signals show a periodic change depending on the direction of I: for LH heating, R_{xy} of Ta increases and R_{xy} of Pt decreases; for RH heating, R_{xy} of Ta decreases and R_{xy} of Pt increases; with the heating current off, R_{xy} gradually returns to 0. These trends are in agreement with the result of the 8-terminal devices shown in **Figure 5-3 (a)** and **(b)**. Again, the *opposite* incremental change of the R_{xy} signal for the Ta sample and the Pt sample confirms the critical role of Joule heating influenced HM layer's resistive property in the Hall measurement.

The R_{xy} signal in **Figure 5-4** is in "steplike" shape, because the Joule heating produced by a continuous DC current is more remarkable than that of pulse current. When the DC current is turned on, the temperature of the Hall cross area (in the HM layer) rises rapidly to a saturated value, so does R_{xy}. Similarly, when the DC current is turned off, the temperature drops rapidly from the saturated point, and R_{xy} returns to 0. It can also be seen

the R_{xy} signal of the Pt sample responds much faster than the Ta sample to the heating current. This could be due to the higher thermal conductivity of Pt, which makes the Pt sample reach thermal equilibrium much faster than the Ta sample. It is noteworthy that, R_{xy} does not originate from the *Seebeck* effect (as opposed to the explanation in [244]). We have measured V_{Hall} with I_{probe} turned off, which is the *Seebeck* voltage. The result is in the level of sub-μV, 2 orders of magnitude smaller than the case with I_{probe} turned on. This means the *Seebeck* voltage is negligible compared to the signal obtained from **Figure 5-2** through **Figure 5-4**. The variation of R_{xy} is resulted from the deviation of I_{probe} due to the "localized Joule heating" mechanism.

5.4 Analysis on the quadratic relationship between I_w and ΔR_{xy}

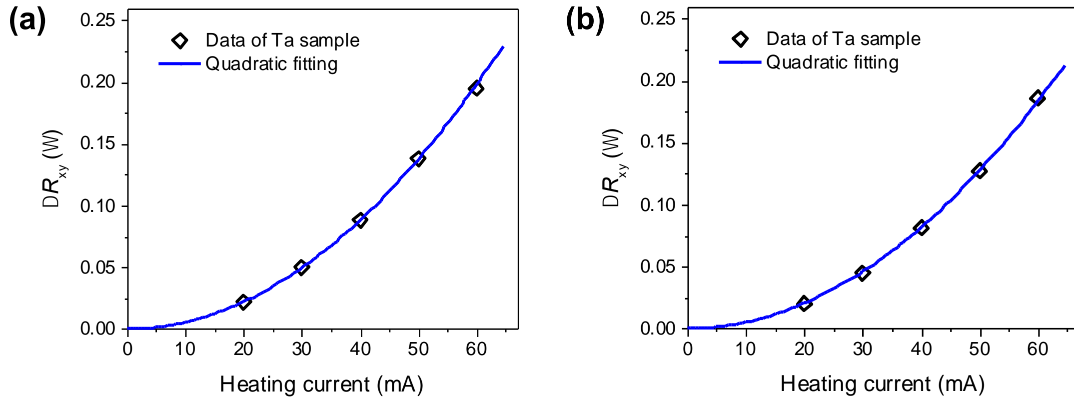

Figure 5-5. The amplitude of the R_{xy} signal changes as a function of heating current amplitude for **(a)** the Ta sample and **(b)** the Pt sample, extracted from **Figure 5-4 (b)** and **(c)**, respectively. The blue lines are quadratic fittings.

It is also noticed that in **Figure 5-4 (b)** and **(c)**, the amplitude of R_{xy} increases with

the increase of the DC current. In order to have a quantitative analysis on the relationship between the Joule heating and the R_{xy} signal, ΔR_{xy} [the amplitude of R_{xy} in **Figure 5-4 (b)** and **(c)**] is plotted as a function of the heating current I in **Figure 5-5 (a)** and **(b)**, for the Ta and Pt samples respectively. From the fitting curves, we can see ΔR_{xy} and the heating current I follows quadratic relationship.

This quadratic relationship (expressed as $\Delta R_{xy} = \phi \bullet I^2$, where ϕ is a constant) can be derived from the *Joule effect*. When the temperature is not very high and varies in a moderate range, the metallic material's resistivity approximately changes linearly as the function of temperature [this is also illustrated in **Figure 5-3 (d)**]. It can be expressed as:

$$\rho_T = \rho_0(1+\alpha T) \quad (5\text{-}1)$$

where ρ_T and ρ_0 is the resistivity of metallic material at temperatures T and T_0, respectively. α represents the TCR of the metal, which is a constant. As we discussed above, Ta and Cr/Pt possess opposite sign of α, see **Figure 5-3 (d)**. According to Eq. (5-1), the variation of resistance (ΔR) due to the change of temperature $\Delta T = T - T_0$ is:

$$\Delta R = \beta \bullet \rho_0 \bullet \alpha \Delta T \quad (5\text{-}2)$$

where β is the geometry factor of the material.

According to the *Joule effect*, the Joule heat (ΔQ) generated by DC current (I) in the conductive current path [the writing path as shown in **Figure 5-4 (a)**, which consists of Ti/Au bilayers] is expressed as:

$$\Delta Q = I^2 \bullet R_w \bullet t \quad (5\text{-}3)$$

where R_w represents the resistance of the Ti/Au writing path and t represents the length of time the DC current passed through. Besides, when heat energy ($\Delta Q'$) is added to a substance, the temperature will change, their relationship is described as:

$$\Delta Q' = c \bullet m \bullet \Delta T \tag{5-4}$$

where c and m are the specific heat capacity and the mass of the material, respectively. If the Joule heat produced from the Ti/Au writing path transfers to the Hall cross HM layer with heat transfer efficiency ε, then $\Delta Q' = \varepsilon \bullet \Delta Q$. Therefore, according to Eq. (5-3) and (5-4),

$$c \bullet m \bullet \Delta \mathrm{T} = \varepsilon \bullet I^2 \bullet R_w \bullet t \tag{5-5}$$

Thus,

$$\Delta T = \frac{\varepsilon \bullet I^2 \bullet R_w \bullet t}{c \bullet m}. \tag{5-6}$$

By combining Eq. (5-6) with Eq. (5-2),

$$\Delta R = \beta \bullet \rho_0 \bullet \alpha \Delta T = \frac{\beta \bullet \rho_0 \bullet \alpha \bullet \varepsilon \bullet I^2 \bullet R_w \bullet t}{c \bullet m} = \chi \bullet I^2 \tag{5-7}$$

where $\chi = \frac{\beta \bullet \rho_0 \bullet \alpha \bullet \varepsilon \bullet R_w \bullet t}{c \bullet m}$ is a constant for a sample. Due to the deviation of I_{probe}, the detected R_{xy} signal actually is a portion of the R (which is the R_{xx} signal). Thus,

$$\Delta R_{xy} = \varphi \bullet \Delta R = \varphi \bullet \chi \bullet I^2 = \phi \bullet I^2 \tag{5-8}$$

where φ is a constant which characterizes the portion of the R_{xx} signal with the value between 0 and 1. Equation (5-8) coincides well with the fitting result plotted in **Figure 5-5**.

In addition, the sign of ΔR_{xy} determined by the TCR coefficient α is also well described in Eq. (5-7) and (5-8). The quadratic relationship furtherly confirms the decisive influence of Joule heating on the generation of the R_{xy} signal.

5.5 Summary

In this chapter, I examined the correctness of the widely used experimental protocol for electrical (SOT) manipulation and detection of AFM, where an 8-terminal Hall crosses geometry is used. I confirmed that the "saw-tooth" shaped R_{xy} signals commonly appeared in the 8-terminal devices even without an antiferromagnetic layer in the film stack, because it originated from an intrinsic thermal artifact of the device geometry. In addition, the opposite R_{xy} signals for the Ta sample and Pt sample were observed, which were attributed to the opposite signs of temperature coefficient of resistivity in Ta and Pt. These results are fully compatible with the "localized Joule heating" mechanism, which is the artifact of the high-density writing current. We thus consider the previous reports, which used such geometry and signal patterns to manifest the SOT switching of AFM, is not conclusive without fully examining the thermal influence of the writing current.

Please note, here we constrained our debate on the specific device geometry and measurement protocol. We are not criticizing all the works on AFM switching. The experiments presented in this chapter were all performed from 2016 through Sep. 2018. Since 2019, other works holding the similar critical point have been published [242,244–246].

Chapter 6 SOT-MTJ for Computational Random-Access Memory (CRAM)

6.1 Background of CRAM

Apart from the memory application, spintronic devices (especially MTJs) also promise the implementation of novel computing platforms that can overcome the energy and delay bottleneck of traditional CPU-centric computing. In Section 1.3.3 of Chapter 1, I have introduced three major in-memory computing paradigms based on MTJs. In particular, computational random-access memory (CRAM) [87–89], where the STT-MTJ memory array is dynamically reconfigured to perform computations, allows *true* in-memory computing and thus meets the energy and throughput requirements of modern data-intensive processing tasks. Following the concept of STT-CRAM, in this chapter, I will implement a new CRAM architecture that uses the 3-terminal SOT-MTJs as unit cells, which would further improve the CRAM efficiency [94,95].

First, let's review the operations of STT-MTJ based CRAM, as shown in **Figure 6-1**. In the standard STT-MRAM array, each bitcell is 1T(ransistor)-1MTJ, where the transistor controls the access of the MTJ. While the STT-CRAM array uses 2T-1MTJ bitcell where the second transistor along with a logic line (LL) enables the logic operations performed *in situ* within the memory array.

In *memory mode*, the word line (WL) is high, thus it turns on the access transistor in each column and enables data to be read from or written into the MTJ through the memory bit line (MBL). This configuration is effectively identical to a standard STT-MRAM array.

In *logic mode*, the logic bit line (LBL) is turned on, which allows the MTJ to be connected to a logic line (LL) in each row. With several MTJs in a row connected to the same LL, a logic function with multiple inputs and one output can be realized. All the input and output operands of the logic function are represented by the resistances of MTJs, with antiparallel (AP) state and parallel (P) state of MTJ define logic ‘1’ and ‘0’, respectively. When a bias voltage V_b is applied, the current passing through the output MTJ depends on the input MTJ resistances, and if it exceeds the critical switching current I_c, the output MTJ state is altered, as has been discussed with **Figure 1-16**.

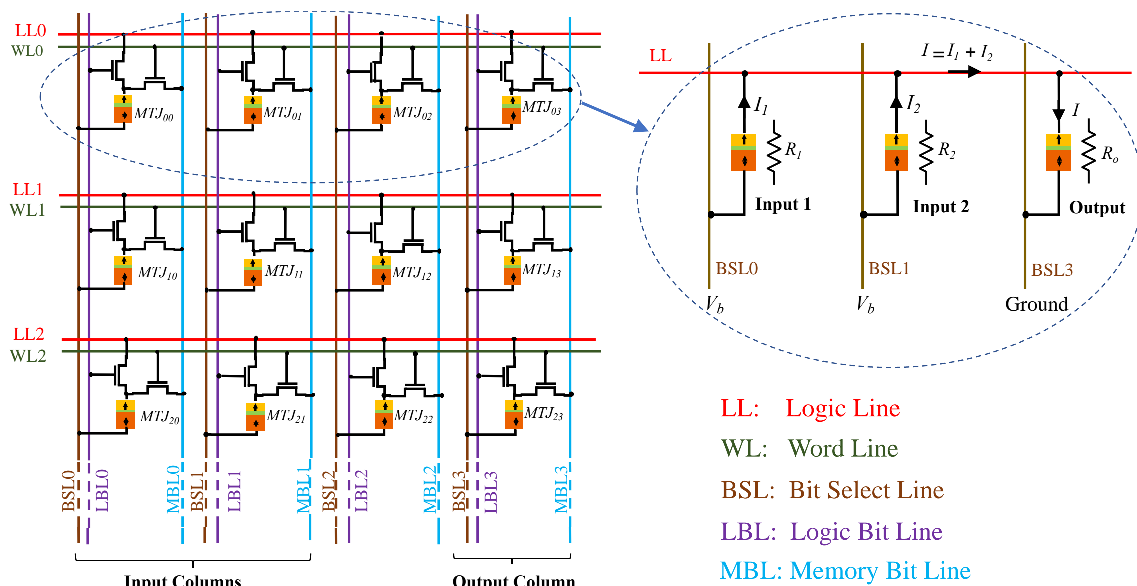

Figure 6-1. A logic operation in the STT-CRAM architecture [89].

It has been shown that STT-CRAM can outperform other in-memory-processing (IMP) or near-memory-processing (NMP) systems with regard to both energy and throughput. With today’s state-of-the-art MTJ technology, STT-CRAM can be 620× faster, and 23×

more energy efficient than the NMP system on processing 2D convolutional neural networks (CNN) [89]. Nevertheless, CRAM can be further optimized from device technology perspective. The STT-MTJ unit cell used in CRAM array, though exhibits many attractive features, still faces some challenging limitations:

- The write latency of STT-MTJ is long (several ns to more than 10 ns). This is because of the long incubation delay at the initial switching stage, which has been discussed with **Figure 1-4**.
- The required large write current leads to high dynamic energy dissipation (10× more than SRAM in a single cell) [250].
- The large writing current passing through the tunnel barrier also increases the risk of tunnel barrier breakdown and degradates the device endurance [251].

Spin-orbit torque (SOT) switching mechanism induced by spin Hall effect (SHE) can address above limitations of STT-MTJ well [252,253]. The SOT-MTJ (also called SHE-MTJ) is a 3-terminal device composed of a MTJ on top of the SH channel, as has been introduced in Section 1.2.1. It exhibits the following unique features:

- SOT-MTJ has separated write and read paths. This improves the device reliability and endurance by reducing the possibility of tunnel barrier breakdown.
- The separated write and read paths also allows each path to be optimized independently. This can be used to reduce the write current / write latency. For example, the write path can be optimized by adopting giant spin Hall efficiency materials as the SH channel [22,23,34–36].

- The read disturb issue of STT-MTJ (i.e., accidental writing while reading) can be avoided in SOT-MTJ, due to the separation of write and read paths.
- In addition, the switching behavior in SOT-MTJ is free of incubation delay that STT-MTJ suffers from [as shown in **Figure 1-5 (f)**]. Therefore, the write latency of SOT-MTJ can be as fast as SRAM (within 1 ns) [252].

These features, especially the faster access speed and potential lower writing energy, makes SOT-MTJ an ideal replacement of the STT-MTJ unit cell in CRAM. On the other hand, the 3-terminal device structure requires reconfiguring the topology of the CRAM architecture. In the rest of this chapter, I will present how this is accomplished. In particular, Section 6.2 presents the architecture design of the SOT-CRAM (also called SHE-CRAM) and the operation protocols. Section 6.3 validates the device feasibility for SOT-CRAM, by fitting in real or projected parameters of SOT devices. Finally, Section 6.4 concludes the chapter by showing some benchmarks. The content of this chapter has been published as a patent [95] as well as as a research article on ISQED [94].

6.2 SOT-CRAM architecture design

Due to the 3-terminal structure of SOT-MTJ and the separation of read and write paths, building a SOT-CRAM is more complex than simply replacing STT-MTJs in the STT-CRAM with SOT-MTJs. We can start from looking at the circuit of a 2-input logic gate implemented by SOT-MTJs, as shown in **Figure 6-2**. Same as the logic gate implemented by STT-MTJs presented in **Figure 1-16**, the logic '1' and '0' are represented by the antiparallel (AP) and parallel (P) resistance states of the MTJ, respectively. And the final state of the output MTJ is determined by the amplitude of $I_1 + I_2$ which is the quotient of

the bias voltage V_b and the overall resistance of the circuit. However, the current paths for the input MTJs and the output MTJ are different in **Figure 6-2**. For an input MTJ, current passes through the MTJ itself (the read path); while for the output MTJ, current should pass through the SH channel (the write path). Therefore, when fitted into the CRAM, the input MTJs and the output MTJs should have different wire arrangements, as opposed to the STT-CRAM array where the wire arrangements for all unit cells are identical.

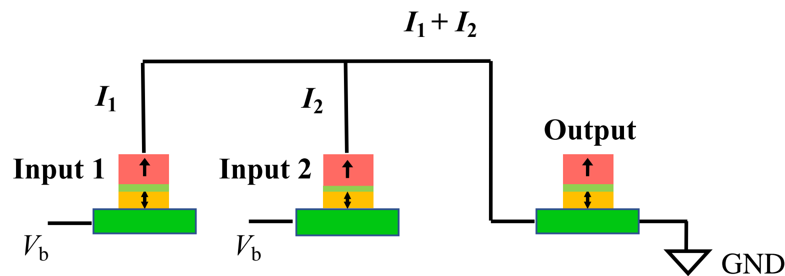

Figure 6-2. Schematic of a 2-input logic gate implemented by SOT-MTJs.

Based on the analysis above, we designed the architecture of the SOT-CRAM array, as shown in **Figure 6-3**. At the bitcell level, this structure is quite different from the STT-CRAM. The 2T-1MTJ bitcell accommodates the 3-terminal SOT-MTJ: each cell has one SOT-MTJ with two terminals gated by access transistors. Each row has two select lines (SLs), ESL and OSL -- which select the even and odd columns, respectively -- and a logic line (LL); each column has a read and write word line (WLR, WLW). At the array level, the arrangement of wires must accommodate the connections required by the 3-terminal SOT-MTJs shown in **Figure 6-2**. The MTJs in the even columns and those in the odd columns are connected to different SLs deliberately, so that during logic operations, the

MTJs in the even columns act as the input cells and the MTJs in the odd columns act as the output cells, or vice versa. Conventionally, the word line in a memory is drawn as a horizontal line, but here we show a rotated array where the word lines run vertically.

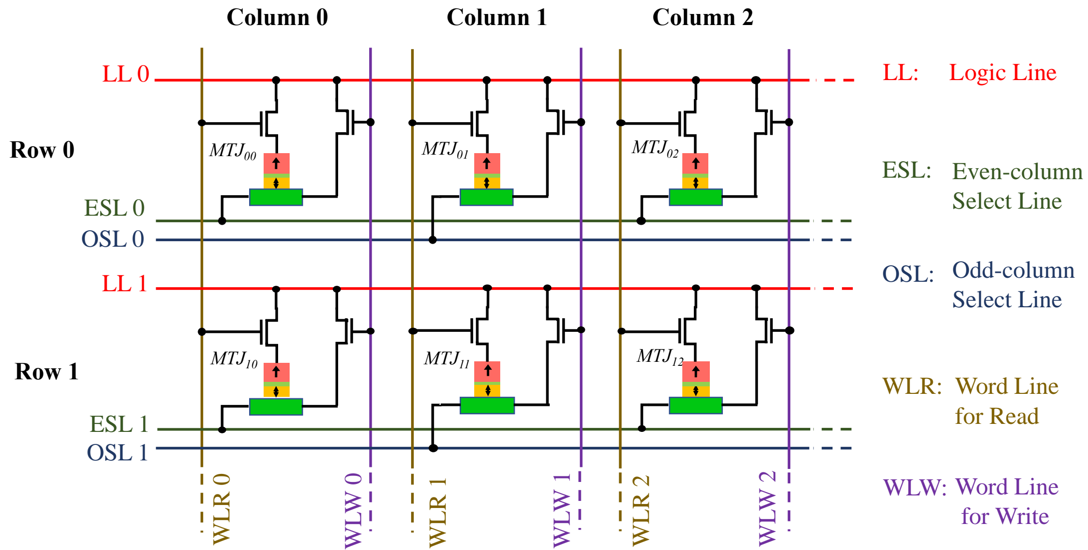

Figure 6-3. Overall structure of the SOT-CRAM.

In *memory write mode* [as shown in **Figure 6-4 (a)**], the transistor connected to WLR is off; WLW is high, turning on the write access transistor, and the SL is either positive or negative (i.e., one of two current directions is applied) depending on whether a 0 or 1 is to be written. The current passing through the SH channel writes to the MTJ. In *memory read mode* [as shown in **Figure 6-4 (b)**], WLR is set high to turn the read transistor on. A current is passed through the MTJ between LL and the SL to sense its resistance, i.e., the memory state, by connecting the SL to a sense amplifier.

In *logic mode* [as shown in **Figure 6-4 (c)**], a logic operation can be performed between cells in a CRAM row. For input cells, the WLR access transistors are turned on, so that current can be passed through their read paths; for the output cell, the WLW access transistor is turned on, to allow current to flow through the write path (SH channel). The LL is left floating. The SLs for the inputs are set to a specified bias voltage V_b, and the SL for the output is grounded. This guarantees the row in **Figure 6-4 (c)** behaves as the logic circuit shown in **Figure 6-2**. As mentioned before, all input operands must be in even-numbered columns, and the output must be in one of the odd-numbered columns -- or vice versa. This is unlike the STT-CRAM, where no such limitation is necessary.

The three modes -- memory read, memory write and logic -- are summarized in **Table 5**.

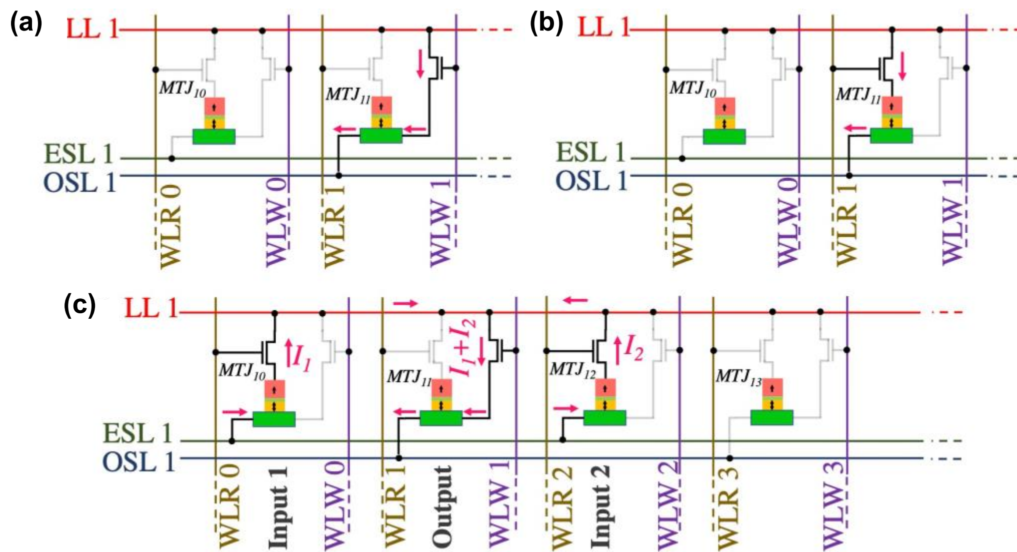

Figure 6-4. Current flow during: **(a)** memory write operation, **(b)** memory read operation, and **(c)** logic mode.

Table 5. Status of lines and transistors in SOT-CRAM for different modes

Operation		WLW	WLR	Transistor Connected to WLW	Transistor Connected to WLR	Active ESL	Active OSL	LL
Memory Mode	Write	High	Low	ON	OFF	Even column	Odd column	Active
	Read	Low	High	OFF	ON	Even column	Odd column	Active
Logic Mode	Input Cells	Low	High	OFF	ON	Any column	Any column	Float
	Output Cells	High	Low	ON	OFF			

6.3 SOT-CRAM device feasibility

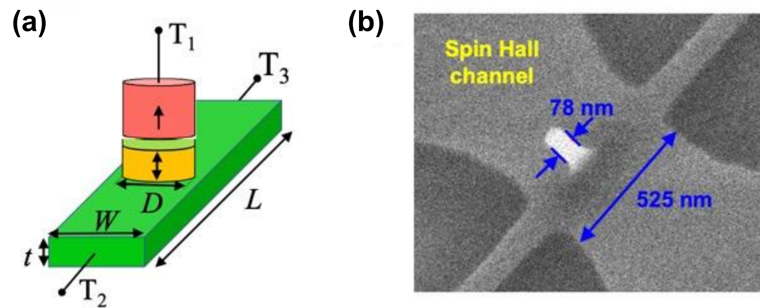

Figure 6-5. **(a)** Schematic of the SOT-MTJ with its dimensions denoted. **(b)** SEM image (taken at 60° from the perpendicular direction) showing a patterned SOT-MTJ (with resist on).

With the SOT-CRAM architecture ready, we still need to validate that SOT-MTJs are feasible to perform the logic functions within SOT-CRAM. For example, the device parameters (dimensions, resistivities, etc.) should be compatible with one another, to

guarantee that the total current flowing through the output cell is large enough to lead to a switching, while the current passing through each input MTJ is small enough to avoid unwanted STT switching or barrier breakdown. With these requirements in mind and by referring to the state-of-the-art SOT technologies, we define the parameters of the SOT-MTJ listed in **Table 6**.

Table 6. SOT-MTJ specifications in SOT-CRAM

Parameters	**Value**
MTJ type	CoFeB/MgO p-MTJ
Spin Hall channel material	Sputtered $BiSe_x$ [35]
MTJ diameter (D)	10 nm
Spin Hall channel length (L)	30 nm
Spin Hall channel width (W)	15 nm
Spin Hall channel thickness (t)	4 nm
Spin Hall channel sheet resistance (R_{Sheet})	32 kΩ
Spin Hall channel resistance (R_{SHE})	64 kΩ
MTJ RA product	20 $\Omega\cdot\mu m^2$
MTJ TMR ratio	100%
MTJ Parallel resistance (R_P)	253.97 kΩ
MTJ Anti-parallel resistance (R_{AP})	507.94 kΩ
STT critical current density (J_{STT})	5×10^6 A/cm^2
SHE threshold current density (J_{SHE})	5×10^6 A/cm^2 [35,159]
STT threshold current (I_{STT})	3.9 µA
SHE threshold current (I_{SHE})	3 µA
SHE pulse width (t_{SHE})	1 ns [32,33,158]
Transistor resistance (R_T)	1 kΩ

The parameters in **Table 6** are appropriately chosen to (a) provide an optimal margin window, (b) provide a low I_{SHE}, and (c) avoid unwanted STT switching during logic operations. In details:

- Device dimensions: The dimensions D, L, W, t of the SOT-MTJ are denoted in **Figure 6-5 (a)**. The ratio of SH channel's length (L) and width (W) is minimized in order to increase the noise margin and decrease the energy for logic operation (described in the following part). **Figure 6-5 (b)** shows a SOT-MTJ patterned with E-beam lithography.
- Spin Hall channel: The novel sputtered $BiSe_x$ is used as the SH channel, due to its high spin Hall efficiency [35]. **Figure 6-6** demonstrates the SOT switching of such a structure which requires a very low switching current density. The device is a micron-size Hall bar, which is composed of $BiSe_x$ (5 nm) / Ta (0.5 nm) as the SH channel and CoFeB (0.6 nm) /Gd (1.2 nm) /CoFeB(1.1 nm) as the perpendicular magnetic layer. The threshold switching current density J_{SHE} is determined to be 4.4×10^5 A/cm^2, which is two orders lower than normal spin Hall structures with a heavy metal (Ta, W, or Pt) as the SH channel.
- SHE threshold current density (J_{SHE}): Although the threshold switching current density obtained from the experiment is 4.4×10^5 A/cm^2, in **Table 6** J_{SHE} is set to be 5×10^6 A/cm^2. This is because when the device is scaled down from micron-size to sub-50 nm, J_{SHE} will be increased by one order [159].
- MTJ: A CoFeB/MgO p-MTJ with a low RA (resistance-area) product barrier is used, so that higher current density is allowed to be passed through the MTJ. And

the STT critical current density J_{STT} guarantees the current through each input cell wouldn't lead to unwanted STT switching.

- Field-free switching: The composite structure for field-free SOT switching presented in Chapter 3 can be directly used here. Actually, ref. [33] has applied the idea to SOT-MRAM.
- SHE pulse width (t_{SHE}): The write pulse t_{SHE} is set to be 1 ns in **Table 6**, much shorter than that used in STT-CRAM (3 ns) [89]. Actually, sub-1ns switching speed has been achieved in the Pt/Co/AlO_x Hall bar device in 2014, as well as in CMOS-integrated SOT-MRAM in 2019 [32,33].

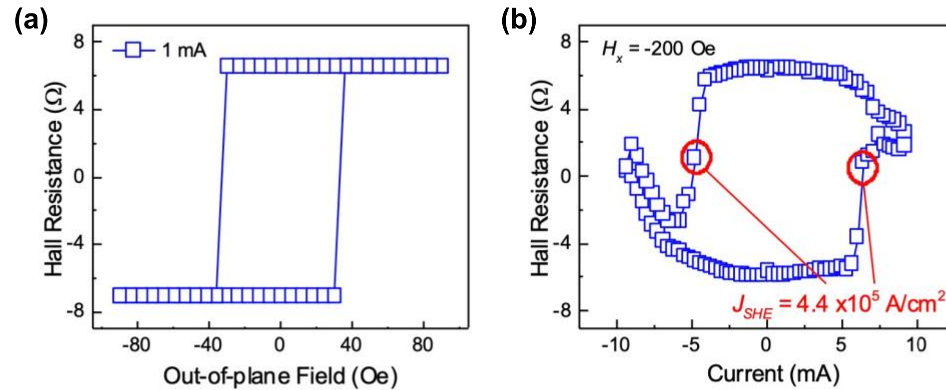

Figure 6-6. Demonstration of SOT switching with ultra-low J_{SHE} [35]. The SH layer is composed of $BiSe_x$ (5) /Ta (0.5), and the perpendicular magnetic layer is composed of CoFeB (0.6) /Gd (1.2) /CoFeB (1.1) (all thicknesses in nm). **(a)** Out-of-plane hysteresis loop of the sample and **(b)** SOT switching loop of the device.

Similar to STT-CRAM, the configuration of the SOT-CRAM into various gate types is controlled by two factors: (a) output preset value, (b) bias voltage, V_b. **Figure 6-7** shows

the circuit model of a 2-input logic gate. By modeling the current path of each gate, we can determine the conditions for implementing each gate type (AND/NAND, OR/NOR, etc.). The voltage V_b applied across the MTJ interconnections in logic mode falls across ESL and OSL. This voltage, applied across $\left(\frac{R_{SHE}}{2}+R_{MTJ1}+R_T\right)\|\left(\frac{R_{SHE}}{2}+R_{MTJ2}+R_T\right)$ in series with $R_{SHE}+R_T$, is shown in **Figure 6-7 (b)**. Here, "||" represents the equivalent resistance of resistors in parallel. Hence, the current I through the logic line is:

$$I=\frac{V_b}{\left(\frac{R_{SHE}}{2}+R_{MTJ1}+R_T\right)\|\left(\frac{R_{SHE}}{2}+R_{MTJ2}+R_T\right)+\left(R_{SHE}+R_T\right)} \tag{6-1}$$

If V_b is too low, $I<I_{SHE}$, and the current is insufficient to switch the output; if it is too high, $I>I_{SHE}$, and the output is switched regardless of the input state.

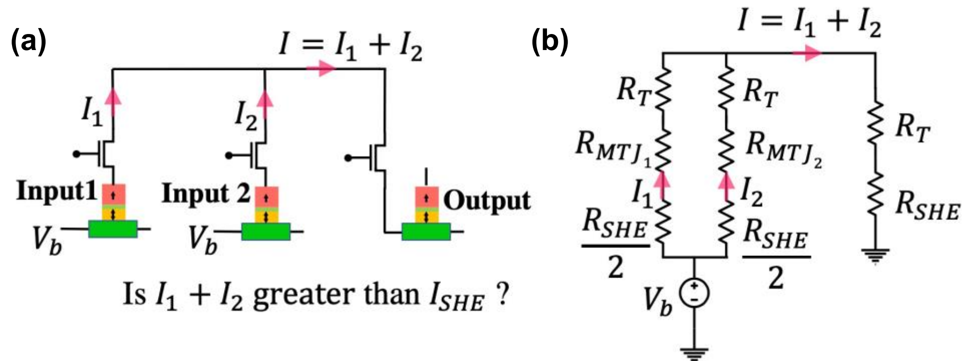

Figure 6-7. **(a)** Schematic showing a logic operation in a row of SOT-CRAM, and **(b)** the equivalent circuit model.

The resistance of the MTJ may take on one of two values, R_P or R_{AP}. For conciseness, we define R_1, R_2, and R_3 as:

$$R_1 = \frac{R_{SHE}}{2} + R_P + R_T \tag{6-2}$$

$$R_2 = \frac{R_{SHE}}{2} + R_{AP} + R_T \tag{6-3}$$

$$R_3 = R_{SHE} + R_T \tag{6-4}$$

Consider the case where the gate in **Figure 6-7 (a)** is used to implement a 2-input AND gate. For each of the input state combinations ('00' through '11'), we can calculate the currents flowing through the SH channel of the output MTJ as:

$$I_{00} = \frac{V_b}{R_1 / 2 + R_3} \tag{6-5}$$

$$I_{01} = I_{10} = \frac{V_b}{(R_1 \parallel R_2) + R_3} \tag{6-6}$$

$$I_{11} = \frac{V_b}{R_2 / 2 + R_3} \tag{6-7}$$

For the AND gate the preset output value is 1. For correct AND operation, we must choose V_b appropriately so that $I_{00} > I_{SHE}$ and $I_{01} = I_{10} > I_{SHE}$ (i.e., for both cases, the preset output is switched to 0), and $I_{11} < I_{SHE}$ (i.e., the output stays at 1). Since $R_P < R_{AP}$, $R_1 < R_2$. Therefore, $I_{11} < I_{01} = I_{10} < I_{00}$. Thus, if we choose V_b to be large enough so that

$I_{01} = I_{10} > I_{SHE}$, then $I_{00} > I_{SHE}$ must always be true. The following constraint must be obeyed:

$$V_b > ((R_1 \parallel R_2) + R_3) I_{SHE} . \tag{6-8}$$

On the other hand, to ensure the correctness of the '11' input case, V_b cannot be too large. Specifically, it is required that $I_{11} < I_{SHE}$, which leads to the second constraint:

$$V_b < (R_2 / 2 + R_3) I_{SHE} . \tag{6-9}$$

By inserting the device parameters listed in **Table 6** into Eq. (6-8) and (6-9), we get the viable range of V_b for the AND gate: 0.768 V < V_b < 1.017 V.

A NAND gate is identical to the AND, except that a preset value of 0 is used and the polarity of V_b is reversed; the range of V_b is identical to the AND. Similar constraints can be derived for other logic gates, and the bias voltage ranges to implement other gates can be calculated similarly.

For each gate, we can define the noise margin (*NM*) of V_b as:

$$NM = \frac{V_{\max} - V_{\min}}{V_{mid}} \tag{6-10}$$

where $V_{mid} = \frac{V_{\max} + V_{\min}}{2}$. Then the *NM* of the AND gate is 27.9%, which is significantly larger than the AND gate in STT-CRAM: 15.4% [89]. This is because the resistance R_{MTJ} (either R_{AP} or R_P) associated with the logic inputs are significantly higher than the

resistance R_{SHE} associated with the logic output, which provides a larger allowable interval for V_b . In contrast, the inputs and outputs for the STT-CRAM are both corresponding to MTJ resistances.

The (expected) energy E dissipated for each gate is:

$$E = V_{mid} I_{SHE} t_{SHE} \tag{6-11}$$

For the AND gate, $E = 0.485$ fJ, which is two orders smaller than STT-CRAM.

6.4 Summary

Computational random-access memory (CRAM) allows *in situ* computational operations in the memory array, and thus solves the memory bottlenecks for data-intensive computing tasks. To further optimize CRAM, the 2-terminal STT-MTJ unit cells should be replaced with 3-terminal SOT-MTJs, which are faster and more energy-efficient. In this chapter, I have presented SOT-CRAM -- a new version of CRAM that is based on SOT-MTJ arrays. The array structure is reconfigured to adapt the separated read and write paths of the 3-terminal SOT devices. Its logic functionality is examined by fitting in device parameters from the state-of-the-art SOT technologies. It has been shown SOT-CRAM is 4× more energy efficient, and 3× faster than STT-CRAM, and over 2000× faster, and 130× more energy-efficient than an NMP system (the operation scheduling and performance analysis which are out of the scope of this thesis, can be found in [94]). So far, the SOT-CRAM platform has been applied to various computing applications, such as neural networks [96], FFT accelerator [98], and sequence matching [99,100].

Chapter 7 Thesis Conclusion

This thesis presented my effort on developing novel spintronics devices and utilizing them for the next generation low-energy, high-performance memory and computing applications.

For the first part, I studied the SOT induced magnetization switching. In Particular, I solved two fundamental limitations related to the switching of a perpendicular magnetized system. First, my work expanded the scope of SOT switchable materials, from interfacial PMA magnets only, to bulk PMA magnets, which have a better thermal stability when scaled down and are regarded as potential candidates in future MRAM. Second, the difficulty of field-free SOT switching was addressed by developing a dipole-coupled composite device. The idea is to use the stray field projected by an in-plane magnetized layer placed on top of the conventional spin Hall structure, to substitute the external magnetic field. Compared with the other solutions for field-free switching, our composite device is the most compatible one with existing MRAM technologies and readily applicable for SOT-based memory and logic devices.

Besides the research on current-induced magnetization switching, the voltage-controlled device was also studied utilizing a piezoelectric / magnetic tunnel junction (MTJ) coupled structure for ultra-low power writing of data. Highly effective voltage manipulation of MTJ was demonstrated via the generation of localized strain from the local gating configurations. This prototype has the potential to be scaled down to a sub 100-nm

memory cell with write energy of a few tens of aJ/bit, and thereby represents a key step towards realistic strain-based MRAM.

Beyond the research of electrical controlling of ferromagnets (FM). I also attempted to tackle the spin torque induced switching in an antiferromagnetic (AFM) system, by characterizing the devices with a widely adopted 8-terminal geometry. Surprisingly, it's found the "saw-tooth" signal, which was previously regarded as the evidence of AFM switching, actually originates from thermal artifacts related to the inhomogeneous Joule heating. My results manifest the AFM switching presented in some previous reports were debatable, and more systematic studies are demanded for this area.

Finally, a new architecture for computational random-access memory (CRAM) that allows *in situ* computational operations in the memory array, is invented based on the SOT/SHE switching mechanism. In this architecture, each single cell is a 3-terminal SOT-MTJ which provides separated paths for reads and writes. Compared with the STT-MTJ based counterpart, SHE-CRAM would have a better latency and energy-efficiency. Therefore, it can be used as a general in-memory computing platform.

Bibliography

[1] S. Yuasa, T. Nagahama, A. Fukushima, Y. Suzuki, and K. Ando, *Giant Room-Temperature Magnetoresistance in Single-Crystal Fe/MgO/Fe Magnetic Tunnel Junctions.*, Nat. Mater. **3**, 868 (2004).

[2] S. S. P. Parkin, C. Kaiser, A. Panchula, P. M. Rice, B. Hughes, M. Samant, and S.-H. Yang, *Giant Tunnelling Magnetoresistance at Room Temperature with MgO (100) Tunnel Barriers.*, Nat. Mater. **3**, 862 (2004).

[3] S. Ikeda, K. Miura, H. Yamamoto, K. Mizunuma, H. D. Gan, M. Endo, S. Kanai, J. Hayakawa, F. Matsukura, and H. Ohno, *A Perpendicular-Anisotropy CoFeB–MgO Magnetic Tunnel Junction*, Nat. Mater. **9**, 721 (2010).

[4] S. Mangin, D. Ravelosona, J. A. Katine, M. J. Carey, B. D. Terris, and E. E. Fullerton, *Current-Induced Magnetization Reversal in Nanopillars with Perpendicular Anisotropy*, Nat. Mater. **5**, 210 (2006).

[5] N. Nishimura, T. Hirai, A. Koganei, T. Ikeda, K. Okano, Y. Sekiguchi, and Y. Osada, *Magnetic Tunnel Junction Device with Perpendicular Magnetization Films for High-Density Magnetic Random Access Memory*, J. Appl. Phys. **91**, 5246 (2002).

[6] L. Berger, *Low-Field Magnetoresistance and Domain Drag in Ferromagnets*, J. Appl. Phys. **49**, 2156 (1978).

[7] J. C. Slonczewski, *Current-Driven Excitation of Magnetic Multilayers*, J. Magn. Magn. Mater. **159**, L1 (1996).

[8] L. Berger, *Emission of Spin Waves by a Magnetic Multilayer Traversed by a Current*, Phys. Rev. B **54**, 9353 (1996).

[9] M. Tsoi, A. G. M. Jansen, J. Bass, W. C. Chiang, M. Seck, V. Tsoi, and P. Wyder, *Excitation of a Magnetic Multilayer by an Electric Current*, Phys. Rev. Lett. **80**, 4281 (1998).

[10] J. Z. Sun, *Current-Driven Magnetic Switching in Manganite Trilayer Junctions*, J. Magn. Magn. Mater. **202**, 157 (1999).

[11] J. A. Katine, F. J. Albert, R. A. Buhrman, E. B. Myers, and D. C. Ralph, *Current-Driven Magnetization Reversal and Spin-Wave Excitations in Co/Cu/Co Pillars*, Phys. Rev. Lett. **84**, 3149 (2000).

[12] T. Kawahara, R. Takemura, K. Miura, J. Hayakawa, S. Ikeda, Y. M. Lee, R. Sasaki, Y. Goto, K. Ito, T. Meguro, F. Matsukura, H. Takahashi, H. Matsuoka, and H. Ohno, *2 Mb SPRAM (SPin-Transfer Torque RAM) With Bit-by-Bit Bi-Directional Current Write and Parallelizing-Direction Current Read*, IEEE J. Solid-State Circuits **43**, 109 (2008).

[13] T. Kishi, H. Yoda, T. Kai, T. Nagase, E. Kitagawa, M. Yoshikawa, K. Nishiyama,

T. Daibou, M. Nagamine, M. Amano, S. Takahashi, M. Nakayama, N. Shimomura, H. Aikawa, S. Ikegawa, S. Yuasa, K. Yakushiji, H. Kubota, A. Fukushima, M. Oogane, T. Miyazaki, and K. Ando, *Lower-Current and Fast Switching of A Perpendicular TMR for High Speed and High Density Spin-Transfer-Torque MRAM*, in *Technical Digest - International Electron Devices Meeting, IEDM* (2008).

[14] D. C. Ralph and M. D. Stiles, *Spin Transfer Torques*, J. Magn. Magn. Mater. **320**, 1190 (2008).

[15] A. Brataas, A. D. Kent, and H. Ohno, *Current-Induced Torques in Magnetic Materials*, Nat. Mater. **11**, 372 (2012).

[16] H. Kubota, A. Fukushima, K. Yakushiji, T. Nagahama, S. Yuasa, K. Ando, H. Maehara, Y. Nagamine, K. Tsunekawa, D. D. Djayaprawira, N. Watanabe, and Y. Suzuki, *Quantitative Measurement of Voltage Dependence of Spin-Transfer Torque in MgO-Based Magnetic Tunnel Junctions*, Nat. Phys. **4**, 37 (2008).

[17] J. C. Sankey, Y. T. Cui, J. Z. Sun, J. C. Slonczewski, R. A. Buhrman, and D. C. Ralph, *Measurement of the Spin-Transfer-Torque Vector in Magnetic Tunnel Junctions*, Nat. Phys. **4**, 67 (2008).

[18] a. Manchon and S. Zhang, *Theory of Spin Torque Due to Spin-Orbit Coupling*, Phys. Rev. B **79**, 094422 (2009).

[19] L. Liu, C.-F. Pai, Y. Li, H. W. Tseng, D. C. Ralph, and R. A. Buhrman, *Spin-Torque Switching with the Giant Spin Hall Effect of Tantalum*, Science (80-.). **336**, 555 (2012).

[20] L. Liu, O. J. Lee, T. J. Gudmundsen, D. C. Ralph, and R. A. Buhrman, *Current-Induced Switching of Perpendicularly Magnetized Magnetic Layers Using Spin Torque from the Spin Hall Effect*, Phys. Rev. Lett. **109**, 096602 (2012).

[21] Z. Zhao, M. Jamali, A. K. Smith, and J.-P. Wang, *Spin Hall Switching of the Magnetization in Ta/TbFeCo Structures with Bulk Perpendicular Anisotropy*, Appl. Phys. Lett. **106**, 132404 (2015).

[22] A. R. Mellnik, J. S. Lee, A. Richardella, J. L. Grab, P. J. Mintun, M. H. Fischer, A. Vaezi, A. Manchon, E.-A. Kim, N. Samarth, and D. C. Ralph, *Spin-Transfer Torque Generated by a Topological Insulator*, Nature **511**, 449 (2014).

[23] M. Jamali, J. S. Lee, J. S. Jeong, F. Mahfouzi, Y. Lv, Z. Zhao, B. K. Nikolić, K. A. Mkhoyan, N. Samarth, and J. P. Wang, *Giant Spin Pumping and Inverse Spin Hall Effect in the Presence of Surface and Bulk Spin-Orbit Coupling of Topological Insulator Bi2Se3*, Nano Lett. **15**, 7126 (2015).

[24] J. Hirsch, *Spin Hall Effect*, Phys. Rev. Lett. **83**, 1834 (1999).

[25] J. Smit, *The Spontaneous Hall Effect in Ferromagnetics II*, Physica **24**, 39 (1958).

[26] L. Berger, *Side-Jump Mechanism for the Hall Effect of Ferromagnets*, Phys. Rev. B

2, 4559 (1970).

[27] I. M. Miron, K. Garello, G. Gaudin, P.-J. Zermatten, M. V Costache, S. Auffret, S. Bandiera, B. Rodmacq, A. Schuhl, and P. Gambardella, *Perpendicular Switching of a Single Ferromagnetic Layer Induced by In-Plane Current Injection*, Nature **476**, 189 (2011).

[28] M. Yamanouchi, L. Chen, J. Kim, M. Hayashi, H. Sato, S. Fukami, S. Ikeda, F. Matsukura, and H. Ohno, *Three Terminal Magnetic Tunnel Junction Utilizing the Spin Hall Effect of Iridium-Doped Copper*, Appl. Phys. Lett. **102**, 212408 (2013).

[29] S. V. Aradhya, G. E. Rowlands, J. Oh, D. C. Ralph, and R. A. Buhrman, *Nanosecond-Timescale Low Energy Switching of in-Plane Magnetic Tunnel Junctions through Dynamic Oersted-Field-Assisted Spin Hall Effect*, Nano Lett. **16**, 5987 (2016).

[30] M. Cubukcu, O. Boulle, M. Drouard, K. Garello, C. Onur Avci, I. Mihai Miron, J. Langer, B. Ocker, P. Gambardella, and G. Gaudin, *Spin-Orbit Torque Magnetization Switching of a Three-Terminal Perpendicular Magnetic Tunnel Junction*, Appl. Phys. Lett. **104**, 042406 (2014).

[31] I. Ahmed, Z. Zhao, M. G. Mankalale, S. S. Sapatnekar, J. P. Wang, and C. H. Kim, *A Comparative Study between Spin-Transfer-Torque and Spin-Hall-Effect Switching Mechanisms in PMTJ Using SPICE*, IEEE J. Explor. Solid-State Comput. Devices Circuits **3**, 74 (2017).

[32] H. Honjo, T. V. A. Nguyen, T. Watanabe, T. Nasuno, C. Zhang, T. Tanigawa, S. Miura, H. Inoue, M. Niwa, T. Yoshiduka, Y. Noguchi, M. Yasuhira, A. Tamakoshi, M. Natsui, Y. Ma, H. Koike, Y. Takahashi, K. Furuya, H. Shen, S. Fukami, H. Sato, S. Ikeda, T. Hanyu, H. Ohno, and T. Endoh, *First Demonstration of Field-Free SOT-MRAM with 0.35 Ns Write Speed and 70 Thermal Stability under 400°C Thermal Tolerance by Canted SOT Structure and Its Advanced Patterning/SOT Channel Technology*, in *2019 IEEE International Electron Devices Meeting (IEDM)*, Vols. 2019-Decem (IEEE, 2019), pp. 28.5.1-28.5.4.

[33] K. Garello, F. Yasin, H. Hody, S. Couet, L. Souriau, S. H. Sharifi, J. Swerts, R. Carpenter, S. Rao, W. Kim, J. Wu, K. K. V. Sethu, M. Pak, N. Jossart, D. Crotti, A. Furnemont, and G. S. Kar, *Manufacturable 300mm Platform Solution for Field-Free Switching SOT-MRAM*, in *2019 Symposium on VLSI Technology* (IEEE, 2019), pp. T194–T195.

[34] Y. Fan, P. Upadhyaya, X. Kou, M. Lang, S. Takei, Z. Wang, J. Tang, L. He, L.-T. Chang, M. Montazeri, G. Yu, W. Jiang, T. Nie, R. N. Schwartz, Y. Tserkovnyak, and K. L. Wang, *Magnetization Switching through Giant Spin–Orbit Torque in a Magnetically Doped Topological Insulator Heterostructure*, Nat. Mater. **13**, 699 (2014).

[35] M. DC, R. Grassi, J.-Y. Chen, M. Jamali, D. Reifsnyder Hickey, D. Zhang, Z. Zhao,

H. Li, P. Quarterman, Y. Lv, M. Li, A. Manchon, K. A. Mkhoyan, T. Low, and J.-P. Wang, *Room-Temperature High Spin–Orbit Torque Due to Quantum Confinement in Sputtered BixSe(1–x) Films*, Nat. Mater. **17**, 800 (2018).

[36] J. Han, A. Richardella, S. A. Siddiqui, J. Finley, N. Samarth, and L. Liu, *Room-Temperature Spin-Orbit Torque Switching Induced by a Topological Insulator*, Phys. Rev. Lett. **119**, 077702 (2017).

[37] S. Manipatruni, D. E. Nikonov, R. Ramesh, H. Li, and I. A. Young, *Spin-Orbit Logic with Magnetoelectric Nodes: A Scalable Charge Mediated Nonvolatile Spintronic Logic*, Arxiv: 1512.05428 (2015).

[38] S. Manipatruni, D. E. Nikonov, C. C. Lin, T. A. Gosavi, H. Liu, B. Prasad, Y. L. Huang, E. Bonturim, R. Ramesh, and I. A. Young, *Scalable Energy-Efficient Magnetoelectric Spin–Orbit Logic*, Nature **565**, 35 (2019).

[39] J.-M. Hu and C.-W. Nan, *Opportunities and Challenges for Magnetoelectric Devices*, APL Mater. **7**, 080905 (2019).

[40] J.-M. Hu, Z. Li, L.-Q. Chen, and C.-W. Nan, *High-Density Magnetoresistive Random Access Memory Operating at Ultralow Voltage at Room Temperature.*, Nat. Commun. **2**, 553 (2011).

[41] M. Ghidini, R. Pellicelli, J. L. Prieto, X. Moya, J. Soussi, J. Briscoe, S. Dunn, and N. D. Mathur, *Non-Volatile Electrically-Driven Repeatable Magnetization Reversal with No Applied Magnetic Field.*, Nat. Commun. **4**, 1453 (2013).

[42] A. K. Biswas, S. Bandyopadhyay, and J. Atulasimha, *Acoustically Assisted Spin-Transfer-Torque Switching of Nanomagnets: An Energy-Efficient Hybrid Writing Scheme for Non-Volatile Memory*, Appl. Phys. Lett. **103**, 232401 (2013).

[43] A. K. Biswas, S. Bandyopadhyay, and J. Atulasimha, *Complete Magnetization Reversal in a Magnetostrictive Nanomagnet with Voltage-Generated Stress: A Reliable Energy-Efficient Non-Volatile Magneto-Elastic Memory*, Appl. Phys. Lett. **105**, 072408 (2014).

[44] A. Khan, D. E. Nikonov, S. Manipatruni, T. Ghani, and I. A. Young, *Voltage Induced Magnetostrictive Switching of Nanomagnets: Strain Assisted Strain Transfer Torque Random Access Memory*, Appl. Phys. Lett. **104**, 262407 (2014).

[45] N. Tiercelin, Y. Dusch, V. Preobrazhensky, and P. Pernod, *Magnetoelectric Memory Using Orthogonal Magnetization States and Magnetoelastic Switching*, J. Appl. Phys. **109**, 1 (2011).

[46] N. a. Pertsev and H. Kohlstedt, *Magnetic Tunnel Junction on a Ferroelectric Substrate*, Appl. Phys. Lett. **95**, 163503 (2009).

[47] J. T. Heron, J. L. Bosse, Q. He, Y. Gao, M. Trassin, L. Ye, J. D. Clarkson, C. Wang, J. Liu, S. Salahuddin, D. C. Ralph, D. G. Schlom, J. Iñiguez, B. D. Huey, and R. Ramesh, *Deterministic Switching of Ferromagnetism at Room Temperature Using*

an Electric Field., Nature **516**, 370 (2014).

[48] X. He, Y. Wang, N. Wu, A. N. Caruso, E. Vescovo, K. D. Belashchenko, P. A. Dowben, and C. Binek, *Robust Isothermal Electric Control of Exchange Bias at Room Temperature.*, Nat. Mater. **9**, 579 (2010).

[49] C. Bi, Y. Liu, T. Newhouse-Illige, M. Xu, M. Rosales, J. W. Freeland, O. Mryasov, S. Zhang, S. G. E. Te Velthuis, and W. G. Wang, *Reversible Control of Co Magnetism by Voltage-Induced Oxidation*, Phys. Rev. Lett. **113**, 267202 (2014).

[50] J.-M. Hu, L.-Q. Chen, and C.-W. Nan, *Multiferroic Heterostructures Integrating Ferroelectric and Magnetic Materials*, Adv. Mater. **28**, 15 (2016).

[51] W. H. Kautz, *Cellular Logic-in-Memory Arrays*, IEEE Trans. Comput. **C–18**, 719 (1969).

[52] W. Kang, E. Deng, Z. Wang, and W. Zhao, *Spintronic Logic-in-Memory Paradigms and Implementations*, in *Applications of Emerging Memory Technology*, Vol. 63 (Springer Verlag, 2020), pp. 215–229.

[53] D. E. Nikonov and I. A. Young, *Benchmarking of Beyond-CMOS Exploratory Devices for Logic Integrated Circuits*, IEEE J. Explor. Solid-State Comput. Devices Circuits **1**, 3 (2015).

[54] R. Perricone, I. Ahmed, Z. Liang, M. G. Mankalale, X. S. Hu, C. H. Kim, M. Niemier, S. S. Sapatnekar, and J. P. Wang, *Advanced Spintronic Memory and Logic for Non-Volatile Processors*, in *Proceedings of the 2017 Design, Automation and Test in Europe, DATE 2017* (Institute of Electrical and Electronics Engineers Inc., 2017), pp. 972–977.

[55] J. Wang, S. S. Sapatnekar, C. H. Kim, P. Crowell, S. Koester, S. Datta, K. Roy, A. Raghunathan, X. S. Hu, M. Niemier, A. Naeemi, C.-L. Chien, C. Ross, and R. Kawakami, *A Pathway to Enable Exponential Scaling for the Beyond-CMOS Era*, in *Proceedings of the 54th Annual Design Automation Conference 2017* (ACM, New York, NY, USA, 2017), pp. 1–6.

[56] B. Behin-Aein, D. Datta, S. Salahuddin, and S. Datta, *Proposal for an All-Spin Logic Device with Built-in Memory.*, Nat. Nanotechnol. **5**, 266 (2010).

[57] D. A. Allwood, G. Xiong, C. C. Faulkner, D. Atkinson, D. Petit, and R. P. Cowburn, *Magnetic Domain-Wall Logic.*, Science **309**, 1688 (2005).

[58] M. Hayashi, L. Thomas, R. Moriya, C. Rettner, and S. S. P. Parkin, *Current-Controlled Magnetic Domain-Wall Nanowire Shift Register.*, Science **320**, 209 (2008).

[59] S. S. P. Parkin, M. Hayashi, and L. Thomas, *Magnetic Domain-Wall Racetrack Memory.*, Science **320**, 190 (2008).

[60] P. Xu, K. Xia, C. Gu, L. Tang, H. Yang, and J. Li, *An All-Metallic Logic Gate Based*

on Current-Driven Domain Wall Motion, Nat. Nanotechnol. **3**, 97 (2008).

[61] A. Lyle, X. Yao, F. Ebrahimi, J. Harms, and J. P. Wang, *Communication between Magnetic Tunnel Junctions Using Spin-Polarized Current for Logic Applications*, in *IEEE Transactions on Magnetics*, Vol. 46 (2010), pp. 2216–2219.

[62] D. Morris, D. Bromberg, J. G. Zhu, and L. Pileggi, *MLogic: Ultra-Low Voltage Non-Volatile Logic Circuits Using STT-MTJ Devices*, in *Proceedings - Design Automation Conference* (2012), pp. 486–491.

[63] H. P. Trinh, W. Zhao, J. O. Klein, Y. Zhang, D. Ravelsona, and C. Chappert, *Magnetic Adder Based on Racetrack Memory*, IEEE Trans. Circuits Syst. I Regul. Pap. **60**, 1469 (2013).

[64] J. A. Currivan, Youngman Jang, M. D. Mascaro, M. A. Baldo, and C. A. Ross, *Low Energy Magnetic Domain Wall Logic in Short, Narrow, Ferromagnetic Wires*, IEEE Magn. Lett. **3**, 3000104 (2012).

[65] J. A. Currivan-Incorvia, S. Siddiqui, S. Dutta, E. R. Evarts, J. Zhang, D. Bono, C. A. Ross, and M. A. Baldo, *Logic Circuit Prototypes for Three-Terminal Magnetic Tunnel Junctions with Mobile Domain Walls*, Nat. Commun. **7**, 1 (2016).

[66] Z. Luo, A. Hrabec, T. P. Dao, G. Sala, S. Finizio, J. Feng, S. Mayr, J. Raabe, P. Gambardella, and L. J. Heyderman, *Current-Driven Magnetic Domain-Wall Logic*, Nature **579**, 214 (2020).

[67] T. Patrick Xiao, M. J. Marinella, C. H. Bennett, X. Hu, B. Feinberg, R. Jacobs-Gedrim, S. Agarwal, J. S. Brunhaver, J. S. Friedman, and J. A. C. Incorvia, *Energy and Performance Benchmarking of a Domain Wall-Magnetic Tunnel Junction Multibit Adder*, IEEE J. Explor. Solid-State Comput. Devices Circuits **5**, 188 (2019).

[68] M. G. Mankalale, Z. Liang, Z. Zhao, C. H. Kim, J. P. Wang, and S. S. Sapatnekar, *CoMET: Composite-Input Magnetoelectric-Based Logic Technology*, IEEE J. Explor. Solid-State Comput. Devices Circuits **3**, 27 (2017).

[69] M. Hosomi, H. Yamagishi, T. Yamamoto, K. Bessho, Y. Higo, K. Yamane, H. Yamada, M. Shoji, H. Hachino, C. Fukumoto, H. Nagao, and H. Kano, *A Novel Nonvolatile Memory with Spin Torque Transfer Magnetization Switching: Spin-RAM*, in *Technical Digest - International Electron Devices Meeting, IEDM*, Vol. 2005 (2005), pp. 459–462.

[70] C. J. Lin, S. H. Kang, Y. J. Wang, K. Lee, X. Zhu, W. C. Chen, X. Li, W. N. Hsu, Y. C. Kao, M. T. Liu, W. C. Chen, Y. Lin, M. Nowak, N. Yu, and L. Tran, *45nm Low Power CMOS Logic Compatible Embedded STT MRAM Utilizing a Reverse-Connection 1T/1MTJ Cell*, in *Technical Digest - International Electron Devices Meeting, IEDM* (2009).

[71] E. Deng, Y. Zhang, J. O. Klein, D. Ravelsona, C. Chappert, and W. Zhao, *Low Power Magnetic Full-Adder Based on Spin Transfer Torque MRAM*, IEEE Trans.

Magn. **49**, 4982 (2013).

[72] W. Zhao, M. Moreau, E. Deng, Y. Zhang, J. M. Portal, J. O. Klein, M. Bocquet, H. Aziza, D. Deleruyelle, C. Muller, D. Querlioz, N. Ben Romdhane, D. Ravelosona, and C. Chappert, *Synchronous Non-Volatile Logic Gate Design Based on Resistive Switching Memories*, IEEE Trans. Circuits Syst. I Regul. Pap. **61**, 443 (2014).

[73] T. Hanyu, T. Endoh, D. Suzuki, H. Koike, Y. Ma, N. Onizawa, M. Natsui, S. Ikeda, and H. Ohno, *Standby-Power-Free Integrated Circuits Using MTJ-Based VLSI Computing*, Proc. IEEE **104**, 1844 (2016).

[74] W. Zhao, E. Belhaire, C. Chappert, and P. Mazoyer, *Spin Transfer Torque (STT)-MRAM - Based Runtime Reconfiguration FPGA Circuit*, Trans. Embed. Comput. Syst. **9**, 14 (2009).

[75] D. Chabi, W. Zhao, E. Deng, Y. Zhang, N. Ben Romdhane, J. O. Klein, and C. Chappert, *Ultra Low Power Magnetic Flip-Flop Based on Checkpointing/Power Gating and Self-Enable Mechanisms*, IEEE Trans. Circuits Syst. I Regul. Pap. **61**, 1755 (2014).

[76] K. Jabeur, G. Di Pendina, F. Bernard-Granger, and G. Prenat, *Spin Orbit Torque Non-Volatile Flip-Flop for High Speed and Low Energy Applications*, IEEE Electron Device Lett. **35**, 408 (2014).

[77] Y. Gang, W. Zhao, J. O. Klein, C. Chappert, and P. Mazoyer, *A High-Reliability, Low-Power Magnetic Full Adder*, IEEE Trans. Magn. **47**, 4611 (2011).

[78] E. Deng, Y. Zhang, W. Kang, B. Dieny, J. O. Klein, G. Prenat, and W. Zhao, *Synchronous 8-Bit Non-Volatile Full-Adder Based on Spin Transfer Torque Magnetic Tunnel Junction*, IEEE Trans. Circuits Syst. I Regul. Pap. **62**, 1757 (2015).

[79] S. Matsunaga, J. Hayakawa, S. Ikeda, K. Miura, H. Hasegawa, T. Endoh, H. Ohno, and T. Hanyu, *Fabrication of a Nonvolatile Full Adder Based on Logic-in-Memory Architecture Using Magnetic Tunnel Junctions*, Appl. Phys. Express **1**, 091301 (2008).

[80] S. Matsunaga, J. Hayakawa, S. Ikeda, K. Miura, T. Endoh, H. Ohno, and T. Hanyu, *MTJ-Based Nonvolatile Logic-in-Memory Circuit, Future Prospects and Issues*, in *2009 Design, Automation & Test in Europe Conference & Exhibition* (IEEE, 2009), pp. 433–435.

[81] W. Kang, L. Chang, Z. Wang, and W. Zhao, *In-Memory Processing Paradigm for Bitwise Logic Operations in STT-MRAM*, in *2017 IEEE International Magnetics Conference (INTERMAG)* (IEEE, 2017), pp. 1–1.

[82] S. Jain, A. Ranjan, K. Roy, and A. Raghunathan, *Computing in Memory with Spin-Transfer Torque Magnetic RAM*, IEEE Trans. Very Large Scale Integr. Syst. **26**, 470 (2017).

[83] Z. He, S. Angizi, F. Parveen, and D. Fan, *High Performance and Energy-Efficient*

in-Memory Computing Architecture Based on SOT-MRAM, in *Proceedings of the IEEE/ACM International Symposium on Nanoscale Architectures, NANOARCH 2017* (Institute of Electrical and Electronics Engineers Inc., 2017), pp. 97–102.

[84] D. Fan, S. Angizi, and Z. He, *In-Memory Computing with Spintronic Devices*, in *Proceedings of IEEE Computer Society Annual Symposium on VLSI, ISVLSI*, Vols. 2017-July (IEEE Computer Society, 2017), pp. 683–688.

[85] A. Lyle, J. Harms, S. Patil, X. Yao, D. J. Lilja, and J.-P. Wang, *Direct Communication between Magnetic Tunnel Junctions for Nonvolatile Logic Fan-out Architecture*, Appl. Phys. Lett. **97**, 152504 (2010).

[86] A. Lyle, S. Patil, J. Harms, B. Glass, X. Yao, D. Lilja, and J.-P. Wang, *Magnetic Tunnel Junction Logic Architecture for Realization of Simultaneous Computation and Communication*, IEEE Trans. Magn. **47**, 2970 (2011).

[87] Z. Chowdhury, J. D. Harms, S. K. Khatamifard, M. Zabihi, Y. Lv, A. P. Lyle, S. S. Sapatnekar, U. R. Karpuzcu, and J. P. Wang, *Efficient In-Memory Processing Using Spintronics*, IEEE Comput. Archit. Lett. **17**, 42 (2018).

[88] *US9224447B2 - General Structure for Computational Random Access Memory (CRAM)*, https://patents.google.com/patent/US9224447B2/en.

[89] M. Zabihi, Z. I. Chowdhury, Z. Zhao, U. R. Karpuzcu, J.-P. Wang, and S. S. Sapatnekar, *In-Memory Processing on the Spintronic CRAM: From Hardware Design to Application Mapping*, IEEE Trans. Comput. **68**, 1159 (2019).

[90] A. Ney, C. Pampuch, R. Koch, and K. H. Ploog, *Programmable Computing with a Single Magnetoresistive Element*, Nature **425**, 485 (2003).

[91] J. Wang, H. Meng, and J.-P. Wang, *Programmable Spintronics Logic Device Based on a Magnetic Tunnel Junction Element*, J. Appl. Phys. **97**, 10D509 (2005).

[92] H. Meng, J. Wang, and J. Wang, *A Spintronics Full Adder for Magnetic CPU*, IEEE Electron Device Lett. **26**, 360 (2005).

[93] X. Yao, S. Member, J. Harms, A. Lyle, F. Ebrahimi, Y. Zhang, J. Wang, and A. Magnetic, *Magnetic Tunnel Junction-Based Spintronic Logic Units Operated by Spin Transfer Torque*, **11**, 120 (2012).

[94] M. Zabihi, Z. Zhao, D. Mahendra, Z. I. Chowdhury, S. Resch, T. Peterson, U. R. Karpuzcu, J.-P. Wang, and S. S. Sapatnekar, *Using Spin-Hall MTJs to Build an Energy-Efficient In-Memory Computation Platform*, in *20th International Symposium on Quality Electronic Design (ISQED)*, Vols. 2019-March (IEEE, 2019), pp. 52–57.

[95] *US20200279597A1 - Computational Random Access Memory (CRAM) Based on Spin-Orbit Torque Devices*, (unpublished).

[96] S. Resch, S. K. Khatamifard, Z. I. Chowdhury, M. Zabihi, Z. Zhao, H. Cilasun, J.-

P. Wang, S. S. Sapatnekar, and U. R. Karpuzcu, *MOUSE: Inference In Non-Volatile Memory for Energy Harvesting Applications*, in *2020 53rd Annual IEEE/ACM International Symposium on Microarchitecture (MICRO)*, Vols. 2020-Octob (IEEE, 2020), pp. 400–414.

[97] S. Resch, S. K. Khatamifard, Z. I. Chowdhury, M. Zabihi, Z. Zhao, J. P. Wang, S. S. Sapatnekar, and U. R. Karpuzcu, *PIMBALL: Binary Neural Networks in Spintronic Memory*, ACM Trans. Archit. Code Optim. **16**, 1 (2019).

[98] H. Cilasun, S. Resch, Z. I. Chowdhury, E. Olson, M. Zabihi, Z. Zhao, T. Peterson, J.-P. Wang, S. S. Sapatnekar, and U. Karpuzcu, *CRAFFT: High Resolution FFT Accelerator In Spintronic Computational RAM*, in *2020 57th ACM/IEEE Design Automation Conference (DAC)*, Vols. 2020-July (IEEE, 2020), pp. 1–6.

[99] Z. I. Chowdhury, S. K. Khatamifard, Z. Zhao, M. Zabihi, S. Resch, M. Razaviyayn, J.-P. Wang, S. Sapatnekar, and U. R. Karpuzcu, *Spintronic In-Memory Pattern Matching*, IEEE J. Explor. Solid-State Comput. Devices Circuits **5**, 206 (2019).

[100] Z. I. Chowdhury, M. Zabihi, S. K. Khatamifard, Z. Zhao, S. Resch, M. Razaviyayn, J.-P. Wang, S. S. Sapatnekar, and U. R. Karpuzcu, *A DNA Read Alignment Accelerator Based on Computational RAM*, IEEE J. Explor. Solid-State Comput. Devices Circuits **6**, 80 (2020).

[101] A. van den Brink, S. Cosemans, S. Cornelissen, M. Manfrini, A. Vaysset, W. Van Roy, T. Min, H. J. M. Swagten, and B. Koopmans, *Spin-Hall-Assisted Magnetic Random Access Memory*, Appl. Phys. Lett. **104**, 012403 (2014).

[102] C. Onur Avci, K. Garello, I. Mihai Miron, G. Gaudin, S. Auffret, O. Boulle, and P. Gambardella, *Magnetization Switching of an MgO/Co/Pt Layer by in-Plane Current Injection*, Appl. Phys. Lett. **100**, 212404 (2012).

[103] C. Bi, L. Huang, S. Long, Q. Liu, Z. Yao, L. Li, Z. Huo, L. Pan, and M. Liu, *Thermally Assisted Magnetic Switching of a Single Perpendicularly Magnetized Layer Induced by an In-Plane Current*, Appl. Phys. Lett. **105**, 022407 (2014).

[104] K. Garello, I. M. Miron, C. O. Avci, F. Freimuth, Y. Mokrousov, S. Blügel, S. Auffret, O. Boulle, G. Gaudin, and P. Gambardella, *Symmetry and Magnitude of Spin-Orbit Torques in Ferromagnetic Heterostructures.*, Nat. Nanotechnol. **8**, 587 (2013).

[105] C. Hin Sim, J. Cheng Huang, M. Tran, and K. Eason, *Asymmetry in Effective Fields of Spin-Orbit Torques in Pt/Co/Pt Stacks*, Appl. Phys. Lett. **104**, 012408 (2014).

[106] T. Yang, M. Kohda, T. Seki, K. Takanashi, and J. Nitta, *Platinum Layer Thickness Dependence of Spin-Hall Induced Effective Magnetic Field in Pt / Co / Pt Structures Platinum Layer Thickness Dependence of Spin-Hall Induced Effective Magnetic Fi Eld in Pt / Co / Pt Structures*, Jpn. J. Appl. Phys. **53**, 04EM06 (2014).

[107] J. Kim, J. Sinha, M. Hayashi, M. Yamanouchi, S. Fukami, T. Suzuki, S. Mitani, and

H. Ohno, *Layer Thickness Dependence of the Current-Induced Effective Field Vector in Ta|CoFeB|MgO.*, Nat. Mater. **12**, 240 (2013).

[108] T. Suzuki, S. Fukami, N. Ishiwata, M. Yamanouchi, S. Ikeda, N. Kasai, and H. Ohno, *Current-Induced Effective Field in Perpendicularly Magnetized Ta/CoFeB/MgO Wire*, Appl. Phys. Lett. **98**, 142505 (2011).

[109] C. Zhang, M. Yamanouchi, H. Sato, S. Fukami, S. Ikeda, F. Matsukura, and H. Ohno, *Magnetization Reversal Induced by In-Plane Current in Ta/CoFeB/MgO Structures with Perpendicular Magnetic Easy Axis*, J. Appl. Phys. **115**, 17C714 (2014).

[110] G. Yu, P. Upadhyaya, K. L. Wong, W. Jiang, J. G. Alzate, J. Tang, P. K. Amiri, and K. L. Wang, *Magnetization Switching through Spin-Hall-Effect-Induced Chiral Domain Wall Propagation*, Phys. Rev. B **89**, 104421 (2014).

[111] C. O. Avci, K. Garello, C. Nistor, S. Godey, B. Ballesteros, A. Mugarza, A. Barla, M. Valvidares, E. Pellegrin, A. Ghosh, I. M. Miron, O. Boulle, S. Auffret, G. Gaudin, and P. Gambardella, *Fieldlike and Antidamping Spin-Orbit Torques in as-Grown and Annealed Ta/CoFeB/MgO Layers*, Phys. Rev. B **89**, 214419 (2014).

[112] S. Emori, U. Bauer, S.-M. Ahn, E. Martinez, and G. S. D. Beach, *Current-Driven Dynamics of Chiral Ferromagnetic Domain Walls*, Nat. Mater. **12**, 611 (2013).

[113] S. Manipatruni, D. E. Nikonov, and I. a. Young, *Energy-Delay Performance of Giant Spin Hall Effect Switching for Dense Magnetic Memory*, Appl. Phys. Express **7**, 103001 (2014).

[114] C.-F. Pai, M.-H. Nguyen, C. Belvin, L. H. Vilela-Leão, D. C. Ralph, and R. a. Buhrman, *Enhancement of Perpendicular Magnetic Anisotropy and Transmission of Spin-Hall-Effect-Induced Spin Currents by a Hf Spacer Layer in W/Hf/CoFeB/MgO Layer Structures*, Appl. Phys. Lett. **104**, 082407 (2014).

[115] J. Sinha, M. Hayashi, A. J. Kellock, S. Fukami, M. Yamanouchi, H. Sato, S. Ikeda, S. Mitani, S. Yang, S. S. P. Parkin, and H. Ohno, *Enhanced Interface Perpendicular Magnetic Anisotropy in Ta|CoFeB|MgO Using Nitrogen Doped Ta Underlayers*, Appl. Phys. Lett. **102**, 242405 (2013).

[116] P. He, L. Ma, Z. Shi, G. Y. Guo, J.-G. Zheng, Y. Xin, and S. M. Zhou, *Chemical Composition Tuning of the Anomalous Hall Effect in Isoelectronic L1_{0}FePd_{1-X}Pt_{x} Alloy Films*, Phys. Rev. Lett. **109**, 066402 (2012).

[117] A. Itabashi, M. Ohtake, S. Ouchi, F. Kirino, and M. Futamoto, *Preparation of L 1 0 Ordered FePd, FePt, and CoPt Thin Films with Flat Surfaces on MgO(001) Single-Crystal Substrates*, EPJ Web Conf. **40**, 07001 (2013).

[118] S. Ouardi, T. Kubota, G. H. Fecher, R. Stinshoff, S. Mizukami, T. Miyazaki, E. Ikenaga, and C. Felser, *Stoichiometry Dependent Phase Transition in Mn-Co-Ga-Based Thin Films: From Cubic in-Plane, Soft Magnetized to Tetragonal Perpendicular, Hard Magnetized*, Appl. Phys. Lett. **101**, 242406 (2012).

[119] H. Kurt, K. Rode, M. Venkatesan, P. Stamenov, and J. M. D. Coey, *High Spin Polarization in Epitaxial Films of Ferrimagnetic Mn_{3}Ga*, Phys. Rev. B **83**, 020405 (2011).

[120] F. Hellman and E. M. Gyorgy, *Growth-Induced Magnetic Anisotropy in Amorphous Tb-Fe*, Phys. Rev. Lett. **68**, 1391 (1992).

[121] H.-R. Lee, K. Lee, J. Cho, Y.-H. Choi, C.-Y. You, M.-H. Jung, F. Bonell, Y. Shiota, S. Miwa, and Y. Suzuki, *Spin-Orbit Torque in a Bulk Perpendicular Magnetic Anisotropy Pd/FePd/MgO System*, Sci. Rep. **4**, 6548 (2014).

[122] A. P. Mihai, J. P. Attané, L. Vila, C. Beigné, J. C. Pillet, and A. Marty, *Magnetization Reversal Dominated by Domain Wall Pinning in FePt Based Spin Valves*, Appl. Phys. Lett. **94**, 122509 (2009).

[123] J. P. Attané, D. Ravelosona, a. Marty, Y. Samson, and C. Chappert, *Thermally Activated Depinning of a Narrow Domain Wall from a Single Defect*, Phys. Rev. Lett. **96**, 1 (2006).

[124] C. Burrowes, a. P. Mihai, D. Ravelosona, J.-V. Kim, C. Chappert, L. Vila, a. Marty, Y. Samson, F. Garcia-Sanchez, L. D. Buda-Prejbeanu, I. Tudosa, E. E. Fullerton, and J.-P. Attané, *Non-Adiabatic Spin-Torques in Narrow Magnetic Domain Walls*, Nat. Phys. **6**, 17 (2010).

[125] L. Qian, K. Wang, Y. Zheng, and G. Xiao, *Spin Hall Effect in the α and β Phases of T Ax W1-x Alloys*, Phys. Rev. B **102**, 094438 (2020).

[126] Q. Hao and G. Xiao, *Giant Spin Hall Effect and Switching Induced by Spin-Transfer Torque in a W/Co40Fe40 B20/MgO Structure with Perpendicular Magnetic Anisotropy*, Phys. Rev. Appl. **3**, 034009 (2015).

[127] A. Hassdenteufel, B. Hebler, C. Schubert, A. Liebig, M. Teich, M. Helm, M. Aeschlimann, M. Albrecht, and R. Bratschitsch, *Thermally Assisted All-Optical Helicity Dependent Magnetic Switching in Amorphous Fe100-XTbx Alloy Films*, Adv. Mater. **25**, 3122 (2013).

[128] S. Alebrand, M. Gottwald, M. Hehn, D. Steil, M. Cinchetti, D. Lacour, E. E. Fullerton, M. Aeschlimann, and S. Mangin, *Light-Induced Magnetization Reversal of High-Anisotropy TbCo Alloy Films*, Appl. Phys. Lett. **101**, (2012).

[129] X. Liu, a. Morisako, H. Sakurai, Y. Sakurai, M. Itou, and a. Koizumi, *Perpendicular Magnetic Anisotropy in Sputtered Amorphous TbFeCo Films*, J. Magn. Magn. Mater. **310**, 1744 (2007).

[130] T. Rahman, X. Liu, A. Morisako, and M. Matsumoto, *TbFeCo Film with W Underlayer and Overlayer for Perpendicular Magnetic Recording*, J. Magn. Magn. Mater. **287**, 250 (2005).

[131] S. Q. Yin, X. Q. Li, X. G. Xu, J. Miao, and Y. Jiang, *Effect of Ta Underlayer on Perpendicular Anisotropy of TbFeCo Films*, IEEE Trans. Magn. **47**, 3129 (2011).

[132] N. Nagaosa, S. Onoda, a. H. MacDonald, and N. P. Ong, *Anomalous Hall Effect*, Rev. Mod. Phys. **82**, 1539 (2010).

[133] N. Anuniwat, M. Ding, S. J. Poon, S. a. Wolf, and J. Lu, *Strain-Induced Enhancement of Coercivity in Amorphous TbFeCo Films*, J. Appl. Phys. **113**, 043905 (2013).

[134] N. Perez, E. Martinez, L. Torres, S.-H. Woo, S. Emori, and G. S. D. Beach, *Chiral Magnetization Textures Stabilized by the Dzyaloshinskii-Moriya Interaction during Spin-Orbit Torque Switching*, Appl. Phys. Lett. **104**, 092403 (2014).

[135] N. Roschewsky, C.-H. Lambert, and S. Salahuddin, *Spin-Orbit Torque Switching of Ultralarge-Thickness Ferrimagnetic GdFeCo*, Phys. Rev. B **96**, 064406 (2017).

[136] Z. Zhao, A. K. Smith, M. Jamali, and J.-P. Wang, *External-Field-Free Spin Hall Switching of Perpendicular Magnetic Nanopillar with a Dipole-Coupled Composite Structure*, ArXiv:1603.09624v2 (2017).

[137] Z. Zhao, A. K. Smith, M. Jamali, and J. Wang, *External-Field-Free Spin Hall Switching of Perpendicular Magnetic Nanopillar with a Dipole-Coupled Composite Structure*, Adv. Electron. Mater. **6**, 1901368 (2020).

[138] H. Meng and J.-P. Wang, *Spin Transfer in Nanomagnetic Devices with Perpendicular Anisotropy*, Appl. Phys. Lett. **88**, 172506 (2006).

[139] G. Yu, P. Upadhyaya, Y. Fan, J. G. Alzate, W. Jiang, K. L. Wong, S. Takei, S. a Bender, L.-T. Chang, Y. Jiang, M. Lang, J. Tang, Y. Wang, Y. Tserkovnyak, P. K. Amiri, and K. L. Wang, *Switching of Perpendicular Magnetization by Spin–Orbit Torques in the Absence of External Magnetic Fields*, Nat. Nanotechnol. **9**, 548 (2014).

[140] S. Fukami, C. Zhang, S. DuttaGupta, A. Kurenkov, and H. Ohno, *Magnetization Switching by Spin–Orbit Torque in an Antiferromagnet–Ferromagnet Bilayer System*, Nat. Mater. **15**, 535 (2016).

[141] G. Yu, L.-T. Chang, M. Akyol, P. Upadhyaya, C. He, X. Li, K. L. Wong, P. K. Amiri, and K. L. Wang, *Current-Driven Perpendicular Magnetization Switching in Ta/CoFeB/[TaO x or MgO/TaO x] Films with Lateral Structural Asymmetry*, Appl. Phys. Lett. **105**, 102411 (2014).

[142] M. Akyol, G. Yu, J. G. Alzate, P. Upadhyaya, X. Li, K. L. Wong, A. Ekicibil, P. Khalili Amiri, and K. L. Wang, *Current-Induced Spin-Orbit Torque Switching of Perpendicularly Magnetized Hf|CoFeB|MgO and Hf|CoFeB|TaO x Structures*, Appl. Phys. Lett. **106**, 162409 (2015).

[143] L. You, O. Lee, D. Bhowmik, D. Labanowski, J. Hong, J. Bokor, and S. Salahuddin, *Switching of Perpendicularly Polarized Nanomagnets with Spin Orbit Torque without an External Magnetic Field by Engineering a Tilted Anisotropy*, Proc. Natl. Acad. Sci. **112**, 10310 (2015).

[144] J. Torrejon, F. Garcia-Sanchez, T. Taniguchi, J. Sinha, S. Mitani, J.-V. Kim, and M. Hayashi, *Current-Driven Asymmetric Magnetization Switching in Perpendicularly Magnetized CoFeB/MgO Heterostructures*, Phys. Rev. B **91**, 214434 (2015).

[145] C.-F. Pai, M. Mann, A. J. Tan, and G. S. D. Beach, *Determination of Spin Torque Efficiencies in Heterostructures with Perpendicular Magnetic Anisotropy*, Phys. Rev. B **93**, 144409 (2016).

[146] Y.-C. Lau, D. Betto, K. Rode, J. M. D. Coey, and P. Stamenov, *Spin–Orbit Torque Switching without an External Field Using Interlayer Exchange Coupling*, Nat. Nanotechnol. **11**, 758 (2016).

[147] A. van den Brink, G. Vermijs, A. Solignac, J. Koo, J. T. Kohlhepp, H. J. M. Swagten, and B. Koopmans, *Field-Free Magnetization Reversal by Spin-Hall Effect and Exchange Bias*, Nat. Commun. **7**, 10854 (2016).

[148] Y.-W. Oh, S.-H. Chris Baek, Y. M. Kim, H. Y. Lee, K.-D. Lee, C.-G. Yang, E.-S. Park, K.-S. Lee, K.-W. Kim, G. Go, J.-R. Jeong, B.-C. Min, H.-W. Lee, K.-J. Lee, and B.-G. Park, *Field-Free Switching of Perpendicular Magnetization through Spin–Orbit Torque in Antiferromagnet/Ferromagnet/Oxide Structures*, Nat. Nanotechnol. **11**, 878 (2016).

[149] W. J. Kong, Y. R. Ji, X. Zhang, H. Wu, Q. T. Zhang, Z. H. Yuan, C. H. Wan, X. F. Han, T. Yu, K. Fukuda, H. Naganuma, and M.-J. Tung, *Field-Free Spin Hall Effect Driven Magnetization Switching in Pd/Co/IrMn Exchange Coupling System*, Appl. Phys. Lett. **109**, 132402 (2016).

[150] S. A. Razavi, D. Wu, G. Yu, Y.-C. Lau, K. L. Wong, W. Zhu, C. He, Z. Zhang, J. M. D. Coey, P. Stamenov, P. Khalili Amiri, and K. L. Wang, *Joule Heating Effect on Field-Free Magnetization Switching by Spin-Orbit Torque in Exchange-Biased Systems*, Phys. Rev. Appl. **7**, 024023 (2017).

[151] J.-Y. Chen, M. DC, D. Zhang, Z. Zhao, M. Li, and J.-P. Wang, *Field-Free Spin-Orbit Torque Switching of Composite Perpendicular CoFeB/Gd/CoFeB Layers Utilized for Three-Terminal Magnetic Tunnel Junctions*, Appl. Phys. Lett. **111**, 012402 (2017).

[152] X. Wang, C. Wan, W. Kong, X. Zhang, Y. Xing, C. Fang, B. Tao, W. Yang, L. Huang, H. Wu, M. Irfan, and X. Han, *Field-Free Programmable Spin Logics via Chirality-Reversible Spin-Orbit Torque Switching*, Adv. Mater. **30**, 1801318 (2018).

[153] S. H. C. Baek, V. P. Amin, Y. W. Oh, G. Go, S. J. Lee, G. H. Lee, K. J. Kim, M. D. Stiles, B. G. Park, and K. J. Lee, *Spin Currents and Spin-Orbit Torques in Ferromagnetic Trilayers*, Nat. Mater. **17**, 509 (2018).

[154] Q. Ma, Y. Li, D. B. Gopman, Y. P. Kabanov, R. D. Shull, and C. L. Chien, *Switching a Perpendicular Ferromagnetic Layer by Competing Spin Currents*, Phys. Rev. Lett. **120**, 117703 (2018).

[155] K. Cai, M. Yang, H. Ju, S. Wang, Y. Ji, B. Li, K. W. Edmonds, Y. Sheng, B. Zhang, N. Zhang, S. Liu, H. Zheng, and K. Wang, *Electric Field Control of Deterministic Current-Induced Magnetization Switching in a Hybrid Ferromagnetic/Ferroelectric Structure*, Nat. Mater. **16**, 712 (2017).

[156] M. Donahue and D. Porter, OOMMF User's Guide, 1999.

[157] A. Vanhaverbeke, A. Bischof, and R. Allenspach, *Control of Domain Wall Polarity by Current Pulses*, Phys. Rev. Lett. **101**, 107202 (2008).

[158] K. Garello, C. O. Avci, I. M. Miron, M. Baumgartner, A. Ghosh, S. Auffret, O. Boulle, G. Gaudin, and P. Gambardella, *Ultrafast Magnetization Switching by Spin-Orbit Torques*, Appl. Phys. Lett. **105**, 212402 (2014).

[159] C. Zhang, S. Fukami, H. Sato, F. Matsukura, and H. Ohno, *Spin-Orbit Torque Induced Magnetization Switching in Nano-Scale Ta/CoFeB/MgO*, Appl. Phys. Lett. **107**, 012401 (2015).

[160] O. J. Lee, L. Q. Liu, C. F. Pai, Y. Li, H. W. Tseng, P. G. Gowtham, J. P. Park, D. C. Ralph, and R. a. Buhrman, *Central Role of Domain Wall Depinning for Perpendicular Magnetization Switching Driven by Spin Torque from the Spin Hall Effect*, Phys. Rev. B **89**, 024418 (2014).

[161] G. Finocchio, M. Carpentieri, E. Martinez, and B. Azzerboni, *Switching of a Single Ferromagnetic Layer Driven by Spin Hall Effect*, Appl. Phys. Lett. **102**, 212410 (2013).

[162] D. B. Carlton, N. C. Emley, E. Tuchfeld, and J. Bokor, *Simulation Studies of Nanomagnet-Based Logic Architecture*, Nano Lett. **8**, 4173 (2008).

[163] A. Thiaville, S. Rohart, É. Jué, V. Cros, and A. Fert, *Dynamics of Dzyaloshinskii Domain Walls in Ultrathin Magnetic Films*, Europhys. Lett. **100**, 57002 (2012).

[164] K. S. Ryu, L. Thomas, S.-H. Yang, and S. S. P. Parkin, *Chiral Spin Torque at Magnetic Domain Walls.*, Nat. Nanotechnol. **8**, 527 (2013).

[165] A. Fernández-Pacheco, E. Vedmedenko, F. Ummelen, R. Mansell, D. Petit, and R. P. Cowburn, *Symmetry-Breaking Interlayer Dzyaloshinskii–Moriya Interactions in Synthetic Antiferromagnets*, Nat. Mater. **18**, 679 (2019).

[166] D. S. Han, K. Lee, J. P. Hanke, Y. Mokrousov, K. W. Kim, W. Yoo, Y. L. W. van Hees, T. W. Kim, R. Lavrijsen, C. Y. You, H. J. M. Swagten, M. H. Jung, and M. Kläui, *Long-Range Chiral Exchange Interaction in Synthetic Antiferromagnets*, Nat. Mater. **18**, 703 (2019).

[167] M. Gajek, J. J. Nowak, J. Z. Sun, P. L. Trouilloud, E. J. O'Sullivan, D. W. Abraham, M. C. Gaidis, G. Hu, S. Brown, Y. Zhu, R. P. Robertazzi, W. J. Gallagher, and D. C. Worledge, *Spin Torque Switching of 20 Nm Magnetic Tunnel Junctions with Perpendicular Anisotropy*, Appl. Phys. Lett. **100**, 10 (2012).

[168] D. Bhowmik, L. You, and S. Salahuddin, *Spin Hall Effect Clocking of Nanomagnetic Logic without a Magnetic Field.*, Nat. Nanotechnol. **9**, 59 (2014).

[169] J. Allibe, S. Fusil, K. Bouzehouane, C. Daumont, D. Sando, E. Jacquet, C. Deranlot, M. Bibes, and A. Barthélémy, *Room Temperature Electrical Manipulation of Giant Magnetoresistance in Spin Valves Exchange-Biased with BiFeO3.*, Nano Lett. **12**, 1141 (2012).

[170] M. Bibes and A. Barthélémy, *Towards a Magnetoelectric Memory Out of the Scalar Sand Box*, Nature **7**, 425 (2008).

[171] W.-G. Wang, M. Li, S. Hageman, and C. L. Chien, *Electric-Field-Assisted Switching in Magnetic Tunnel Junctions.*, Nat. Mater. **11**, 64 (2012).

[172] P. K. Amiri and K. L. Wang, *Voltage-Controlled Magnetic Anisotropy in Spintronic Devices*, Spin **02**, 1240002 (2012).

[173] F. Matsukura, Y. Tokura, and H. Ohno, *Control of Magnetism by Electric Fields.*, Nat. Nanotechnol. **10**, 209 (2015).

[174] T. Brintlinger, S.-H. Lim, K. H. Baloch, P. Alexander, Y. Qi, J. Barry, J. Melngailis, L. Salamanca-Riba, I. Takeuchi, and J. Cumings, *In Situ Observation of Reversible Nanomagnetic Switching Induced by Electric Fields.*, Nano Lett. **10**, 1219 (2010).

[175] M. Liu, J. Lou, S. Li, and N. X. Sun, *E-Field Control of Exchange Bias and Deterministic Magnetization Switching in AFM/FM/FE Multiferroic Heterostructures*, Adv. Funct. Mater. **21**, 2593 (2011).

[176] Y. Chen, T. Fitchorov, C. Vittoria, and V. G. Harris, *Electrically Controlled Magnetization Switching in a Multiferroic Heterostructure*, Appl. Phys. Lett. **97**, 052502 (2010).

[177] S. Zhang, Y. Zhao, X. Xiao, Y. Wu, S. Rizwan, L. Yang, P. Li, J. Wang, M. Zhu, H. Zhang, X. Jin, and X. Han, *Giant Electrical Modulation of Magnetization in Co40Fe40B20/Pb(Mg1/3Nb2/3)0.7Ti0.3O3(011) Heterostructure.*, Sci. Rep. **4**, 3727 (2014).

[178] T. Jin, L. Hao, J. Cao, M. Liu, H. Dang, Y. Wang, D. Wu, J. Bai, and F. Wei, *Electric Field Control of Anisotropy and Magnetization Switching in CoFe and CoNi Thin Films for Magnetoelectric Memory Devices*, Appl. Phys. Express **7**, 043002 (2014).

[179] M. Buzzi, R. V. Chopdekar, J. L. Hockel, A. Bur, T. Wu, N. Pilet, P. Warnicke, G. P. Carman, L. J. Heyderman, and F. Nolting, *Single Domain Spin Manipulation by Electric Fields in Strain Coupled Artificial Multiferroic Nanostructures*, Phys. Rev. Lett. **111**, 027204 (2013).

[180] N. D'Souza, M. S. Fashami, S. Bandyopadhyay, and J. Atulasimha, *Experimental Clocking of Nanomagnets with Strain for Ultralow Power Boolean Logic*, Nano Lett. **16**, 1069 (2016).

[181] H. Ahmad, J. Atulasimha, and S. Bandyopadhyay, *Reversible Strain-Induced Magnetization Switching in FeGa Nanomagnets: Pathway to a Rewritable, Non-Volatile, Non-Toggle, Straintronic Memory Cell for Extremely Low Energy Operation*, Sci. Rep. **5**, 18264 (2015).

[182] J. Cui, C. Y. Liang, E. A. Paisley, A. Sepulveda, J. F. Ihlefeld, G. P. Carman, and C. S. Lynch, *Generation of Localized Strain in a Thin Film Piezoelectric to Control Individual Magnetoelectric Heterostructures*, Appl. Phys. Lett. **107**, 092903 (2015).

[183] K. Roy, S. Bandyopadhyay, and J. Atulasimha, *Energy Dissipation and Switching Delay in Stress-Induced Switching of Multiferroic Nanomagnets in the Presence of Thermal Fluctuations*, J. Appl. Phys. **112**, 023914 (2012).

[184] A. K. Biswas, S. Bandyopadhyay, and J. Atulasimha, *Energy-Efficient Magnetoelastic Non-Volatile Memory*, Appl. Phys. Lett. **104**, 232403 (2014).

[185] K. Roy, S. Bandyopadhyay, and J. Atulasimha, *Hybrid Spintronics and Straintronics: A Magnetic Technology for Ultra Low Energy Computing and Signal Processing*, Appl. Phys. Lett. **99**, 063108 (2011).

[186] P. Li, A. Chen, D. Li, Y. Zhao, S. Zhang, L. Yang, Y. Liu, M. Zhu, H. Zhang, and X. Han, *Electric Field Manipulation of Magnetization Rotation and Tunneling Magnetoresistance of Magnetic Tunnel Junctions at Room Temperature.*, Adv. Mater. **26**, 4320 (2014).

[187] C.-Y. Liang, S. M. Keller, A. E. Sepulveda, W.-Y. Sun, J. Cui, C. S. Lynch, and G. P. Carman, *Electrical Control of a Single Magnetoelastic Domain Structure on a Clamped Piezoelectric Thin Film—Analysis*, J. Appl. Phys. **116**, 123909 (2014).

[188] J. Cui, J. L. Hockel, P. K. Nordeen, D. M. Pisani, C. Liang, G. P. Carman, and C. S. Lynch, *A Method to Control Magnetism in Individual Strain-Mediated Magnetoelectric Islands*, Appl. Phys. Lett. **103**, 232905 (2013).

[189] Z. Wang, Y. Wang, W. Ge, J. Li, and D. Viehland, *Volatile and Nonvolatile Magnetic Easy-Axis Rotation in Epitaxial Ferromagnetic Thin Films on Ferroelectric Single Crystal Substrates*, Appl. Phys. Lett. **103**, 132909 (2013).

[190] Z. Zhao, M. Jamali, N. D'Souza, D. Zhang, S. Bandyopadhyay, J. Atulasimha, and J.-P. Wang, *Giant Voltage Manipulation of MgO-Based Magnetic Tunnel Junctions via Localized Anisotropic Strain: A Potential Pathway to Ultra-Energy-Efficient Memory Technology*, Appl. Phys. Lett. **109**, 092403 (2016).

[191] C. Thiele, K. Dörr, O. Bilani, J. Rödel, and L. Schultz, *Influence of Strain on the Magnetization and Magnetoelectric Effect in <math Display="inline"> <mrow> <msub> <mi Mathvariant="normal">La</Mi> <mn>0.7</Mn> </Msub> <msub> <mi>A</Mi> <mn>0.3</Mn> </Msub> <mi Mathvariant="normal">Mn</Mi> <msub> <mi Mathvaria*, Phys. Rev. B **75**, 054408 (2007).

[192] N. Lei, T. Devolder, G. Agnus, P. Aubert, L. Daniel, J.-V. Kim, W. Zhao, T. Trypiniotis, R. P. Cowburn, C. Chappert, D. Ravelosona, and P. Lecoeur, *Strain-Controlled Magnetic Domain Wall Propagation in Hybrid Piezoelectric/Ferromagnetic Structures.*, Nat. Commun. **4**, 1378 (2013).

[193] L. M. Loong, X. Qiu, Z. P. Neo, P. Deorani, Y. Wu, C. S. Bhatia, M. Saeys, and H. Yang, *Strain-Enhanced Tunneling Magnetoresistance in MgO Magnetic Tunnel Junctions.*, Sci. Rep. **4**, 6505 (2014).

[194] M. Liu, S. Li, O. Obi, J. Lou, S. Rand, and N. X. Sun, *Electric Field Modulation of Magnetoresistance in Multiferroic Heterostructures for Ultralow Power Electronics*, Appl. Phys. Lett. **98**, 222509 (2011).

[195] H. Cao, V. H. Schmidt, R. Zhang, W. Cao, and H. Luo, *Elastic, Piezoelectric, and Dielectric Properties of 0.58Pb(Mg[Sub 1/3]Nb[Sub 2/3])O[Sub 3]-0.42PbTiO[Sub 3] Single Crystal*, J. Appl. Phys. **96**, 549 (2004).

[196] D. Wang, C. Nordman, Z. Qian, J. M. Daughton, and J. Myers, *Magnetostriction Effect of Amorphous CoFeB Thin Films and Application in Spin-Dependent Tunnel Junctions*, J. Appl. Phys. **97**, 10C906 (2005).

[197] A. V Khvalkovskiy, D. Apalkov, S. Watts, R. Chepulskii, R. S. Beach, A. Ong, X. Tang, A. Driskill-Smith, W. H. Butler, P. B. Visscher, D. Lottis, E. Chen, V. Nikitin, and M. Krounbi, *Basic Principles of STT-MRAM Cell Operation in Memory Arrays*, J. Phys. D. Appl. Phys. **46**, 139601 (2013).

[198] A. N. Bogdanov, A. V. Zhuravlev, and U. K. Rößler, *Spin-Flop Transition in Uniaxial Antiferromagnets: Magnetic Phases, Reorientation Effects, and Multidomain States*, Phys. Rev. B **75**, 094425 (2007).

[199] O. Gomonay, T. Jungwirth, and J. Sinova, *High Antiferromagnetic Domain Wall Velocity Induced by Néel Spin-Orbit Torques*, Phys. Rev. Lett. **117**, 017202 (2016).

[200] P. E. Roy, R. M. Otxoa, and J. Wunderlich, *Robust Picosecond Writing of a Layered Antiferromagnet by Staggered Spin-Orbit Fields*, Phys. Rev. B **94**, 014439 (2016).

[201] T. Jungwirth, X. Marti, P. Wadley, and J. Wunderlich, *Antiferromagnetic Spintronics*, Nat. Nanotechnol. **11**, 231 (2016).

[202] K. Olejník, T. Seifert, Z. Kašpar, V. Novák, P. Wadley, R. P. Campion, M. Baumgartner, P. Gambardella, P. Nemec, J. Wunderlich, J. Sinova, P. Kužel, M. Müller, T. Kampfrath, and T. Jungwirth, *Terahertz Electrical Writing Speed in an Antiferromagnetic Memory*, Sci. Adv. **4**, eaar3566 (2018).

[203] P. Bowlan, S. A. Trugman, D. A. Yarotski, A. J. Taylor, and R. P. Prasankumar, *Using Ultrashort Terahertz Pulses to Directly Probe Spin Dynamics in Insulating Antiferromagnets*, J. Phys. D. Appl. Phys. **51**, 194003 (2018).

[204] V. Baltz, A. Manchon, M. Tsoi, T. Moriyama, T. Ono, and Y. Tserkovnyak, *Antiferromagnetic Spintronics*, Rev. Mod. Phys. **90**, 015005 (2018).

[205] H. Seinige, M. Williamson, S. Shen, C. Wang, G. Cao, J. Zhou, J. B. Goodenough, and M. Tsoi, *Electrically Tunable Transport and High-Frequency Dynamics in Sr3Ir2O7*, Phys. Rev. B **94**, 214434 (2016).

[206] G. R. Hoogeboom, A. Aqeel, T. Kuschel, T. T. M. Palstra, and B. J. van Wees, *Negative Spin Hall Magnetoresistance of Pt on the Bulk Easy-Plane Antiferromagnet NiO*, Appl. Phys. Lett. **111**, 052409 (2017).

[207] A. A. Sapozhnik, R. Abrudan, Y. Skourski, M. Jourdan, H. Zabel, M. Kläui, and H.-J. Elmers, *Manipulation of Antiferromagnetic Domain Distribution in Mn $_2$ Au by Ultrahigh Magnetic Fields and by Strain*, Phys. Status Solidi - Rapid Res. Lett. **11**, 1600438 (2017).

[208] X. Marti, I. Fina, C. Frontera, J. Liu, P. Wadley, Q. He, R. J. Paull, J. D. Clarkson, J. Kudrnovský, I. Turek, J. Kuneš, D. Yi, J. H. Chu, C. T. Nelson, L. You, E. Arenholz, S. Salahuddin, J. Fontcuberta, T. Jungwirth, and R. Ramesh, *Room-Temperature Antiferromagnetic Memory Resistor*, Nat. Mater. **13**, 367 (2014).

[209] D. Petti, E. Albisetti, H. Reichlová, J. Gazquez, M. Varela, M. Molina-Ruiz, A. F. Lopeandía, K. Olejník, V. Novák, I. Fina, B. Dkhil, J. Hayakawa, X. Marti, J. Wunderlich, T. Jungwirth, and R. Bertacco, *Storing Magnetic Information in IrMn/MgO/Ta Tunnel Junctions via Field-Cooling*, Appl. Phys. Lett. **102**, 192404 (2013).

[210] B. G. Park, J. Wunderlich, X. Martí, V. Holý, Y. Kurosaki, M. Yamada, H. Yamamoto, A. Nishide, J. Hayakawa, H. Takahashi, A. B. Shick, and T. Jungwirth, *A Spin-Valve-like Magnetoresistance of an Antiferromagnet-Based Tunnel Junction*, Nat. Mater. **10**, 347 (2011).

[211] Y. Y. Wang, C. Song, B. Cui, G. Y. Wang, F. Zeng, and F. Pan, *Room-Temperature Perpendicular Exchange Coupling and Tunneling Anisotropic Magnetoresistance in an Antiferromagnet-Based Tunnel Junction*, Phys. Rev. Lett. **109**, 137201 (2012).

[212] A. Scholl, M. Liberati, E. Arenholz, H. Ohldag, and J. Stöhr, *Creation of an Antiferromagnetic Exchange Spring*, Phys. Rev. Lett. **92**, 247201 (2004).

[213] X. Martí, B. G. Park, J. Wunderlich, H. Reichlová, Y. Kurosaki, M. Yamada, H. Yamamoto, A. Nishide, J. Hayakawa, H. Takahashi, and T. Jungwirth, *Electrical Measurement of Antiferromagnetic Moments in Exchange-Coupled IrMn/NiFe Stacks*, Phys. Rev. Lett. **108**, 017201 (2012).

[214] A. V. Kimel, A. Kirilyuk, A. Tsvetkov, R. V. Pisarev, and T. Rasing, *Laser-Induced Ultrafast Spin Reorientation in the Antiferromagnet TmFeO3*, Nature **429**, 850 (2004).

[215] A. V. Kimel, C. D. Stanciu, P. A. Usachev, R. V. Pisarev, V. N. Gridnev, A. Kirilyuk, and T. Rasing, *Optical Excitation of Antiferromagnetic Resonance in TmFeO3*, Phys. Rev. B **74**, 060403 (2006).

[216] R. V. Mikhaylovskiy, E. Hendry, V. V. Kruglyak, R. V. Pisarev, T. Rasing, and A. V. Kimel, *Terahertz Emission Spectroscopy of Laser-Induced Spin Dynamics in TmFeO3 and ErFeO3 Orthoferrites*, Phys. Rev. B **90**, 184405 (2014).

[217] M. Fiebig, K. Miyano, Y. Tokura, and Y. Tomioka, *Visualization of the Local Insulator-Metal Transition in Pr0.7Ca0.3MnO3*, Science **280**, 1925 (1998).

[218] D. Afanasiev, B. A. Ivanov, A. Kirilyuk, T. Rasing, R. V. Pisarev, and A. V. Kimel, *Control of the Ultrafast Photoinduced Magnetization across the Morin Transition in DyFeO3*, Phys. Rev. Lett. **116**, 097401 (2016).

[219] A. V. Kimel, B. A. Ivanov, R. V. Pisarev, P. A. Usachev, A. Kirilyuk, and T. Rasing, *Inertia-Driven Spin Switching in Antiferromagnets*, Nat. Phys. **5**, 727 (2009).

[220] T. Kampfrath, A. Sell, G. Klatt, A. Pashkin, S. Mährlein, T. Dekorsy, M. Wolf, M. Fiebig, A. Leitenstorfer, and R. Huber, *Coherent Terahertz Control of Antiferromagnetic Spin Waves*, Nat. Photonics **5**, 31 (2011).

[221] S. Baierl, M. Hohenleutner, T. Kampfrath, A. K. Zvezdin, A. V. Kimel, R. Huber, and R. V. Mikhaylovskiy, *Nonlinear Spin Control by Terahertz-Driven Anisotropy Fields*, Nat. Photonics **10**, 715 (2016).

[222] Y. Mukai, H. Hirori, T. Yamamoto, H. Kageyama, and K. Tanaka, *Nonlinear Magnetization Dynamics of Antiferromagnetic Spin Resonance Induced by Intense Terahertz Magnetic Field*, New J. Phys. **18**, 013045 (2016).

[223] S. Baierl, J. H. Mentink, M. Hohenleutner, L. Braun, T. M. Do, C. Lange, A. Sell, M. Fiebig, G. Woltersdorf, T. Kampfrath, and R. Huber, *Terahertz-Driven Nonlinear Spin Response of Antiferromagnetic Nickel Oxide*, Phys. Rev. Lett. **117**, 197201 (2016).

[224] T. Kubacka, J. A. Johnson, M. C. Hoffmann, C. Vicario, S. De Jong, P. Beaud, S. Grübel, S. W. Huang, L. Huber, L. Patthey, Y. D. Chuang, J. J. Turner, G. L. Dakovski, W. S. Lee, M. P. Minitti, W. Schlotter, R. G. Moore, C. P. Hauri, S. M. Koohpayeh, V. Scagnoli, G. Ingold, S. L. Johnson, and U. Staub, *Large-Amplitude Spin Dynamics Driven by a THz Pulse in Resonance with an Electromagnon*, Science **343**, 1333 (2014).

[225] T. Satoh, R. Iida, T. Higuchi, M. Fiebig, and T. Shimura, *Writing and Reading of an Arbitrary Optical Polarization State in an Antiferromagnet*, Nat. Photonics **9**, 25 (2015).

[226] C. Bordel, J. Juraszek, D. W. Cooke, C. Baldasseroni, S. Mankovsky, J. Minár, H. Ebert, S. Moyerman, E. E. Fullerton, and F. Hellman, *Fe Spin Reorientation across the Metamagnetic Transition in Strained FeRh Thin Films*, Phys. Rev. Lett. **109**, 117201 (2012).

[227] R. O. Cherifi, V. Ivanovskaya, L. C. Phillips, A. Zobelli, I. C. Infante, E. Jacquet, V. Garcia, S. Fusil, P. R. Briddon, N. Guiblin, A. Mougin, A. A. Ünal, F. Kronast,

S. Valencia, B. Dkhil, A. Barthélémy, and M. Bibes, *Electric-Field Control of Magnetic Order above Room Temperature*, Nat. Mater. **13**, 345 (2014).

[228] T. Zhao, A. Scholl, F. Zavaliche, K. Lee, M. Barry, A. Doran, M. P. Cruz, Y. H. Chu, C. Ederer, N. A. Spaldin, R. R. Das, D. M. Kim, S. H. Baek, C. B. Eom, and R. Ramesh, *Electrical Control of Antiferromagnetic Domains in Multiferroic BiFeO 3 Films at Room Temperature*, Nat. Mater. **5**, 823 (2006).

[229] D. Lebeugle, D. Colson, A. Forget, M. Viret, A. M. Bataille, and A. Gukasov, *Electric-Field-Induced Spin Flop in BiFeO3 Single Crystals at Room Temperature*, Phys. Rev. Lett. **100**, 227602 (2008).

[230] T. Kosub, M. Kopte, R. Hühne, P. Appel, B. Shields, P. Maletinsky, R. Hübner, M. O. Liedke, J. Fassbender, O. G. Schmidt, and D. Makarov, *Purely Antiferromagnetic Magnetoelectric Random Access Memory*, Nat. Commun. **8**, 13985 (2017).

[231] Z. Zhao, W. Echtenkamp, M. Street, C. Binek, and J.-P. Wang, *Magnetoelectric Device Feasibility Demonstration — Voltage Control of Exchange Bias in Perpendicular Cr2]]>O*, in *2016 74th Annual Device Research Conference (DRC)* (IEEE, 2016), pp. 1–2.

[232] C. Song, Y. You, X. Chen, X. Zhou, Y. Wang, and F. Pan, *How to Manipulate Magnetic States of Antiferromagnets*, Nanotechnology **29**, 112001 (2018).

[233] P. Wadley, B. Howells, J. Elezny, C. Andrews, V. Hills, R. P. Campion, V. Novak, K. Olejnik, F. Maccherozzi, S. S. Dhesi, S. Y. Martin, T. Wagner, J. Wunderlich, F. Freimuth, Y. Mokrousov, J. Kune, J. S. Chauhan, M. J. Grzybowski, A. W. Rushforth, K. W. Edmonds, B. L. Gallagher, and T. Jungwirth, *Electrical Switching of an Antiferromagnet*, Science **351**, 587 (2016).

[234] M. Meinert, D. Graulich, and T. Matalla-Wagner, *Electrical Switching of Antiferromagnetic Mn2Au and the Role of Thermal Activation*, Phys. Rev. Appl. **9**, 064040 (2018).

[235] S. Y. Bodnar, L. Šmejkal, I. Turek, T. Jungwirth, O. Gomonay, J. Sinova, A. A. Sapozhnik, H.-J. Elmers, M. Kläui, and M. Jourdan, *Writing and Reading Antiferromagnetic Mn2Au by Néel Spin-Orbit Torques and Large Anisotropic Magnetoresistance*, Nat. Commun. **9**, 348 (2018).

[236] X. F. Zhou, J. Zhang, F. Li, X. Z. Chen, G. Y. Shi, Y. Z. Tan, Y. D. Gu, M. S. Saleem, H. Q. Wu, F. Pan, and C. Song, *Strong Orientation-Dependent Spin-Orbit Torque in Thin Films of the Antiferromagnet Mn2Au*, Phys. Rev. Appl. **9**, 054028 (2018).

[237] X. Z. Chen, R. Zarzuela, J. Zhang, C. Song, X. F. Zhou, G. Y. Shi, F. Li, H. A. Zhou, W. J. Jiang, F. Pan, and Y. Tserkovnyak, *Antidamping-Torque-Induced Switching in Biaxial Antiferromagnetic Insulators*, Phys. Rev. Lett. **120**, 207204 (2018).

[238] T. Moriyama, K. Oda, T. Ohkochi, M. Kimata, and T. Ono, *Spin Torque Control of*

Antiferromagnetic Moments in NiO, Sci. Rep. **8**, 14167 (2018).

[239] L. Baldrati, O. Gomonay, A. Ross, M. Filianina, R. Lebrun, R. Ramos, C. Leveille, F. Fuhrmann, T. R. Forrest, F. MacCherozzi, S. Valencia, F. Kronast, E. Saitoh, J. Sinova, and M. Klaüi, *Mechanism of Neél Order Switching in Antiferromagnetic Thin Films Revealed by Magnetotransport and Direct Imaging*, Phys. Rev. Lett. **123**, 177201 (2019).

[240] I. Gray, T. Moriyama, N. Sivadas, G. M. Stiehl, J. T. Heron, R. Need, B. J. Kirby, D. H. Low, K. C. Nowack, D. G. Schlom, D. C. Ralph, T. Ono, and G. D. Fuchs, *Spin Seebeck Imaging of Spin-Torque Switching in Antiferromagnetic Pt/NiO Heterostructures*, Phys. Rev. X **9**, 041016 (2019).

[241] P. Zhang, J. Finley, T. Safi, and L. Liu, *Quantitative Study on Current-Induced Effect in an Antiferromagnet Insulator/Pt Bilayer Film*, Phys. Rev. Lett. **123**, 247206 (2019).

[242] Y. Cheng, S. Yu, M. Zhu, J. Hwang, and F. Yang, *Electrical Switching of Tristate Antiferromagnetic Néel Order in α-Fe2 O3 Epitaxial Films*, Phys. Rev. Lett. **124**, 027202 (2020).

[243] M. Dunz, T. Matalla-Wagner, and M. Meinert, *Spin-Orbit Torque Induced Electrical Switching of Antiferromagnetic MnN*, Phys. Rev. Res. **2**, 013347 (2020).

[244] C. C. Chiang, S. Y. Huang, D. Qu, P. H. Wu, and C. L. Chien, *Absence of Evidence of Electrical Switching of the Antiferromagnetic Néel Vector*, Phys. Rev. Lett. **123**, 227203 (2019).

[245] A. Churikova, D. Bono, B. Neltner, A. Wittmann, L. Scipioni, A. Shepard, T. Newhouse-Illige, J. Greer, and G. S. D. Beach, *Non-Magnetic Origin of Spin Hall Magnetoresistance-like Signals in Pt Films and Epitaxial NiO/Pt Bilayers*, Appl. Phys. Lett. **116**, 022410 (2020).

[246] T. Matalla-Wagner, J.-M. Schmalhorst, G. Reiss, N. Tamura, and M. Meinert, *Resistive Contribution in Electrical-Switching Experiments with Antiferromagnets*, Phys. Rev. Res. **2**, 033077 (2020).

[247] M. Meinert, B. Büker, D. Graulich, and M. Dunz, *Large Exchange Bias in Polycrystalline MnN/CoFe Bilayers at Room Temperature*, Phys. Rev. B **92**, 144408 (2015).

[248] J. Liu, D. Zhang, K. Wu, X. Hang, and J. P. Wang, *Magnetic Field Enhanced Coercivity of Fe Nanoparticles Embedded in Antiferromagnetic MnN Films*, J. Phys. D. Appl. Phys. **53**, 035003 (2020).

[249] N. Schwartz, W. A. Reed, P. Polash, and M. H. Read, *Temperature Coefficient of Resistance of Beta-Tantalum Films and Mixtures with b.c.c.-Tantalum*, Thin Solid Films **14**, 333 (1972).

[250] Y. Seo, K. W. Kwon, X. Fong, and K. Roy, *High Performance and Energy-Efficient*

On-Chip Cache Using Dual Port (1R/1W) Spin-Orbit Torque MRAM, IEEE J. Emerg. Sel. Top. Circuits Syst. **6**, 293 (2016).

[251] J. J. Kan, C. Park, C. Ching, J. Ahn, Y. Xie, M. Pakala, and S. H. Kang, *A Study on Practically Unlimited Endurance of STT-MRAM*, IEEE Trans. Electron Devices **64**, 3639 (2017).

[252] F. Oboril, R. Bishnoi, M. Ebrahimi, and M. B. Tahoori, *Evaluation of Hybrid Memory Technologies Using SOT-MRAM for on-Chip Cache Hierarchy*, IEEE Trans. Comput. Des. Integr. Circuits Syst. **34**, 367 (2015).

[253] G. Prenat, K. Jabeur, P. Vanhauwaert, G. Di Pendina, F. Oboril, R. Bishnoi, M. Ebrahimi, N. Lamard, O. Boulle, K. Garello, J. Langer, B. Ocker, M. C. Cyrille, P. Gambardella, M. Tahoori, and G. Gaudin, *Ultra-Fast and High-Reliability SOT-MRAM: From Cache Replacement to Normally-Off Computing*, IEEE Trans. Multi-Scale Comput. Syst. **2**, 49 (2016).

Appendix A. Source Code of SOT Switching Macrospin Model

Here, I put the MATLAB codes of the macrospin model for the STT/SOT switching simulation described in Chapter 1. The simulation is based on the LLG equation, as expressed in Eq. (1-3) or Eq. (1-4).

Part 1: Illustration of torques

This part contains the code to plot the 3d vector diagram of torques, show both the directions and strengths of torques, as plotted in **Figure 1-4 (a)** and **Figure 1-5 (a)**.

```
% 3d vector diagram to show directions of spin torques

clc
clear all
tranparency=0.7;

r = 1;
th = 0:0.1*pi:pi;
phi = 0:0.1*pi:2*pi;
[th,phi]=meshgrid(th,phi);

x=r.*sin(th).*cos(phi);
y=r.*sin(th).*sin(phi);
z=r.*cos(th);

h = [0; 1; 0]; % unit vector of external field
s = [1; 0; 0]; % vector of spin polarization
mx=reshape(x,1,[]);
my=reshape(y,1,[]);
mz=reshape(z,1,[]);
m=[mx; my; mz];

torque_ext = zeros(3,length(mx));
torque_ad = zeros(3,length(mx));
torque_fl = zeros(3,length(mx));
```

```
for i = 1:length(mx)
    torque_ext(:,i) = -cross(m(:,i),h);
    torque_ad(:,i) = -cross(m(:,i),cross(m(:,i),s));
    torque_fl(:,i) = -cross(m(:,i),s);
end

figure
mesh(x,y,z,'EdgeColor',[0.7,0.7,0.7])
alpha(tranparency)
axis equal
hold on
xlabel('x','FontSize',12);
ylabel('y','FontSize',12);
zlabel('z','FontSize',12);
campos([9,11,4.8])  %'CameraPosition'
quiver3(mx,my,mz,torque_ext(1,:),torque_ext(2,:),torque_ext
(3,:), 'LineWidth',2)
title('Torque of external field H = Hy', 'FontSize',14)

figure
mesh(x,y,z,'EdgeColor',[0.7,0.7,0.7])
alpha(tranparency)
axis equal
hold on
xlabel('x','FontSize',12);
ylabel('y','FontSize',12);
zlabel('z','FontSize',12);
campos([9,11,4.8])  %'CameraPosition'
quiver3(mx,my,mz,torque_ad(1,:),torque_ad(2,:),torque_ad(3,
:), 'LineWidth',2)
title('Anti-damping Torque', 'FontSize',14)

figure
mesh(x,y,z,'EdgeColor',[0.7,0.7,0.7])
alpha(tranparency)
axis equal
hold on
xlabel('x','FontSize',12);
ylabel('y','FontSize',12);
zlabel('z','FontSize',12);
campos([9,11,4.8])  %'CameraPosition'
quiver3(mx,my,mz,torque_fl(1,:),torque_fl(2,:),torque_fl(3,
:), 'LineWidth',2)
title('Field-like Torque', 'FontSize',14)
```

Part 2: Macrospin model using the time-derivative form of LLG equation

The time-derivative form of LLG equation is expressed Eq. (1-3).

```
% Use time-derivative form of LLG equation.
% Use un-normalized form of LLG equation.
% dt should be smaller than 0.1e-12s,
% if dt is large, Error = dM/Ms is large, and results will
not converge.
% For example, if dt = 0.5e-12s, Error = dM/Ms > 5%
happens.

clear all

% define parameters:
gamma = 1.76e7;  %% Gyromagnetic ratio with unit rad/s-Oe
alph = 0.02; % damping constant
p = gamma;
q = gamma * alph;


Ms = 1185; % emu/cc
Hk = 20000; %%%%%%%%%%%%% amplitude of anisotropy field,
unit: Oe; Hk > 4 pi*Ms to preserve perpendicular
s = [-1; 0; 0];  % spin polarization
s = s/norm(s);
A = [0; 0; 1]; % A is the anisotropy axis
A = A/norm(A);
H = [000; -2000; 00]; %%%%%%%%%%%%%% external field

eta = 0.15; % spin polarization
J = 15*1e11; %%%%%%%%%%%%%%%%%%% charge current density,
unit: 1e4 A/m^2
h_bar = 1.054e-34; % plank constant, unit: m^2-kg/s
thickness = 1e-9; % unit: m
e_charge = 1.6e-19; % electron charge, unit: C = A*s
miu0 = 4*pi*1e-7;  % unit: H/m
Ms_SI = Ms * 1000;  % unit: A/m
gamma_SI = gamma*4*pi/1000; % unit: m/A/s
a = gamma_SI *
0.5*h_bar*eta*J/(miu0*Ms_SI*thickness*e_charge); %%%%%%%%%
%%%%%%%%% unit: 1/s
```

```
H_ad = a/gamma; % anti-damping effective field, unit: Oe
b = 0 * a;  %%%%%%%%%%%%%%%%%%%%%%%%%%%%%%%%%%%
% a = 0;

% define assignment:
t_max = 5e-9; %%%%%%%%%%%%%%%%%%%%%%%%%%%%%%%
dt = 0.05e-12;
t_step = t_max/dt;
t = 0:dt:t_max;

Mnorm = zeros(3,length(t)); % Mnorm is normalized
magnetization
M = zeros(3,length(t)); % M is unnormalized magnetization
dM = zeros(3,length(t));
ddM = zeros(3,length(t)); % ddM = dM/dt
theta = zeros(1,length(t)); % the angle between M and A,
theta = dot(A, Mnorm)
Nd = [0 0 0; 0 0 0; 0 0 4*pi]; % thin film with normal
along z
Hd = zeros(3,length(t)); % Demag field, Hd = -Nd * M
Han = zeros(3,length(t)); % anisotropy field, Han = Hk *
cos(theta) * A = Hk * (dot(A,Mnorm)) * A, since torque of
Han = Hk*M*cos(theta)*sin(theta)
Heff = zeros(3,length(t)); % Heff = Han + Hd + H
T_eff = zeros(3,length(t)); % Torque of H_eff
T_damp = zeros(3,length(t)); % Damping Torque
T_ad = zeros(3,length(t)); % Anti-damping torque
T_fl = zeros(3,length(t)); % field-like torque
Error = zeros(1,length(t));  % Error = dM/M should be small
enough at each step.

Mnorm(:,1) = [0; 0; 1];  %%%%%%%%%%%%%%%%%%%%%%%%%%%%%
Mnorm(:,1) = Mnorm(:,1)/norm(Mnorm(:,1));
M(:,1) = Ms*Mnorm(:,1);
dM(:,1) = [0; 0; 0];
theta(1) = acos(dot(A,Mnorm(:,1)));
Hd(:,1) = -Nd*M(:,1);
Han(:,1) = Hk*(dot(A,Mnorm(:,1)))*A;
Heff(:,1) = Hd(:,1) + Han(:,1) + H;
T_eff(:,1) = -cross(M(:,1),Heff(:,1))*dt;
T_damp(:,1) = [0; 0; 0];
T_ad(:,1) = -a*cross(Mnorm(:,1),cross(M(:,1),s))*dt/gamma;
T_fl(:,1) = -b*cross(M(:,1),s)*dt/gamma;
dM(:,1) = gamma * dt * (T_eff(:,1) + T_damp(:,1)/gamma +
T_ad(:,1) + T_fl(:,1));
```

```
ddM(:,1) = dM(:,1)/dt;
Error(1) = norm(dM(:,1))/norm(M(:,1));

flag = round(length(t)/10);
for i = 2:length(t);
    if mod(i,flag)==0
        fprintf('%d%% completed. \n', 10*i/flag)
    end
    M(:,i) = M(:,i-1) + dM(:,i-1);
    Mnorm(:,i) = M(:,i)/norm(M(:,i)); % keep M normalized
    M(:,i) = Ms*Mnorm(:,i);
    theta(i) = acos(dot(A,Mnorm(:,i)));
    Hd(:,i) = -Nd*M(:,i);
    Han(:,i) = Hk*(dot(A,Mnorm(:,i)))*A;
    Heff(:,i) = Hd(:,i) + Han(:,i) + H;
    T_eff(:,i) = -cross(M(:,i),Heff(:,i));
    T_damp(:,i) = alph*cross(Mnorm(:,i),ddM(:,i-1));  %
recurrence form
    T_ad(:,i) = -
a*cross(Mnorm(:,i),cross(M(:,i),s))/gamma;   %%%%%%%%%%%%%%
%%%%%%
    T_fl(:,i) = -b*cross(M(:,i),s)/gamma;
    dM(:,i) = gamma * dt * (T_eff(:,i) + T_damp(:,i)/gamma
+ T_ad(:,i) + T_fl(:,i));
    ddM(:,i) = dM(:,i)/dt;
    Error(i) = norm(dM(:,i))/norm(M(:,i));
end

figure
hold on
plot(t,Mnorm(1,:),'r.')
plot(t,Mnorm(2,:),'g.')
plot(t,Mnorm(3,:),'b.')
grid on
xlabel('Time (s)','FontSize',12);
ylabel('M/Ms','FontSize',12);
legend Mx My Mz


figure
plot(t,Error)
grid on

figure
[x y z]=sphere;
```

```
mesh(x,y,z,'EdgeColor',[0.9,0.9,0.9]);
alpha(0.3)  % set transparency
axis equal
hold on
plot3(Mnorm(1,:),Mnorm(2,:),Mnorm(3,:),'LineWidth',1.5)
xlabel('Mx/M','FontSize',12);
ylabel('My/M','FontSize',12);
zlabel('Mz/M','FontSize',12);
campos([9,11,4.8])  %'CameraPosition'
```

Part 3: Macrospin model using the cross-product form of LLG equation

The cross-product form (Landau-Lifshitz form) of LLG equation is expressed in Eq. (1-4). The simulation result using the cross-product form of LLG equation is the same as using the time-derivative form of LLG equation.

```
% Use cross-product form of LLG equation.
% Use un-normalized form of LLG equation.
% dt should be smaller than 0.1e-12s,
% if dt is large, Error = dM/Ms is large, and results will
not converge.
% For example, if dt = 0.5e-12s, Error = dM/Ms > 5%
happens.


clear all

% define parameters:
gamma = 1.76e7;  %% Gyromagnetic ratio with unit rad/s-Oe
alph = 0.02; % damping constant
p = gamma;
q = gamma * alph;


Ms = 1185; % emu/cc
Hk = 20000; %%%%%%%%%%%%%% amplitude of anisotropy field,
unit: Oe; Hk > 4pi*Ms to preserve perpendicular
s = [-1; 0; 0];  % spin polarization
A = [0; 0; 1]; % A is the anisotropy axis
H = [00; -2000; 00]; %%%%%%%%%%%%%%% external field
```

```
eta = 0.15; % spin polarization
J = 20e11; %%%%%%%%%%%%%%%%%%%% charge current density,
unit: 1e4 A/m^2
h_bar = 1.054e-34; % plank constant, unit: m^2-kg/s
thickness = 1e-9; % unit: m
e_charge = 1.6e-19; % electron charge, unit: C = A*s
miu0 = 4*pi*1e-7;  % unit: H/m
Ms_SI = Ms * 1000;  % unit: A/m
gamma_SI = gamma*4*pi/1000; % unit: m/A/s
a = gamma_SI *
0.5*h_bar*eta*J/(miu0*Ms_SI*thickness*e_charge); %%%%%%%%%%
%%%%%%%%% unit: 1/s
H_ad = a/gamma; % anti-damping effective field, unit: Oe
b = 0 * a;  %%%%%%%%%%%%%%%%%%%%%%%%%%%%%%%%%%%
% a = 0;

% define assignment:
t_max = 5e-9;  %%%%%%%%%%%%%%%%%%%%%%%%%%%%%%%
dt = 0.05e-12;
t_step = t_max/dt;
t = 0:dt:t_max;

Mnorm = zeros(3,length(t)); % Mnorm is normalized
magnetization
M = zeros(3,length(t)); % M is unnormalized magnetization
dM = zeros(3,length(t));
theta = zeros(1,length(t)); % the angle between M and A,
theta = dot(A, Mnorm)
Nd = [0 0 0; 0 0 0; 0 0 4*pi]; % thin film with normal
along z
Hd = zeros(3,length(t)); % Demag field, Hd = -Nd * M
Han = zeros(3,length(t)); % anisotropy field, Han = Hk *
cos(theta) * A = Hk * (dot(A,Mnorm)) * A, since torque of
Han = Hk*M*cos(theta)*sin(theta)
Heff = zeros(3,length(t)); % Heff = Han + Hd + H
T_eff = zeros(3,length(t)); % Torque of H_eff
T_damp = zeros(3,length(t)); % Damping Torque
T_ad = zeros(3,length(t)); % Anti-damping torque
T_fl = zeros(3,length(t)); % field-like torque
Error = zeros(1,length(t));  % Error = dM/M should be small
enough at each step.

Mnorm(:,1) = [0; 0.0; 1];  %%%%%%%%%%%%%%%%%%%%%%%%%%%%%
Mnorm(:,1) = Mnorm(:,1)/norm(Mnorm(:,1));
M(:,1) = Ms*Mnorm(:,1);
```

```
dM(:,1) = [0; 0; 0];
theta(1) = acos(dot(A,Mnorm(:,1)));
Hd(:,1) = -Nd*M(:,1);
Han(:,1) = Hk*(dot(A,Mnorm(:,1)))*A;
Heff(:,1) = Hd(:,1) + Han(:,1) + H;
T_eff(:,1) = -cross(M(:,1),Heff(:,1))*dt;
T_damp(:,1) = alph*cross(Mnorm(:,1),T_eff(:,1));
T_ad(:,1) = -
(a+alph*b)*cross(Mnorm(:,1),cross(M(:,1),s))*dt/gamma;
T_fl(:,1) = -(b+alph*a)*cross(M(:,1),s)*dt/gamma;
dM(:,1) = gamma / (1+alph^2) * dt * (T_eff(:,1) +
T_damp(:,1) + T_ad(:,1) + T_fl(:,1));
Error(1) = norm(dM(:,1))/norm(M(:,1));

flag = round(length(t)/10)
for i = 2:length(t);
    if mod(i,flag)==0
        fprintf('%d%% completed. \n', 10*i/flag)
    end
    M(:,i) = M(:,i-1) + dM(:,i-1);
    Mnorm(:,i) = M(:,i)/norm(M(:,i)); % keep M normalized
    M(:,i) = Ms*Mnorm(:,i);
    theta(i) = acos(dot(A,Mnorm(:,i)));
    Hd(:,i) = -Nd*M(:,i);
    Han(:,i) = Hk*(dot(A,Mnorm(:,i)))*A;
    Heff(:,i) = Hd(:,i) + Han(:,i) + H;
    T_eff(:,i) = -cross(M(:,i),Heff(:,i));
    T_damp(:,i) = alph*cross(Mnorm(:,i),T_eff(:,i));  %
recurrence form
    T_ad(:,i) = -
(a+alph*b)*cross(Mnorm(:,i),cross(M(:,i),s))/gamma;
    T_fl(:,i) = -(b+alph*a)*cross(M(:,i),s)/gamma;
    dM(:,i) = gamma / (1+alph^2) * dt * (T_eff(:,i) +
T_damp(:,i) + T_ad(:,i) + T_fl(:,i));
    Error(i) = norm(dM(:,i))/norm(M(:,i));
end

figure
hold on
plot(t,Mnorm(1,:),'r.')
plot(t,Mnorm(2,:),'g.')
plot(t,Mnorm(3,:),'b.')
grid on

figure
```

```
plot(t,Error)
grid on

figure
[x y z]=sphere;
mesh(x,y,z,'EdgeColor',[0.9,0.9,0.9]);
alpha(0.3)  % set transparency
axis equal
hold on
plot3(Mnorm(1,:),Mnorm(2,:),Mnorm(3,:),'LineWidth',1.5)
xlabel('Mx/M','FontSize',12);
ylabel('My/M','FontSize',12);
zlabel('Mz/M','FontSize',12);
campos([9,11,4.8])  %'CameraPosition'
```

Appendix B. Source Code of SOT Switching Micromagnetic Model

Here, I put the micromagnetic simulation codes (with OOMMF) for the SOT switching simulation in Chapter 3. The simulation setup is described in 3.2.2. Three pieces of simulation codes are put below, used for different scenarios.

Part 1: SOT switching with an external field

Use *Oxs_SpinXferEvolve* extension.

```
# MIF 2.1
# Description: Spin valve example, with no exchange coupling between the layers.

set pi [expr 4*atan(1.0)]
set mu0 [expr 4*$pi*1e-7]
set  multi [expr 0.0001/$mu0]
set xlim 150e-9
set ylim 300e-9
set hbottom 1e-9
set hspacer 2e-9
set htop 3e-9
set zlimp [expr {$htop}]
set zlimn [expr {-$hspacer-$hbottom}]
set cellx 5e-9
set celly 5e-9
set cellz 1e-9


Specify Oxs_ScriptAtlas:EllipticalAtlas [subst {
xrange { [expr {-1.0*$xlim}]  [expr {1.0*$xlim}] }
yrange { [expr {-1.0*$ylim}]  [expr {1.0*$ylim}] }
zrange {$zlimn $zlimp}
regions {bottom spacer top }
script {Elliptical $htop $hspacer $hbottom $xlim $ylim $zlimn $zlimp}
}]


Specify Oxs_RectangularMesh:mesh [subst {
  cellsize { $cellx  $celly  $cellz }
  atlas :EllipticalAtlas
```

```
}]


Specify Oxs_Exchange6Ngbr {
  atlas :EllipticalAtlas
  default_A 0
  A {
    bottom bottom 20e-12
  }
}


Specify Oxs_Demag {}


# Add biasing field to bottom layer. 40 kA/m is approximately 500 Oe.
Specify Oxs_FixedZeeman:Bias [subst {
  field { Oxs_AtlasVectorField {
    atlas :EllipticalAtlas
    default_value {0. 0. 0.}
    values {
  bottom {0. 500. 0.}
    }
  }}
  multiplier [expr 0.0001/$mu0]
}]


Specify Oxs_UniaxialAnisotropy {
   Ha  { Oxs_AtlasScalarField {
      atlas :EllipticalAtlas
      multiplier 79.5775
      default_value 0
      values {
         bottom 18e3
      }
   }}

   axis { Oxs_AtlasVectorField {
      atlas :EllipticalAtlas
      default_value {0 0 1}
      values {
         bottom {0 0 1}
      }
```

```
  }}
}


Specify Oxs_SpinXferEvolve:evolve {
  alpha 0.02
  J 20e11
  mp {-0.15 0 0}
  P 1
  Lambda 1
  J_profile Jprofile
  J_profile_args total_time

}


Specify Oxs_TimeDriver {
 basename spinvalve
 evolver :evolve
 comment {1 deg/ns = 17453293 rad/sec; If Ms=8.6e5, and lambda is small,
        then mxh=1e-6 translates into dm/dt = 2e5 rad/sec = 0.01 deg/ns}
stopping_dm_dt 20
 mesh :mesh
 Ms  { Oxs_AtlasScalarField {
     atlas :EllipticalAtlas
     default_value 0
     values {
       bottom 1200e3
     }
 }}
 m0 {0.001 0 -1}
}


proc Jprofile { t } {
    set scale 0.0;
    if {$t<0.e-9} {
        set scale 0
    } elseif {$t<10e-9} {
        set scale 1.0
    } else {
        set scale 0
    }
    return $scale
```

```
}

proc Elliptical { htop hspacer hbottom xlim ylim zlimn zlimp x y z } {
set xrad [expr {2.*$x-1.}]
set yrad [expr {2.*$y-1.}]
set test [expr $xrad*$xrad+$yrad*$yrad]
if { $test<0.25 && $z>0 && $z<=[expr {$hbottom}]/[expr {$zlimp-$zlimn}]} {return
1}
if { $test<0.25 && $z>[expr {$hbottom}]/[expr {$zlimp-$zlimn}]  && $z<=[expr
{$hbottom+$hspacer}]/[expr {$zlimp-$zlimn}]} {return 2}
if { $test<0.25 && $z>[expr {$hbottom+$hspacer}]/[expr {$zlimp-$zlimn}]} {return 3}
return 0
}
```

Part 2: SOT switching with an external field, considering STT-driven domain wall motion and DMI

Use *Anv_SpinTEvolve*, *Xf_STT*, and *Oxs_DMExchange6Ngbr* extensions.

```
# MIF 2.1
# MIF Example File: spinvalve.mif, dw-160-8-4-3D.mif
# Description: PMA CoFeB spin Hall device, considering the current induced DW
motion.
# Created by Zhengyang Zhao, University of Minnesota, Apr. 2017.

set pi [expr 4*atan(1.0)]
set mu0 [expr 4*$pi*1e-7]
set multi [expr 0.0001/$mu0]
set xlim 300e-9
set ylim 150e-9
set hbottom 1e-9
set hspacer 2e-9
set htop 3e-9
set zlimp [expr {$htop}]
set zlimn [expr {-$hspacer-$hbottom}]
set cellx 5e-9
set celly 5e-9
set cellz 1e-9
```

```
set Ms 1200e3
set J 20e11
set Pfm 0.5
set SHA 0.15
set u [expr -1*$Pfm*$J/$Ms*5.8e-5]
set Hext 500
# If u=0, DW motion is not considered.
# u>0 means DW move to +x.
# For current along +x, u<0.

set D +0.5
set DD [expr {$D/1000}]
# DMI constant of Ta/CoFeB/MgO from [PHYSICAL REVIEW B 91, 014433 (2015)].

Specify Oxs_ScriptAtlas:EllipticalAtlas [subst {
xrange { [expr {-1.0*$xlim}]  [expr {1.0*$xlim}] }
yrange { [expr {-1.0*$ylim}]  [expr {1.0*$ylim}] }
zrange {$zlimn $zlimp}
regions {bottom spacer top }
script {Elliptical $htop $hspacer $hbottom $xlim $ylim $zlimn $zlimp}
}]

Specify Oxs_RectangularMesh:mesh [subst {
  cellsize { $cellx  $celly  $cellz }
  atlas :EllipticalAtlas
}]

Specify Oxs_UniformExchange {
  A 20e-12
}

#uniform DMI is used here
Specify Oxs_DMExchange6Ngbr:DMEx [subst {
  default_D $DD
  atlas :EllipticalAtlas
  D {
    bottom bottom $DD
  }
}]

Specify Oxs_Demag {}

Specify Oxs_FixedZeeman:Bias [subst {
```

```
 field { Oxs_AtlasVectorField {
   atlas :EllipticalAtlas
   default_value {0. 0. 0.}
   values {
  bottom {$Hext 00. 00.}
   }
  }}
 multiplier [expr 0.0001/$mu0]
}]

Specify Oxs_UniaxialAnisotropy [subst {
  Ha  { Oxs_AtlasScalarField {
     atlas :EllipticalAtlas
     multiplier [expr 0.0001/$mu0]
     default_value 0
     values {
       bottom 18e3
     }
  }}
  axis { Oxs_AtlasVectorField {
     atlas :EllipticalAtlas
     default_value {0 0 1}
     values {
       bottom {0 0 1}
     }
  }}
}]

Specify Xf_STT:PL0 [subst {
 P $SHA
 Lambda 1
 J $J
 J_direction +z
 J_profile Jprofile
 J_profile_args total_time
 mp {0 1 0}
 propagate_mp 0
}]
# Comments of Xf_STT: kelvinxyfong.wordpress.com/research/research-interests/oommf-extensions/xf_stt/
# If J_direction is +x, then thickness = xcell, which is not true.

Specify Anv_SpinTEvolve:evolve [subst {
 do_precess 1
```

```
  gamma_LL 2.21e5
  method rkf54s
  alpha 0.02
  u {Oxs_UniformScalarField {
   value $u
   }}
  beta 0.02
}]
# --DW only moves along x direction. See spintevolve.cc Line 460-500.
# That means, current direction is along x.
# --Method: Choose different R-K methods. " rk2, rk4, rk54, rkf54m, or rk54s."
# --beta = tau_ex/tau_sf, the degree of nonadiabacity, which is the ratio between
# the exchange relaxation time tau_ex and the spin-flip relaxation time. See
# spintevolve.cc Line 481 and J. Appl. Phys. 105, 113914 (2009), Equ(2).
# --u=P*u_b*J/e/Ms=P*J/Ms*5.8E-5 (SI units)

Specify Oxs_TimeDriver [subst {
 basename spinvalve
 evolver :evolve
 comment {1 deg/ns = 17453293 rad/sec; If Ms=8.6e5, and lambda is small,
        then mxh=1e-6 translates into dm/dt = 2e5 rad/sec = 0.01 deg/ns}
stopping_dm_dt 20
 mesh :mesh
 Ms  { Oxs_AtlasScalarField {
     atlas :EllipticalAtlas
     default_value 0
     values {
       bottom $Ms
     }
 }}
 m0 {0.001 0 -1}
}]

proc Jprofile { t } {
    set scale 0.0;
    if {$t<0.e-9} {
       set scale 0
    } elseif {$t<10e-9} {
       set scale 1.0
    } else {
       set scale 0
    }
    return $scale
}
```

```
proc Elliptical { htop hspacer hbottom xlim ylim zlimn zlimp x y z } {
set xrad [expr {2.*$x-1.}]
set yrad [expr {2.*$y-1.}]
set test [expr $xrad*$xrad+$yrad*$yrad]
if { $test<0.25 && $z>0 && $z<=[expr {$hbottom}]/[expr {$zlimp-$zlimn}]} {return
1}
if { $test<0.25 && $z>[expr {$hbottom}]/[expr {$zlimp-$zlimn}]  && $z<=[expr
{$hbottom+$hspacer}]/[expr {$zlimp-$zlimn}]} {return 2}
if { $test<0.25 && $z>[expr {$hbottom+$hspacer}]/[expr {$zlimp-$zlimn}]} {return 3}
return 0
}
```

Part 3: SOT switching with the stray field, considering STT-driven domain wall motion and DMI

Use *Anv_SpinTEvolve*, *Xf_STT*, and *Oxs_DMExchange6Ngbr* extensions.

The stray field is pre-calculated and stored in *File1*.

```
# MIF 2.1
# MIF Example File: spinvalve.mif, dw-160-8-4-3D.mif
# Description: PMA CoFeB spin Hall device, considering the current induced DW
motion.
# Created by Zhengyang Zhao, University of Minnesota, Apr. 2017.

set pi [expr 4*atan(1.0)]
set mu0 [expr 4*$pi*1e-7]
set multi [expr 0.0001/$mu0]
set xlim 300e-9
set ylim 150e-9
set hbottom 15e-9
set hspacer 2e-9
set htop 3e-9
set zlimp [expr {$htop}]
set zlimn [expr {-$hspacer-$hbottom}]
set ztot [expr {$zlimp-$zlimn}]
set thick 1e-9
set cellx 5e-9
```

```
set celly 5e-9
set cellz 1e-9
set distance 2e-9

set Ms 1200e3
set J 30e11
set Pfm 0.5
set SHA 0.15
set u [expr -0*$Pfm*$J/$Ms*5.8e-5]
set Hext 0
# If u=0, DW motion is not considered.
# u>0 means DW move to +x.
# For current along +x, u<0.

set D 0.
set DD [expr {$D/1000}]
# DMI constant of Ta/CoFeB/MgO from [PHYSICAL REVIEW B 91, 014433 (2015)].


Specify Oxs_ScriptAtlas:EllipticalAtlas [subst {
xrange { [expr {-1.0*$xlim}]  [expr {1.0*$xlim}] }
yrange { [expr {-1.0*$ylim}]  [expr {1.0*$ylim}] }
zrange {$zlimn $zlimp}
regions {bottom spacer top }
script {Elliptical $htop $hspacer $hbottom $xlim $ylim $zlimn $zlimp}
}]

Specify Oxs_RectangularMesh:mesh [subst {
  cellsize { $cellx  $celly  $cellz }
  atlas :EllipticalAtlas
}]

Specify Oxs_UniformExchange {
  A 20e-12
}

#uniform DMI is used here
Specify Oxs_DMExchange6Ngbr:DMEx [subst {
  default_D $DD
  atlas :EllipticalAtlas
  D {
    bottom bottom $DD
  }
}]
```

```
Specify Oxs_Demag {}

Specify Oxs_FileVectorField:File1 {
  file CompositeSH_CFB_3_150x300_final_demag_Recgrid
  spatial_scaling {1 1 1}
  spatial_offset  {0 0 0}
 }

Specify Oxs_FixedZeeman:Bias {
  field :File1
  multiplier 1
}



Specify Oxs_UniaxialAnisotropy [subst {
  Ha  { Oxs_AtlasScalarField {
    atlas :EllipticalAtlas
    multiplier [expr 0.0001/$mu0]
    default_value 0
    values {
      bottom 18e3
    }
  }}
  axis { Oxs_AtlasVectorField {
    atlas :EllipticalAtlas
    default_value {0 0 1}
    values {
      bottom {0 0 1}
    }
  }}
}]

Specify Xf_STT:PL0 [subst {
 P $SHA
 Lambda 1
 J $J
 J_direction +z
 J_profile Jprofile
 J_profile_args total_time
 mp {0 1 0}
 propagate_mp 0
```

```
}]
# Comments of Xf_STT: kelvinxyfong.wordpress.com/research/research-
interests/oommf-extensions/xf_stt/
# If J_direction is +x, then thickness = xcell, which is not true.

Specify Anv_SpinTEvolve:evolve [subst {
  do_precess 1
  gamma_LL 2.21e5
  method rkf54s
  alpha 0.02
  u {Oxs_UniformScalarField {
   value $u
   }}
  beta 0.04
}]
# --DW only moves along x direction. See spintevolve.cc Line 460-500.
# That means, current direction is along x.
# --Method: Choose different R-K methods. " rk2, rk4, rk54, rkf54m, or rk54s."
# --beta = tau_ex/tau_sf, the degree of nonadiabacity, which is the ratio between
# the exchange relaxation time tau_ex and the spin-flip relaxation time. See
# spintevolve.cc Line 481 and J. Appl. Phys. 105, 113914 (2009), Equ(2).
# --u=P*u_b*J/e/Ms=P*J/Ms*5.8E-5 (SI units)

Specify Oxs_TimeDriver [subst {
 basename spinvalve
 evolver :evolve
 comment {1 deg/ns = 17453293 rad/sec; If Ms=8.6e5, and lambda is small,
        then mxh=1e-6 translates into dm/dt = 2e5 rad/sec = 0.01 deg/ns}
stopping_dm_dt 20
 mesh :mesh
 Ms  { Oxs_AtlasScalarField {
     atlas :EllipticalAtlas
     default_value 0
     values {
        bottom $Ms
     }
 }}
 m0 {0.001 0 -1}
}]

proc Jprofile { t } {
    set scale 0.0;
    if {$t<0.e-9} {
        set scale 0
```

```
    } elseif {$t<15e-9} {
        set scale 1.0
    } else {
        set scale 0
    }
    return $scale
}


proc Elliptical { htop hspacer hbottom xlim ylim zlimn zlimp x y z } {
global distance
global ztot
global thick
set xrad [expr {2.*$x-1.}]
set yrad [expr {2.*$y-1.}]
set test [expr $xrad*$xrad+$yrad*$yrad]
if {$test<0.25} {
  if {$z> 1-[expr {$distance+$htop+$thick}]/$ztot && $z<= 1-[expr
{$distance+$htop}]/$ztot } {return 1}
  if {$z> 1-[expr {$distance+$htop}]/$ztot  } {return 3}
  if {$z< 1-[expr {$distance+$htop+$thick}]/$ztot} {return 2}
  }
return 0
}
```

Appendix C. Publication List

Research articles:

[1] P. Sheng*, **Z. Zhao***, O. J. Benally, D. Zhang, and J. Wang, *Thermal Contribution in the Electrical Switching Experiments with Heavy Metal / Antiferromagnet Structures*, Submitted (2021).

[2] **Z. Zhao**, A. K. Smith, M. Jamali, and J. Wang, *External-Field-Free Spin Hall Switching of Perpendicular Magnetic Nanopillar with a Dipole-Coupled Composite Structure*, Adv. Electron. Mater. **6**, 1901368 (2020). **[Cited by: 34]**

[3] **Z. Zhao**, W. Echtenkamp, M. Street, C. Binek, and J.-P. Wang, *Magnetoelectric Device Feasibility Demonstration — Voltage Control of Exchange Bias in Perpendicular Cr2O3 Hall Bar Device*, in *2016 74th Annual Device Research Conference (DRC)*, Vols. 2016-Augus (IEEE, 2016), pp. 1–2.

[4] **Z. Zhao**, M. Jamali, N. D'Souza, D. Zhang, S. Bandyopadhyay, J. Atulasimha, and J.-P. Wang, *Giant Voltage Manipulation of MgO-Based Magnetic Tunnel Junctions via Localized Anisotropic Strain: A Potential Pathway to Ultra-Energy-Efficient Memory Technology*, Appl. Phys. Lett. **109**, 092403 (2016). **[Cited by: 79]**

[5] **Z. Zhao**, M. Jamali, A. K. Smith, and J.-P. Wang, *Spin Hall Switching of the Magnetization in Ta/TbFeCo Structures with Bulk Perpendicular Anisotropy*, Appl. Phys. Lett. **106**, 132404 (2015). **[Cited by: 97]**

[6] D. Bhattacharya, P. Sheng, M. A. Abeed, **Z. Zhao**, H. Li, J.-P. Wang, S. Bandyopadhyay, B. Ma, and J. Atulasimha, *Surface Acoustic Wave Induced Modulation of Tunneling Magnetoresistance in Magnetic Tunnel Junctions*, ArXiv: 2103.15303 (2021).

[7] S. Resch, S. K. Khatamifard, Z. I. Chowdhury, M. Zabihi, **Z. Zhao**, H. Cilasun, J.-P. Wang, S. S. Sapatnekar, and U. R. Karpuzcu, *MOUSE: Inference In Non-Volatile Memory for Energy Harvesting Applications*, in *2020 53rd Annual IEEE/ACM International Symposium on Microarchitecture (MICRO)*, Vols. 2020-Octob (IEEE, 2020), pp. 400–414.

[8] H. Cilasun, S. Resch, Z. I. Chowdhury, E. Olson, M. Zabihi, **Z. Zhao**, T. Peterson, J.-P. Wang, S. S. Sapatnekar, and U. Karpuzcu, *CRAFFT: High Resolution FFT Accelerator In Spintronic Computational RAM*, in *2020 57th ACM/IEEE Design Automation Conference (DAC)*, Vols. 2020-July (IEEE, 2020), pp. 1–6.

[9] H. Cılasun, S. Resch, Z. I. Chowdhury, E. Olson, M. Zabihi, **Z. Zhao**, T. Peterson, K. Parhi, J.-P. Wang, S. S. Sapatnekar, and U. Karpuzcu, *An Inference and Learning Engine for Spiking Neural Networks in Computational RAM (CRAM)*, ArXiv: 2006.03007 (2020).

[10] Z. I. Chowdhury, M. Zabihi, S. K. Khatamifard, **Z. Zhao**, S. Resch, M. Razaviyayn, J.-P. Wang, S. S. Sapatnekar, and U. R. Karpuzcu, *A DNA Read Alignment Accelerator Based on Computational RAM*, IEEE J. Explor. Solid-State Comput. Devices Circuits **6**, 80 (2020).

[11] M. Zabihi, A. K. Sharma, M. G. Mankalale, Z. I. Chowdhury, **Z. Zhao**, S. Resch, U. R. Karpuzcu, J.-P. Wang, and S. S. Sapatnekar, *Analyzing the Effects of Interconnect Parasitics in the STT CRAM In-Memory Computational Platform*, IEEE J. Explor. Solid-State Comput. Devices Circuits **6**, 71 (2020).

[12] D. Zhang, M. Bapna, W. Jiang, D. P. de Sousa, Y.-C. Liao, **Z. Zhao**, Y. Lv, A. Naeemi, T. Low, S. A. Majetich, and J.-P. Wang, *Bipolar Electric-Field Switching of Perpendicular Magnetic Tunnel Junctions through Voltage-Controlled Exchange Coupling*, ArXiv: 1912.10289 (2019).

[13] Z. I. Chowdhury, S. K. Khatamifard, **Z. Zhao**, M. Zabihi, S. Resch, M. Razaviyayn, J.-P. Wang, S. Sapatnekar, and U. R. Karpuzcu, *Spintronic In-Memory Pattern Matching*, IEEE J. Explor. Solid-State Comput. Devices Circuits **5**, 206 (2019).

[14] S. Resch, S. K. Khatamifard, Z. I. Chowdhury, M. Zabihi, **Z. Zhao**, J. P. Wang, S. S. Sapatnekar, and U. R. Karpuzcu, *PIMBALL: Binary Neural Networks in Spintronic Memory*, ACM Trans. Archit. Code Optim. **16**, 1 (2019).

[15] M. Zabihi, **Z. Zhao**, Z. I. Chowdhury, S. Resch, M. DC, T. Peterson, U. R. Karpuzcu, J. P. Wang, and S. S. Sapatnekar, *True In-Memory Computing with the CRAM: From Technology to Applications*, in *Proceedings of the ACM Great Lakes Symposium on VLSI, GLSVLSI*, Vol. 17 (ACM, New York, NY, USA, 2019), p. 379.

[16] M. DC, T. Liu, J.-Y. Chen, T. Peterson, P. Sahu, H. Li, **Z. Zhao**, M. Wu, and J.-P. Wang, *Room-Temperature Spin-to-Charge Conversion in Sputtered Bismuth Selenide Thin Films via Spin Pumping from Yttrium Iron Garnet*, Appl. Phys. Lett. **114**, 102401 (2019).

[17] M. Zabihi, **Z. Zhao**, D. Mahendra, Z. I. Chowdhury, S. Resch, T. Peterson, U. R. Karpuzcu, J.-P. Wang, and S. S. Sapatnekar, *Using Spin-Hall MTJs to Build an Energy-Efficient In-Memory Computation Platform*, in *20th International Symposium on Quality Electronic Design (ISQED)*, Vols. 2019-March (IEEE, 2019), pp. 52–57. **[Best paper]**

[18] M. G. Mankalale, **Z. Zhao**, J.-P. Wang, and S. S. Sapatnekar, *SkyLogic—A Proposal for a Skyrmion-Based Logic Device*, IEEE Trans. Electron Devices **66**, 1990 (2019).

[19] J. Song, I. Ahmed, **Z. Zhao**, D. Zhang, S. S. Sapatnekar, J.-P. Wang, and C. H. Kim, *Evaluation of Operating Margin and Switching Probability of Voltage-Controlled Magnetic Anisotropy Magnetic Tunnel Junctions*, IEEE J. Explor.

Solid-State Comput. Devices Circuits **4**, 76 (2018).

[20] M. Wang, W. Cai, D. Zhu, Z. Wang, J. Kan, **Z. Zhao**, K. Cao, Z. Wang, Y. Zhang, T. Zhang, C. Park, J.-P. Wang, A. Fert, and W. Zhao, *Field-Free Switching of a Perpendicular Magnetic Tunnel Junction through the Interplay of Spin–Orbit and Spin-Transfer Torques*, Nat. Electron. **1**, 582 (2018).

[21] Z. Liang, M. G. Mankalale, J. Hu, **Z. Zhao**, J.-P. Wang, and S. S. Sapatnekar, *Performance Characterization and Majority Gate Design for MESO-Based Circuits*, IEEE J. Explor. Solid-State Comput. Devices Circuits **4**, 51 (2018).

[22] M. DC, R. Grassi, J.-Y. Chen, M. Jamali, D. Reifsnyder Hickey, D. Zhang, **Z. Zhao**, H. Li, P. Quarterman, Y. Lv, M. Li, A. Manchon, K. A. Mkhoyan, T. Low, and J.-P. Wang, *Room-Temperature High Spin–Orbit Torque Due to Quantum Confinement in Sputtered BixSe(1–x) Films*, Nat. Mater. **17**, 800 (2018).

[23] M. Zabihi, Z. I. Chowdhury, **Z. Zhao**, U. R. Karpuzcu, J.-P. Wang, and S. S. Sapatnekar, *In-Memory Processing on the Spintronic CRAM: From Hardware Design to Application Mapping*, IEEE Trans. Comput. **68**, 1159 (2019).

[24] D. L. Zhang, C. Sun, Y. Lv, K. B. Schliep, **Z. Zhao**, J. Y. Chen, P. M. Voyles, and J. P. Wang, *L10 Fe-Pd Synthetic Antiferromagnet through an Fcc Ru Spacer Utilized for Perpendicular Magnetic Tunnel Junctions*, Phys. Rev. Appl. **9**, 044028 (2018).

[25] D. L. Zhang, K. B. Schliep, R. J. Wu, P. Quarterman, D. Reifsnyder Hickey, Y. Lv, X. Chao, H. Li, J. Y. Chen, **Z. Zhao**, M. Jamali, K. A. Mkhoyan, and J. P. Wang, *Enhancement of Tunneling Magnetoresistance by Inserting a Diffusion Barrier in L10-FePd Perpendicular Magnetic Tunnel Junctions*, Appl. Phys. Lett. **112**, 152401 (2018).

[26] I. Ahmed, **Z. Zhao**, M. G. Mankalale, S. S. Sapatnekar, J. P. Wang, and C. H. Kim, *A Comparative Study between Spin-Transfer-Torque and Spin-Hall-Effect Switching Mechanisms in PMTJ Using SPICE*, IEEE J. Explor. Solid-State Comput. Devices Circuits **3**, 74 (2017).

[27] J.-Y. Chen, M. DC, D. Zhang, **Z. Zhao**, M. Li, and J.-P. Wang, *Field-Free Spin-Orbit Torque Switching of Composite Perpendicular CoFeB/Gd/CoFeB Layers Utilized for Three-Terminal Magnetic Tunnel Junctions*, Appl. Phys. Lett. **111**, 012402 (2017).

[28] M. G. Mankalale, Z. Liang, **Z. Zhao**, C. H. Kim, J. P. Wang, and S. S. Sapatnekar, *CoMET: Composite-Input Magnetoelectric-Based Logic Technology*, IEEE J. Explor. Solid-State Comput. Devices Circuits **3**, 27 (2017).

[29] M. Jamali, **Z. Zhao**, D. C. Mahendra, D. Zhang, H. Li, A. K. Smith, and J. P. Wang, *Planar Hall Effect Based Characterization of Spin Orbital Torques in Ta/CoFeB/MgO Structures*, J. Appl. Phys. **119**, 133902 (2016).

[30] M. Jamali, J. S. Lee, J. S. Jeong, F. Mahfouzi, Y. Lv, **Z. Zhao**, B. K. Nikolić, K. A. Mkhoyan, N. Samarth, and J. P. Wang, *Giant Spin Pumping and Inverse Spin Hall Effect in the Presence of Surface and Bulk Spin-Orbit Coupling of Topological Insulator Bi2Se3*, Nano Lett. **15**, 7126 (2015).

[31] M. Jamali, Y. Lv, **Z. Zhao**, and J. P. Wang, *Sputtering of Cobalt Film with Perpendicular Magnetic Anisotropy on Disorder-Free Graphene*, AIP Adv. **4**, 107102 (2014).

Patents:

[1] *Computational random access memory (CRAM) based on spin-orbit torque devices*. US20200279597A1 (2020).

[2] *Fast magnetoelectric device based on current-driven domain wall propagation*. US10217522B2 (2019).

Book chapter:

[1] J.-P. Wang, M. Jamali, A.K. Smith, **Z. Zhao**, *Magnetic Tunnel Junction Based and Integrated Logic and Computation*, in: S. Bandyopadhyay, et al. *Nanomagnetic and Spintronic Devices for Energy Efficient Memory and Computing*, John Wiley & Sons, (2016).